

N 70 37226

N 70 37240

NATIONAL AERONAUTICS AND SPACE ADMINISTRATION CR 112344

*Technical Report 32-1475*

*Proceedings of the Conference on Scientific  
Applications of Radio and Radar Tracking  
in the Space Program*

*Held at the Jet Propulsion Laboratory  
Pasadena, California  
April 9-10, 1969*

*Edited by  
L. Efron  
C. B. Solloway*

CAGE FILE  
COPY

JET PROPULSION LABORATORY  
CALIFORNIA INSTITUTE OF TECHNOLOGY  
PASADENA, CALIFORNIA

July 1, 1970

NATIONAL AERONAUTICS AND SPACE ADMINISTRATION

*Technical Report 32-1475*

*Proceedings of the Conference on Scientific  
Applications of Radio and Radar Tracking  
in the Space Program*

*Held at the Jet Propulsion Laboratory  
Pasadena, California  
April 9–10, 1969*

*Edited by  
L. Efron  
C. B. Solloway*

**JET PROPULSION LABORATORY  
CALIFORNIA INSTITUTE OF TECHNOLOGY  
PASADENA, CALIFORNIA**

July 1, 1970

Prepared Under Contract No. NAS 7-100  
National Aeronautics and Space Administration

## Preface

A century ago, in 1864, James Clerk Maxwell foresaw the possibility of the propagation of electromagnetic waves in space from waves originating in wires. In his paper, "On A Dynamical Theory of the Electromagnetic Field," he was the first to demonstrate mathematically the laws of the transfer of electromagnetic energy through space at the speed of light.

When, in 1879, the Anglo-U.S. inventor David Edward Hughes received a signal one-quarter of a mile away from a spark generator, many scientists were of the opinion that this was a case of ordinary induction, and so, Heinrich Rudolf Hertz of Germany is credited with the production and detection of radio signals in 1886. In the early 1890s the achievements of O. Lodge (England), E. Branly (France), and A. S. Popov (Russia) progressively pushed back frontiers with transmissions across distances from 100 yards to over a mile.

Guglielmo Marconi attained operating ranges of several miles with improved equipment and, in December 1901, culminated one era and began another by successfully sending a signal from Cornwall, England across the Atlantic Ocean to a station in St. John's, Newfoundland.

By the beginning of this century, the phenomena of radio reflection or echo had been repeatedly observed and comments were often made regarding possible uses and applications. Nikola Tesla wrote in *Century Magazine* (June 1900) that by means of radio, a moving object, such as a ship at sea, might be detected and located. Simple radar or radio echo detectors were patented, as exemplified by a device to prevent ship collisions (1904) by a German engineer, Christian Hülsmeyer; interest in such a device was lacking at the time.

After 1925, radio waves began to be used to explore the ionosphere and our upper atmosphere. The 1930s saw the start of passive radio astronomy and the development of practical radar. Radio echoes from the moon were detected in 1946, and in 1958, the first successful attempt to receive a return from our next nearest neighbor, Venus, was reported. In the following year, the sun was successfully used as a reflector.

The dawning of the "space age" permits another advance, the ability to put receivers, transmitters, and transponders at sites remote from the vicinity of the earth. Controlled coherent radio sources are now used to explore the geometry and mechanics of the solar system, determine planetary masses, figures, topographies, atmospheric and gravitational fields, explore the interplanetary medium, and perform tests of general relativity theory. The horizon of limitations as to the knowledge yet to be gained from radio and radar experiments is still a long way off.



## Preface (contd)

Because no conference devoted exclusively to the field of radio and radar exploration of the solar system with earth and spacecraft based sources had ever been convened, it has been a pleasure for the Jet Propulsion Laboratory to host this conference on the subject of "Scientific Applications of Radio and Radar Tracking in the Space Program." Although nearly all the active participants were acquainted with each other and communicate or cross paths periodically, this was the first time that so large a group of researchers, representing nearly every involved center, were gathered together. The conference and the publishing of the papers thereof was under the auspices of the Mission Analysis Division of the Jet Propulsion Laboratory.

In the proceedings of the conference, the editors have reproduced those addresses for which the authors have provided manuscripts. Since some attendees reported on work in progress, these papers are, in general, represented by abstract only. In cases where the contents of the address is already available in the literature, the reference is given.

L. Efron  
C. B. Solloway  
Conference Chairmen

## Contents

### Session I Data Taking Techniques

<b>A Binary Coded Sequential Acquisition Ranging System . . . . .</b>	<b>3</b>
<i>W. L. Martin</i>	
<b>Investigations of Very Long Baseline Interferometry at Smithsonian Astrophysical Observatory . . . . .</b>	<b>15</b>
<i>R. D. Michelini</i>	
<b>The Haystack Planetary Ranging Radar . . . . .</b>	<b>27</b>
<i>J. V. Evans, R. P. Ingalls, and G. H. Pettengill</i>	
<b>Improvements in Radar Ranging Accuracy Using Correlation Techniques . . .</b>	<b>37</b>
<i>G. H. Pettengill</i>	
<b>Deep Space Ranging . . . . .</b>	<b>37</b>
<i>R. C. Tausworthe</i>	
<b>S-Band Faraday Rotation Measurements of the Solar Corona Using Signals from Pioneer VI Solar Occultation . . . . .</b>	<b>39</b>
<i>G. S. Levy</i>	

### Session II Data Processing and Modeling Techniques

<b>Application of a Model Fitting Procedure to the Determination of Unknown Parameters in Several Theoretical Backscatter Models of Venus at 70-cm Wavelength . . . . .</b>	<b>43</b>
<i>R. F. Jurgens</i>	
<b>Parameter Estimation From Sets of Two-Dimensional Maps . . . . .</b>	<b>51</b>
<i>R. F. Jurgens</i>	
<b>The Potential of Interplanetary Spacecraft Data for Testing Gravitational Theories . . . . .</b>	<b>57</b>
<i>L. D. Friedman</i>	
<b>Reconstruction of JPL 1967 Range Data for Venus and the Processing of Radar Data . . . . .</b>	<b>63</b>
<i>D. A. O'Handley</i>	
<b>Limitations to Navigation Accuracy in Support of the Planetary Encounter Phase of a Deep Space Mission . . . . .</b>	<b>81</b>
<i>D. W. Trask</i>	
<b>Deductions of Observations of the Solar System . . . . .</b>	<b>81</b>
<i>M. E. Ash, I. I. Shapiro, and W. B. Smith</i>	

## Contents (contd)

### Session III Scientific Exploitation of the Data

<b>Selected Results From Analysis of Radar and Optical Observations of Icarus and the Inner Planets . . . . .</b>	<b>85</b>
<i>W. B. Smith, I. I. Shapiro, M. E. Ash, G. H. Pettengill, and R. P. Ingalls</i>	
<b>The Obliquity of Mercury . . . . .</b>	<b>91</b>
<i>S. J. Peale</i>	
<b>Lunar Gravimetrics . . . . .</b>	<b>91</b>
<i>P. M. Muller and W. L. Sjogren</i>	
<b>Mascons: Local Lunar Gravity Features . . . . .</b>	<b>93</b>
<i>P. Gottlieb</i>	
<b>Interpretation of Lunar Mass Concentrations . . . . .</b>	<b>93</b>
<i>W. M. Kaula</i>	
<b>Radar Photograph of the Moon at 3.8-cm Wavelength . . . . .</b>	<b>95</b>
<i>S. H. Zisk</i>	
<b>Recent Results on the Gravitational Field of the Moon and Some Geophysical Applications . . . . .</b>	<b>95</b>
<i>W. H. Michael, Jr.</i>	

### Session IV Planetary Structure and Atmosphere

<b>Remarks on the Inference of Neutral Atmospheric Parameters From Microwave Occultation Data . . . . .</b>	<b>99</b>
<i>F. F. Fishbach</i>	
<b>Profile Inversion Processing of Radio Occultation Data for the Determination of Planetary Atmospheres . . . . .</b>	<b>105</b>
<i>I. Shear, R. R. Bravoco, P. E. Langevin, and M. D. Grossi</i>	
<b>Inverting Radio Occultation Data Using Empirical Orthogonal Functions . . . .</b>	<b>115</b>
<i>B. Lusignan</i>	
<b>Some Characteristics of the Solar Atmosphere That May Be Investigated by a VHF Antenna System . . . . .</b>	<b>119</b>
<i>J. C. James</i>	
<b>Radar Studies of Venus at 3.8-cm Wavelength . . . . .</b>	<b>127</b>
<i>J. V. Evans, et al.</i>	
<b>Radar Measurements of Lunar Surface Roughness . . . . .</b>	<b>145</b>
<i>A. Shapiro, E. A. Uliana, and B. S. Yaplee</i>	

## Contents (contd)

**Topography and the Surface of Mars . . . . . 161**

*A. B. Binder*

**Probing Planetary Surface and Subsurface Structures with Bistatic Radar . . . 161**

*G. L. Tyler*

## List of Attendees

ANDERSON, J. D.  
Jet Propulsion Laboratory  
ASH, MICHAEL E.  
Lincoln Laboratory

BAYLEY, W. H.  
Jet Propulsion Laboratory  
BINDER, ALAN B.  
Illinois Institute of Technology  
Research Institute  
BORN, GEORGE H.  
National Aeronautics and  
Space Administration  
BOURKE, R. D.  
Jet Propulsion Laboratory  
BRAVOCO, RALPH R.  
Raytheon  
BROUCKE, R. A.  
Jet Propulsion Laboratory  
BRUNK, WILLIAM E.  
National Aeronautics and  
Space Administration  
BURKE, J. D.  
Jet Propulsion Laboratory

CAIN, D. L.  
Jet Propulsion Laboratory  
COLELLA, F. J.  
Jet Propulsion Laboratory  
CONEL, J. E.  
Jet Propulsion Laboratory  
CROFT, THOMAS A.  
Stanford University  
CROSS, ROBERT K.  
Raytheon  
CUTTING, E.  
Jet Propulsion Laboratory

DALLAS, S. S.  
Jet Propulsion Laboratory

EFRON, L.  
Jet Propulsion Laboratory  
ESHLEMAN, VON R.  
Stanford University  
EVANS, J. V.  
Lincoln Laboratory

FISCHBACH, FREDERICK F.  
University of Michigan  
FJELDBO, G.  
Jet Propulsion Laboratory  
FRIEDMAN, LOUIS D.  
Massachusetts Institute of Technology

GATES, C. R.  
Jet Propulsion Laboratory  
GEORGEVIC, R. M.  
Jet Propulsion Laboratory

GOLDSTEIN, R. M.  
Jet Propulsion Laboratory  
GORDON, H.  
Jet Propulsion Laboratory  
GOTTLIEB, P.  
Jet Propulsion Laboratory

HAMILTON, T. W.  
Jet Propulsion Laboratory  
HOLDRIDGE, D. B.  
Jet Propulsion Laboratory  
HOWARD, H. T.  
Stanford University

INGRAM, DOUGLAS S.  
University of Texas

JAMES, JESSE C.  
Massachusetts Institute of Technology  
JONES, D. W.  
University of Texas  
JONES, J. COLIN  
Illinois Institute of Technology  
Research Institute  
JURGENSE, RAYMOND F.  
Arecibo Ionospheric Observatory

KAULA, W. M.  
University of California, Los Angeles  
KHATIB, A.  
Jet Propulsion Laboratory  
KIZNER, W.  
Jet Propulsion Laboratory  
KLEPCZYNSKI, W. J.  
Naval Observatory  
KLIORE, A. J.  
Jet Propulsion Laboratory

LAIRMORE, G. E.  
Jet Propulsion Laboratory  
LASS, H.  
Jet Propulsion Laboratory  
LEVY, G. S.  
Jet Propulsion Laboratory  
LIESKE, J. H.  
Jet Propulsion Laboratory  
LIWSHITZ, M.  
Bellcomm  
LORELL, J.  
Jet Propulsion Laboratory  
LUBOWE, A. G.  
Bell Telephone Laboratories

MACDORAN, P.  
Jet Propulsion Laboratory  
MARTIN, W. L.  
Jet Propulsion Laboratory  
MAYO, WILBUR L.  
Langley Research Center

## List of Attendees (contd)

MEGHREBLIAN, R. V.  
Jet Propulsion Laboratory  
MELBOURNE, W. G.  
Jet Propulsion Laboratory  
MICHAEL, W. H.  
Langley Research Center  
MICHELINI, R. D.  
Smithsonian Astrophysical Laboratory  
MOTTINGER, N. A.  
Jet Propulsion Laboratory  
MOYER, T. D.  
Jet Propulsion Laboratory  
MUHLEMAN, D. O.  
Owens Valley Radio Observatory  
MULHOLLAND, J. D.  
Jet Propulsion Laboratory  
MULLER, P. M.  
Jet Propulsion Laboratory  
  
NULL, G. W.  
Jet Propulsion Laboratory  
  
OESTERWINTER, CLAUS  
Naval Weapons Laboratory  
O'HANDLEY, D. A.  
Jet Propulsion Laboratory  
ONDRASIK, J.  
Jet Propulsion Laboratory  
  
PEALE, STANTON J.  
University of California, Santa Barbara  
PETTENGILL, GORDON H.  
Arecibo Ionospheric Observatory  
POSNER, C.  
Jet Propulsion Laboratory  
POUNDER, E.  
Jet Propulsion Laboratory  
PRINGLE, RALPH, JR.  
Bell Telephone Laboratories  
  
REED, R.  
Jet Propulsion Laboratory  
ROSS, DENNIS K.  
Iowa State University

ROURKE, K.  
Jet Propulsion Laboratory  
  
SCHNEIDERMAN, D.  
Jet Propulsion Laboratory  
SEIDELMANN, P. K.  
Naval Observatory  
SHAPIRO, A.  
Naval Research Laboratory  
SHEAR, IRWIN  
Raytheon  
SINCLAIR, W. S.  
Jet Propulsion Laboratory  
SJOGREN, W. L.  
Jet Propulsion Laboratory  
SMITH, W. B.  
Lincoln Laboratory  
SOLLOWAY, C. B.  
Jet Propulsion Laboratory  
STEPHENSON, R. R.  
Jet Propulsion Laboratory  
STIFFLER, J. J.  
Raytheon  
  
TAPLEY, B. D.  
University of Texas  
TAUSWORTHE, R. C.  
Jet Propulsion Laboratory  
THOMAS, DAVID L.  
Department of Defense  
THOMPSON, T. W.  
Arecibo Ionospheric Observatory  
TRASK, D. W.  
Jet Propulsion Laboratory  
TYLER, G. L.  
Stanford University  
  
WINN, F. B.  
Jet Propulsion Laboratory  
  
ZIELENBACH, J. W.  
Jet Propulsion Laboratory  
ZISK, S. H.  
Lincoln Laboratory

*Session I*  
*Data Taking Techniques*

*Session Chairman*  
*Dr. Gordon H. Pettengill*  
*Arecibo Ionospheric Observatory*





# A Binary Coded Sequential Acquisition Ranging System

W. L. Martin

Communications Systems Research  
Jet Propulsion Laboratory  
Pasadena, California

*This paper describes an R&D ranging system built by the Jet Propulsion Laboratory. Utilization of spacecraft doppler to provide a synchronous model of the received signal is discussed. The correlation properties of binary codes, as well as the resultant simplifications of the spacecraft regenerative transponder (necessary for very deep space probes) are reviewed. Brief mention is made of the integrated circuit packaging scheme that yielded a twentyfold reduction in system size together with a concomitant increase in reliability. Finally, the system accuracy, its relationship to the hardware, and a description of the data output and its meaning to the user are considered.*

## I. Introduction

The advent of high-speed digital logic (100 MHz and above) has made possible a dramatic simplification in the design of high-precision ranging equipment. The employment of sequential transmission of binary code components and a phase estimation program has resulted in a minimum acquisition time machine.

In the past, ranging systems could be conveniently assigned to one of two classifications depending upon their method of coding:

- (1) The single component systems that utilized a pseudonoise code of sufficient period to resolve range ambiguities and a bit length short enough to provide the required resolution. Examples include lunar and planetary mapping systems in which simplicity of design and acquisition procedure

have been traded for relatively long acquisition times.

- (2) The multicomponent systems that combined a group of short sequences into a code of the desired length. Examples are the *Apollo* Mark I, *Mariner* 67-69, and *Sidetone* ranging systems in which the intent was clearly to minimize the acquisition time.

It has been shown by Titsworth (Ref. 1) that the best acquisition time for a multicomponent, single correlator system is achieved when the individual component lengths  $v_i$  are

$$v_i \simeq p^{1/n} \simeq e \quad (1)$$

where  $p$  is the combined code period,  $n$  is the number of components, and  $e$  is the component length. Unfortunately, an additional constraint on pseudonoise coded

systems demands that the individual component periods must all be relatively prime. Thus, the designer is forced to trade optimality for reality and select components lengths that best fit both criteria. Typical choices for component lengths include 2, 7, 11, 15, 19, 23, etc.

While offering a substantial reduction in acquisition time, the multicomponent combinatorial units do suffer some degradation due to component sharing of the transmitted power (Ref. 1). This degradation can be overcome by sequentially transmitting components, one at a time, so that full transmitted power is available to each. For example, a 3-dB improvement is realized over combinational systems allocating 50% of the power to each component, and a 6-dB gain is realized over those assigning 25% to each component. Thus it appears that the optimal system would sequentially transmit  $n$  components of length  $e$ .

## II. A Binary-Coded Sequential Ranging Machine

Figure 1 is a simplified block diagram of a binary-coded sequential acquisition ranging system. A frequency synthesizer generates a frequency  $f_s$  (nominally 22 MHz) that is multiplied by three and is phase modulated by the transmitter coder. The code is generated by dividing the 66-MHz output from the  $\times 3$  multiplier by 64

and applying the result to an 18-stage binary counter. Each of the 18 outputs from the binary counter is individually selectable for modulating the transmitter. Thus, the code period  $t_n$  of the  $n$ th component is given by

$$t_n = \frac{64 \times 2^n}{3 f_s} \quad (2)$$

From Eq. (2), it can be seen that the code period is irrevocably tied to the transmitter frequency. Changing the transmitter frequency, as is done from time to time to assure optimum reception at the spacecraft, also changes the coder frequency in direct proportion.

A virtually identical set of hardware exists in the receiver; however, the  $\div 64$  is preceded by a doppler pulse adder circuit. The latter accepts as one of its inputs the 66 MHz signal from the  $\times 3$  multiplier in the transmitter chain. A second input connects the RF doppler  $f_d$ , properly scaled, from the Deep Space Instrumentation Facility (DSIF) receiver. In the ranging mode, the output from the pulse adder circuit is the algebraic sum of the two inputs:

$$3f_s + f_d$$

The receiver coder is a duplicate of its counterpart in the transmitter except for the inclusion of a second out-

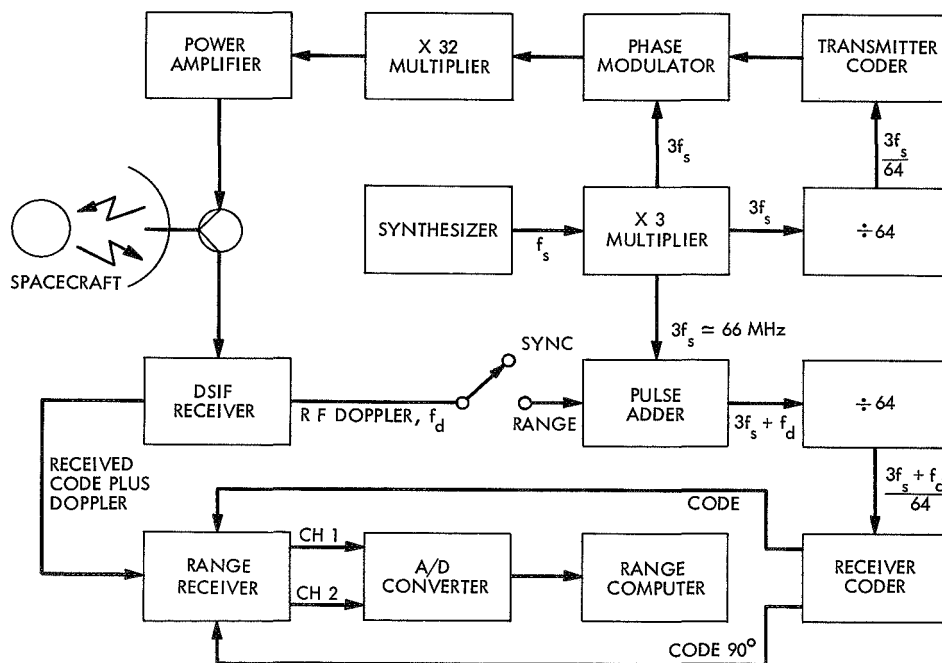


Fig. 1. Binary-coded sequential acquisition ranging system

put providing code delaying by  $\pi/2$ . This second channel is combined with the first to establish the amplitude of the returning signal, a necessary step in measuring its phase.

When the Range-Sync switch is in SYNC position, the two coders will be operating synchronously. Because of the doppler frequency shift due to the relative motion of the spacecraft, the received signal will be slipping in phase with respect to the coders. If, at some time  $t_0$ , the switch is changed to the RANGE position, the receiver coder frequency is instantly modified by the RF doppler and becomes coherent with the signal being received from the spacecraft. Assuming that the two coders have been synchronized prior to the changeover, the phase difference between the receiver coder and the incoming signal is a measure of range. Since this phase displacement is constant by virtue of the doppler rate aiding, the range measurement can be made at leisure.

Thus, a coherent model of the received signal is generated by modifying the frequency of the transmitted code with the spacecraft doppler. The tracking operation is open-loop, eliminating any settling time and greatly simplifying the hardware design. Two conditions are necessary to make the system workable. First, before the RF doppler can be used as a rate aiding signal, the code must bear some simple, fixed relationship to the transmitted frequency. This condition is apparent from Eq. (2),

which can be conveniently rewritten in terms of the transmitted frequency  $f_T$

$$t_n = \frac{2048}{f_T} \times 2^n \quad (3)$$

Second, the mechanization required the availability of high-speed digital logic that could conveniently handle 66 MHz. Since the pulse adder serves to add or delete cycles from the 66-MHz reference, the logic must have a speed capacity well in excess of that frequency.

The question might well arise as to why such a high frequency was selected for the doppler addition. The answer can be best explained by an example. Consider a target whose distance is increasing at a uniform rate resulting in a constant doppler frequency. Since the spacecraft is receding, the received frequency will be lower than that transmitted by the two-way doppler. Each doppler cycle detected by the DSIF receiver serves to delete one 66-MHz cycle in the pulse adder. Therefore, the receiver coder phase will be delayed in a step-wise manner causing a small phase jitter with respect to the incoming signal. The higher the frequency at which the doppler addition is done, the less the phase jitter.

The ranging receiver is shown in a simplified block diagram in Fig. 2. The input, obtained from the DSIF receiver, consists of 10-MHz phase modulated signal

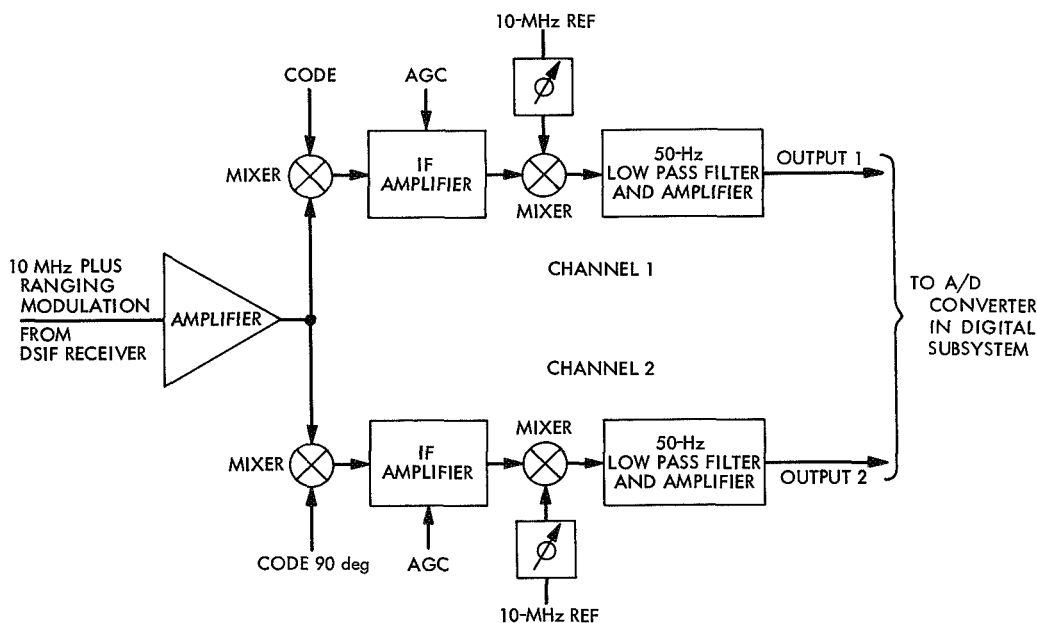


Fig. 2. Ranging receiver

with the code modified by two-way doppler. Two identical channels mix this signal with that from the receiver coder. The mixers are simple, rather inexpensive, diode switches that pass or invert the received signal depending upon whether the local code is a 1 or a 0. When the receiver coder is in phase with the code returning from the spacecraft, the mixer output will be a pure 10-MHz sine wave. Any phase displacement will result in a phase inversion of the sine wave. After amplification, a second identical mixer removes the 10-MHz reference, translating the received signal to baseband form for further processing.

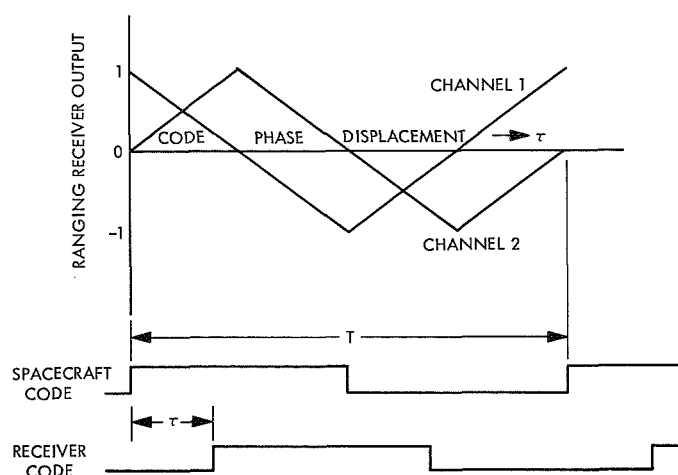
To eliminate effects due to dc drift or changes in amplification between the two channels, the code inputs are interchanged once per second. For example, if "code" is directed to channel 1, then "code delayed by  $\pi/2$ " is used in channel 2. Coincident with the 1-s time tick, the inputs would be inverted so that "not code" and "not code delayed by  $\pi/2$ " would be entered into channel 1 and channel 2, respectively. Again at the next 1-s tick, the two inputs would be exchanged and the procedure repeated until all four possible combinations were exhausted. The last two bits of the data input word specify the state of the code-channel assignment, allowing the computer to sort the data.

Table 1 describes the system operation, which will be recognized as the Exclusive Or function. Figure 3 presents the same information graphically, showing the relative channel outputs as the phase is shifted between the received and local codes. A 12-bit analog-to-digital (A/D) converter is used to measure channel amplitudes, and the result is transferred to a computer that calculates the phase displacement  $\tau$ .

Two channels are required to measure the phase difference between the received code and that generated by the receiver coder. The method is analogous to the optimum phase estimator for sine waves. Both channels

**Table 1. Ranging receiver truth table**

Received spacecraft code	Receiver coder	Ranging receiver output
0	0	+1
0	1	-1
1	0	-1
1	1	+1



**Fig. 3. Ranging receiver output characteristics**

are sampled every 10 ms, and the results  $V_N$  are summed over some integration time  $t_i$ . After sufficient samples have been accumulated, the phase displacement can be computed using the relationship

$$\tau = \frac{\sum_{t=0}^{t_i} V_{CH1}}{\left| \sum_{t=0}^{t_i} V_{CH1} \right| + \left| \sum_{t=0}^{t_i} V_{CH2} \right|} \times \frac{T}{4}$$

$$0 < \tau < \frac{\pi}{2} \quad (4)$$

Equation (4) holds only for the first quadrant and similar expressions are necessary for the others. A summary of the respective equations is given in Table 2.

The highest frequency component, with a period of approximately 2 ms, provides the system resolution. Unfortunately, any range measurement will have an ambiguity modulo 2 ms; hence, a lower frequency code component must be used to resolve this uncertainty. Restated, the single function of all lower frequency components is simply to resolve the range ambiguity associated with the highest frequency code.

Eighteen code components have been designed into the system, the lowest frequency of which has a period of more than 0.25 s. The user is not required to employ all eighteen, but rather, should use only those necessary to resolve the range uncertainty. For example, if the range is known to within 1 ms (150 km), only the first

**Table 2. Phase angle calculation**

Phase displacement	Quadrant
$\tau = \left( \frac{\sum_{t=0}^{t_i} V_{CH1}}{\left  \sum_{t=0}^{t_i} V_{CH1} \right  + \left  \sum_{t=0}^{t_i} V_{CH2} \right } \right) \frac{T}{4}$	$0 < \tau < \frac{\pi}{2}$
$\tau = \left( 2 - \frac{\sum_{t=0}^{t_i} V_{CH1}}{\left  \sum_{t=0}^{t_i} V_{CH1} \right  + \left  \sum_{t=0}^{t_i} V_{CH2} \right } \right) \frac{T}{4}$	$\frac{\pi}{2} < \tau < \pi$
$\tau = \left( 2 + \frac{\sum_{t=0}^{t_i} V_{CH1}}{\left  \sum_{t=0}^{t_i} V_{CH1} \right  + \left  \sum_{t=0}^{t_i} V_{CH2} \right } \right) \frac{T}{4}$	$\pi < \tau < \frac{3\pi}{2}$
$\tau = \left( 4 - \frac{\sum_{t=0}^{t_i} V_{CH1}}{\left  \sum_{t=0}^{t_i} V_{CH1} \right  + \left  \sum_{t=0}^{t_i} V_{CH2} \right } \right) \frac{T}{4}$	$\frac{3\pi}{2} < \tau < 2\pi$

ten components are required. Table 3 summarizes the range resolving capabilities of the various components.

It has been shown by Goldstein (Ref. 2) that a 3-dB improvement in system performance can be obtained by shifting the receiver coder to make  $\tau = 0 + K (T/2)$  for  $K = 1, 2, 3, \dots N$ . This shifting is equivalent to moving to a peak on the correlation function. Adopting the further constraint that the highest frequency code will always be shifted to make  $\tau_1 = 0$  guarantees that the next lower code will also be at a peak (positive or negative). The procedure is best illustrated by a diagram, shown in Fig. 4.

Figure 4 shows the relative code correlation characteristics of the first three components. If we assume that the range to a target results in a  $\tau = \tau_R$  and that the range uncertainty  $\hat{R}$  is in the interval  $T_2 < \hat{R} < T_3$ , then the measurement of code  $C_1$  will indicate that the correlation amplitude is not at its peak value (i.e.,  $\tau_1 \neq 0$ ), and that a phase shift of the receiver coder is necessary.

For simplicity of design, the shifting is accomplished by deleting coder drive pulses, in effect delaying the receiver coder. This shifting is equivalent to reducing the range of the targets and, of course, the value of  $\tau$ . The high frequency component is shifted by dropping 66-MHz cycles, resulting in a phase displacement of approximately 15 ns. A total of 128 shifts is required to slip the phase by one cycle.

After the requisite number of shifts is calculated, the receiver coder is delayed to bring the correlation value to a positive peak, point A on Fig. 4 (i.e.,  $\tau_1 = 0$ ). It is obvious from the diagram that now  $C_2$  must also be at a peak, either positive or negative. Thus, when correlating with  $C_2$ , it is sufficient to determine the sign of the output without regard for magnitude. Had the result been positive, no shifting would be required. However, the measurement is clearly negative and a shift of  $T_2/2$  is necessary to bring the component into alignment. This alignment is accomplished by delaying  $C_2$  by one-half

Table 3. Code range resolving power

Component $C_n$	Approximate period $t_n, \mu s$	Approximate ambiguity resolving power, km	Component $C_n$	Approximate period $t_n, \mu s$	Approximate ambiguity resolving power, km
1	1.94	$2.85 \times 10^{-1}$	10	$9.93 \times 10^2$	$1.46 \times 10^2$
2	3.88	$5.70 \times 10^{-1}$	11	$1.99 \times 10^3$	$2.92 \times 10^2$
3	7.76	1.14	12	$3.97 \times 10^3$	$5.83 \times 10^2$
4	$1.55 \times 10^1$	2.28	13	$7.94 \times 10^3$	$1.17 \times 10^3$
5	$3.10 \times 10^1$	4.56	14	$1.59 \times 10^4$	$2.33 \times 10^3$
6	$6.21 \times 10^1$	9.11	15	$3.18 \times 10^4$	$4.67 \times 10^3$
7	$1.24 \times 10^2$	$1.82 \times 10^1$	16	$6.36 \times 10^4$	$9.33 \times 10^3$
8	$2.48 \times 10^2$	$3.65 \times 10^1$	17	$1.27 \times 10^5$	$1.87 \times 10^4$
9	$4.97 \times 10^2$	$7.29 \times 10^1$	18	$2.54 \times 10^5$	$3.73 \times 10^4$

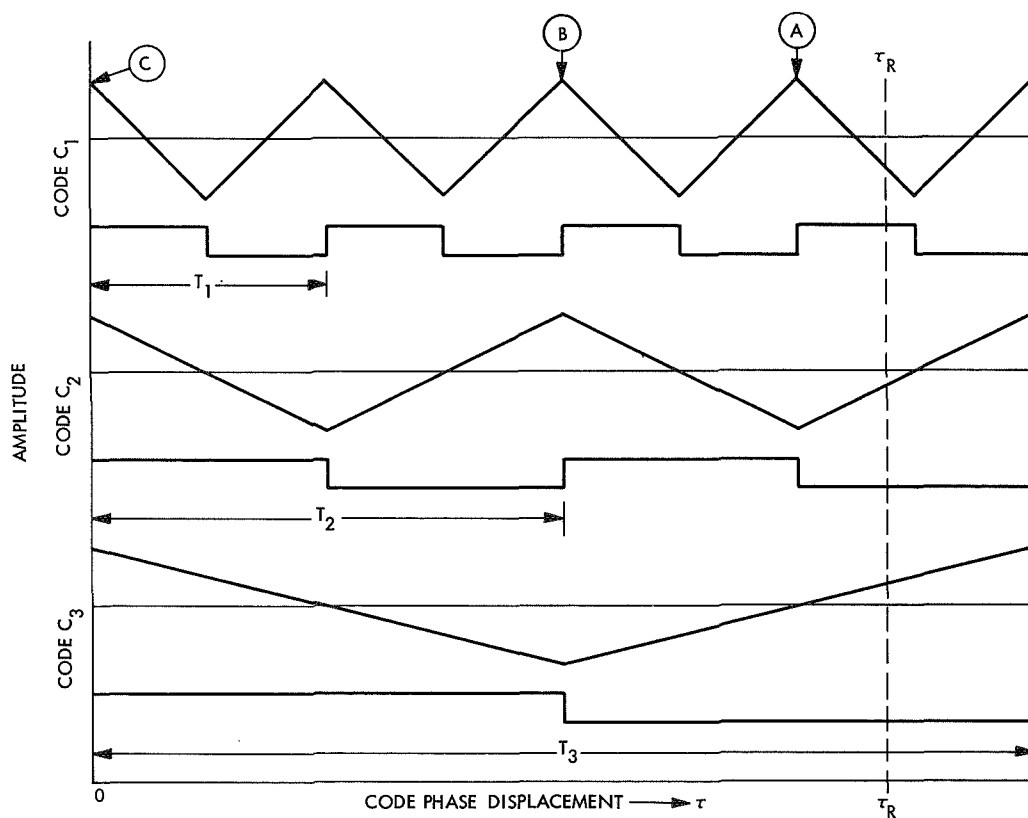


Fig. 4. Relative code correlation characteristics

cycle. All lower order components will be shifted by the same amount. We now have arrived at point B of Fig. 4; the procedure is repeated and  $C_3$  is delayed by  $T_3/2$  to reach point C. The number of shifts required to reach point C is a direct measure of the phase delay  $\tau_R$  and hence the range.

Thus far the effect of noise in the received signal has not been considered. Its presence introduces a variance in the measured value of  $\tau_R$ , which is a function of the integration time  $t_i$ . Two separate cases need to be examined. First, there is the highest frequency component  $C_1$ , which determines the system accuracy and must be measured very carefully. Second, there are the remaining components  $C_2$  through  $C_{18}$ , which serve to resolve the ambiguity and need only a positive-negative determination.

A system analysis by Goldstein (Ref. 2) has shown that the integration time required to achieve an acceptable variance  $\sigma_\tau^2$  is given by

$$t_i = \frac{T^2 N_0}{32 \sigma_\tau^2 s} \quad (5)$$

where  $s$  is the power in the ranging signal. Assuming that an uncertainty of  $\pm 15$  m would be acceptable and employing component  $C_1$ , Eq. (5) simplifies to

$$t_i = 12.5 \frac{N_0}{s} \quad (6)$$

This result is plotted in Fig. 5 for several values of  $s/N_0$ .

For the remaining components  $C_2$  through  $C_{18}$ , the probability of correctly identifying the phase is (Ref. 2):

$$p(\text{correct}) = \frac{1}{\pi^{1/2}} \int_{-\infty}^{(st/N_0)^{1/2}} -e^{-z^2} dz \quad (7)$$

If an error is made in determining the phase of any component during the acquisition process, the entire range measurement will be incorrect. The probability of this occurring can be expressed as

$$P_e = 1 - p(\text{correct})^{n-1} \quad (8)$$

Figure 6 graphically depicts the probability of error in resolving the code ambiguities. Curves are shown for

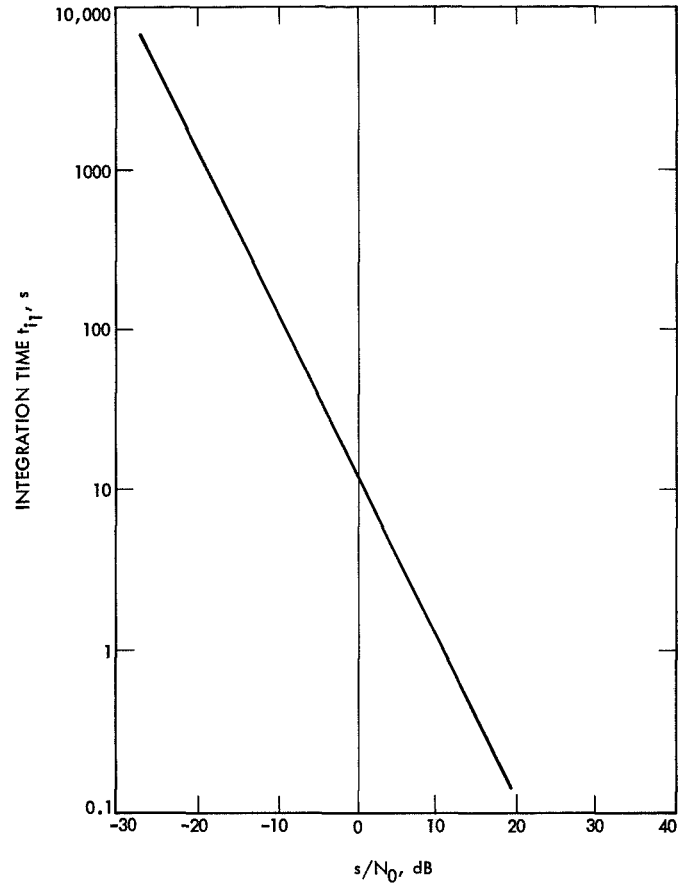


Fig. 5. Integration time  $t_{i_1}$  for first component  $\pm 15$ -m accuracy

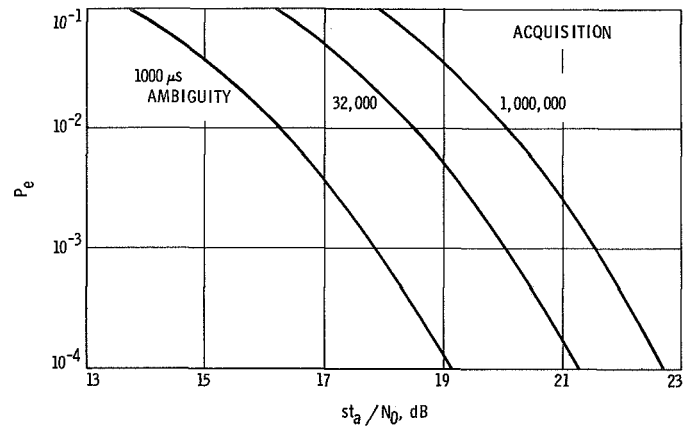


Fig. 6. Probability of an error in resolving code ambiguities

three different values of range uncertainties that affect the number of components used. Thus, knowing the range uncertainty  $\hat{R}$  and the expected  $s/N_0$ , the user can

easily find the acquisition time of all components, except  $C_1$ . Total acquisition time is found by summing this result with  $t_{i_1}$  as determined from Fig. 5.

### III. Peripheral Equipment

#### A. Computer

In addition to the standard DSIF transmitter and receiver, a computer is required to control the equipment and to calculate the range. Since Scientific Data Systems series 920 computers are already installed in all tracking stations, it was decided to utilize these as part of the ranging equipment.

Programming inputs include the integration times for the first and other components, the number of components to be used, and the time to begin the transmission of  $C_1$ . Also, an estimate for the round trip time-of-flight of the signal is required. The computer then calculates a set of critical times and stores them for constant scanning during a ranging operation. These times specify the beginning and end of each component transmission and the periods during which individual components should be available at the receiver for correlation. When a critical time is reached, a command is sent to the ranging equipment to instigate the appropriate action. A guard band of 1-2 s is left between critical times to allow for an uncertainty in the time-of-flight.

#### B. Transponder

A design constraint required that the ranging equipment be compatible with existing spacecraft transponders. The turnaround transponder detects and removes ranging modulation from the received carrier, which is then multiplied in frequency by 240/221. The new carrier is remodulated with the previously detected code and is retransmitted to the ground station. Since present transponders have a bandwidth of about 3.5 MHz, the high-frequency code component must have a bit period of at least 1  $\mu$ s.

Although turnaround transponders perform adequately on missions to Venus and Mars, achieving adequate performance in very deep space probes where the signal level is weak may necessitate additional processing in the spacecraft. In these cases, a regenerative transponder that literally locks to and reconstructs the ranging code is essential. Regenerative ranging transponders for pseudo-noise encoded signals become rather complex devices. Not only are there  $n$  coders for an  $n$  component sequence,

but these must be individually locked to the received signal. In short, the spacecraft must execute an acquisition procedure identical to that of the ground equipment, a formidable task for something 500,000,000 miles away.

Unfortunately, code acquisition is required of all regenerative transponders and the best that one can hope for is to simplify the process. In this respect, square wave codes, harmonically related by a factor of two and executed in a known and consistent manner, seem to offer a decided advantage. This advantage derives in part from the possibility of constructing a tracking filter (phase locked loop) that can acquire the ranging modulation. By utilizing two such devices and associated lock detectors, the system could be tracking one component while simultaneously waiting for the next. Studies are under way to investigate the feasibility of such a design that would make a regenerative transponder practical for the first time.

### IV. Ranging Operation

The following is a description of a typical ranging operation with the assumptions that the range to a spacecraft is  $1.5 \times 10^6 \pm 100$  km and that the received  $s/N_0 = -10$  dB. The objective is to refine the range measurement to  $\pm 15$  m with a  $p_e = 10^{-4}$ .

From Fig. 5 the integration time required for the first component is  $t_i = 125$  s. Figure 6 shows the acquisition time for the remaining 9 components to be a total of 800 s, or 88.8 s each. These numbers together with the test starting time are entered into the computer, which then calculates the critical time table.

The computer then enters a wait phase where it stays until the first critical time is reached, at which point transmission of component  $C_1$  commences for a period  $t_{i_1}$ . Since the round trip time-of-flight will be 10 min, the first six components and part of the seventh can be transmitted before  $C_1$  returns from the spacecraft. Just after the  $C_1$  arrival, the computer disables the doppler rate aiding, commands the receiver coder to generate component  $C_1$ , and synchronizes the receiver coder and its  $\div 64$  driver with their counterparts in the transmitter chain. Coincident with the second 1-s time tick following coder synchronization, the doppler rate aiding will be enabled and an interrupt signal will be generated to cause the computer to read the time of day. It is at this time  $t_0$  that the range measurement will be valid, since



this is the instant that the relationship between the receiver coder and the incoming signal becomes fixed.

The computer samples both channels every 10 ms for a period  $t_{i_1}$ . It then calculates the phase displacement  $\tau_1$ , and shifts the receiver coder to reach a positive peak on the correlation curve. The procedure is repeated for the lower frequency components until all have been completed and the final value of  $\tau_R$  can be computed.

When the time was reached for the transmission of the tenth component, the computer, at the user's option, could have commanded a chopper frequency. The system is designed so that any one of the six higher frequency components can be used to chop the lower nine. Operation is defined by

$$C_{1-6} \oplus C_{10-18} \quad (9)$$

where  $\oplus$  denotes modulo two. This feature was included because ranging components below 1 kHz may interfere with the command decoding subsystem on some spacecraft.

After all components have been acquired, the user may wish to return to  $C_1$  to further refine the range measurement. However, it must be understood that, no matter how long the operation is continued, the output will be a single range that is valid at  $t_0$ . To obtain a new range number, the acquisition procedure must be repeated.

## V. System Errors

In addition to errors due to noise, which were discussed in the Section II, there are other sources including the ground equipment, the spacecraft transponder, and charged particle effects. These uncertainties are important only insofar as they cannot be measured and, hence, removed from the range determination.

The ground equipment is calibrated by actually ranging a target at a known distance. The difference between measured and surveyed range is due to system delay and must be subtracted from any measured range. Since the test is simple and the equipment is close at hand, the calibration can be done daily if desired. Practically, the system has been designed to have a minimum delay, thus any changes are likely to be negligible.

The biggest problems are to be found in the transponder. Before launch, the system delay is measured as a function of temperature and signal level. Although these tests are meticulously made, once the spacecraft has been launched there is no way to repeat the calibration nor to check the device stability. Some insight into the magnitude of this error can be gained from studying the calibration data. The total delay for recent units seems to be on the order of 1  $\mu$ s. Moreover, the change in delay over realistic temperature and signal levels has been less than 75 ns. These values correspond to 150 and 11 m of range, respectively. Ignoring long-term drift, which has not been shown to be a problem, the latter number should represent an upper bound on the uncertainty for the transponder. Both temperature and signal levels are available in the telemetry data and can be used to apply corrections for increased accuracy if the user desires.

A second problem arises from the spacecraft bandpass limitations. Its effect will be a slight distortion of component  $C_1$ ; this distortion results in a rounding of the correlation curve peaks (Fig. 3) at  $KT/4$  for  $K = 1, 2, 3$ , and 4. The degree of distortion can be calculated and an appropriate correction applied if desired.

The final source of errors, charged particles, is likely to be so small that it can be ignored in most instances. It occurs because the doppler rate aiding for the receiver coder is generated by dividing RF doppler. Restated, RF doppler is used to simulate code doppler by appropriate scaling. In the presence of charged particles, the two dopplers will be shifted in frequency in opposing directions, causing the receiver coder to slowly drift off the correlation peak. Recent studies show the range variation to be between 1 and 4 m at zenith and about 4 times that amount when the antenna is pointed toward the horizon.

## VI. System Construction

In packaging the system, both the relative simplicity and the high frequencies involved suggested a small physical size. Furthermore, if this system was a prototype for future Deep Space Network ranging equipment, then reliability would also be important. With these things considered, the mechanization with integrated circuits was determined as mandatory, and the Motorola MECL II was selected for the digital portion. Emitter coupler logic offers the advantage of very high speed

(120 MHz), small propagation delays (2–4 ns), and a relatively constant power drain. Fourteen lead flat packs were selected over dual-in-line packs because of an inherent size advantage.

A scheme was sought to mount the integrated circuits to preserve both flexibility and space. Several methods were evaluated, but one developed by JPL and marketed by Microtechnology Corp., Canoga Park, seemed considerably better than the rest.

The basic unit (Fig. 7) consists of an etched circuit board on which are mounted 20 integrated circuits, 22 test points, and 44 connector pins. Because of the high packing density, it is possible to make each card a complete, functional unit. For example, the unit shown in Fig. 7 is a nine-stage coder with associated select gating, word detector, and a quadrature clock generator. Four of these cards, all identical, are required to mechanize the transmitter and receiver coders. A total of 20 cards are used in the digital portion of the ranging equipment and provide space for over 300 integrated circuits.

Figure 8 shows the interconnection side of the card. Number 30 gauge, teflon insulated, nickel wire is welded

to stainless steel posts that in turn are soldered to the leads of the integrated circuits. This method combines the inherent reliability of welded connections with the flexibility of an individually tailored card.

The digital subsystem and the ranging receiver are each contained in a 7-in. slide-out drawer, which is 18 in. deep. Thus the entire system, exclusive of DSIF equipment, occupies a volume of less than 3 ft<sup>3</sup>.

## VII. Conclusions

This paper has described a ranging system designed to extend the threshold to weaker signals without sacrificing the present high level of accuracy. The system employs up to 18 sequentially transmitted square wave components with periods from 2  $\mu$ s to 0.25 s. Unlike previous ranging equipment, the system is open loop and uses received doppler, properly scaled, to establish the incoming symbol rate. High-frequency digital logic, operating at decision rates on the order of 4 ns, is used for implementation. Total system size is less than 3 ft<sup>3</sup>. A simplified transponder for use on very deep space probes is currently under investigation. The system is presently undergoing performance tests with the intent that it will be tried on *Mariners VI* and *VII* at some future date.

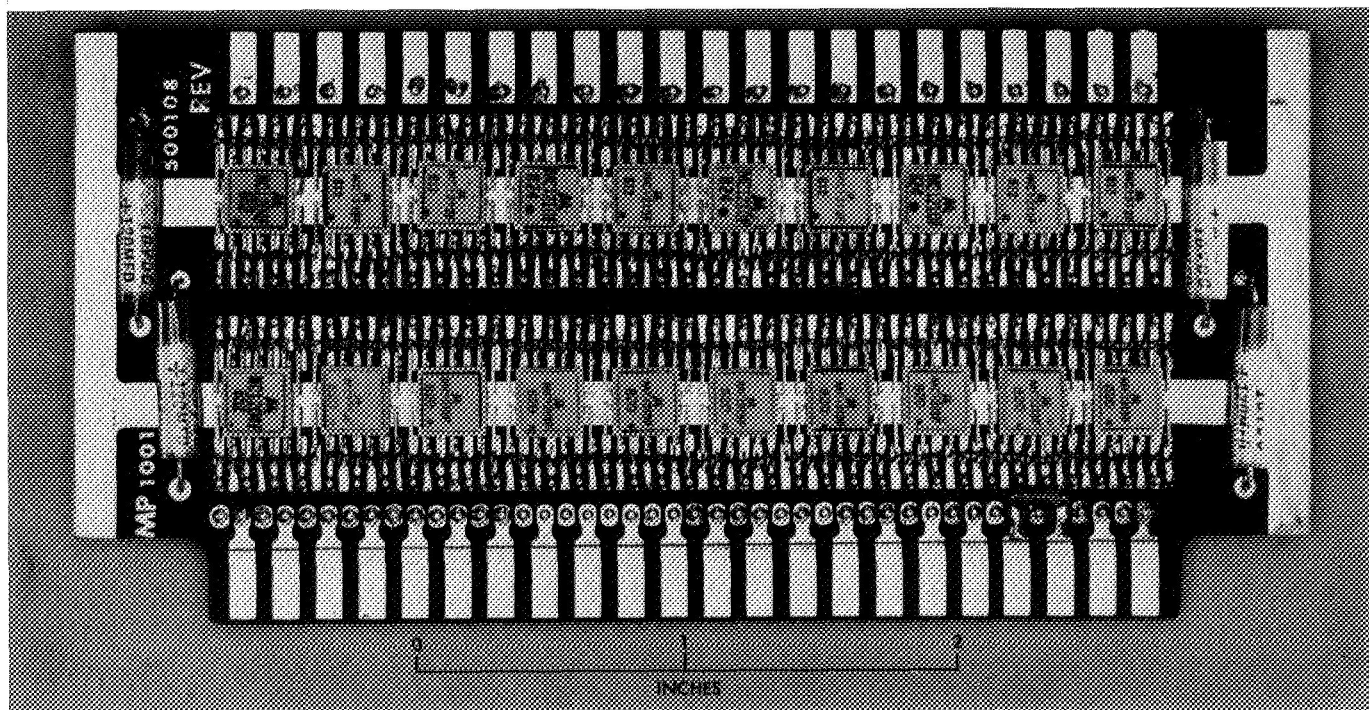


Fig. 7. Etched circuit board, component side

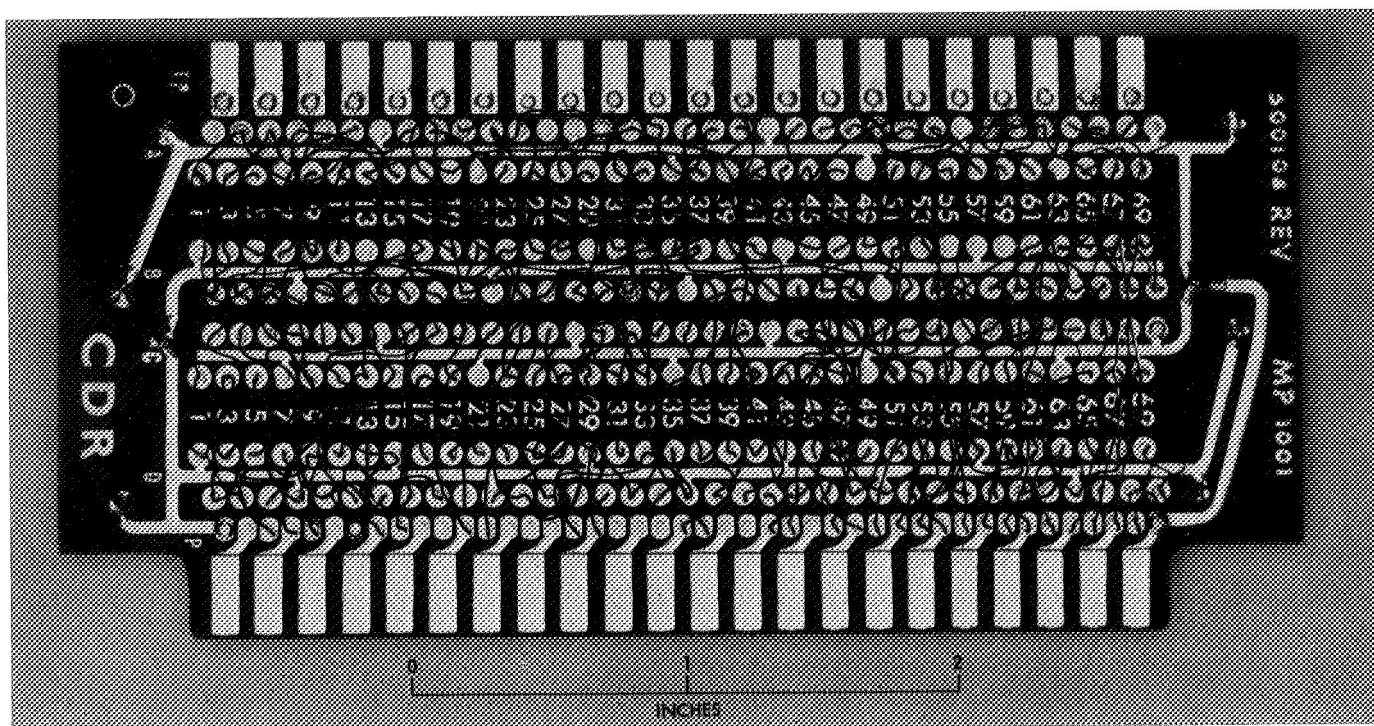


Fig. 8. Etched circuit board, interconnection side

### References

1. Tittsworth, R. C., *Optimal Ranging Codes*, Technical Report 32-411. Jet Propulsion Laboratory, Pasadena, Calif., Apr. 15, 1963.
2. Goldstein, R. M., "Ranging with Sequential Components," in *The Deep Space Network*, Space Programs Summary 37-52, Vol. II, pp. 46-49. Jet Propulsion Laboratory, Pasadena, Calif., July 31, 1968.



# Investigations of Very Long Baseline Interferometry at Smithsonian Astrophysical Observatory

R. D. Michelini

Smithsonian Astrophysical Observatory  
Cambridge, Massachusetts

*This paper informally describes current ideas and work in progress at the Smithsonian Astrophysical Observatory in preparation for several very long baseline interferometry (VLBI) experiments. These VLBI experiments are intended to demonstrate the precise measurement of baselines, and may ultimately be extended to the study of continental drift, polar motion, and UT1 determination. The paper discusses the possibilities of augmenting laser and optical satellite tracking techniques with VLBI methods to refine geophysical measurements. Some developing ideas on the potential of conducting independent clock interferometry experiments with a global and easily transportable network of receiver terminals are also presented.*

## I. Introduction

Early in 1968, the Smithsonian Astrophysical Observatory (SAO) began to study the application of the techniques of very long baseline interferometry (VLBI) to geophysical and geodetic measurements. This interest was generated principally by the desire to augment and intercompare the geodetic and geopotential measurements that SAO has been making through its satellite-tracking program since 1958 (Refs. 1 and 2). In addition, two other possibilities were very attractive. The first was the extension of the accuracy of synoptic earth measurements by perhaps two orders of magnitude, from approximately  $\pm 1.5$ -m uncertainty with present laser trackers to

2 or 3 cm. The second possibility, that of obtaining very precise timing information, was a result almost coincidental with the improvement in accuracy.

Such a significant increase in earth position accuracy will permit SAO to ascertain the existence of continental motion and to observe diurnal earth tides, as well as to fix absolute rates of crustal motions on a worldwide basis.

Sidereal timing information is an important need in the reduction of satellite data, since the required terrestrial and orbital coordinates are related to celestial coordinates through the sidereal system (Ref. 2). The sidereal

system is the celestial system as it rotates under the influence of precession, nutation, and nonsystematic variations. At present, the measure of rotation, or UT1, is determined at a value not better than 3 ms, which corresponds to about 1 m at the equator. Consequently, improvements in measuring earth rotational effects by VLBI (i.e., in determining UT1) will increase the accuracy of the position measurements made by satellite observations, particularly those by laser tracking.

Regardless of the tracking method used, synchronization and coordination of time over the SAO field network (Fig. 1) are a fundamental requirement. Control of time to about 50  $\mu$ s is needed by present laser trackers, and ranging with subnanosecond laser pulses will demand correspondingly greater resolution. Universal dissemination of time to this accuracy is tedious at best, and the control of this basic observational requirement by a VLBI network would fulfill a basic need of all tracking

operations that are not superannuated by VLBI tracking of stellar and artificial sources.

## II. Early VLBI Programs

An initial investigation (Ref. 3) of the application of VLBI to continental-drift determination was concluded in mid-1968. This study examined the feasibility of using techniques of ultrashort-pulse laser ranging and independent-clock radio interferometry to test for the existence of continental drift.

The relative motions between pairs of stations in the Baker-Nunn network, as predicted by several crustal-drift theories, are listed in Table 1 (Ref. 4).

It was found that both techniques could be used to measure these motions. With satellite-ranging laser systems, the resolution  $\delta R$  is largely determined by pulse



Fig. 1. Field stations of Smithsonian Astrophysical Observatory

width  $\tau$ , as shown by  $\delta R \approx c\tau/(S/N)^{1/2}$ , where  $c$  is the velocity of light and  $S/N$  is the received signal-to-noise (power) ratio. Two means of generating the required subnanosecond pulses, cavity dumping (Ref. 5) and mode locking (Ref. 6), appear to be attractive approaches to the needed precision. For radio-interferometric measurements of comparable accuracy, by use of emissions from radio stars or satellites, the angular position of the source must be determined with a precision of  $1/50 \mu\text{rad}$ . This corresponds to measuring the atmospheric and the ionospheric differential-phase path lengths above each of the interferometer terminals with an rms error of 5 to 10 cm.

During the second phase of study (Ref. 7), emphasis was placed on VLBI using stellar sources, in recognition of the fact that potentially more useful and precise measurements can be obtained by that method than by range-only methods; for example, with lasers. This is

**Table 1. Relative crustal motions of Baker-Nunn station sites<sup>a</sup>**

Station pairs <sup>b</sup>	Motion, <sup>c</sup> cm yr <sup>-1</sup>	Azimuth of relative motion, deg
MI — CL	6	100
— RO (MH)	6	120
— AR	5	120
— DO	9	270
JI — RO (MH)	9	120
— DO	9	270
— IL	10	90
BI — SF	2.5	160
— AT	2.5	180
— NT	2.5	40
— NA	5	260
OL — SF	2.5	160
— AT	2.5	180
— NT	3	50
— NA	4.5	270
SF — NA	3.5	270
AT — NT	4	000
NT — DO	6	200
— JI	10	260
IL — DO	5	200

<sup>a</sup>Calculated from continental-drift models of Morgan (1968) and Le Pichon (1968).

<sup>b</sup>The reference station is given first; the station abbreviations are:  
 OL — Olifantsfontein    MH — Mt. Hopkins    CR — Comodoro Rivadavia  
 SF — San Fernando    IL — Island Lagoon    AT — Athens  
 NT — Naini Tal    DO — Dodaira    RO — Rosamond  
 AR — Arequipa    DZ — Debre Zeit    CL — Cold Lake  
 MI — Maui    NA — Natal    JI — Johnston Island

<sup>c</sup>No relative motions predicted between: MI and JI; CL, RO, and MH; AR, NA, and CR; DZ and OL; NT and IL; AT and SF.

achieved because the simple interferometer permits calculation of both the baseline direction and the baseline length, in contrast to the laser system, which measures only distance. Consequently, rigid rotations of the interferometer geometry can be sensed, so that true continental drift can be distinguished from polar wandering. A dynamical approach based on such a network of interferometers could be used to determine absolute positions for individual stations with respect to the center of mass of the earth.

In another part of the study, a VLBI system capable of resolving delay time to  $1/10 \mu\text{s}$  was analyzed for its sensitivity to phase, baseline, and angular errors. It was concluded that its 30-m precision would be sufficient to provide comparison with the present long-arc geodetic standards achieved with conventional tracking methods. The data-processing procedure that was considered employed a digital-recording technique using clipped and sampled data. A special-purpose, programable cross-correlator was suggested to make differential bit-stream corrections. Details of antenna utilization, source selection, and receiver characteristics were also worked out. Most aspects of this study, including recommendations for propagation-study instrumentation, were incorporated in the design of several proposed experiments, which are described in some detail in the following section.

### III. Proposed VLBI Experiments

As part of a continuing investigation into the means by which space-related systems might be applied in a program of detection and measurement of crustal motions associated with continental drift and other geophysical phenomena, SAO has endorsed the program shown in Fig. 2 (Ref. 8).

The short-baseline precursor experiment is intended to serve both as a checkout of the front end and the data-conditioning equipment that are now being fabricated and as a debugging exercise for the data-processing routine, which, at this point of investigation, is planned to be done on a general-purpose computer (CDC 6400). The narrow-band digital recording and processing equipment are shown schematically in Figs. 3-5.

Several programing checks have already been made by processing fringe-phase data made on operating interferometers. The short-baseline experiment will verify the ability of the system to make measurements to within  $\pm 30$  m by operating over a precisely surveyed baseline

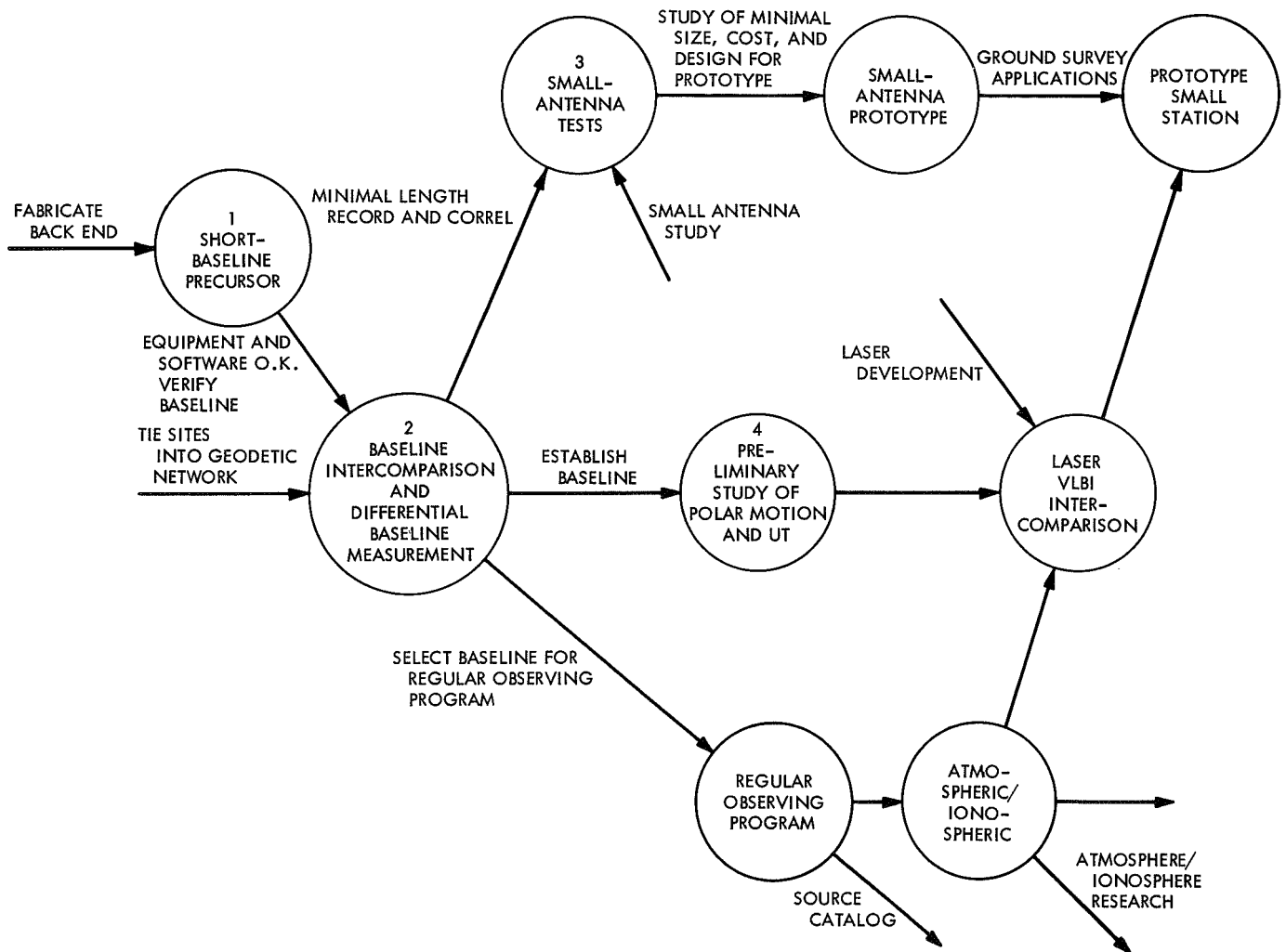


**Fig. 2. Tentative long-range program for VLBI**



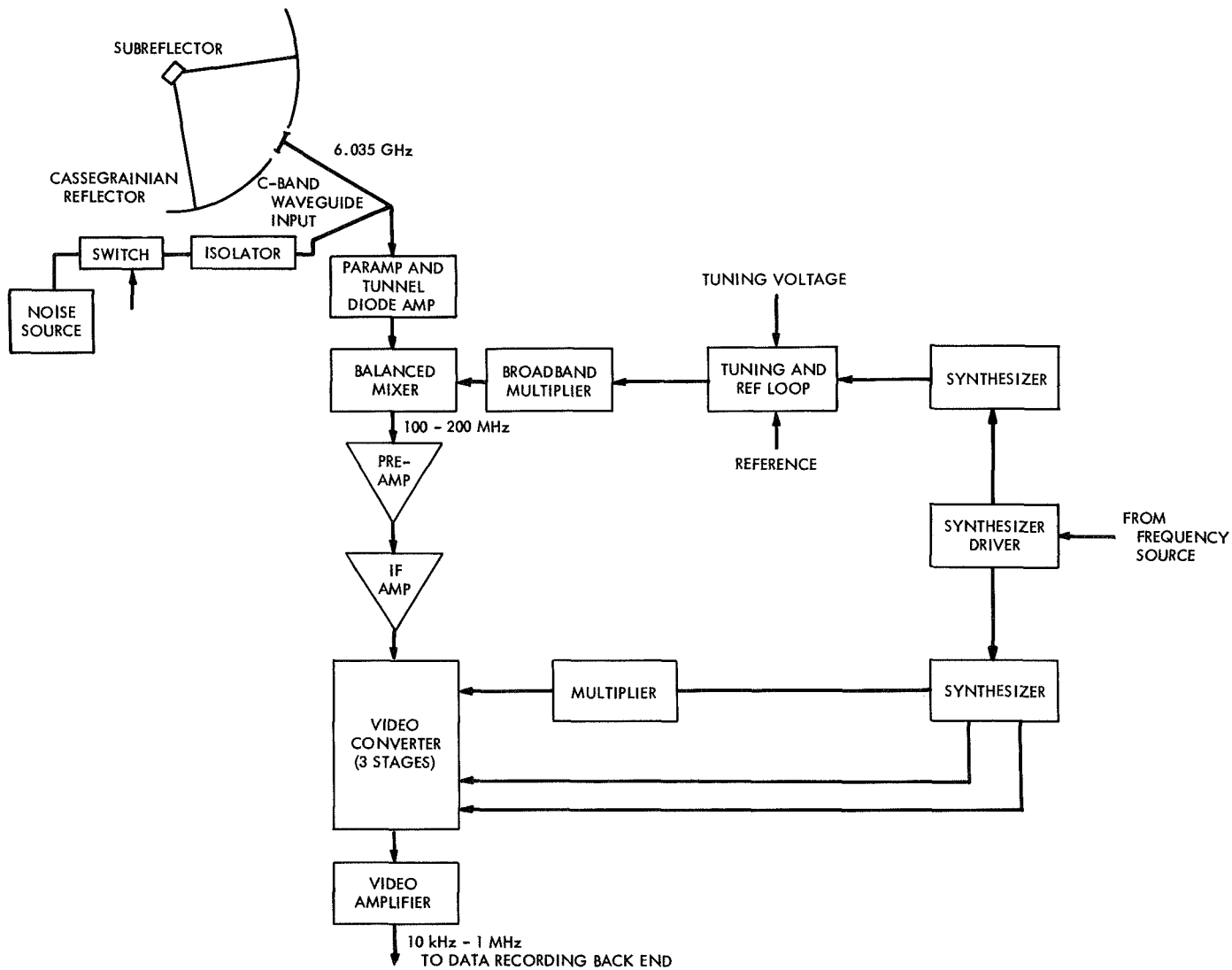


**Fig. 3. VLBI receiver front end (each terminal)**

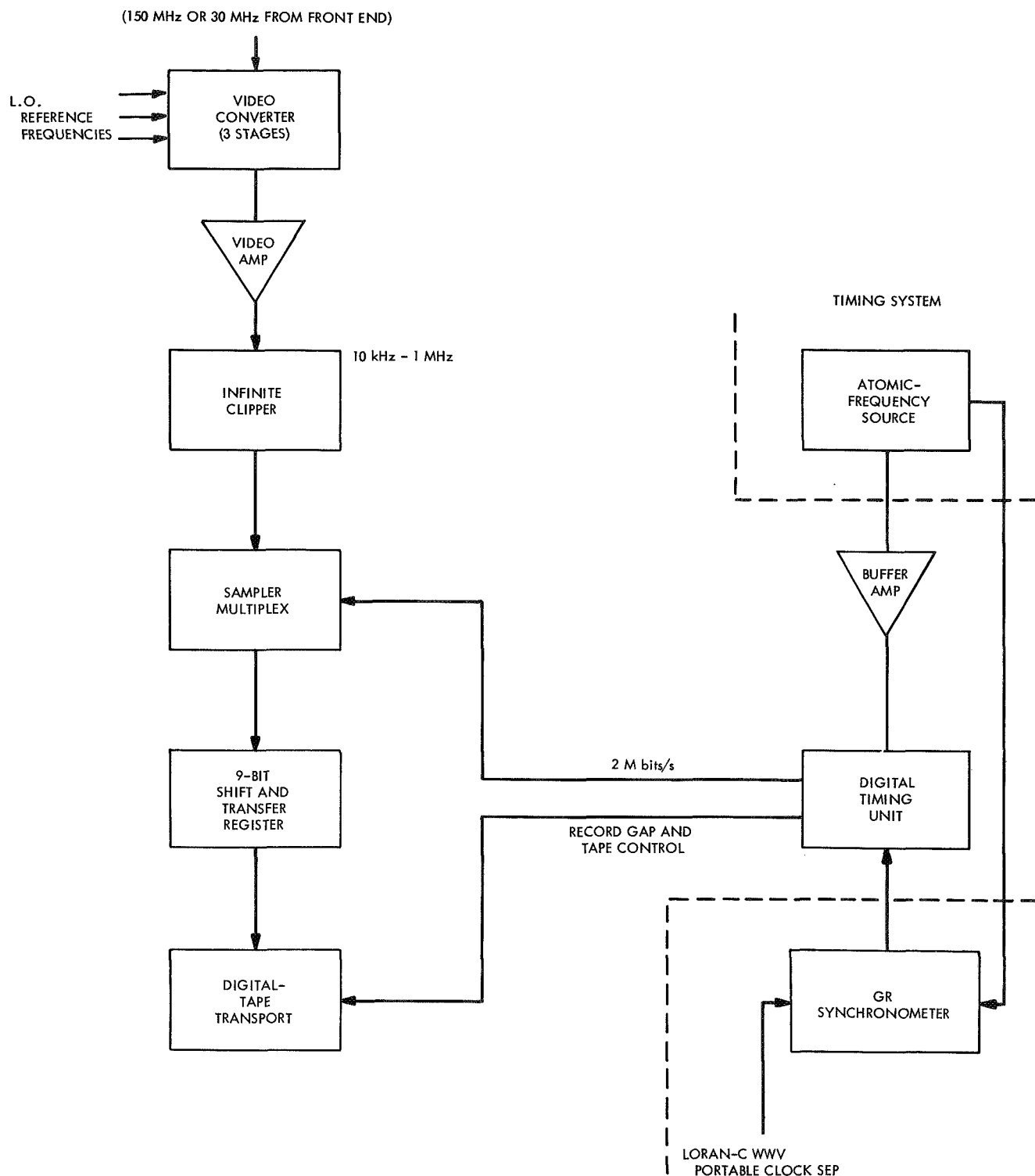


**Fig. 4. VLBI data-recording back end (each terminal)**

of less than 20 km. At present, the planned operating frequency of this interferometer is at L band (1.6 GHz), and since no great precision is sought, propagation studies to support the experiment are not required.

The principal experiment, planned for late 1969, will seek to measure a 5000-km transcontinental baseline, again with an initial objective of 30-m resolution. Information that will tie a number of possible radio-telescope

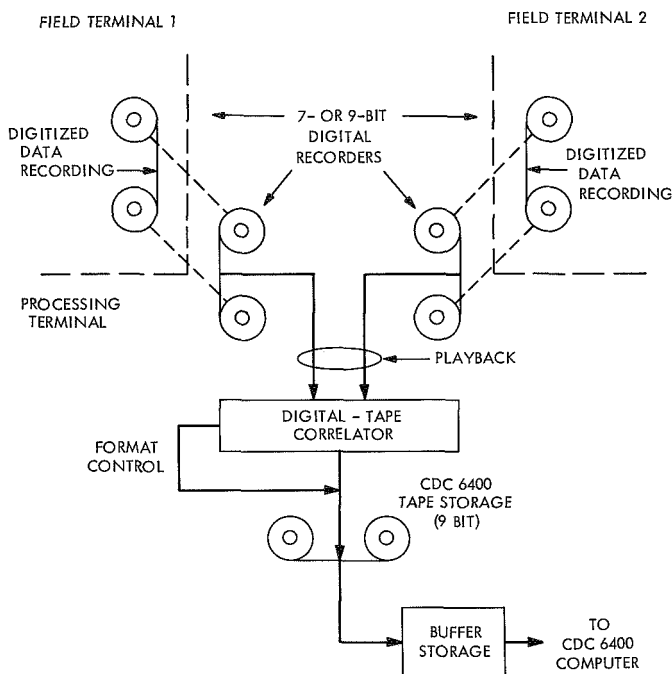


**Fig. 5. Data-processing schematic**

sites in the geodetic datums is currently being acquired so that the geodetic significance of the measurement can be assessed *vis à vis* optical and doppler satellite-tracking data. For a more conclusive test of the resolution of the system, we plan to make a differential baseline measurement by combining a fixed antenna terminus with a movable antenna, so that the magnitude and the rotation of the baseline can be altered by several times the standard variation of the measurement. The purpose of the differential measurement, besides providing an unambiguous test of resolution, is to assess instrumentation limitations, particularly time and frequency control (Figs. 6 and 7), and to test for systematic scale errors in the data processing.

The tests made on the long, variable baseline will be made at C band (about 5 GHz), with receiving equipment and antenna hardware scheduled for later use in a regular observing program. This frequency band represents the best immediate compromise between reasonable antenna and receiver availability and tolerable propagation conditions.

If the results of the above tests are satisfactory and if a documented baseline can be established, the interferometer will be used for preliminary studies of polar motion and of UT, within the relatively wide limits set by

the 1.2-MHz bandwidth of the system and the rubidium-vapor frequency standards used.

Ultimately, we plan to select a baseline where, with suitably refined equipment and a regular observing schedule, improvements can be made to approach baseline accuracies of several centimeters. This, of course, presupposes that ultrastable frequency sources are available and that source positions and atmospheric and ionospheric corrections have been very refined. To accomplish the latter, the permanent laser and microwave backscatter instrumentation shown in Fig. 8 (Ref. 9) will be required.

In setting up an operational interferometer capability, it is important to reduce the data-processing requirements. The VLBI data reduction performed on a general-purpose computer consumes from 1 to 2 h of computer time per minute of data record; hence, a more efficient approach must be adopted for a regular observation program. The most attractive idea is to use a special-purpose correlator with a number of parallel delay channels. An adaptation of a so-called parallel circulating page-loose processor (Ref. 10) currently used for processing radar-echo data appears to be one possible approach. This machine has the capacity to make fast Fourier analyses of the correlation coefficients and to do a limited amount of data reformatting.

If successful operation of a precision interferometer can be achieved, it would be desirable to extend the technique to cover selected baselines located in various parts of the world. Since the principal difficulty in establishing a baseline is the local availability of a suitable antenna, the idea of a transportable and inexpensive antenna, perhaps no larger than 10 m in diameter and operating at C or X band, is attractive. Not only could sites be more freely selected for crustal-motion monitoring and for other remote-site ground surveys, but also collocation experiments and correlative studies could be conducted at stations where other types of geodetic tracking systems have been, or are, located. An evaluation of appropriate signal sources at these frequency bands indicates that suitable ratios of antenna to system temperatures can be obtained with cooled RF preamplifiers that will be commensurate with the recording time dictated by the system frequency stability.

It is predictable that, in the immediate future, globally distributed VLBI will be used as an independent means

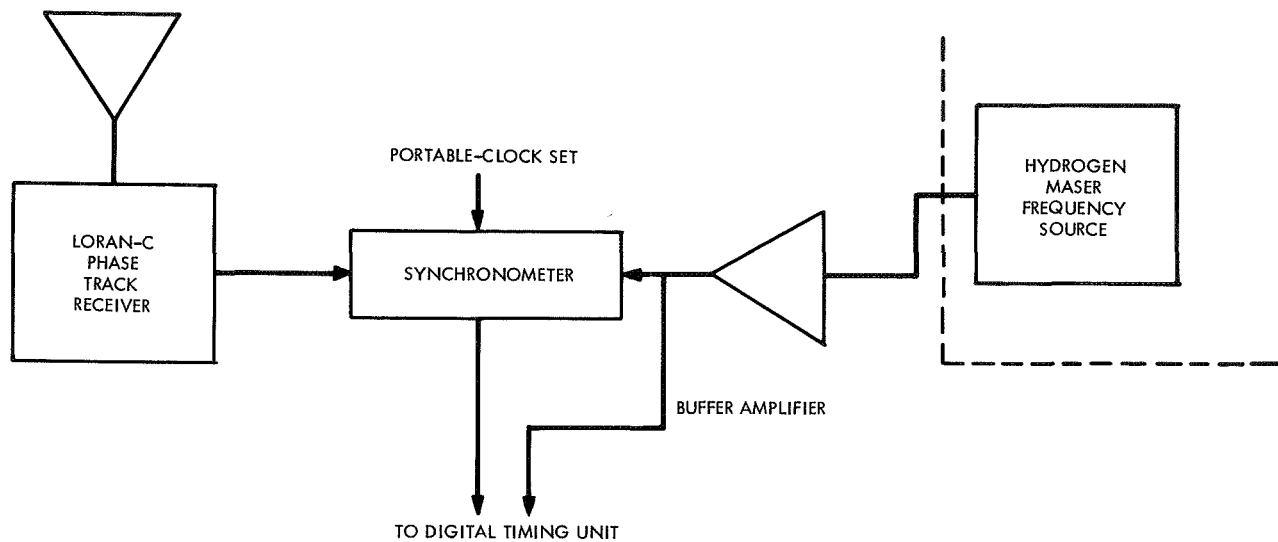


**Fig. 6. Timing system for Agassiz station terminal**

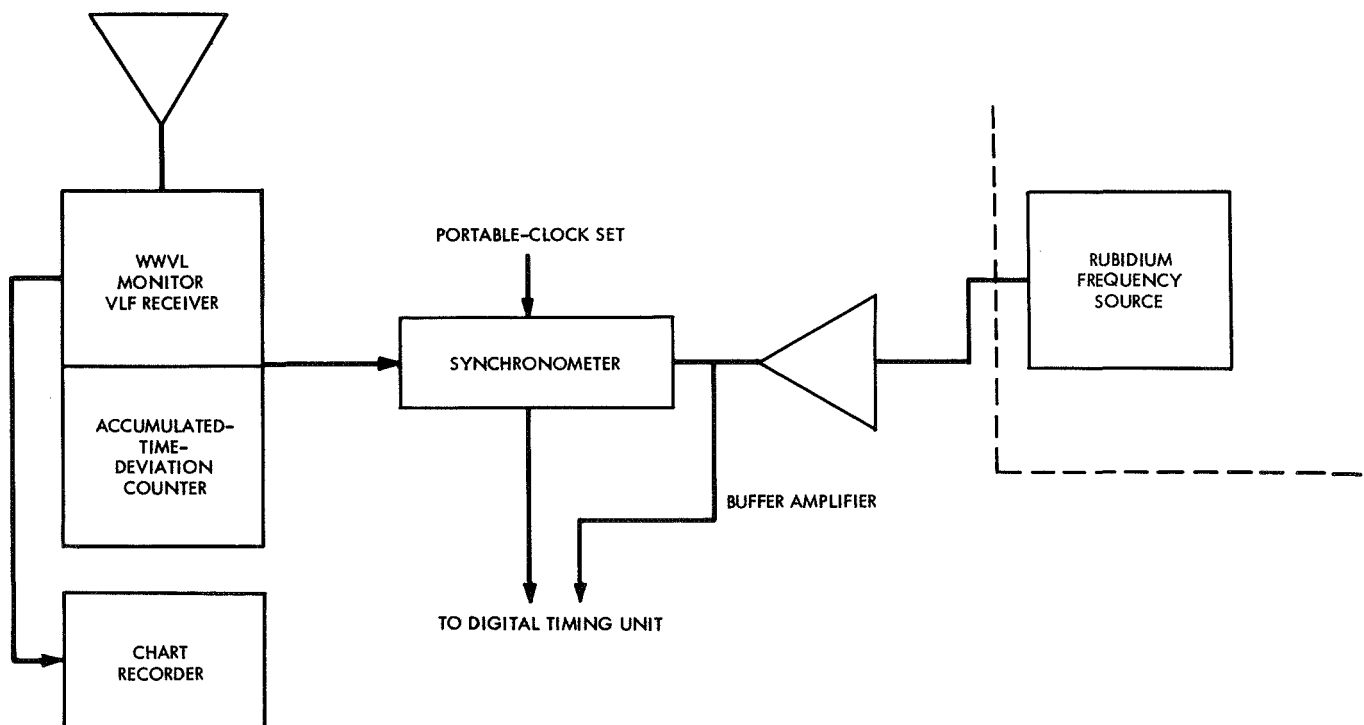


**Fig. 7. Timing system for West Coast terminal**

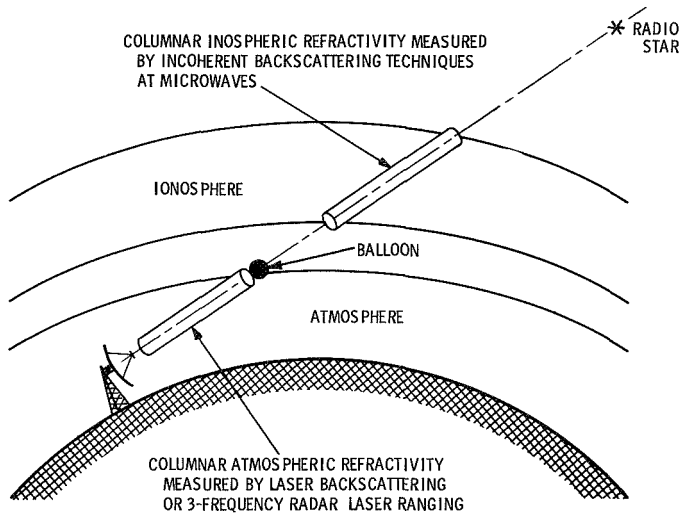


**Fig. 8. Proposed radar arrangement for monostatic measurement of atmospheric and ionospheric columnar refractivity in wanted direction of observation**

of acquiring data with an accuracy more or less comparable to present doppler, laser, and photographic tracking. In the next stage of development, it will exceed by as much as 2 orders of magnitude the precision of present systems based on tracking artificial satellites. This will be achieved through refined stellar observations. Ultimately, VLBI methods will be expanded to include VLBI tracking of artificial sources, which will allow precise terrestrial positions to be measured (with a common geocenter) by means of geometric observations.

At present, it is particularly desirable to establish the accuracy that can be attained by the optimum utilization of doppler tracking (especially TRANET and GRARR doppler systems) so that certain discrepancies between doppler and optical data, which amount to about 15 m in standard deviation of geocentric coordinates (Ref. 11), can be resolved. The use of selected VLBI terminals to make long-term, precisely coordinated measurements would produce a much improved basis for comparisons between the systems.

#### IV. Artificial Sources

The stellar interferometer furnishes information on baseline length and direction only, and not on the absolute position of any of its points. Thus, for example, if a series of stellar measurements were to show no change in the baseline vector, it would be impossible to determine (without other information) whether the baseline

had truly suffered a change in actual position or whether it had been translated parallel to itself. This question is important for geophysical measurements, not because we expect that baseline vectors will show strictly parallel displacements, but rather because baseline deformation will generally be due to a number of forces, such as those of tidal origin, earth tremors, or (perhaps) true continental drift. Knowing only the vectorial change of the baseline does not suffice to separate radial from transverse components of the motion. However, this difficulty may be avoided by means of an artificial radio source.

The use of a radio beacon, placed in an artificial satellite or on the moon, as a source for an independent-clock long-baseline interferometer is a logical variant of the stellar-source situation. It is an attractive possibility because, even at widely separated terminals, increased power margin (for a deep-space vehicle, typically 20 to 30 dB greater than an average stellar source) can be secured in spite of the need for broad-bandwidth signals. Detection can be enhanced by the use of coded signals, and orbits can be selected to provide optimum visibility for specific ground stations.

Since the source is not an infinitely great distance from the earth, the simple relation  $\Delta\phi = (D/\lambda) \cos \theta$  no longer holds, and a corrected equation must be supplied. From Fig. 9, we see that

$$R \cos \gamma = R + d - D \cos \theta$$

from which

$$d = D \cos \theta - D \sin \theta \left( \frac{1 - \cos \gamma}{\sin \gamma} \right)$$

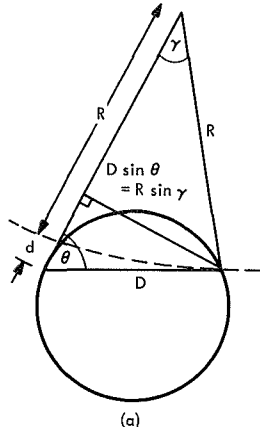
where  $\gamma$  is the angle subtended at the source by the two range vectors. Thus,

$$\Delta\phi = \frac{d}{\lambda} \left[ \cos \theta - \sin \theta \left( \frac{1 - \cos \gamma}{\sin \gamma} \right) \right] \quad (1)$$

represents the corrected equation for  $\Delta\phi$ .

If the vector from the first station to the source is denoted by  $\mathbf{R}_1$  and that from the second station to the source by  $\mathbf{R}_2$ , and if the vectors from the center of

$$R \cos \gamma = R + d - D \cos \theta$$



$$d = D \cos \theta - D \sin \theta \left( \frac{1 - \cos \gamma}{\sin \gamma} \right)$$

$$\Delta \phi = \frac{D}{\gamma} \left[ \cos \theta - \sin \theta \left( \frac{1 - \cos \gamma}{\sin \gamma} \right) \right]$$

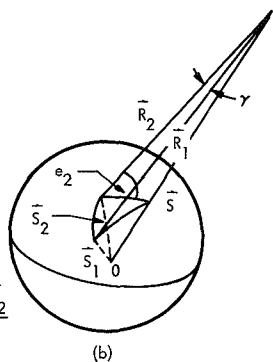
is related to  $R$  by (Fig. 9a)

$$R \sin \gamma = D \sin \theta$$

with  $R$  depending upon the absolute distance of the source (and the station) from some reference point. Thus, it becomes evident that, to make use of this type of interferometer, it will be necessary to know some characteristic length to sufficient precision. This length might be the source distance from the earth center of mass, or it might be the source-antenna range.

The most serious limitation to the geodetic use of an artificial source is the uncertainty in its range to the baseline terminals. For an artificial satellite, this uncertainty might arise from imperfect knowledge of the perturbation of the satellite orbit by the geoid, radiation forces, outgassing, and lunisolar forces, to mention a few possible sources of error. For the moon, the uncertainty is caused by the imprecision of the lunar ephemeris and by the lunar librational motion, which can produce large positional displacements of the source.

$$\begin{aligned} \vec{R}_1 &= \vec{S} - \vec{S}_1 \\ \vec{R}_2 &= \vec{S} - \vec{S}_2 \\ \cos \gamma &= \frac{\vec{R}_1 \cdot \vec{R}_2}{R_1 R_2} = \frac{|\vec{S}|^2 - \vec{S} \cdot (\vec{S}_1 + \vec{S}_2) + \vec{S}_1 \cdot \vec{S}_2}{R_1 R_2} \end{aligned}$$



$$R \sin \gamma = D \sin \theta$$

**Fig. 9. Baseline-satellite geometries for various aspects of satellite interferometry**

the earth to the two stations and to the source are given by  $S_1$ ,  $S_2$ , and  $S$ , respectively, then (Fig. 9b)

$$\vec{R}_1 = \vec{S} - \vec{S}_1$$

$$\vec{R}_2 = \vec{S} - \vec{S}_2$$

so that

$$\cos \gamma = \frac{\vec{R}_1 \cdot \vec{R}_2}{R_1 R_2} = \frac{|\vec{S}|^2 - \vec{S} \cdot (\vec{S}_1 + \vec{S}_2) + \vec{S}_1 \cdot \vec{S}_2}{R_1 R_2}$$

This last expression yields  $\gamma$  in terms of the station and source positions, from which it is possible to determine  $\Delta \phi$  by Eq. (1).

Satellite or lunar interferometry brings the actual position of the baseline vector into play through the variable  $\gamma$  as it appears in the term  $(D/\lambda) \sin \theta [(1 - \cos \gamma)/\sin \gamma]$  found in the fringe-phase expression of Eq. (1), where  $\gamma$

Laser ranging holds promise of permitting distance measurements of sufficient accuracy to be made. With ruby lasers, pulse lengths less than 10 ns have been achieved in the laboratory; reduction of pulses to the order of picoseconds appears feasible. Even with nanosecond pulse widths, the laser can be expected to yield round-trip transit times to a reflecting satellite; the times are accurate to the order of a nanosecond, which is equivalent to a 15-cm uncertainty in the one-way range (Ref. 12).

The characteristics of several practical laser systems for ranging on artificial satellites and on lunar targets are given in Tables 2 (Ref. 13) and 3, respectively. The highest powered satellite-ranging system in Table 2 is capable of ranging to earth-synchronous satellites. For the lunar-ranging case, the mutual-visibility requirement is much less difficult than for the low earth satellites, which will generally not be simultaneously visible to terminals separated by more than 1500 km.

The ranging information required by the artificial-source interferometer may be supplied by tracking systems other than lasers. However, laser systems might be more efficient in augmenting a terminal since they can also serve as backscatter sources for tropospheric probing, as shown in Fig. 8, and as independent tracking instruments, producing a coordinated approach to high-accuracy measurements.

**Table 2. Characteristics of geodetic laser-ranging systems**

System	GSFC <sup>a</sup> (Maryland)	CNES <sup>b</sup> (France and Spain)	AFCRL <sup>c</sup> (Massachusetts)	SAO		
				Hawaii	Greece	Arizona
Pulse duration, ns	12-18	25-30	30	40-60	10	15
Pulse energy, J	1	1	1.8	0.5	1	7.5
Power output, MW	70	30	60	8	100	500
Pulse-repetition rate, min <sup>-1</sup>	60	15	20 <sup>d</sup>	2	2	1
Counter resolution, ns	1	10	1	10	10	1
Transmitter beamwidth, mrad	1	0.5-2	3	1	1	0.6-6
Receiver aperture, in.	16	14	5	16	16	20
Receiver bandwidth, nm	1	1.8	1	2	2	0.6
Receiver beamwidth, mrad	1.5-5	0.5-2	1-5	2	2	0.6-6
Tracking	Programed	Visual	Programed	Visual	Visual	Positioned

<sup>a</sup>GSFC: Goddard Space Flight Center, National Aeronautics and Space Administration, U.S.A.  
<sup>b</sup>CNES: Centre National d'Etudes Spatiales, France.  
<sup>c</sup>AFCRL: Air Force Cambridge Research Laboratory, U.S.A.  
<sup>d</sup>Each transmission is a burst of 10 pulses, 60 ns apart.

**Table 3. Characteristics of lunar-ranging systems**

Characteristic	Russian <sup>a</sup>	AFCRL	Proposed	Characteristic	Russian <sup>a</sup>	AFCRL	Proposed
<b>Laser</b>				<b>Receiving telescope</b>			
Pulse duration, ns	50	10	23	Aperture, in.	102	60	60
Wavelength, nm	694	694	530	Actual area, m <sup>2</sup>	5.3	1.8	1.8
Energy, J	6	10	20	Effective area, m <sup>2</sup>	1.3	0.71	0.71
Power, MW	120	1000	880	Beamwidth, arc-s	(5)	6	5
Repetition rate, m <sup>-1</sup>	6	12	0.06	Beamwidth, sr	$4.6 \times 10^{-10}$	$6.8 \times 10^{-10}$	$4.6 \times 10^{-10}$
Divergence, mrad	2.5	1	0.080	Filter bandwidth, nm	1	1	2
(times diffraction limit)	50	23	4.7	Filter transmission	(0.5)	0.5	0.5
Rod diameter, mm	13	15	38	Quantum efficiency	0.04	0.1	0.2
<b>Transmitting telescope</b>				<b>Received signal</b>			
Aperture, in.	102	60	8	From retroreflector, electrons	0.7	8	16
Aperture, m	2.6	1.5	0.2	From lunar surface, electrons	0.06	0.2	0.5
Efficiency	0.6	0.8	0.8	<b>Received noise</b>			
Beamwidth, arc-s	5	2.5	3	Full moon, electrons/pulse	$2 \times 10^{-2}$	$10^{-2}$	$3 \times 10^{-2}$
Beamwidth, sr	$4.6 \times 10^{-10}$	$1.2 \times 10^{-10}$	$1.7 \times 10^{-10}$	Dark moon, electrons/pulse	$2 \times 10^{-6}$	$10^{-6}$	$10^{-5}$
Area on moon, km <sup>2</sup>	68	17	26				

<sup>a</sup>The values in parentheses are estimates.

## References

1. Whipple, F. L., and Hynek, J. A., "Optical and Visual Tracking of Artificial Satellites," in *Proceedings of the VIIIth International Astronautical Congress*, pp. 429-435. Springer-Verlag, Vienna, 1958.
2. *Geodetic Parameters for a 1966 Smithsonian Institution Standard Earth*, Special Report No. 200. Edited by C. A. Lundquist and G. Veis. Smithsonian Astrophysical Observatory, Cambridge, Mass., 1966.
3. *Investigation of Continental Drift, Phase-I Effort*, Final Report of Contract NSR 09-015-079. Smithsonian Astrophysical Observatory, Cambridge, Mass., 1968.
4. Mohr, P., "Geological Considerations," in *Investigation of Continental Drift, Phase-I Effort*, Final Report of Contract NSR 09-015-079, pp. 6-17. Smithsonian Astrophysical Observatory, Cambridge, Mass., 1968.
5. Hook, W. R., Dishington, R. H., and Hilberg, R. P., "Laser Cavity Dumping Using Time Variable Reflection," *Appl. Phys. Lett.*, Vol. 9, pp. 125-127, 1966.
6. Heynau, H. A., and Foster, M. C., "Single-Subnanosecond Laser Pulse Generation and Amplification: the Second Generation of Q-Switched Lasers," *Laser Focus*, pp. 20-24, Aug. 1968.
7. *Investigation of Continental Drift, Phase-II Effort*, Final Report of Contract NSR 09-015-079. Smithsonian Astrophysical Observatory, Cambridge, Mass., 1969.
8. Criswell, S. J., *Proposal to NASA for the Application of VLB Interferometry to Earth Measurements*, Proposal P 163-2-69. Smithsonian Astrophysical Observatory, Cambridge, Mass., 1969.
9. Grossi, M. D., "Atmospheric and Ionospheric Influences," in *Investigation of Continental Drift, Phase-I Effort*, Final Report of Contract NSR 09-015-079, pp. 65-77. Smithsonian Astrophysical Observatory, Cambridge, Mass., 1968.
10. Schaffner, M. R., *The Circulating Page-Loose System: A New Solution for Data Processing*, Report No. 15. Harvard-Smithsonian Radio Meteor Project Research, 1966.
11. Gaposchkin, E. M., and Veis, G., "Comparison of Results Obtained From Observing Systems," in *Space Research VIII*, pp. 42-48. Edited by A. P. Mitra, L. G. Jacchia, and W. S. Newman. North-Holland Publishing Co., Amsterdam, 1968.
12. Bender, P. L., Alley, C. O., Currie, D. G., and Faller, J. E., "Satellite Geodesy Using Laser Range Measurements Only," *J. Geophys. Res.*, Vol. 73, pp. 5353-5358, 1968.
13. Lehr, C. G., "Laser Systems," in *Investigation of Continental Drift, Phase-I Effort*, Final Report of Contract NSR 09-015-079, pp. 43-64. Smithsonian Astrophysical Observatory, Cambridge, Mass., 1968.



# The Haystack Planetary Ranging Radar

J. V. Evans, R. P. Ingalls, and G. H. Pettengill

Lincoln Laboratory\*  
Massachusetts Institute of Technology  
Lexington, Massachusetts

*The Haystack 3.8-cm wavelength continuous wave radar system operated by the Lincoln Laboratory is described. This radar has been employed routinely for observations of the Moon, Mercury, Venus, and Mars. By virtue of the high operating frequency, increased transmitter power, and reduced system temperature, the sensitivity of this instrument exceeds that of earlier planetary radar systems operated by the Lincoln Laboratory at 23- and 68-cm wavelength by as much as 36 dB. Besides giving a description of the apparatus, the paper provides an account of the coding scheme employed for making range measurements and the data processing procedures for optimally determining the best estimate of the range and velocity of the planet rear surface.*

## I. Introduction

The earliest unsuccessful attempts to detect radar echoes from a planet at the Lincoln Laboratory were made at UHF in 1958 and 1959 using the newly completed Millstone Hill radar (Refs. 1 and 2). The parameters of this system as employed in 1959 are given in Table 1. Full power operation of the Millstone Hill radar was achieved in 1961 (Table 1) affording real-time detection of Venus echoes using on-line computer processing (Ref. 3) and providing enough information to permit the recovery of echoes from tapes recorded during 1959 inferior conjunction (Ref. 4). The observations carried out in 1961 were chiefly performed using uncoded pulses of 4.0- or 2.0-ms duration and yielded many range determinations of Venus to an accuracy of  $\pm 100/\text{km}$ .

The Millstone Hill radar system was later rebuilt to operate at a higher frequency (Table 1), and was employed in 1964, 1965–1966, and 1967 for further delay determinations to the planet Venus (Refs. 5 and 6). In these measurements, a pulse compression system was employed and operated by reversing the phase of the transmitted pulse by 0 or 180 deg according to a Barker sequence. The echo waveform was decoded by means of a delay-line with taps connected together via 0- or 180-deg phase shifters arranged in the reverse order to the transmitted code. This scheme gave round-trip flight-time determinations with an estimated uncertainty (in most cases) of  $\pm 10 \mu\text{s}$ .

In 1966, the high-power Haystack X-band facility (Ref. 7) came into operation and was first employed in planetary ranging experiments (Ref. 8). This system

---

\*Operated with support from the U. S. Air Force.

**Table 1. Parameters of Lincoln Laboratory Planetary Range Radar**

Parameter	Millstone Hill			Haystack 1967
	1959	1961	1964	
Frequency $f$ , MHz	440	440	1295	7840
Antenna diameter, ft	84	84	84	120
Gain $G$ , dB	37.5	37.5	46.5	66.6
Aperture $A$ , m <sup>2</sup>	210	210	190	470
Average power $P$ , kW	50	120	120	200-400
System temperature $T_s$ , °K	185	250	~100	~60
Shortest effective pulse length, $\mu$ s	2000	500	40	24
Sensitivity <sup>a</sup> relative to 1961, dB	-2.7	0	+10.0	+36.6

<sup>a</sup>Computed as  $PGA/T_s(f)^{1/2}$ .

(Table 1) provides approximately 26 dB greater sensitivity than Millstone and has, therefore, superseded it for all planetary operations. Besides being capable of following Mercury and Venus over their entire orbits (Ref. 9), Haystack can yield accurate ranging results for Mars at opposition from which topographic information can be derived (Ref. 10).

This paper presents a brief description of the Haystack planetary radar system and the data processing schemes that are a major contributor to its successful operation.

## II. Haystack Antenna System

Figure 1 shows the Haystack antenna system. A 120-ft diameter parabola with an rms surface tolerance of about 0.03 in. is mounted inside a rigid space-frame radome having a diameter of 150 ft. A cassegrain feed arrange-

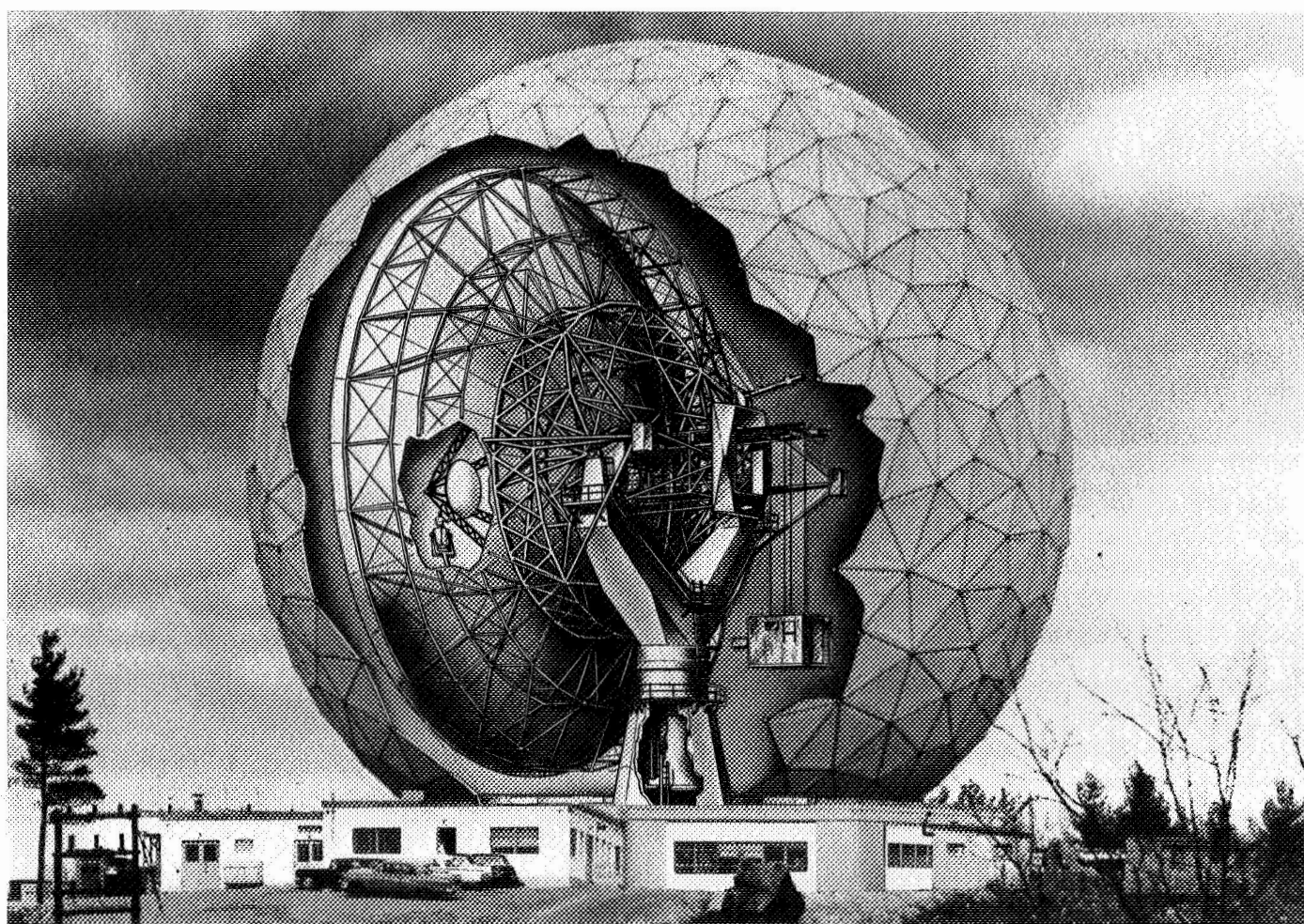


**Fig. 1. Haystack antenna system, artist's conception**

ment is employed to permit the RF components (i.e., transmitter, final amplifier, and receiver maser) to be mounted inside an equipment shelter ( $8 \times 8 \times 12$  ft), which can be hoisted into a keyway and secured immediately behind the apex of the parabola. The feed horn projects through the front face of this shelter toward the subreflector via a hole in the primary reflector. The system has been described by Weiss (Refs. 7 and 11).

When operated at 8000 MHz, the beamwidth of the antenna is 0.07 deg. This narrow beamwidth requires that the antenna be pointed under the control of a digital electronic computer (Ref. 12). A Univac 490 computer is employed for this purpose and, for planetary operations, the required astronomical information is obtained from standard ephemerides stored on magnetic tape (Ref. 13). Normally the computer directs the antenna at the apparent position of an object in the sky, and this direction would be correct for radar reception or radio astronomical observations of the planet. For experiments on Venus near inferior conjunction, however, the antenna must be commanded to "lead" the planet during periods of transmission; i.e., the antenna must be directed at that point in the planetary orbit where the planet will be when the signals arrive.

### III. The Haystack Transmitter System

As noted previously, all the microwave components of the radar system are housed in an equipment shelter located immediately behind the apex of the antenna. This location serves to keep the length of waveguide between the transmitter and feed system to an absolute minimum. The final amplifier in the transmitter employs a pair of VA-949 klystrons driven by a traveling-wave tube amplifier. Power is taken from each of the klystron output cavities via two separate water-cooled waveguides. Each waveguide is connected via a ferrite circulator to one of four horns that form the feed system (Ref. 14). The transmitter is designed to operate in a continuous wave mode with an average output power of 400 kw. To date, however, reliable operation has been achieved only at power levels of about 300 kW.

Figure 2 shows in schematic form the transmitter frequency control system employed at Haystack. The basic frequency standard is a 5-MHz crystal oscillator that is locked in frequency to a hydrogen maser and has a long-term stability of better than 1 part in  $10^{12}$ . A 1-MHz signal derived from this master oscillator is converted to the required signal frequency (7840 MHz) by means of

an inverse superheterodyne system. This arrangement permits all frequency multipliers to run continuously and contributes significantly to the spectral purity of the radiated signal. By mixing the transmitted signal with the output of a similar but completely separate exciter system, the spectral purity of the transmitter has been found to be  $\sim 0.05$  Hz.

To obtain range information, it is necessary to apply some form of modulation to the transmitted signal. Phase modulation has been chosen, in part because of its earlier successful use at Millstone, and in part because an analysis of the computer processing required to perform the

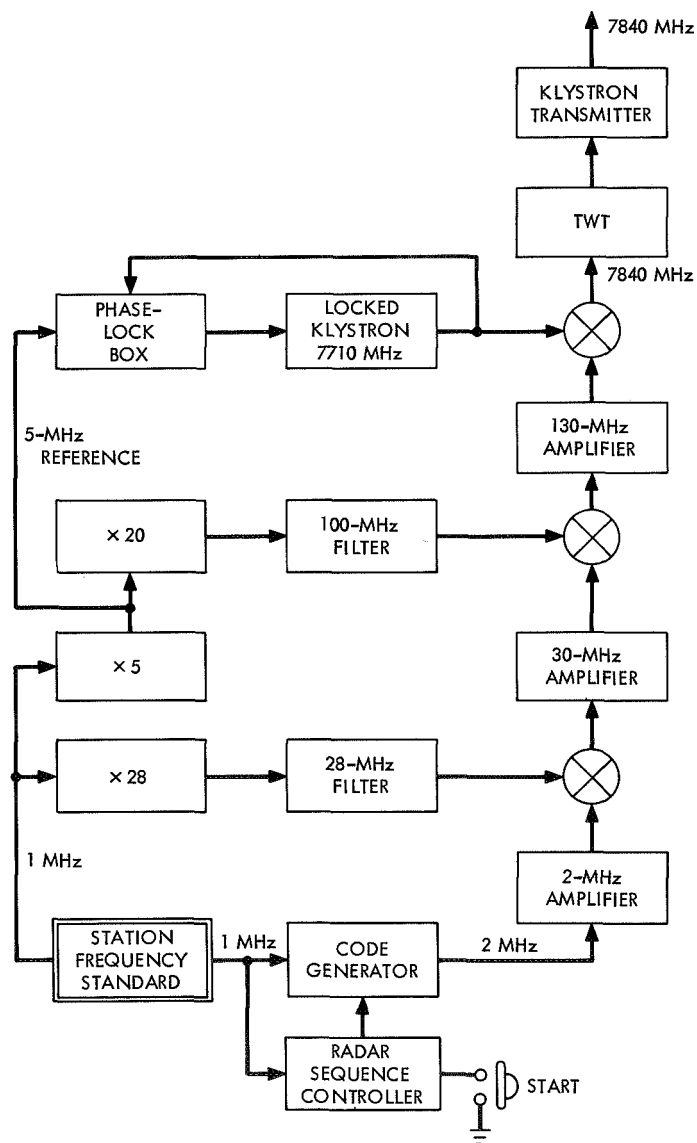


Fig. 2. Frequency control system for Haystack planetary radar transmitter

decoding showed some advantages for this type of modulation over frequency modulation. The modulation is applied by reversing the phase of the 2-MHz input signal to the up-converter chain (Fig. 2). This is done by generating the required 2 MHz from a binary flip-flop driven at 4 MHz, and inhibiting a change of state whenever a phase-reversal is required. The code employed is a "maximal length" shift-register sequence (for example, see Ref. 15) and is generated by driving a digital shift-register with appropriate feedback connections from the station 1-MHz master signal. A variety of codes are available, and the minimum interval between phase reversals (the so-called baud length) may also be changed. Table 2 summarizes the coding schemes that have been employed to-date. In general, codes having elements  $N \leq 63$  have been employed (where  $N = 2^n - 1$ ), causing the transmitted waveform to repeat in an interval that is short compared with the radar depth of the planet. The fortunate circumstance that the strongest echoes are returned from the immediate vicinity of the subradar point serves to minimize the effects of "self noise" to which this short unambiguous length gives rise.

Operation of the transmitter is under control of a radar "sequencer." This unit determines the length of the transmit period (which is set equal to the flight-time), and controls the change-over from transmitting to receiving, and the duration of the receive interval. All transmit/receive runs are arranged to begin precisely on a minute mark as defined by the station timing system.

**Table 2. Table of coding schemes employed at Haystack**

Parameter	Code scheme				
	1	2	3	4	5
Baud length, $\mu s$	500	126	60	60 <sup>a</sup>	24 <sup>b</sup>
Sample spacing, $\mu s$	500	63	30	30	12
Number of elements	31	15	15	63	63
Unambiguous length, ms	15.5	1.89	0.9	3.78	1.512
Number of samples processed	31	16	6	32	16
Window covered, ms	15.5	1.008	0.180	0.960	0.192
<sup>a</sup> Employed against Venus and Mercury where four successive codes can be summed before decoding.					
<sup>b</sup> Employed against Venus and Mercury where twelve successive codes can be summed before decoding.					

Prior to the start time, the transmitter is allowed to radiate an unmodulated carrier. At the start time, the phase code modulation is impressed on the signal commencing with the code generator in some known initial state. The transmit period is allowed to continue until the signals transmitted at the instant of start would be expected to arrive back at the radar according to the computed ephemerides. This time interval is measured to the nearest microsecond; the transmitter is then run-down, and the equipment switched to its receive mode.

Timekeeping at the station is performed by counting the master oscillator frequency. Adjustments to this frequency are made at intervals to maintain the clocks on UTC (as defined by the signals radiated by the East Coast Loran C network) to an accuracy of about  $\pm 10 \mu s$ .

#### IV. Haystack Receiver System

As presently configured, the receiver system includes two separate channels that are employed to amplify the expected (left-circular) component of the signals (transmitted with right-circular polarization) and the "depolarized" component, which has the same sense as transmitted. The first stage of amplification in each channel is a maser cooled to liquid helium temperature. A system temperature of about 60°K is achieved when the antenna is directed toward Venus at inferior conjunction.

Figure 3 shows the frequency control system employed for the receiver, which uses essentially the same local oscillators as the transmitter. The received signals are converted to 2 MHz and then are applied to phase-orthogonal detectors. Low-pass filters following the phase detectors serve to define the receiver bandwidth, which is usually adjusted to match the transmitted baud length. Samples of the video signals are taken by a pair of digital voltmeters under control of a sample generator. In general, two samples are taken (of each channel) in an interval of one baud (Table 2), but the timing of these samples is continuously varied to keep in step with the arriving signals; i.e., the continuously changing flight-time is compensated by smoothly adjusting the time at which receiver samples are taken. In order to do this, use is made of the relation

$$\Delta f = f_0 \dot{\tau}$$

where  $\Delta f$  is the expected doppler shift,  $\dot{\tau}$  is the rate of change of the flight time (both measured at the instant of reception), and  $f_0$  is the radar frequency. Thus, by

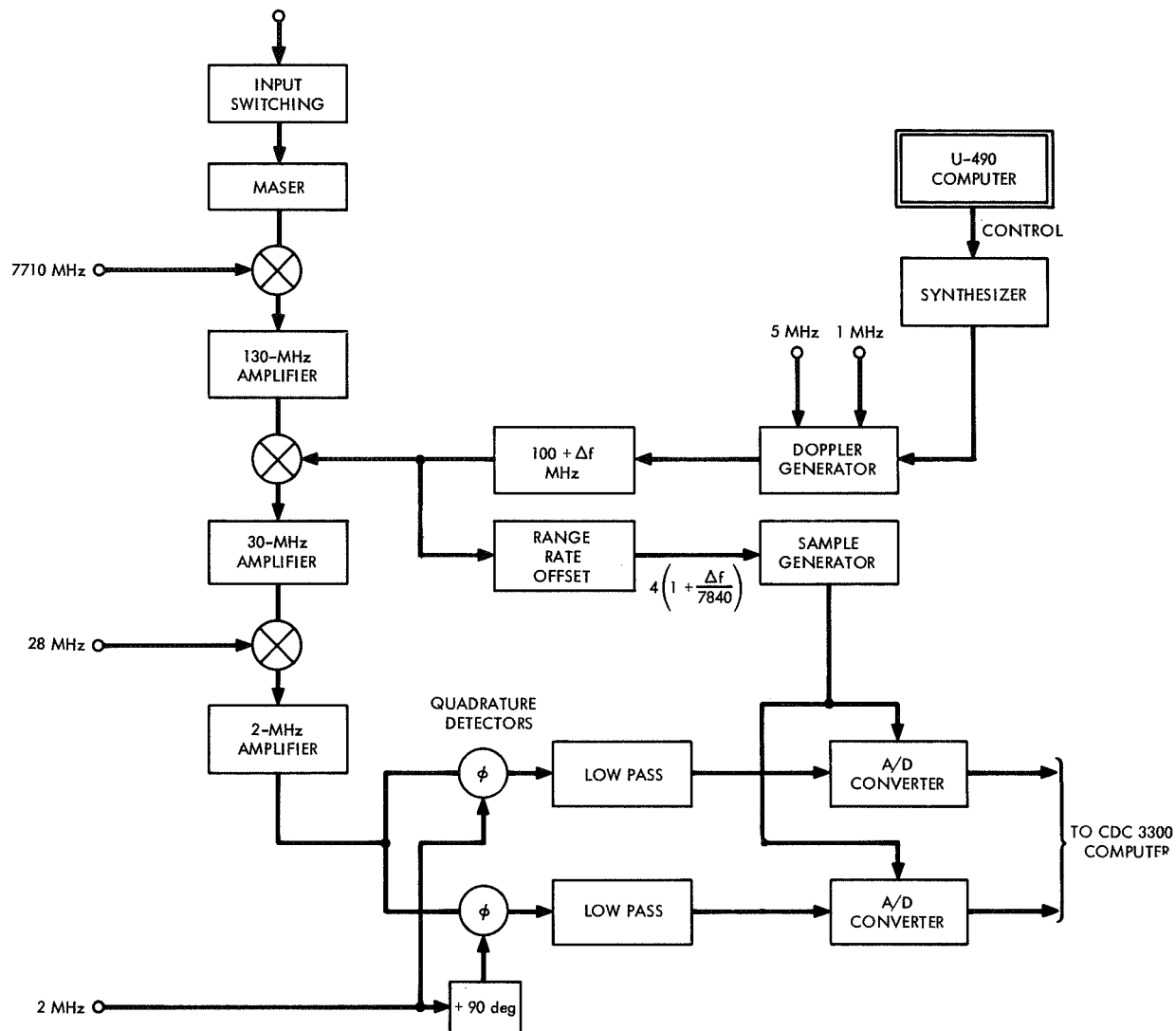


Fig. 3. Frequency control system for planetary radar receiver

dividing the doppler shift  $\Delta f$  by 7840 we obtain a frequency shift that must be applied to the 1-MHz station standard to obtain a new timing reference that stays in step with the arriving signals. The actual means of accomplishing this step is substantially more complicated than Fig. 3 suggests.

The doppler shift  $\Delta f$  is continuously compensated by varying the 100-MHz local oscillator in 0.1-Hz steps. This compensation is performed by placing a digitally controlled frequency synthesizer under command of the U490 antenna pointing computer, which changes the frequency at 1/20-s intervals. This is sufficiently often so that the required and actual frequency offsets never depart by more than the minimum change that the synthesizer

can make (i.e., 0.1 Hz). The doppler information is fed into the computer prior to the start of the operations in the form of computed value vs time, and the U490 computer is then merely required to interpolate smoothly between these values. These doppler shifts together with the expected flight-times are computed in advance of the observations based upon the best available elements for the earth and the planet, the planetary radius, the astronomical unit, and a number of other constants (Ref. 16).

## V. Computer Processing

The data samples taken by the two digital voltmeters are applied to a high-speed general purpose digital computer (CDC 3300). During the receive period,

the computer is employed to decode the signals; that is, a train of samples occupying a length of time equal to the transmitted code is treated to remove the effect of the phase modulation by reversing the sign of certain of the signal samples (both video components) according to the same pattern as transmitted, and then summing separately all the samples for the two channels. In this way, a phasor is generated and stored on magnetic tape. On receipt of the next data sample pair, the earliest pair in the memory are dropped and the procedure repeated to generate another vector sum. This scheme is identical in concept to the tapped-filter delay-line scheme, but suffers none of the practical difficulties encountered with the latter scheme, which can cause the performance to be less than ideal (typically by 2 dB in the case of the system employed at Millstone).

Limitations of computer speed allow, in general, only the processing of the data samples to recover a vector sum for a certain number of the possible delays within the unambiguous interval occupied by the code (Table 2). Thus, the window examined is typically substantially less than the code length, and this necessitates an adjustment of the start of the sampling to insure that the echo from the leading edge of the planet lies at an appropriate position. This adjustment is set by a preset dwell counter, which defines the interval that may be required between the end of the transmit period and the commencement of sampling the receiver output.

In the case of observations of Mars (Ref. 10), the processing of the vector sums is carried out during the receive time, and consists merely of squaring each phasor and adding it to all others taken at the same relative delay. This incoherent addition, in effect, synthesizes a filter at zero frequency with a bandwidth of  $\sim 1$  kHz in the case of the 60- $\mu$ s baud length code, and  $\sim 0.5$  kHz for 126- $\mu$ s baud length (Table 2).

For observations of Mercury and Venus, the phasors are written onto magnetic tape and later (during the next transmit period) subjected to a Fourier analysis employing an algorithm developed by Cooley and Tukey (Ref. 17). This process determines the amount of echo power as a function of frequency for each range delay examined. The spectral resolution is determined by the number of phasors coherently summed in the Fourier analysis.

For example, in the case of the 60- $\mu$ s baud length code employed for Venus observations (Table 2), the raw data

samples occupying four code intervals are gathered and summed to reduce the amount of decoding required by a factor of 4. (This operation synthesizes a filter centered at zero frequency with a bandwidth of  $\sim 66$  Hz.)

Of the possible 126 range boxes spaced 30  $\mu$ s apart, only 32 are demodulated. In this fashion we obtain complex samples of the echo at a given delay at intervals of 15.12 ms. By coherently summing 64 such samples, a spectral resolution of  $(64 \times 0.01512)^{-1} = 1.033$  Hz is achieved. An ensemble average of the Fourier series is obtained for the entire receive period or several such periods, providing a complex two-dimensional array of 64 frequencies by 32 delays.

The power is obtained from the squared modulus of the complex coefficients. Figure 4 provides an example of an array of echo power obtained in this fashion.

## VI. Estimation of the Range and Doppler Shift

Price (in Ref. 18; also see Green in Ref. 19) has discussed the optimum means of estimating the delay and doppler shift for a distributed target such as a planet. The best estimate of delay  $\tau$  and doppler shift  $\nu$  is that for which the product  $C(\tau\nu)$  maximizes with

$$C(\tau\nu) = \int_t \int_f P'(t', f') P(t + \tau, f + \nu) dt df$$

where  $P'(t', f')$  is the measured echo power as a function of delay  $t'$  and frequency  $f'$ , and  $P(t, f)$  is the *expected* echo power function in the absence of noise where delay  $t$  is measured with respect to the leading edge of the planet. In essence,  $P(t, f)$  is a template that is moved over the observed array of power vs frequency and delay, and is employed to weight the echo power at each point. The trial position of the template for which the weighted sum appears to maximize is the best estimate of the delay and doppler shift. That this should be so depends upon the theory of matched filter processing.

In the case of the array of  $P'(t', f')$  determined in Mercury and Venus observations, the first step is interpolation to provide values of power at delay intervals of 5  $\mu$ s and frequency intervals of 0.25 Hz. Next, these values are weighted by the template function and summed. Because of the large size of the template used,



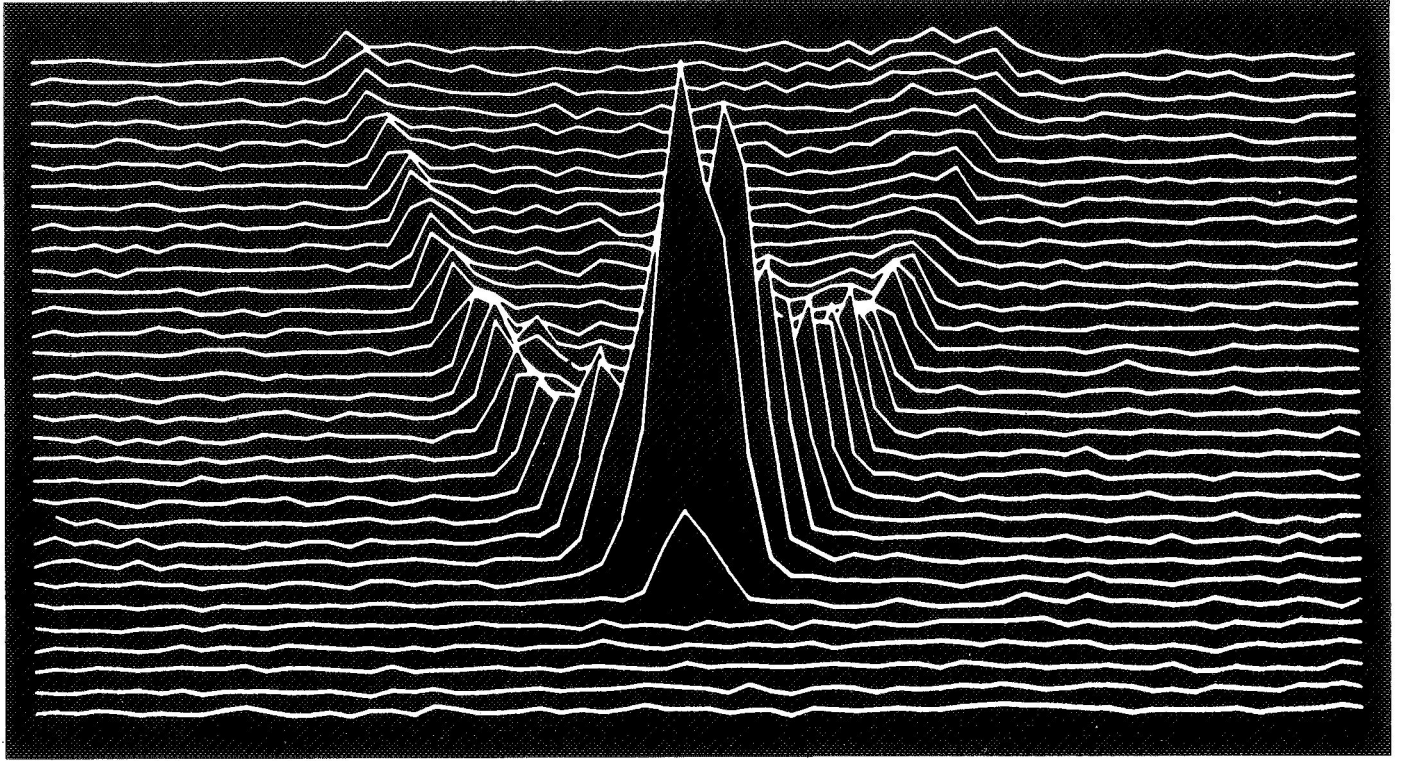


Fig. 4. Example of distribution of echo power with delay and doppler shift obtained by computer processing of received signals

the weighted sum is calculated only for a comparatively small number of positions of the template with respect to the array of echo power. These offsets nevertheless span a region ( $330 \mu\text{s}$  in delay and  $40 \text{ Hz}$  in frequency) that is large compared to the *a priori* uncertainty. This search is first performed with a coarse grid ( $15\text{-}\mu\text{s}$  delay steps and  $2\text{-Hz}$  frequency intervals) and then the peak is explored with a finer grid ( $5 \mu\text{s}$  in delay and  $0.5 \text{ Hz}$  in frequency) to determine the best location for the template.

The expected distribution of echo power  $P(t, f)$  is determined from observations near inferior conjunction when the signals are strong. Unfortunately it is not possible to employ as a template the actual echo power distribution  $P'(t, f)$  observed at such times, because the apparent spin-rate changes with time cause the doppler spreading of the signals to vary also. Instead, the angular scattering law  $P(\phi)$  is determined from observations of either the total echo power vs delay, or the echo power vs frequency (for example, see Refs. 8 and 20). By assuming that the scattering properties are uniform over the sphere, the expected distribution of echo power with delay measured from the leading edge of the echo  $P(t, f)$

is given by (Ref. 19)

$$P(t, f) = \frac{c^2 P \left[ \cos^{-1} \left( \frac{1 - ct}{2a} \right) \right]}{2 f_0 \Omega \cos \alpha} \times \left[ \frac{ct}{2a} \left( \frac{2 - ct}{2a} \right) - \left( \frac{fc}{2f_0 a \Omega \cos \alpha} \right)^2 \right]^{-1/2}$$

(real values only)

where  $c$  is the velocity of light,  $a$  is the planetary radius,  $f_0$  is the radar frequency,  $\Omega$  is the apparent angular velocity, and  $\alpha$  is the angle between the apparent spin axis and the plane perpendicular to the line-of-sight. A template generated in this way is displayed in Fig. 5.

The template obtained in the manner outlined is not an exact match to the observed echo power distribution, because the effects of the finite pulse length and filter width on the measurement have not specifically been included. To some extent, these effects are introduced

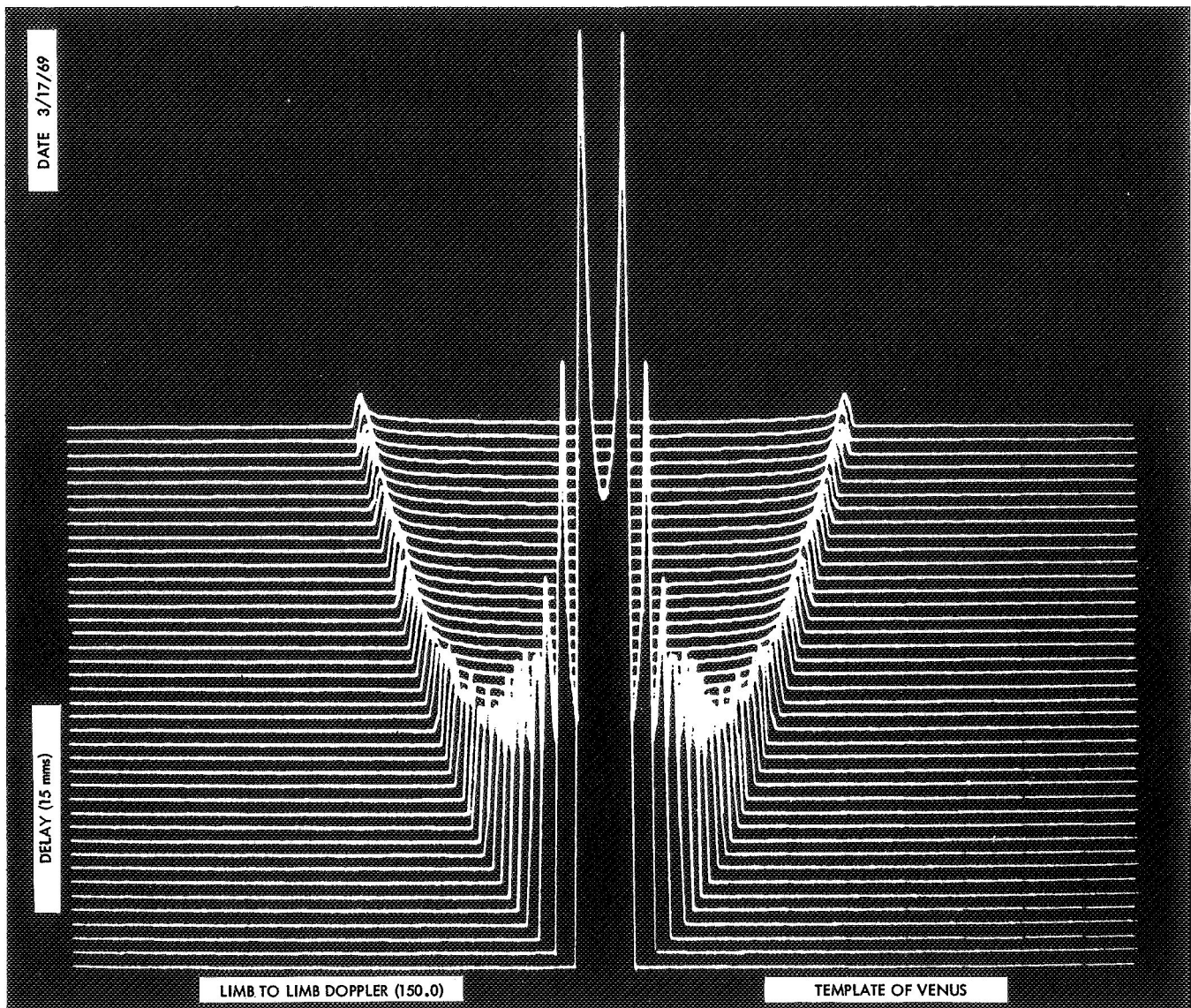


Fig. 5. Example of template function calculated from observed angular scattering law

by virtue of their influence on the original measurement of the scattering function  $P(\phi)$ . However, since it is assumed that  $P(\phi) = 0$  for  $\phi \leq 0$  deg, the template has a steeply rising edge at  $t = 0$  while the true echo voltage rises almost linearly over an interval equal to one baud length. This difference is thought to introduce a small systematic shift in the delay at which the weighted sum  $C(\tau v)$  maximizes.

A search for this effect has been made by comparing the computed delays with hand-fit estimates based upon the total echo power vs delay observed with different width filters. Figure 6 shows the results of this analysis, which seems to indicate that the error is

$\leq 8 \mu\text{s}$ . However, additional work is required to determine this value precisely. Figure 6 also serves to show that large systematic errors can arise in estimating the range by simply picking out the peak observed in a single filter if the bandwidth includes a sizable fraction of the total frequency extent of the echoes. By increasing the filter width, more echo power is included from greater delays causing a systematic bias of the peak to a later position.

The template matching approach described above automatically eliminates this problem, besides increasing the signal-to-noise ratio through gathering up all the echo energy into a single number by the weighted summation.



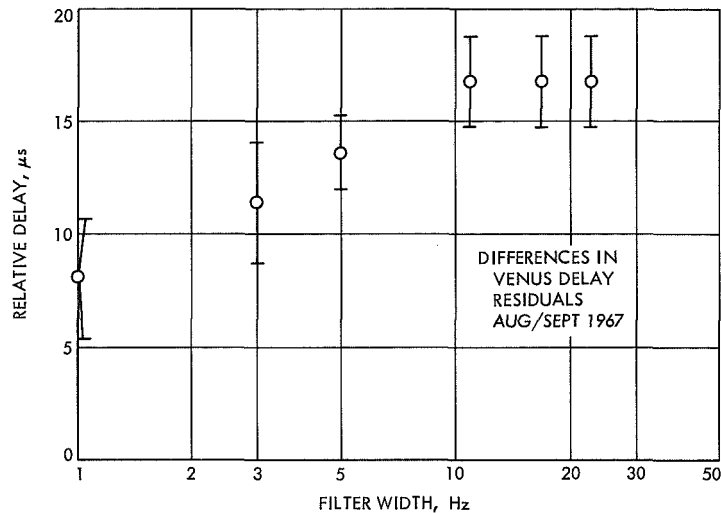


**Fig. 6. Differences between computer estimates of echo delay based upon template matching and hand estimates obtained by noting position of peak echo power in a filter of width indicated**

## References

1. Price, R., et al., "Radar Echoes from Venus," *Science*, Vol. 129, pp. 751-753, 1959.
2. Pettengill, G. H., and Price, R., "Radar Echoes From Venus and a New Determination of the Solar Parallax," *Planet. Space Sci.*, Vol. 5, pp. 71-74, 1961.
3. Pettengill, G. H., et al., "A Radar Investigation of Venus," *Astron. J.*, Vol. 67, pp. 181-190, 1962.
4. Smith, W. B., "Radar Observations of Venus 1961 and 1959," *Astron. J.*, Vol. 68, pp. 15-21, 1963.
5. Evans, J. V., et al., "Radio Echo Observations of Venus and Mercury at 23-cm Wavelength," *Astron. J.*, Vol. 70, pp. 486-501, 1965.
6. Evans, J. V., et al., "Radar Observations of Venus in 1965/1966," *Astron. J.*, Vol. 71, pp. 897-901, 1966.
7. Weiss, H. G., "The Haystack Microwave Research Facility," *Spectrum*, Vol. 2, pp. 50-69, 1965.
8. Evans, J. V., et al., "Radar Observations of Venus at 3.8-cm Wavelength," *Astron. J.*, Vol. 71, pp. 902-915, 1966.
9. Shapiro, I. I., et al., "Fourth Test of General Relativity: Preliminary Results," *Phys. Rev. Lett.*, Vol. 20, pp. 1265-1269, 1968.

## References (contd)

10. Pettengill, G. H., Counselman, C. C., Rainville, L. P., and Shapiro, I. I., "Radar Measurements of Martian Topography," *Astron. J.*, Vol. 74, No. 3, Apr. 1969.
11. Weiss, H. G., *The Haystack Experimental Facility*, Technical Report 365. Lincoln Laboratory, Massachusetts Institute of Technology, Lexington, Mass., 1964.
12. Heart, F. E., Mathiasen, A. A., and Smith, P. D., *The Haystack Computer Control System*, Technical Report 406. Lincoln Laboratory, Massachusetts Institute of Technology, Lexington, Mass., 1965.
13. Frachtman, H. E., *Haystack Pointing System: Planet*, Group Report 1964-46. Lincoln Laboratory, Massachusetts Institute of Technology, Lexington, Mass., 1964.
14. Jones, C. W., *The Microwave System of the Haystack Planetary Radar*, Technical Report 457. Lincoln Laboratory, Massachusetts Institute of Technology, Lexington, Mass., 1968.
15. Evans, J. V., "Radar Measurements of Target Scattering Properties," in *Radar Astronomy*, Chapter 9. Edited by J. V. Evans and T. Hagfors. McGraw-Hill Book Co., Inc., New York, 1968.
16. Ash, M. E., *Generation of Planetary Ephemerides on an Electronic Computer*, Technical Report 391. Lincoln Laboratory, Massachusetts Institute of Technology, Lexington, Mass., 1965.
17. Cooley, J. W., and Tukey, J. W., "An Algorithm for Machine Calculation of Complex Fourier Series," *Math. Comput.*, Vol. 19, pp. 297-301, 1965.
18. Price, R., "Detectors for Radar Astronomy," in *Radar Astronomy*, Chapter 10. Edited by J. V. Evans and T. Hagfors. McGraw-Hill Book Co., Inc., New York, 1968.
19. Green, P. E., "Modulation, Demodulation, and Data Processing Applied to Radar Astronomy," in *Radar Astronomy*, Chapter 1. Edited by J. V. Evans and T. Hagfors. McGraw-Hill Book Co., Inc., New York, 1968.
20. Ingalls, R. P., and Evans, J. V., "Scattering Properties of Venus at 3.8 cm," *Astron. J.*, Vol. 74, pp. 259-272, 1969.

# Improvements in Radar Ranging Accuracy Using Correlation Techniques

G. H. Pettengill

Arecibo Ionospheric Observatory  
Cornell University Center for Radiophysics and Space Research  
Arecibo, Puerto Rico

*Correlation techniques in the time and frequency domain have been applied to the task of maximizing measurement accuracy in the reception of radar echoes from a planetary target. Using an average scattering law for the target obtained at times of closest approach to earth, the signal-to-noise ratio of the echo can be significantly improved during periods when the target is more distant, without sacrifice in measurement accuracy.*

## Deep Space Ranging\*

R. C. Tausworthe

Telecommunications Division  
Jet Propulsion Laboratory  
Pasadena, California

*The ranging of Mariner V extended direct range measurements of spacecraft from lunar to interplanetary distances, with a somewhat better absolute accuracy. The method was basically the same technique as used in the previous system, but refined to take advantage of many system improvements, optimizations, etc. This paper presented the basic ranging concepts, its evolution to the present capability (which will also be used during the Mariner 1969 flight to Mars and beyond), the resulting data type accuracy, and a groundwork for advanced systems with still greater performance potential.*

---

\*Tausworthe, R. C., "Ranging the Mariner to Venus," in *Proceedings of IEEE International Convention and Exhibition*, March 1967, pp. 294-295; also, "Digital Communications and Tracking: Ranging Measurement," in *The Deep Space Network*, Space Programs Summary 37-42, Vol. III, pp. 52-56. Jet Propulsion Laboratory, Pasadena, Calif., Nov. 30, 1966.



# S-Band Faraday Rotation Measurements of the Solar Corona Using Signals From *Pioneer VI* Solar Occultation\*

G. S. Levy

Communication Elements Research  
Jet Propulsion Laboratory  
Pasadena, California

*Faraday rotation measurements were conducted for solar occultation of Pioneer VI. To make these measurements it was necessary to develop a closed-loop polarization servo tracking system. The feed provided two channels of orthogonal linear polarization. Each channel employed a traveling-wave maser amplifier. One channel was treated as the information signal and went through the reference receiver channel of the standard communication receiver. The orthogonal mode was treated as an error signal and used most of the monopulse intermediate frequency circuitry to develop the servo error signal. The implementation of this equipment are discussed as well as some of the experiment results due both to the earth ionosphere and the solar corona.*

---

\*Levy, G. S., et al., "*Pioneer VI: Measurement of Transient Faraday Rotation Phenomena Observed During Solar Occultation*," *Science*, Vol. 166, No. 3905, pp. 596-598, Oct. 1969.



*Session II*  
*Data Processing and Modeling Techniques*

*Session Chairman*  
*Dr. William G. Melbourne*  
*Jet Propulsion Laboratory*





# Application of a Model Fitting Procedure to the Determination of Unknown Parameters in Several Theoretical Backscatter Models of Venus at 70-cm Wavelength

R. F. Jurgens

Arecibo Ionospheric Observatory\*  
Cornell University Center for Radiophysics and Space Research  
Arecibo, Puerto Rico

*A procedure of model fitting has been applied to the determination of the backscatter characteristics of Venus using the radar observations at 70-cm wavelength made during the inferior conjunction of 1967. The principle of weighted least squares was used to minimize the rms error between the observed echo power as a function of delay and a model echo based on the convolution of the radar ambiguity function and several theoretical backscatter models by adjusting the arbitrary parameters in the models. Several backscatter models which have been found to fit the lunar radar observations over a wide range of incidence angles were tested. Results of the procedure indicate that the backscatter law of Venus is variable depending upon the locations of certain surface features, and that these surface features contribute significantly to the backscattered power for a given delay annulus if the angle of incidence is large. Therefore, certain models which attempt to extract physical information about the roughness of the bulk of the surface of Venus are likely to be strongly biased by the surface features. Data are presented which indicate that a scattering model by Muhleman generally gives a good fit to the observations. However, large departures are sometimes observed especially when pulse lengths shorter than 50  $\mu$ s are used to measure the backscattering law near the subradar point.*

---

\*The Arecibo Ionospheric Observatory is operated by Cornell University with the support of the Advanced Research Projects Agency and the National Science Foundation under contract with the Air Force Office of Scientific Research.

## I. Introduction

The backscatter law of Venus is of considerable importance to the problem of determining the mean-squared slope of the surface and for estimating the strength of diffuse scattering components which indicates the abundance of debris having a scale size near that of the radar wavelength. Direct measurement of the backscatter law of Venus has been difficult due to the relatively poor signal-to-noise ratio which results if sufficiently short pulse lengths are used. Short pulse lengths are required for making the measurement if the effects of the convolution of the radar ambiguity function with the scattering law are to be neglected such as is customary with lunar observations. To obtain a reasonably large signal-to-noise ratio, at large angles of incidence, it is necessary to use fairly long pulse lengths. However, at smaller angles of incidence the signal is strong enough to use much shorter pulses. In this discussion a fairly long pulse length is considered to be approximately 4 ms (roughly 1/10 the round trip delay to the limb) and a short pulse would be perhaps 10  $\mu$ s in length. By using a number of intermediate pulse lengths it is possible to examine the backscatter law of Venus with varying degrees of convolutional smearing. The construction of an accurate scattering law from such observations is a difficult problem, since the effects of convolution are of varying degrees of importance at different angles of incidence. If we are only interested in determining whether a given scattering model is in agreement with the observations, a simpler procedure can be used. For example, the model

can be convolved with the various ambiguity functions and compared with observations.

Model fitting was accomplished by using the methods of weighted least squares. The theoretical echoes were based on the scattering models convolved with accurate representations of the radar ambiguity function including the effects of various electrical filters. The model does neglect the effects of quantizing errors caused by the seven-bit analog-to-digital conversion. These errors are generally small except in the cases where the average signal-to-noise ratio is large (50 to 1 or greater). Such large signal-to-noise ratios occur only with the long pulse observations.

A block diagram of a typical receiving system is shown in Fig. 1. The voltages at the outputs of the electrical filters are sampled and the squaring operation is accomplished within the digital computer rather than prior to sampling. Such a procedure is necessary if the large dynamic range of the echo is to be preserved with the seven-bit sampler. The system response is controlled primarily by the filters in the baseband amplifier and by the digital processing.

## II. Model Fitting

The echo model used in this analysis is considered to be given by the convolution of the scattering model  $S(\tau)$  and the radar ambiguity function  $A(\tau)$ . Although  $A(\tau)$  is

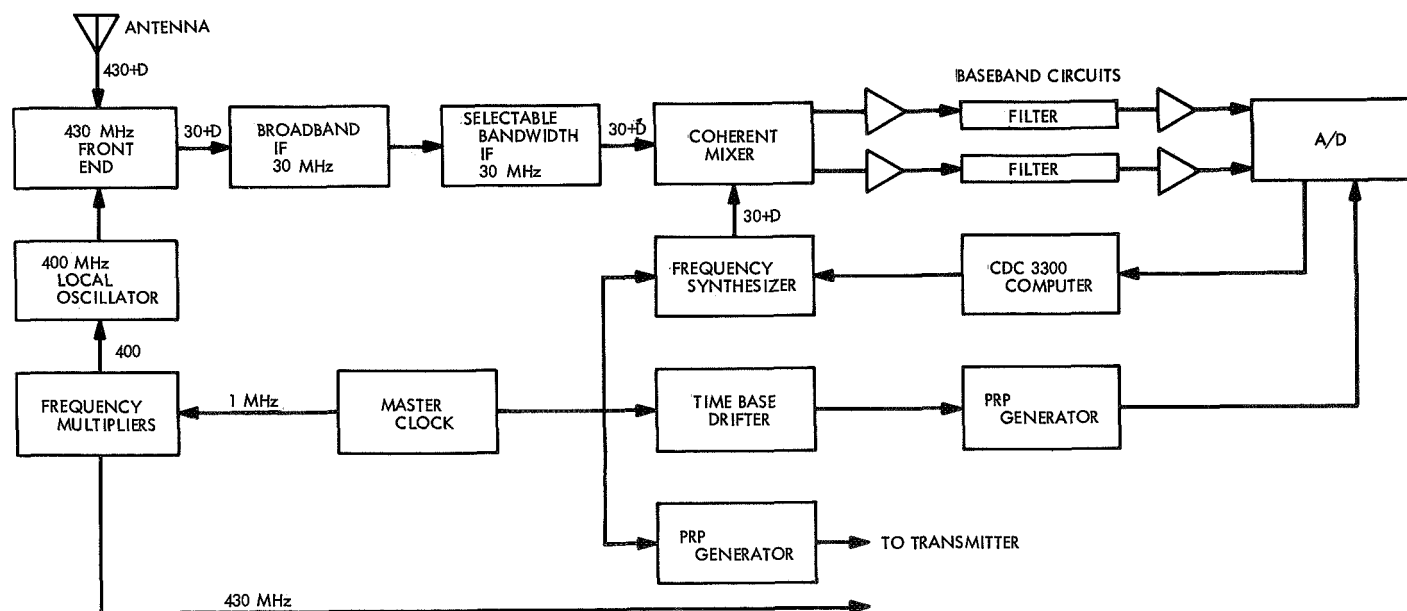


Fig. 1. Block diagram of planetary radar system used at AIO during 1967-1969 observation period

in reality frequency dependent, the frequency dispersion  $f_m$  of Venus at 70-cm wavelength is always much smaller than the reciprocal of the pulse length  $1/\tau_p$ . If  $\tau_m$  is the delay depth of the planet, it is also assumed that the pulses are spaced by at least  $\tau_m + 2\tau_p$  so that no ambiguity exists in the delay dimension. The response of the electrical filters is such that their impulse response  $h(t)$  is insignificant for times greater than several pulse lengths. The response of the system shown in Fig. 1 to a single rectangular pulse is

$$Q(\tau) = \left[ \int_0^\tau p(t) h(t - \tau) dt \right]^2$$

where  $p(t)$  is the transmitted pulse envelope.

$$p(\tau) = 1, \quad 0 \leq \tau \leq \tau_p \\ = 0, \quad \text{elsewhere}$$

The impulse response  $h(t)$  is either that of an RC (resistance capacitance) filter or a rectangular response matched to the pulse length depending upon the availability of various filters at the time of the observation.

$$h_1(\tau) = \frac{\exp(-\tau/\tau_f)}{\tau_f}, \quad 0 \leq \tau < \infty \\ = 0, \quad \tau < 0 \\ h_2(\tau) = 1/\tau_p, \quad 0 \leq \tau \leq \tau_p \\ = 0, \quad \text{elsewhere}$$

For convenience in evaluating cross-sections, the Fourier transform of  $h(\tau)$  at zero frequency has been adjusted to equal one.

$$H(0) = \int_0^\infty h(\tau) d\tau = 1$$

If a periodic set of pulses are transmitted, the ambiguity function becomes approximately

$$A(\tau) = Q(\tau) * \sum_{n=-\infty}^{\infty} \delta(\tau - n\tau_i), \quad \tau_i > \tau_p \\ \tau_f \sim \tau_p$$

where  $\delta$  is the Dirac delta function,  $\tau_i$  is the pulse repetition period, and the asterisk indicates convolution. The

average power response of the system to a planetary target having a backscatter law  $S(\tau)$  at an arbitrary delay  $\tau_o$  is

$$P(\tau) = S(\tau - \tau_o) * A(\tau)$$

The average can be assembled by considering an ensemble of identical experiments or, in reality, from a time average of the individual echoes. In the case of a time average, the echoes are correlated for times longer than  $1/f_m$ , and therefore, one obtains a statistically independent echo approximately every ten seconds near the time of inferior conjunction. From the point-of-view of the echo statistics, there is no point in making  $\tau_i$  much smaller than  $1/f_m$ , however, the signal is always contaminated with noise which has a nearly constant spectral density prior to the baseband filtering. Therefore, the noise at the output of the baseband filter is uncorrelated in a time scale of approximately  $\tau_p$  depending upon the filters  $h(\tau)$ . From the point-of-view of increasing the signal-to-noise ratio it is obvious that  $\tau_i$  should be made as small as possible without causing a serious ambiguity in the delay dimension.

The complete model  $S_m(\tau)$  required in the least-squares solution is given by

$$S_m(\tau) = C_n + C_a [A(\tau) * S(x, \tau - \tau_o)]$$

where  $C_a$  is the amplitude,  $C_n$  the average noise level, and  $x$  represents a vector of unknown quantities upon which  $S$  is functionally dependent. Quantity  $\tau_o$  may or may not be known, and therefore it is often necessary to include it as an unknown in the solution. The observation is specified by a set of  $K + 1$  power measurements made at equally spaced intervals of time  $\tau_g$ .  $K + 1$  is not generally large enough to preserve the entire echo but does include a signal-free region before the arrival of the echo. The mean-square error between the observed echo power and the echo model is given by  $\epsilon$  where

$$\epsilon(C_a, C_n, \tau_o, x) = \sum_{k=0}^K W_k [S_o(k\tau_g) - S_m(C_a, C_n, k\tau_g - \tau_o, x)]^2$$

where  $W_k$  is the statistical weights associated with the power measurement at each delay.

### III. Scattering Models

Three scattering models which fit the lunar backscattering law over a wide range of incidence angles are given in Eqs. (1), (2), and (3). The first two were given by Muhleman (Ref. 1) and are based on a simple geometric optics theory. The third equation was given by Hagfors (Ref. 2) and is based on a physical optics approach. Modifications of Eq. (3) by Beckmann and Klemperer (Ref. 3), and Fung (Ref. 4) have been made to bring the large angle characteristics into agreement with observations.

$$S(\phi) = \frac{(\alpha')^3 \cos \phi}{[\sin^2 \phi + (\alpha')^2 \cos^2 \phi]^{3/2}} \quad \begin{array}{l} \text{Gaussian} \\ \text{Rayleigh} \end{array} \quad (1)$$

$$S(\phi) = \frac{\alpha^3 \cos \phi}{(\sin \phi + \alpha \cos \phi)^3} \quad \begin{array}{l} \text{exponential} \\ \text{Poisson} \end{array} \quad (2)$$

$$S(\phi) = (\cos^4 \phi + C \sin^2 \phi)^{-3/2} \quad \begin{array}{l} \text{Gaussian} \\ \text{exponential} \end{array} \quad (3)$$

where

$$\phi = \cos^{-1} \frac{1 - \tau}{\tau_m}$$

Inspection of the three models reveals that, at small angles of incidence, Eqs. (1) and (3) are essentially identical. At large angles of incidence, Eq. (3) does not provide a reasonable characteristic without modifications. Therefore, the choice is really between model 2 and the other two at small angles of incidence. At large angles of incidence, one can check to see if the simple  $\cos \phi$

characteristic agrees with the observations. Figures 2 and 3 show typical characteristics of the three scattering models. The model of Eq. (2) is very much more specular than the other two, while at the same time it is possible to obtain a similar functional form over the remainder of the curve by properly choosing  $\alpha$ . In Fig. 3,  $\alpha$  is the typical value found for Venus at 70-cm wavelength and  $C$  is chosen to produce a similar characteristic over a wide range of angles of incidence. Figure 4 shows the two models of Fig. 3 after convolution with the radar ambiguity function formed from a pulse of 1.0 ms and an RC filter having a time constant of 0.330 ms. It is clear that it would be very difficult to choose between the two models on the basis of the 1.0 ms pulse observations alone. Pulse lengths less than 50  $\mu$ s are required to reveal the scattering behavior of Venus in this range of incidence angles.

### IV. Observations

The use of 1.0- and 2.0-ms pulse observations in the model fitting program appears to give the most satisfactory results as opposed to shorter and longer pulse lengths. As shorter pulse lengths are used, the higher resolution gives poorer averages, and anomalous scattering regions cause greater departures from the average characteristic. When pulse lengths of 10  $\mu$ s are used, it is often impossible to represent the scattering behavior even crudely. At long pulse lengths (4.0 ms and greater), the essential characteristics of the scattering law are so badly blurred by the convolution that small systematic errors in the ambiguity function and other measurement errors cause fairly large biases in the measurement of the

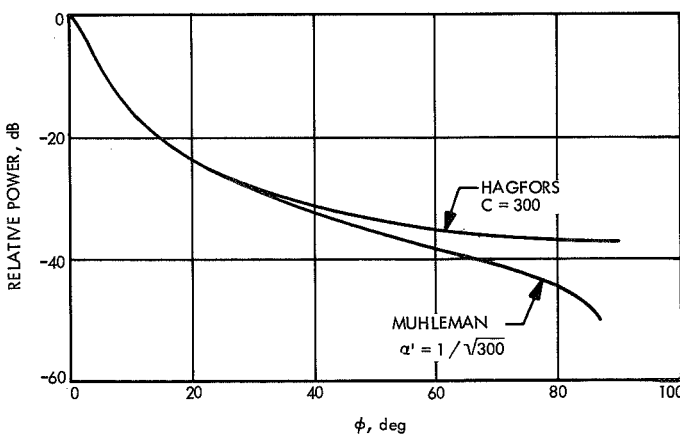


Fig. 2. Comparison of the scattering functions given in Eqs. (1) and (3)

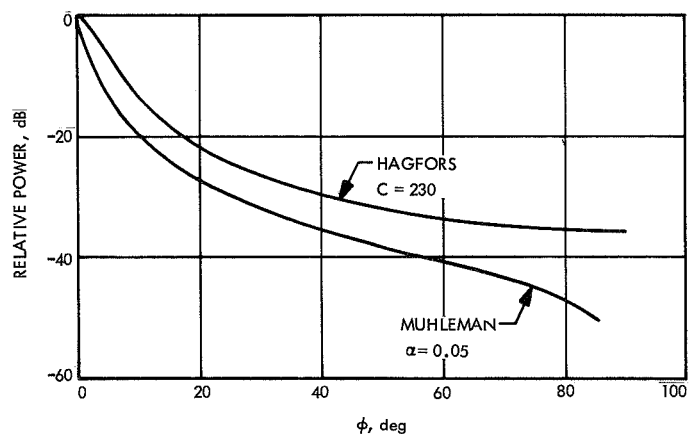
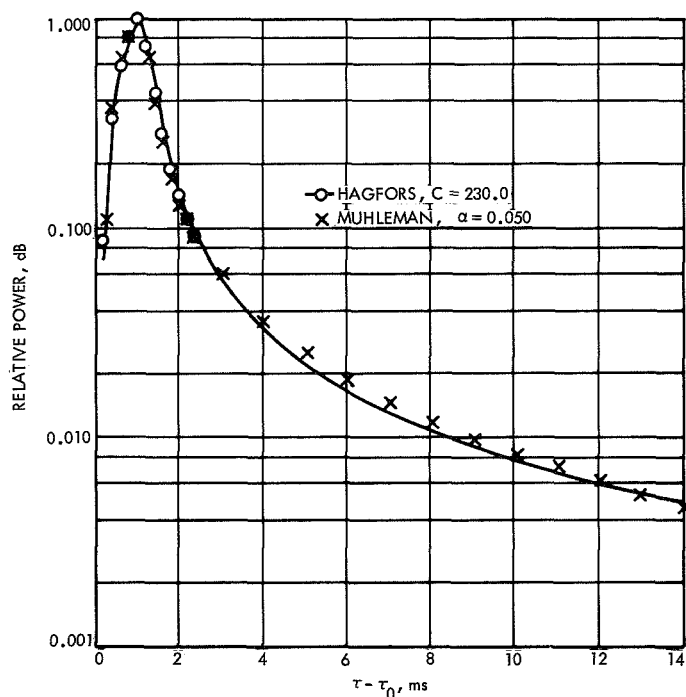


Fig. 3. Comparison of the scattering functions of Eqs. (2) and (3)



**Fig. 4. The scattering functions of Fig. 3 after convolution with the radar ambiguity function**

parameters  $\alpha$ ,  $\alpha'$ , and  $C$ . Also at such long pulse widths, it becomes impossible to eliminate the effects of anomalous features which tend to increase the roughness of the model.

By far the largest number of observations which are useful for model fitting were made by using a pulse length of 1.0 ms. The examples shown in Figs. 5 and 6 were processed with uniform weights over the first 3.0 ms of the echo and zero weight elsewhere using the model of Eq. (2). It is clear that the model in Fig. 5 fits relatively well beyond the 3.0 ms weighted area, however, the fit in Fig. 6 is not as good. Notice that the required values of the roughness parameter in the model are different in the two cases, and in the second case, the model clearly underestimates power at large delays. At this time, a relatively smooth surface occupied the region near the subradar point resulting in a more specular model which is not consistent with the roughness of the planet at larger angles of incidence. However, further investigation using delay-doppler mapping techniques indicates that the roughness near the subradar point is typical of much of the surface of Venus, and that the excess power at larger angles of incidence is caused primarily by anomalous scattering regions. The relative roughness of the region near the subradar point can be monitored by the model fitting procedure described

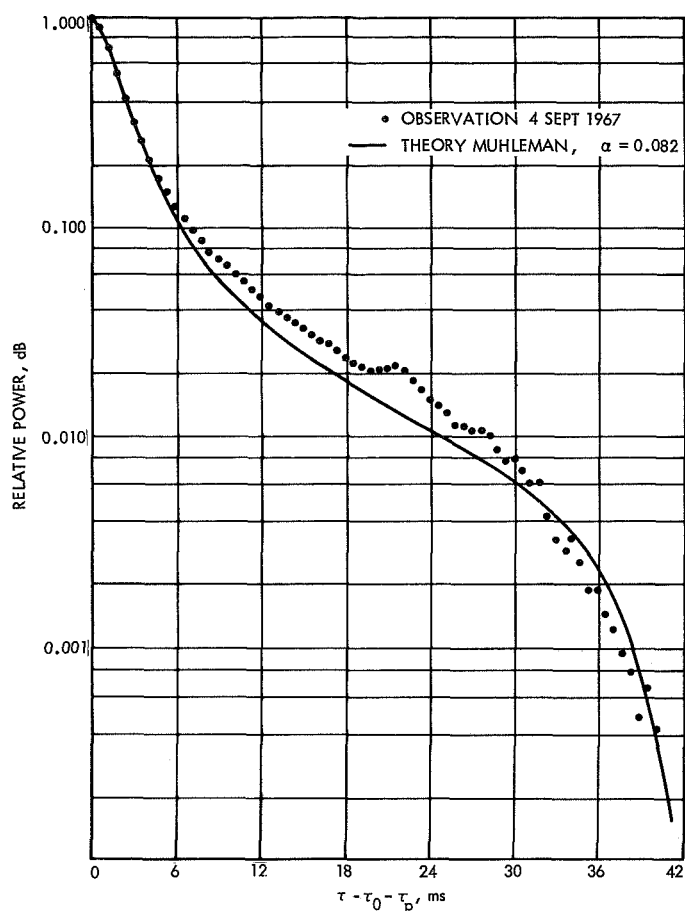


**Fig. 5. Observation September 3, 1967, using a 1.0-ms pulse and model fitting over the first three ms of data**

above. Such data are now available for many of the observations made in 1964 and 1967. Measurements made during inferior conjunctions spaced by eight years when the Venus-earth geometry is nearly identical would be expected to yield nearly identical results. The first test of this using the Arecibo data will be possible in 1972.

Model fitting to the 4.0-ms data has yielded results which are consistently in disagreement with the observations made at shorter pulse lengths during the observation period of a given day. The required roughness in the models is always greater than that of the other observations. Various systematic errors were considered, but none would give consistent results for all of the data. It is now apparent that the problem is caused by the limited dynamic range of the analog-to-digital converter.

The present system converts the voltages to odd numbers from  $-255$  to  $255$  (essentially 7 bits plus sign). If the signal-to-noise ratio is large and the dynamic range of

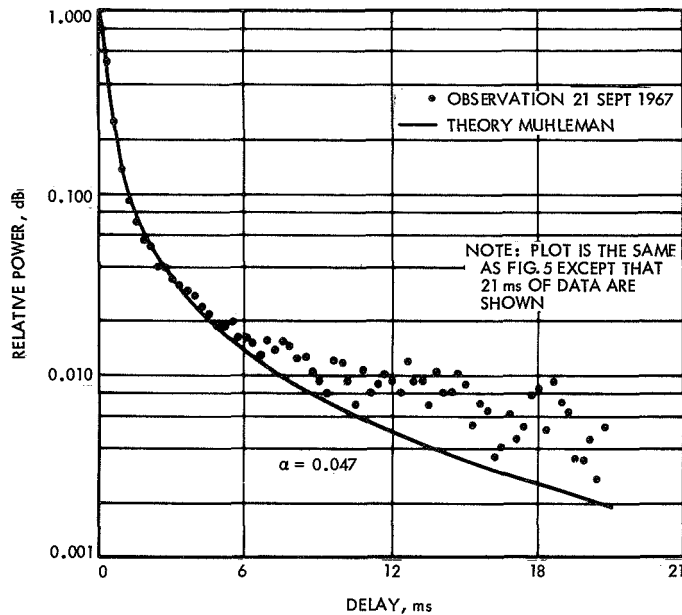


Fig. 6. Observation September 21, 1967, using a 1.0-ms pulse and model fitting over the first three ms of data

the echo is large, it is clear that it will be impossible to measure the maximum echo power and the noise level simultaneously. The error is such that measurement of the maximum echo power will be too small especially if the echo is occasionally clipped, while the measurement of the noise level and the echo power from large angles of incidence will be too large. The resulting decrease in dynamic range is then construed to be due to greater apparent roughness of the surface which is not the case.

Figure 7 shows a typical observation using a 4.0 ms pulse. The value of  $\alpha$  found by the model fitting program is indicated on the figure. The unusually large value of  $\alpha$  is caused by distortion of the data by the limited dynamic range of the digital sampler.

Anomalous scattering regions begin to contribute extensively to the backscattered power at angles greater than 30 deg. Such features are completely smeared out by the long pulse and cause no apparent distortion of the curve. Thus, it is impossible to arrange the weights to avoid regions of the curve which contain such anomalies. Again a systematic increase of the roughness parameter results in the model.

Short pulse observations are made at the Arecibo Ionospheric Observatory primarily for ranging purposes,

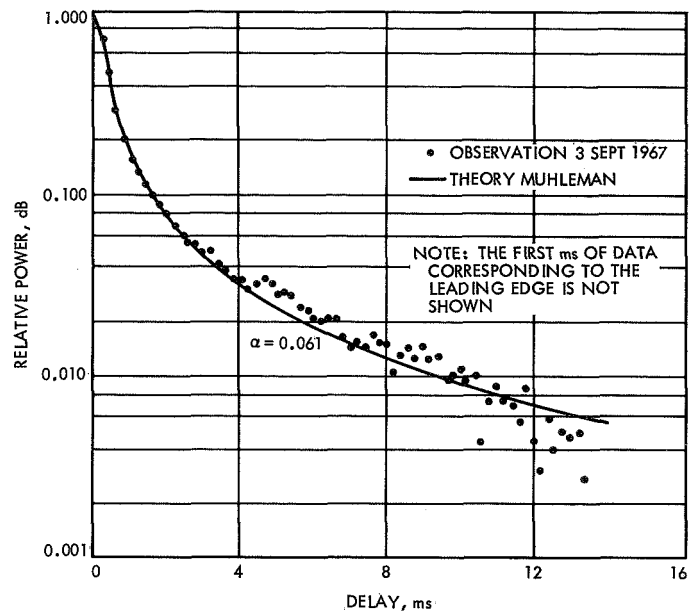


Fig. 7. Observation September 4, 1967, using a 4.0-ms pulse and an RC filter having a time constant of 2.67 ms

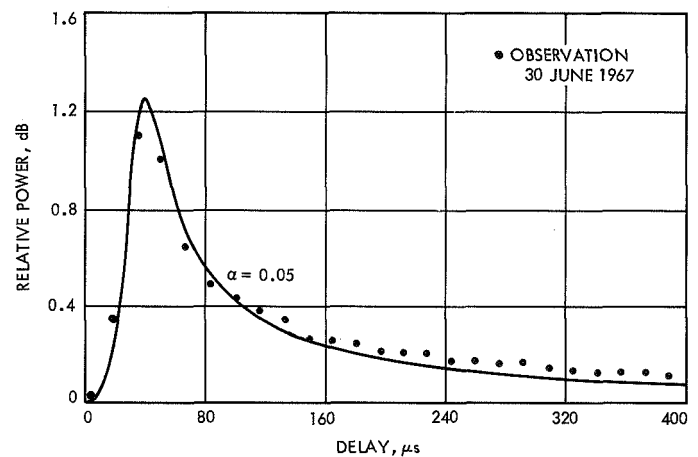


Fig. 8. Observation September 30, 1967, using a 40- $\mu$ s pulse and matched filters

but some information about the surface properties near the subradar point can be gained from these observations. First of all, they occasionally show great variability in form and in the percentage of reflectivity. However, the great majority of the 40- $\mu$ s pulse observations appear similar to the one shown in Fig. 8. The solid curve was computed from Eq. (2) using  $\alpha = 0.05$  and is in relatively good agreement with the data. A value of  $\alpha = 0.06$  would give a better fit, but the value near 0.05 is typically found from the 1.0-ms pulse observations. The model of Eq. (3) yields an echo which is much too broad and is in obvious disagreement with the data if the typi-

cal value of  $C = 230$  found from the 1.0-ms observations is used in the model.

## V. Comments

The scattering model of Eq. (2) tends to give a good estimate of the backscattering properties of Venus over a wide range of incidence angles if  $\alpha$  is near 0.05 or perhaps slightly less. The scattering model of Eq. (3) requires a value of  $C$  near 230 in the case of the 1.0 ms pulse observations and a value of  $C$  greater than 400 for

most of the 40  $\mu$ s observations. It is apparent that this model is not in agreement with the backscatter law of Venus at this wavelength. The application of more complicated scattering models for the purpose of measuring other physical parameters as suggested by Beckmann and Klemperer (Ref. 3), and Fung (Ref. 4), is likely to be difficult due to the variability of the surface and the large effects of certain surface features. Model fitting to delay-doppler maps offers the best possibility for continued study of the average surface properties since the anomalous regions can be isolated and appropriately weighted,

## References

1. Muhleman, D. O., "Radar Scattering from Venus and the Moon," *Astron. J.*, Vol. 69, p. 34, 1964.
2. Hagfors, T., "Backscattering from an Undulating Surface with Applications to Radar Returns from the Moon," *J. Geophys. Res.*, Vol. 69, p. 3779, 1964.
3. Beckmann, P., and Klemperer, W. K., "Interpretation of the Angular Dependence of Backscattering from the Moon and Venus," *Radio Sci.*, Vol. 69D, p. 1669, 1965.
4. Fung, A. K., "Vector Scatter Theory Applied to Moon and Venus Radar Return," *Proc. IEEE*, Vol. 54, p. 996, 1966.





# Parameter Estimation From Sets of Two-Dimensional Maps

R. F. Jurgens

Arecibo Ionospheric Observatory\*

Cornell University Center for Radiophysics and Space Research

Arecibo, Puerto Rico

*A procedure is presented for determining a set of unknown parameters which establish the transformation equations between a set of two-dimensional maps and a single map which is considered to be invariant once the proper parameters have been established; that is, any single map of the set would yield the same map after the transformation is applied. The procedure is based on the maximization of a cross-correlation coefficient which is a function of the two dimensional maps, and the parameters. The particular application of the procedure to the determination of the spin vector of Venus is considered where the parameters are the vector components of the spin axis, and the two-dimensional map set corresponds to a sequence of delay-doppler radar maps. The procedure also appears to be useful for parameter determination from sequences of two-dimensional optical or photographic maps.*

## I. Introduction

The discovery of a number of regions on the surface of Venus which cause anomalous backscattering of UHF radar waves has provided a means of accurately measuring the rotation period and the direction of the spin axis of the planet. The first measurement of the spin vector based on feature data was reported by Carpenter (Ref. 1), and more recently a more accurate measurement was

reported by Shapiro (Ref. 2) who combined both the feature data and the spectral width data in a simultaneous solution. At the present time, all of the procedures based on the motion of features require the measurement of location of relatively distinct anomalies in either doppler frequency, delay, or a combination of delay-doppler. These data are then reduced using the method of weighted least squares to determine the locations of the features on the surface of the planet and spin vector. The measurements of the locations of the features in doppler frequency, delay, and delay-doppler must be decided by visual inspection of the data. This is often difficult, if not impossible.

---

\*The Arecibo Ionospheric Observatory is operated by Cornell University with the support of the Advanced Research Projects Agency and the National Science Foundation under contract with the Air Force Office of Scientific Research.

The radar features observed at 70-cm wavelength appear to be too complicated to be described by a single coordinate or pair of coordinates. In fact, it is generally difficult to separate various features or to define a unique boundary for a given feature. To eliminate these problems, a few machine procedures which directly utilize the delay-doppler maps to obtain a best estimate of the spin vector were considered. The procedure considered here is based on the maximization of the cross-correlation coefficient formed from a sequence of radar maps which include the anomalous scattering regions by adjusting the spin vector.

## II. General Theory

The normalized cross-correlation coefficients for a sequence of two-dimensional maps  $S$  is given by

$$C = \sum_{k=1}^K \sum_{i=1}^{I_k} \sum_{j>i}^{I_k} W_{ijk} \times \int_{A_k} da S_i S_j \left( \int_{A_k} da S_i^2 \int_{A_k} da S_j^2 \right)^{-1/2} \quad (1)$$

where  $k$  specifies the region for each set of  $I_k$  maps to be used in the two-by-two cross correlations.  $W_{ijk}$  designates the weights which are based on the significance of each pair of maps. Integration over the surface is indicated by

$$\int_A da$$

A surface map  $S$  may be thought of as being constructed by a transformation procedure  $T(p_m)$  which is dependent upon  $M$  unknown quantities  $p_m$ . This transformation procedure operates on an observational map  $R$  such that

$$S = T(p_m) R$$

If the observational maps are noise-free and the operation  $T(p_m)$  is unique, then we assume that any map  $R$  selected from the set will yield the same map  $S$  if the transformation  $T$  is properly specified by the parameters  $p_m$ . Therefore, in the case where the proper  $p_m$  are unknown,  $C$  may be maximized by adjusting  $p_m$ . In reality,

each of the maps  $R$  are contaminated by noise or grain, and certain distortions in the imaging process which are not accounted for in the transformation  $T$  will cause perturbations in the maps of  $S$ . These perturbations in  $S$  will cause the correlation coefficient  $C$  to be less than unity at the maximum, and values of  $p_m$  which cause the maximum will be different than those obtained from the ideal case.

The maximization of  $C$  can generally be carried out using only the unnormalized cross-correlation coefficient  $C'$  which is obtained by absorbing the term

$$\left( \int_{A_k} da S_i^2 \int_{A_k} da S_j^2 \right)^{-1/2}$$

within  $W_{ijk}$  in Eq. (1) and assuming that this term is essentially independent of  $p$ . This may be justified in the cases where the maps are considered to be generated by a stationary random process or in the case where certain prominent objects are surrounded by such a field.

For convenience, the operation

$$\sum_{k=1}^K \sum_{i=1}^{I_k} \sum_{j>i}^{I_k} W_{ijk} \int_{A_k} da$$

is replaced by  $Z$  such that

$$C' = Z (S_i S_j)$$

The condition that  $C'$  is maximum is given by  $\nabla p C' = 0$  or

$$\frac{\partial C'}{\partial p_m} = Z \left( S_i \frac{\partial S_j}{\partial p_m} + S_j \frac{\partial S_i}{\partial p_m} \right) = 0 \quad (2)$$

If  $S$  is expanded as a power series in  $p$  about a point  $p^0$  as shown in Eq. (3), a set of  $M$  linear equations can be written when the terms greater than first order in  $\Delta p$  are neglected in the series by replacing the  $S_i$  and  $S_j$  in Eq. (2) with the series of Eq. (3).

$$S(p^0 + \Delta p) = S(p^0) + \sum_{n=1}^M \frac{\partial S}{\partial p_n} \Delta p_n + \dots \quad (3)$$

The solution of the resulting equation set is given as Eq. (4)

$$\Delta p = A^{-1} \cdot q \quad (4)$$

where the matrix coefficients  $A_{mn}$  of the linear equation set are

$$A_{mn} = Z \left( \frac{\partial S_j}{\partial p_m} \frac{\partial S_i}{\partial p_n} + \frac{\partial S_i}{\partial p_m} \frac{\partial S_j}{\partial p_n} \right) \quad (5)$$

and  $q$  is

$$q_m = -Z \left( S_i \frac{\partial S_j}{\partial p_m} + S_j \frac{\partial S_i}{\partial p_m} \right) \quad (6)$$

The corrected value of  $p^{\ell+1}$  is given by  $p^\ell + \Delta p^\ell$  and the procedure iterated until  $\Delta p^{\ell+1}$  is suitably small.

$$\Delta p^{\ell+1} = p^\ell + \Delta p^\ell \quad (7)$$

### III. Coordinate Transformations

The particular mapping procedure considered here involves a transformation between a coordinate pair which is fixed to the surface of a sphere; i.e., latitude and longitude which are specified by  $(\theta, \phi)$ . These are related to coordinates of the observation maps  $(u, v)$  by a rotation matrix, which is dependent upon  $p$ . The maps  $S$  can then be replaced by the maps  $R$  in Eqs. (5) and (6)

$$S(\theta, \phi) = R(u, v)$$

where  $u = f_1(\theta, \phi)$  and  $v = f_2(\theta, \phi)$ .  $f_1$  and  $f_2$  are dependent upon  $p$ . The partial derivatives in Eqs. (5) and (6) can be evaluated as shown in Eq. (8)

$$\frac{\partial S(\theta, \phi)}{\partial p_m} = \frac{\partial R(u, v)}{\partial u} \frac{\partial u}{\partial p_m} + \frac{\partial R(u, v)}{\partial v} \frac{\partial v}{\partial p_m} \quad (8)$$

and the area  $da$  in the operation  $Z$  is  $\cos \theta \, d\theta \, d\phi$ . Since  $u$  and  $v$  are functionally related to  $p_m$ , the partial derivatives  $\partial u / \partial p_m$  and  $\partial v / \partial p_m$  are easily evaluated and are the same functions required in programs involving the theory of weighted least squares. The evaluation of  $\partial R / \partial u$  and  $\partial R / \partial v$  must be accomplished from the observational map data which are usually given by a rectangular array of data points for equally spaced values of  $u$  and  $v$ . Two-dimensional linear interpolation and

differentiating is perhaps the easiest way to obtain the partial derivatives, although more complicated schemes which fit simple surfaces by least squares to a larger collection of points would perhaps be valuable in cases where the quality of the data warrants such treatment. The linear interpolation and differentiating procedure is adequate if the spacing of the points in both  $u$  and  $v$  is smaller than the resolution of the imaging procedure in both dimensions.

### IV. Errors in the Estimation of the Vector $p$

The matrix  $A$  and the vector  $q$  are dependent upon the observational data, and for this reason it is not easy to develop a simple method for estimating the formal errors in the solution vector  $p$ . That is, each element in the matrix  $A^{-1}$  is dependent upon all of the small errors associated with each element of the matrix  $A$ . For example we can consider the  $A$  matrix to be the sum of a noise free matrix and a noise matrix which contains elements having certain statistical properties such as zero mean value and a finite standard deviation. The same considerations can be applied to the vector  $q$ . Therefore, after  $\Delta p^{\ell+1}$  is driven sufficiently small, the variations  $\delta p$  of the solution vector caused by an independent realization of the experiment are given by Eq. (9)

$$\delta p = (A + \delta A)^{-1} \cdot (q + \delta q) - (A)^{-1} \cdot q \quad (9)$$

The variation  $\delta p$  can be expressed more simply in the case of small errors

$$\delta p \cong (A)^{-1} \cdot \delta q + \delta E \cdot p \quad (10)$$

where

$$\delta E = (A + \delta A)^{-1} - (A)^{-1}$$

The first term in Eq. (10) is easily found, however, the second term causes some difficulty. An upper bound can be found for the norm of the matrix  $\delta E$  by standard procedures used for estimating the errors in matrix inversion caused by numeric truncation of the data (Ref. 3). Unfortunately such upper bounds tend to give gross over estimates of the actual errors encountered in many cases. An accurate approach is possible, however because of its complexity, its use is limited to cases where the number of unknowns are few. The error  $\delta p_i$  can be written as a linear function of all of the perturbations in the system in the limit of small errors by expressing the terms  $(A^{-1})_{ij}$

as functions of all the elements  $(A)_{kl}$  and their corresponding perturbations.

$$\delta \mathbf{p}_i = \sum_j (A^{-1})_{ij} \delta \mathbf{q}_j + \sum_j \sum_k \sum_l \frac{\partial (A^{-1})_{ij}}{\partial (A)_{kl}} (\delta A)_{kl} \mathbf{q}_j \quad (11)$$

The information in which we are interested is the expectation  $E(\delta \mathbf{p}_i \delta \mathbf{p}_j)$ , which can be found by using Eq. (11) in combination with Eqs. (5), (6), and (8) to give the result in terms of the  $E(\delta R^2)$  and  $E[\delta(\partial R/\partial u, v)^2]$ . The first term is simply the mean-square noise associated with each map, and the second term is the mean square

of the slope of the noise function and is simply the second derivative, the autocorrelation function of the noise. The operation  $Z$  provides an average of a large number of independent measurements for a given map pair reducing the effective error by the square root of the number of independent measurements used in the average.

## V. Application of Procedure to Delay-Doppler Radar

When delay-doppler radar is the imaging technique, the quantities  $u$  and  $v$  become delay and doppler frequency. These are related to  $\theta$  and  $\phi$  by a simple matrix transformation as shown in Eq. (12)

$$\begin{pmatrix} \cos \theta \cos \theta \\ \cos \theta \sin \phi \\ \sin \theta \end{pmatrix} = \begin{pmatrix} \mathbf{B} \end{pmatrix} \begin{pmatrix} 1 - \frac{d}{d_m} \\ \frac{f}{f_m} \\ \pm \left[ 1 - \left( \frac{f}{f_m} \right)^2 - \left( 1 - \frac{d}{d_m} \right)^2 \right]^{1/2} \end{pmatrix} \quad (12)$$

where  $\mathbf{B}$  is a rotation matrix dependent upon time, the relative position and velocity of the planet, the spin vector  $\mathbf{p}$ , and a coordinate reference or constraint.  $d_m$  and  $f_m$  are the maximum delay and the maximum doppler frequency, and  $d$  and  $f$  are the delay-doppler coordinates corresponding to  $u$  and  $v$ . The  $\pm$  in the vector on the right hand side of Eq. (12) indicates that the transformation is not unique. This is the usual two-fold ambiguity encountered in the delay-doppler mapping procedure. The maps  $R$  made at any time contain the information from two hemispheres superimposed. Therefore, to minimize the possibility of obtaining an erroneous result in the determination of  $\mathbf{p}$ , it is advisable to select the maps such that an entirely independent conjugate region is superimposed with any given feature for each of the maps in the set. Under this condition the conjugate region will be treated the same as random noise except that its autocorrelation function will be different. It is also advisable to select maps which contain a given feature during a period when the delay-doppler contours form a nearly orthogonal grid over the

feature. Such a selection eliminates distortions in the maps  $S$  which could cause errors in the determination of  $\mathbf{p}$ .

Amplitude distortions caused by the non-equal area characteristics of the delay-doppler technique and the effects of the average scattering law must be removed from the maps  $R$  before the process is started. Maps made in the cross polarized sense are most desirable in this case because the scattering law dependence is small, however, at this wavelength the backscattered power is significantly less than the power received with the polarization matched.

Following the 1969 inferior conjunction, data will be available to carry out this procedure covering a time span of five years. It appears that the procedure could detect an apparent drift in the longitude of a feature of less than one degree corresponding to an accuracy of about 4 parts in  $10^4$  in the rotation period. The angular direction of the pole would be accurately measured to less than one degree of arc.

## References

1. Carpenter, R. L., "Study of Venus by CW Radar—1964 Results," *Astron. J.*, Vol. 71, p. 142, 1966.
2. Shapiro, I. I., "Resonant Rotation of Venus," *Science*, Vol. 157, p. 423, 1967.
3. Fox, L., *An Introduction to Numerical Linear Algebra*, Oxford University Press, New York, 1965.



# The Potential of Interplanetary Spacecraft Data for Testing Gravitational Theories\*

L. D. Friedman

Measurement Systems Laboratory  
Department of Aeronautics and Astronautics  
Massachusetts Institute of Technology  
Cambridge, Massachusetts

*The description of the solar system forces affecting the motions and observations of interplanetary spacecraft is discussed for purposes of examining the potential of using the observations of such spacecraft to test gravitational theories. The use of the data depends not only on the inherent quality of the measurement, but also the limitations of the model. The investigation of gravitational and non-gravitational forces reveals the limiting factors on the test and the requirements of the modeling. Inadequate understanding of the low thrust forces is discussed. By consideration of the Mariner IV mission and other interplanetary missions, progress in the investigation of the potential of estimating the critical parameters of gravitational theories is discussed.*

## I. Introduction

The radio tracking data from interplanetary spacecraft consists of a large number of very high quality observations which are of great value in testing gravitational theory. For such tests the theory of spacecraft motion and radio signal propagation must be modeled to high accuracy using a complete description of the gravitational and non-gravitational forces affecting the motion and of the gravitational and dispersive media perturbations affecting the signal propagation. The solution to a

many dimensional orbit estimation problem is then performed which contains the desired estimates of gravitational theory parameters. This procedure is thus more than an isolated test of a gravitational effect. Current studies and work in this area are being performed at the Jet Propulsion Laboratory and the Massachusetts Institute of Technology (MIT), Lincoln Laboratory (Refs. 1-4).

## II. Discussion

In this paper some aspects of the modeling are examined and a preliminary investigation of the potentialities of the data for testing gravitational theory is presented. General relativity and the Brans-Dicke theory (Ref. 5) currently are the only two well-formulated theories of

---

\*This research was performed at MIT, Lincoln Laboratory, supported by the U. S. Air Force, while the author held a National Defense Education Act Fellowship, and was partially supported by NASA grant NGR-22-009-366.

gravitation, consistent with observations. The Brans-Dicke theory starts with a weaker form of the principle of equivalence than does general relativity. The field equations then have an arbitrariness in them that permits a scalar field with an undetermined parameter to be introduced. However, this field does not alter the equations of motion (Ref. 5). The two theories differ in their basic physical assumptions, but both have the same form for the equations of motion and can, therefore, be tested simultaneously. This is achieved by the introduction of motion of the spacecraft and then estimating the values of the parameters.

The full "restricted"  $N$  body problem (an infinitesimal mass in the field of  $N$  significant masses) should be considered. In the theory of the post-Newtonian equations of motion (due to Droste (Ref. 6), deSitter (Ref. 7), Eddington (Ref. 8), and more recently described by Tausner (Ref. 3) and Weinberg (Ref. 9) it is shown that, in an expansion in powers of  $\mu/r_0 c^2$  (where  $\mu = GM$  is the gravitational parameter,  $r_0$  is the astronomical unit, and  $c$  is the speed of light), the motion of the spacecraft in the heliocentric phase of the flight, when the sun is the central body and all other bodies contribute perturbative forces, is given by the usual Newtonian equations plus an additional general relativistic term due to the sun. The  $\mu/r_0 c^2$  analysis is justified since the spacecraft radial distance is always within one order of magnitude of  $r_0$ . The errors introduced are of the order of  $10^{-16}$  over the flight, several orders of magnitude smaller than the data. This modeling has been discussed also by Tausner (Refs. 3 and 4) and Moyer (Ref. 2).

The equations of motion are of the form

$$\ddot{\mathbf{r}} + \frac{\mu}{r^3} \mathbf{r} = \Sigma \mathbf{F}_{\text{grav}} + \Sigma \mathbf{F}_{\text{non-grav}} \quad (1)$$

where  $\Sigma \mathbf{F}_{\text{grav}}$  includes all the gravitational forces besides the Newtonian sun, and  $\Sigma \mathbf{F}_{\text{non-grav}}$  contains all the non-gravitational forces.

Since some of the time delay data are expected to have errors on the order of one nanosecond, accelerations causing distance perturbations of this order must be considered. The distance perturbation can be very conservatively estimated by  $(1/2)a_{\text{max}}t^2$ . Over a 300-day mission the nanosecond limit requires considering accelerations as small as  $10^{-15} \text{ ms}^2$ . The gravitational forces then will include the solar general relativistic term, the Newtonian planetary contributions, the moon, hypothesized forces

from solar oblateness and time varying gravitational constant, the force from the gravity of the asteroids and for close approach flybys the higher harmonic terms from the planets.

The solar general relativistic term is obtained once the metric is known. The metric is given by the well known Schwarzschild (restricted two-body) solution (justified by the post-Newtonian analysis) and in harmonic coordinates is (Ref. 9) (to order  $\mu/r_0 c^2$ )

$$\left. \begin{aligned} g_{ij} &= - \left( 1 + \frac{2\gamma\mu}{c^2 r} \right) \delta_{ij} \\ g_{0i} &= 0 \\ g_{44} &= \left( 1 - \frac{2\alpha\mu}{c^2 r} + \frac{2\beta\mu^2}{c^4 r^2} \right) c^2 \end{aligned} \right\} \quad (2)$$

where  $\alpha, \beta, \gamma$  the metric parameters have been introduced as parameters to be estimated. Values of unity for  $\alpha, \beta, \gamma$  are predicted by general relativity.

The Brans-Dicke metric (Ref. 5) for this problem contains the parameter  $\omega$  related to the scalar field contribution and by comparison it is found that values of  $\alpha = \beta = 1$  and  $\gamma = (\omega + 1)/(\omega + 2)$  are predicted by that theory. The inverse relation is  $\omega = (1 - 2\gamma)/(\gamma - 1)$  and is plotted in Fig. 1. The two theories merge for  $\omega \rightarrow \infty$ . The measured perihelion precession of Mercury, coupled with his optical measurements of solar oblateness, have led Dicke to conclude that  $\omega \approx 6$  (Refs. 5 and 10).

The value of  $\alpha = 1$  is non-controversial; it operationally only scales the gravitational constant. Thus  $\beta$  and  $\gamma$  are the significant parameters to estimate in the test. In a first order analysis (in  $\mu/r_0 c^2$ ) it is noted that  $\beta$  and  $\gamma$  enter the equations of motion while only  $\gamma$  enters the equations of signal propagation. To separate motion of masses and light-signal propagation (arbitrarily) it is sometimes convenient to introduce an alternate set of relativistic scalars:  $R_f$ , which multiplies all the relativistic terms in the equations of motion and  $R_p$ , which multiplies the relativistic terms in the equations of signal propagation. These parameters are unity in general relativity and vanish in Newtonian theory. For considering secular effects  $R_f$  is approximately  $(4 + 3\omega)/(6 + 3\omega)$  in the Brans-Dicke theory (hence for  $\omega = 6$ ,  $R_f = 0.92$ ; i.e., an 8% difference in perihelion precession of the body).

In addition, two other parameters have significance in a test of general relativity:  $J_2$ , the second order term's



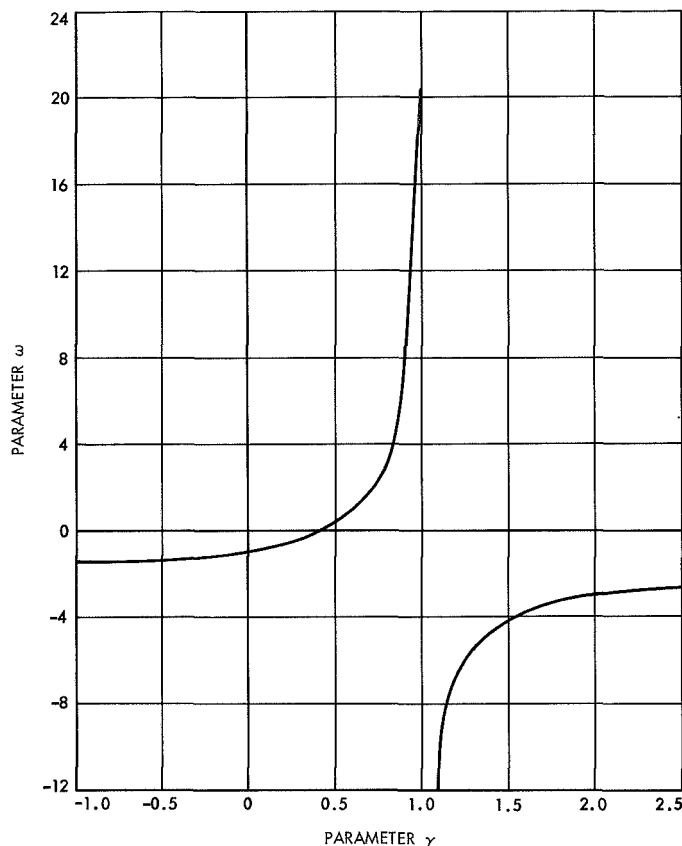


Fig. 1. Parameter relationship

coefficient in the harmonic expansion of the solar gravitational potential; and  $\dot{\mu}$ , the time varying part of the gravitational constant. The non-dimensional oblateness quantity  $S_2 = J_2/R_\odot^2$  ( $R_\odot$  is the radius of the sun) is related to the flattening  $f$  by

$$S_2 = \frac{2}{3} \left( f - \frac{1}{2} \frac{\Omega^2 R_\odot^3}{\mu} \right)$$

where  $\Omega$  is the solar rotation rate. If Dicke's value (Ref. 9) for the visual flattening is used ( $f \approx 5 \times 10^{-5}$  arc s) a value of  $S_2 \approx 2.8 \times 10^{-5}$  results. This value is consistent with a value of 6 for the Brans-Dicke parameter  $\omega$ . The agreement of the general relativistic prediction for Mercury's excess perihelion precession and that observed suggests however that  $S_2$  is much smaller. The quantity  $\dot{\mu}$  is significant since it is non-zero in the Brans-Dicke theory and zero in general relativity.

The Newtonian forces are straightforwardly included except perhaps the contribution from the asteroids. The uncertainty in the total mass of the asteroidal belt is sufficiently large to prevent the true significance of this

perturbation from being evaluated. We model the belt as a uniform circular ring inclined to the ecliptic and treat the mass ( $m$ ), distance ( $d$ ), and inclination of this ring as parameters to be estimated. The potential inside (for inner planet missions) this ring is

$$V = - \frac{GM}{d} \sum_0^\infty P_n(0) P_n(\sin I) \left( \frac{r}{d} \right)^n \quad (3)$$

where  $I$  is the inclination of the ring to the osculating plane of the spacecraft,  $r$  is the spacecraft-sun distance and  $P_n$  is the Legendre polynomial. Upon taking the gradient the force is found:

$$\begin{aligned} \mathbf{f} = & \frac{GM}{r^2 d} \sum_{n=0}^\infty \left( \frac{r}{d} \right)^n P_n(0) \\ & \times [nP_n(\sin I) \mathbf{r} - rP'_n(\sin I) \cos I \mathbf{e}_I] \end{aligned} \quad (4)$$

where  $\mathbf{e}_I$  is the unit vector perpendicular to  $\mathbf{r}$  and directed positive in the direction of increasing  $I$ . The inhomogeneities in the ring from the largest asteroids may be included by considering the few largest ones directly, and estimating their individual masses.

The limitation in the modeling will not, however, be with the gravitational forces but rather will occur due to our lack of knowledge concerning the low thrust forces. These forces primarily arise from solar radiation pressure and gas emission on board the spacecraft, and are significant enough to require severe demands upon their modeling. The solar radiation pressure force will, in general, have arbitrary direction and may be expressed as

$$\mathbf{f}_{SR} = \frac{m}{r_0^2} (g_r \mathbf{e}_r + g_t \mathbf{e}_t + g_N \mathbf{e}_N)$$

where  $\mathbf{e}_r$ ,  $\mathbf{e}_t$ , and  $\mathbf{e}_N$  are unit vectors along the radial, tangential and normal axes, respectively, and  $m$  is the spacecraft mass. The parameters  $g_i$  (units of length<sup>3</sup>/time<sup>2</sup>) are to be estimated from the data and if desired may be related to the reflectivity properties of the spacecraft and the solar flux constant. In addition, account will have to be taken of the aspect changes (with respect to the sun) of the surface and the possible time varying change in the solar radiation flux. This latter would occur due to inhomogeneities in the solar emission, and may be cyclical with the solar rotation. Surface property changes on the spacecraft occurring during its flight might also be

included in the description of the solar radiation pressure force. An investigation by Bourke and McReynolds (Ref. 11) has shown the gas leakage forces to be a factor in celestial mechanics experiments, but a definitive model has not yet been produced. For such a model, other independent data will probably be needed. Currently, attitude measurements are being studied. The inclusion on board the spacecraft of accelerometers capable of measuring accelerations in the  $10^{-8}$  to  $10^{-12}$  g range would also supply useful independent measurements of the non-gravitational forces.

In order to analyze the effect of our insufficient knowledge about the low-thrust forces, the introduction of a stochastic process to represent the unknown random part of this force can be considered. We find that the random process results in an increase of the final error in the estimate (the correlation matrix) by an amount depending on the assumed correlation matrix of the random process. By including this addition to the correlation matrix we obtain no improvement in the estimate of the parameters but do obtain more realistic values of the variances of the estimates. It should be emphasized, however, that the result is dependent on the assumed correlation matrix for the process noise.

The model of motion is, thus, given by Eq. (1) where the forces discussed above are included and their parameters (constants of reflectivity, gas leakage components, solar oblateness, etc.) are treated as quantities to be estimated. But it is clear that parameterized modeling cannot be used as a substitute for physical understanding, for with too many parameters we end up with a model that will fit any set of data.

The modeling of radio-signal propagation must next be considered. In this modeling, additional effects not affecting the motion will be included. The theory of signal propagation is analogous to that for motion, for the path of the radio signal is described by the same equations except that the particle mass is zero, being a photon. Shapiro (Refs. 12-14) has derived expressions for the time delay and doppler shift of a signal in general relativity space. Using the generalized metric, we include these in our model.

The accurate treatment of time is required to relate the observer, using atomic clocks for his measurements, and the equations of motion (which have coordinate time as their independent variable). The former is a function of the observer's location and speed in the gravitational

field. This subject is not discussed here except to note its importance, its requirement for high accuracy and the need for careful consideration of the actual operational procedures in use.

The data from the past *Mariner* missions have been chiefly measurements of the frequency difference between transmitted and received signals. The difference of the phase delay of two signals sent 1-10 minutes apart is actually measured. In future missions, time or group delay measurements will be available. The doppler quantity is a count of the number of cycles in a fixed (atomic) time interval, rather than an instantaneous frequency. Depending on the instrumentation, the measurement is subject to quantization error as well as the usual error of transmitter frequency instability. Since this quantity is an observation of the difference of phase delay, it represents an averaged frequency (a point treated adequately in various JPL reports). Alternately the direct expression of phase path delay may be computed, viz., the difference between the time delay of the wave "sent" at the end of the time interval and that of the wave "sent" at the beginning of the interval. The received atomic times at the interval end points must be converted to coordinate times and the time delay for each ray (the zeroth and the  $N^{\text{th}}$ , where  $N$  is the number of cycles counted) calculated so as to obtain the transmitted times for each ray. The difference in transmitted times is then converted to an atomic time interval for the transmitter and the value of transmitted frequency times this interval represents the theoretical value of the doppler observable.

To both the time delay and doppler observables, corrections due to dispersive media must be applied. These depend on the assumed model of the interplanetary medium, ionosphere, and neutral atmosphere. For the latter two, accuracy considerations may require detailed numerical maps of electron and neutral particle density rather than theoretical formulas. The modeling of the ionosphere and atmosphere is currently under study. In addition, the estimation of station location quantities is necessary in reducing the data.

To examine the potentialities of the use of interplanetary spacecraft data, a possible future mission was examined: a 1973-1975 interplanetary mission to Venus and Mercury (through the use of a Venus swingby method). The basic trajectory considerations for the spacecraft mission have been reported by Sturms (Ref. 15). Looking at the post-Venusian part of this mission, a general relativity test may be quite promising. Detailed aspects such

as the shape of the probe, guidance, and communications will have to be dealt with before an overall evaluation can be made. However, as a first analysis, the errors in the estimates of the critical parameters for a gravitational theory test were examined using simulated data as the observables. The initial conditions of the probe were taken at an epoch 6 days past Venus encounter, i.e., on February 11, 1974. The orbit had an eccentricity of 0.25 and periastris distance of 0.44 AU (i.e.,  $a = 0.585$  AU). This probe had a 163-day period. The orbit plane was inclined to the ecliptic by 6 deg and inclined to the solar equator by about 8.8 deg. The errors in the estimates were calculated for the critical parameters: the relativity motion factor  $R_f$ ; the sun harmonic  $S_2$ ; the AU; the radiation pressure components  $g_r$ ,  $g_t$ , and  $g_N$ ; the probe initial conditions  $a$ ,  $e$ , and  $i$  (initial orbit elements); and a factor for the interplanetary medium constant, IM, representing the number of electrons per cc at 1 AU (based on an inverse square model for particle density beyond four solar radii). In addition, the initial conditions for the earth's orbit, as well as the other three probe orbital element initial conditions, were included in the solution vector. The results are shown in Table 1.

The cases considered represent different numbers of measurements with different assumed measurement errors. Taking case 4 as representative and presently realistic in its assumptions, we note that the relativity motion factor has a formal error of less than 4%. The simplifying considerations inherent in this study indicate that this estimate is marginal, at best, in terms of providing a test that discriminates between the Brans-Dicke and general relativity theories. Errors in the estimates of the low-thrust parameters were about 1% of their nominal values but again there was no consideration of the probable complications of these forces. With improvement of the noise values of the data, e.g., to ns in time delay and  $10^{-3}$  Hz in doppler, a corresponding improvement in the error estimates is obtained (case 1), and definite conclusions from this test might be feasible. It should be emphasized that the values of error in case 4 are presently realized and it is not unreasonable to expect improvements in the early 1970s.

Also from the results of these cases several interesting and important correlations are noted (values quoted are from case 4). The relativity factor has a correlation with solar oblateness of  $-0.87$  and with two components of solar pressure force,  $g_r$  and  $g_N$  of  $-0.95$  and  $-0.96$  respectively. The latter were also found to be somewhat correlated with estimates of the shape of the probe and the earth's orbit. The tangential component  $g_t$  was also

**Table 1. One-sigma values of estimates of certain parameters in a 1973 300-day solar-probe mission, based on time delay and doppler observations**

Measurement	Case <sup>a</sup>			
	1	2	3	4
$\sigma_{TD}$ , s <sup>b</sup>	$10^{-9}$	$10^{-8}$	$10^{-8}$	$5 \times 10^{-8}$
$\sigma_{\Delta f}$ , Hz <sup>b</sup>	$10^{-3}$	$10^{-2}$	$10^{-2}$	$7 \times 10^{-2}$
$R_f$	$1.7 \times 10^{-3}$	$1.7 \times 10^{-2}$	$2.4 \times 10^{-2}$	$3.5 \times 10^{-2}$
$S_2$	$1 \times 10^{-6}$	$1.0 \times 10^{-5}$	$1.5 \times 10^{-5}$	$1.9 \times 10^{-5}$
AU, s	$2.7 \times 10^{-8}$	$2.7 \times 10^{-7}$	$3.8 \times 10^{-7}$	$6.1 \times 10^{-7}$
$g_r$ , AU <sup>3</sup> /d <sup>2</sup>	$4.6 \times 10^{-14}$	$4.6 \times 10^{-13}$	$6.6 \times 10^{-13}$	$1.07 \times 10^{-12}$
$g_t$ , AU <sup>3</sup> /d <sup>2</sup>	$7.3 \times 10^{-16}$	$7.4 \times 10^{-15}$	$1.0 \times 10^{-14}$	$1.4 \times 10^{-14}$
$g_N$ , AU <sup>3</sup> /d <sup>2</sup>	$1.8 \times 10^{-15}$	$1.8 \times 10^{-14}$	$2.5 \times 10^{-14}$	$3.62 \times 10^{-14}$
$a$ , AU	$5.6 \times 10^{-11}$	$5.6 \times 10^{-10}$	$7.9 \times 10^{-10}$	$1.2 \times 10^{-9}$
$e$	$7.3 \times 10^{-11}$	$7.3 \times 10^{-10}$	$1.0 \times 10^{-9}$	$1.5 \times 10^{-9}$
$i$ , deg	$1.3 \times 10^{-7}$	$1.4 \times 10^{-6}$	$6 \times 10^{-6}$	$6.1 \times 10^{-6}$

<sup>a</sup>Case 1—1534 Observations: Equal number of time-delay and doppler measurements. 300 at one day intervals, the remainder at one hour intervals near periastris and after Venus encounter.  
Case 2—The same observing schedule as Case 1.  
Case 3—767 Observations: The intervals between measurements in Case 1 were doubled.  
Case 4—A uniform schedule of 4736 observations (2368 each of time delay and doppler—at 3 hour intervals).  
<sup>b</sup>The assumed one-sigma noise levels in the measurements.

found to be significantly correlated with  $S_2$  ( $-0.84$ ). The correlations of the low-thrust components, with the significant parameters of the relativity test, underlie the importance of good modeling of the low-thrust forces.

### III. Conclusion

We conclude from this preliminary examination that the mission does have potentialities for contributing new results to gravitational tests. However, because of the simplifications of this preliminary analysis, it is probable that the results of this test will be marginal in providing the critical measurements to distinguish between general relativity and the Brans-Dicke theory. Independent measurements of the non-gravitational forces, as might be provided from the instrumentation of the spacecraft with low-level accelerometers having sufficient dynamic range, could allow a big reduction in the uncertainty of the relativistic parameters. The reduction of the error in the observed signal, along with the increased knowledge of the low thrust forces obtained from the intervening missions, can be expected to improve the determination.

## References

1. Anderson, J. D., *Determination of the Masses of the Moon and Venus and the Astronomical Unit from Radio Tracking Data of the Mariner II Spacecraft*, Technical Report 32-816, Jet Propulsion Laboratory, Pasadena, Calif., July 1, 1967.
2. Moyer, T. D., "Relativistic Equations of Motion for the Generation of Ephemerides for the Planets, the Moon, and a Space Probe," in *Supporting Research and Advanced Development*, Space Programs Summary 37-49, Vol. III, p. 40. Jet Propulsion Laboratory, Pasadena, Calif., Feb. 29, 1968.
3. Tausner, M. J., *General Relativity and its Effects on Planetary Orbits and Interplanetary Observations*, Technical Report 425, Massachusetts Institute of Technology, Lincoln Laboratory, Lexington, Mass., October 7, 1966.
4. Tausner, M. J., Massachusetts Institute of Technology, Lincoln Laboratory Memorandum, Unpublished.
5. Brans, C., and Dicke, R. H., "Mach's Principle and a Relativistic Theory of Gravitation," *Phys. Rev.*, Vol. 124, p. 925, 1961.
6. Droste, J., "The Field of  $n$  Moving Centres in Einstein's Theory of Gravitation," *Proc. Roy. Acad. of Sci., Amsterdam*, Vol. XIX, pp. 447-455, 1916.
7. deSitter, W., "On Einstein's Theory of Gravitation II," *Mon. Not. Roy. Astron. Soc.*, Vol. 77, pp. 155-184, 1916.
8. Eddington, A. S., and Clark, G. L., "The Problem of  $n$  Bodies in General Relativity Theory," *Proc. Roy. Soc. London, Ser. A*, Vol. 166, pp. 465-475, 1938.
9. Weinberg, *Classical Relativity*, John Wiley & Sons, Inc., New York (not yet published).
10. Dicke, R. H., and Goldenberg, H. M., "Solar Oblateness and General Relativity," *Phys. Rev. Lett.*, Vol. 18, p. 313, 1967.
11. Bourke, R. D., McReynolds, S. R., and Thuleen, K. L., "Translational Forces on the Mariner V Spacecraft Stemming from the Attitude Control System," *AIAA Aerospace Sciences Meeting*, New York, N.Y., January 1969.
12. Shapiro, I. I., "Fourth Test of General Relativity," *Phys. Rev. Lett.*, Vol. 13, p. 789, 1964.
13. Shapiro, I. I., "Testing General Relativity with Radar," *Phys. Rev.*, Vol. 141, p. 1219, 1966.
14. Shapiro, I. I., et al., "Radar Verification of the Doppler Formula," *Phys. Rev. Lett.*, Vol. 17, p. 933, 1966.
15. Sturms, F. M., Jr., *Trajectory Analysis of an Earth-Venus-Mercury Mission in 1973*, Technical Report 32-1062, Jet Propulsion Laboratory, Pasadena, Calif., Jan. 1, 1967.

# Reconstruction of JPL 1967 Range Data for Venus and the Processing of Radar Data

D. A. O'Handley  
Ephemeris Development Group  
Jet Propulsion Laboratory  
Pasadena, California

*Planetary range data on Venus were obtained in 1967 at the JPL-Goldstone tracking station. The range-value was constructed through combining the measured residual with the computed range. These range data together with similar data from the Massachusetts Institute of Technology and the Arecibo Ionospheric Observatory were used in the development of a simultaneous integration of all the planets over 20 years. Upon the extension of this ephemeris to 60 years, and an increased radar and optical data set, an anomaly has appeared in the residuals. A discussion of the time base and results are given.*

## I. Introduction

Planetary time delay to Venus has been taken at the JPL-Goldstone Tracking Station since 1961. Over the period 1964-1967 this set of data has been of sufficient accuracy and has covered a sufficient amount of the orbit to incorporate it into ephemeris development.

The most recently published radar data (see Fig. 1) from the Venus site of the Goldstone Tracking Station were reconstructed in the following manner:

- (1) The planetary ephemeris DE 26 was used to compute the time delay or range from the surface of the earth to the front cap of the planet Venus.
- (2) These predictions were punched on cards in the form of 15 coefficients for a Chebyshev polynomial

of degree 14. (A set covers a single day for the predictions of range, doppler, hour angle, and declination.)

- (3) The cards were taken to Goldstone where the polynomial representation of the variables was evaluated for specific observation times.
- (4) A paper tape was made, providing information to the computer which controls the antenna.

## II. Discussion

The 1967 range data were taken in the monostatic mode. The antenna is used to transmit a signal to the planet. After an interval of time equal to the round trip

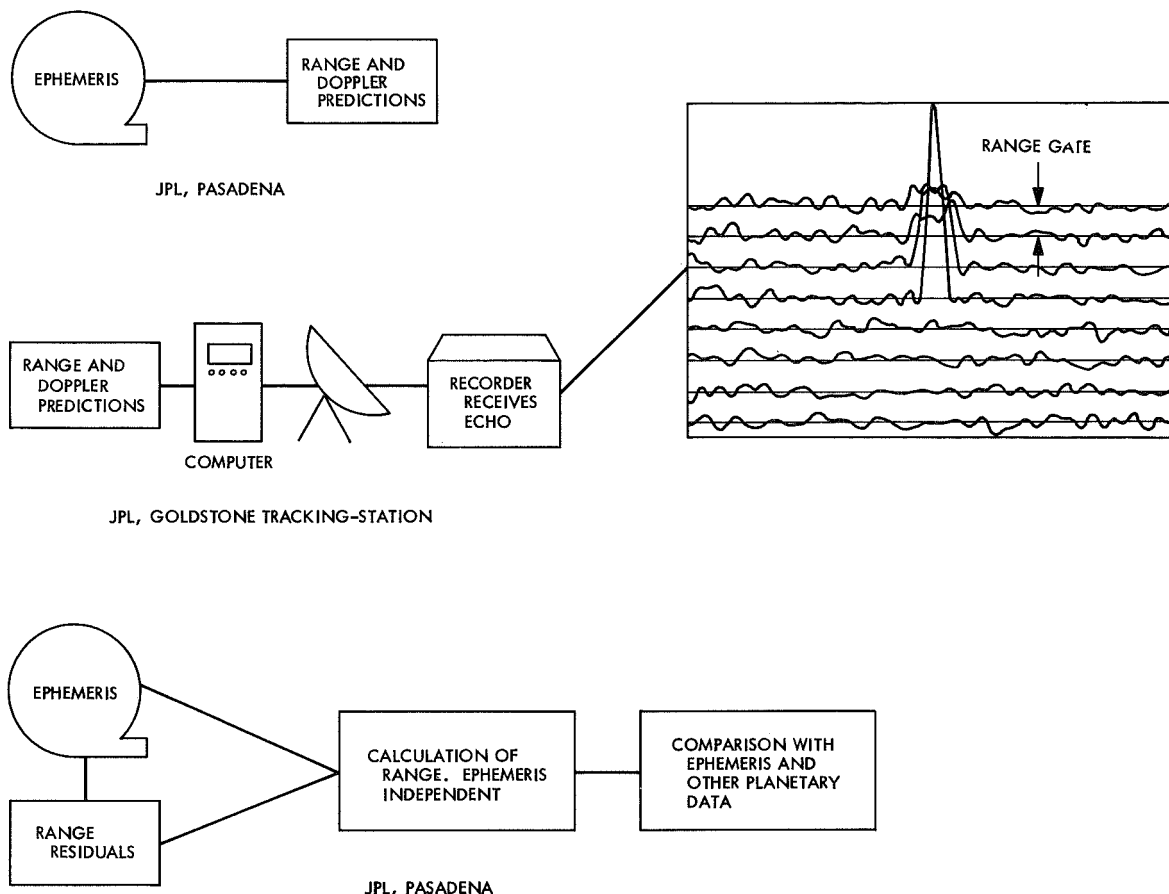


**Fig. 1. Planetary range observations**

travel time of the signal, the antenna is placed in a receiving mode. At this time, the echo is received with a small delay or advance. The received signal is shown in the inset of Fig. 1. The width of these lines represents the range gate resolution of a signal. Upon an analysis of this type of plot, the time at which the signal reached the front cap can be determined. This time is referred to some center point which represents a zero residual with respect to the ephemeris.

The residuals are then combined with the theoretical calculation of the range and form an ephemeris independent range point. The clock attached to the antenna keeps UTC time and all calculations are carried out in ephemeris or uniform time. These range points are therefore in units of universal time. All of these calculations use relativistic expressions where applicable.

The use of radar data for determining the astronomical unit and planetary radii, along with ephemeris improvement has been reported on since 1961. Early in 1967, a system of computer programs referred to as the Solar

System Data Processing System (SSDPS) was completed. In the spring of 1968, the first simultaneous integration of all the planets was made at JPL. The initial set of elements were close to Newcomb and the ephemerides of the U.S. Naval Observatory. The initial comparison with the combined set of planetary range data of the Arecibo Ionospheric Observatory (AIO), the Millstone Hill and Haystack sites of MIT, and JPL's Venus site are shown in Figs. 2, 3, and 4. The variations are seen to be quite large:

- (1)  $+4000 \mu s$  to  $-2000 \mu s$  for Mercury (Fig. 2).
- (2)  $+1500 \mu s$  to approximately  $0 \mu s$  for Venus (note positive offset in Fig. 3).
- (3)  $+3000 \mu s$  to  $-1000 \mu s$  for Mars (Fig. 4).

These radar residuals along with the optical data set of Transit Circle Observations over the period 1950–1967 were used to correct the orbital elements of all the planets except Pluto along with the radii and the astronomical unit.

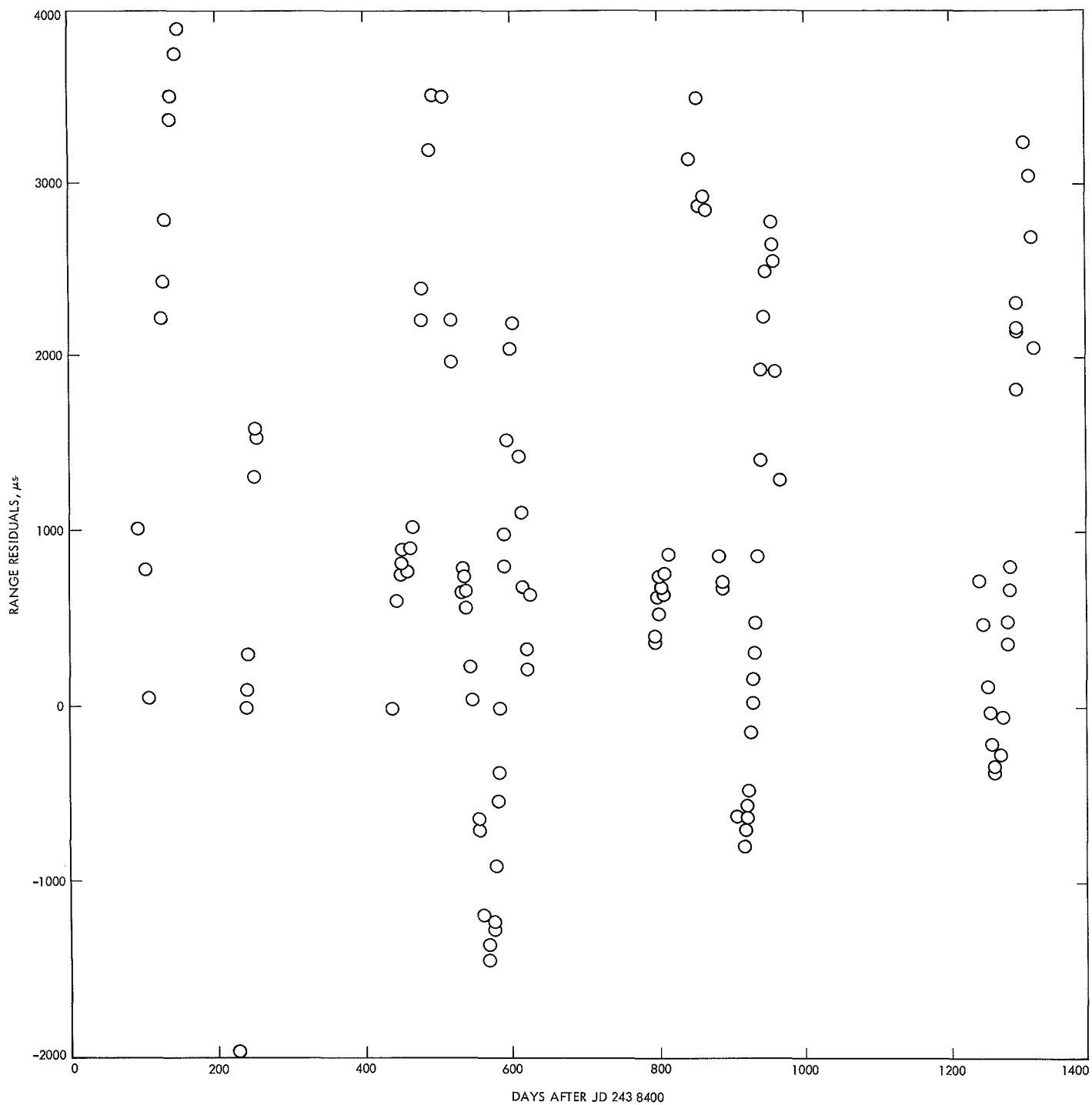


**Fig. 2. Mercury radar range residuals with DE 35**

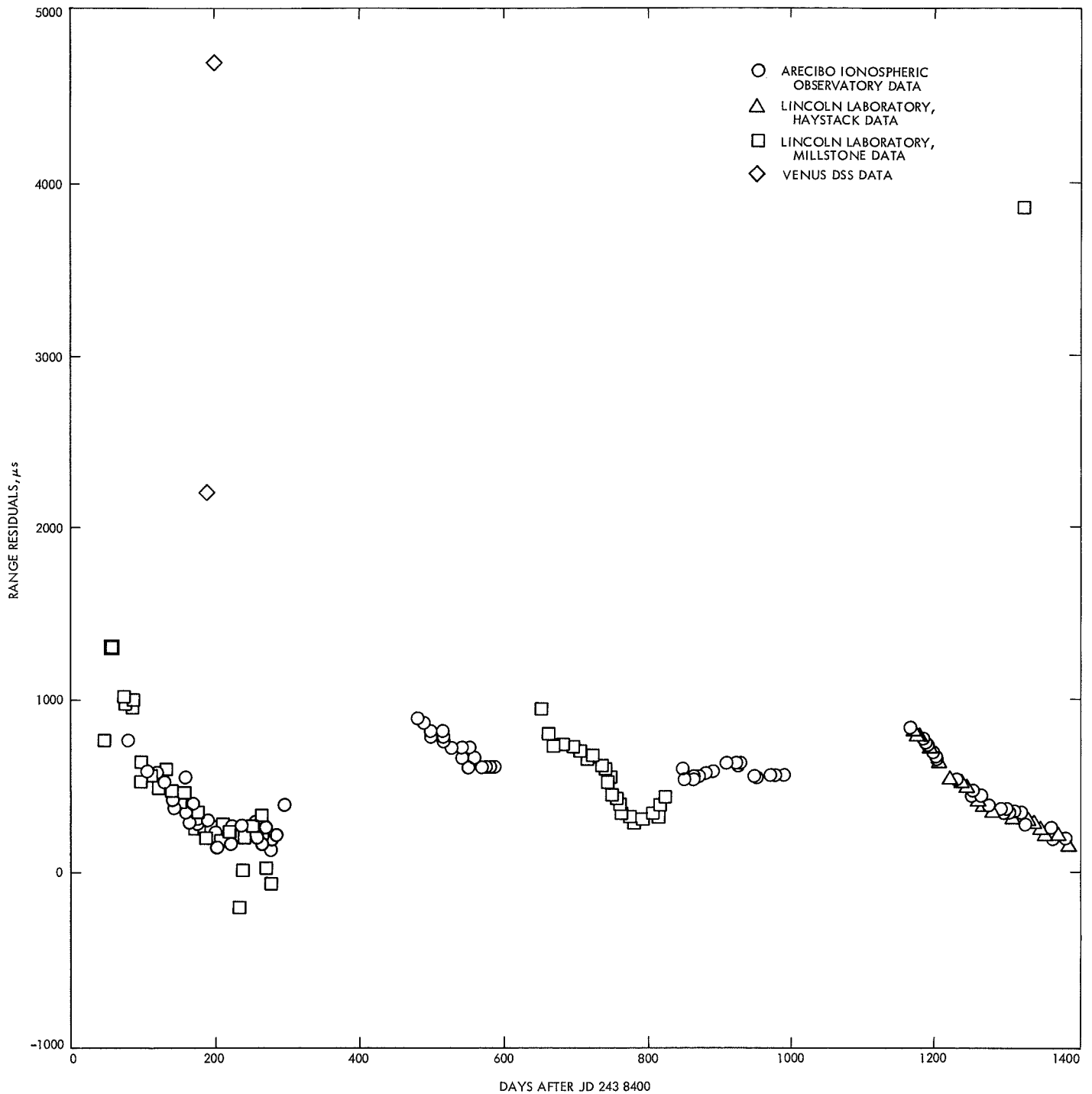


**Fig. 3. Venus radar residuals with DE 35**



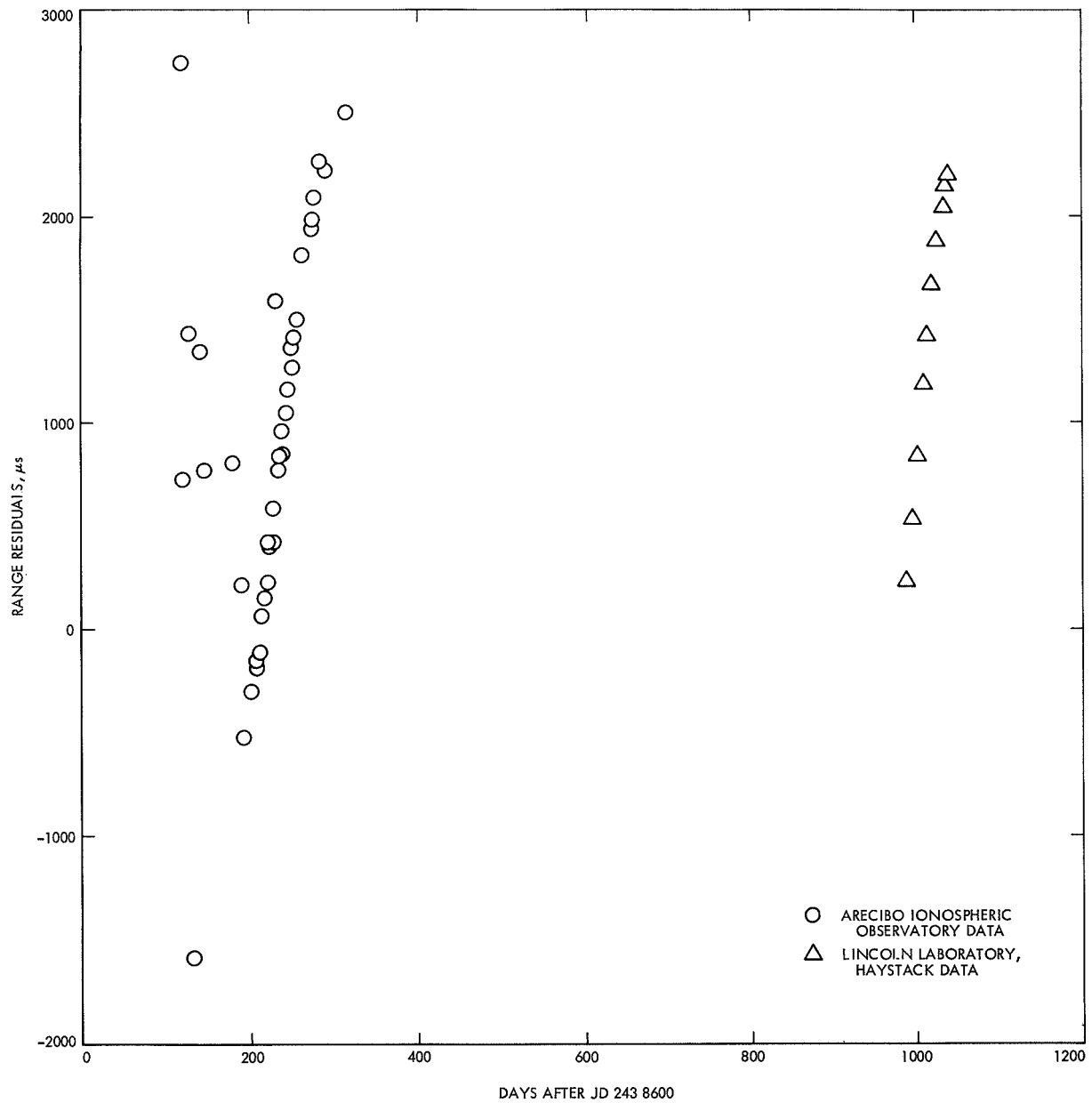


**Fig. 4. Mars residuals compared to DE 35**

A 56-parameter solution was made using these data. A rank-49 solution of an eigenvector-eigenvalue analysis was applied to the original osculating elements and a new integration performed. The results of comparing this integration with radar range data from Mercury, Venus, and Mars are shown in Figs. 5, 6, and 7 respectively. The magnitudes of the radar range residuals have been reduced by two orders of magnitude.

#### A. Mercury

Mercury data are from AIO and Haystack (see Fig. 5). There are 151 points shown here. Note the positive bias in the AIO data. In our subsequent studies, the Arecibo data have been removed where data from other radar sites are available.

#### B. Venus

Venus data in this ephemeris are from all of the U.S. radar sites. In Fig. 6 the residuals appear to have an anomaly around 1965 and 1966. The increased radar detectability is evident each year from the decreasing limits of radar residuals as the data become more current.

The structure in these residuals was initially thought to be a second-order effect of fixed parameters. The possibility of program errors in the SSDPS was also considered. Although Venus, earth-moon, and Mars mass values are better known through spacecraft radio tracking, the mass of Mercury is poorly determined. The determination of the mass of Mercury was stated by Dirk Brouwer as one of the most difficult mass determinations in the solar system. In the past century the values of the reciprocal mass have ranged from 3,000,000 (Le Verrier) to 9,700,000 (Backlund). The IAU adopted value of 6,000,000 is the value used by Newcomb in his tables of the inner planets.

An analysis of the periodic perturbations of the longitude and radius vector of Venus from Newcomb's tables verified that a variation of this size in the mass of Mercury produced an effect on Venus time-delay observables of the same order of magnitude as this deviation. This led us to an improvement of the mass of Mercury.

It is possible to determine mass values of all of the inner planets in a simultaneous solution using radar and optical observations of the planets. This has been done at MIT. Because the spacecraft determinations are two orders of magnitude more precise, it was decided to fix the values for the masses of the inner planets at the spacecraft determined values until it becomes practicable

to simultaneously process radio tracking and radar data for all the inner planets.

It was found that the feature in the radar range residuals must be regarded as an anomaly in the modeling of the masses. If one considers the masses better known from spacecraft tracking, and therefore fix the values, the reduction of degrees of freedom will cause the "feature" to appear in the Venus residuals. By altering the mass of Mercury, the feature and the overall sum of squared residuals are diminished.

Although not obvious on Fig. 6, the AIO data had a positive 30- $\mu$ s bias and has subsequently been removed.

#### C. Mars

The 39 observations of Mars taken in 1964 at AIO and the 10 high-precision points taken at Haystack in 1967 are shown in Fig. 7. Except for the early observations the improvement is considerable.

In recent months, the optical data set has been extended over the interval 1911-1967 and includes two instruments, the six-inch transit circle and nine-inch transit circle as shown in Table 1.

The radar data set which was originally used contained 796 observations. The current one, shown in Table 2, has 704 observations. This reflects the removal of most of the AIO data and the extension of these data into early 1968.

These data combined with 214 ranging points from the *Mariner V* spacecraft were used in a new integration over the period 1910 to 1970.

The first integration over 60 years was designated as DE 61. This integration differed from an extension of the 20-year ephemeris in the masses used for the planets and the form of the relativistic terms. The planetary masses used in the 60-year integration reflect more recent determinations of the masses of Mercury by JPL; Neptune by Miss Gill of NASA, and Pluto by Duncombe, et al., at the U.S. Naval Observatory.

The integration portion of the SSDPS system contains the basic  $n$ -body integration equations for the planets. Until now, the metric for the relativistic terms has been the standard form of the Schwarzschild metric given by Brouwer and Clemence. Due to operational requirements, the SSDPS has been converted to the Robertson

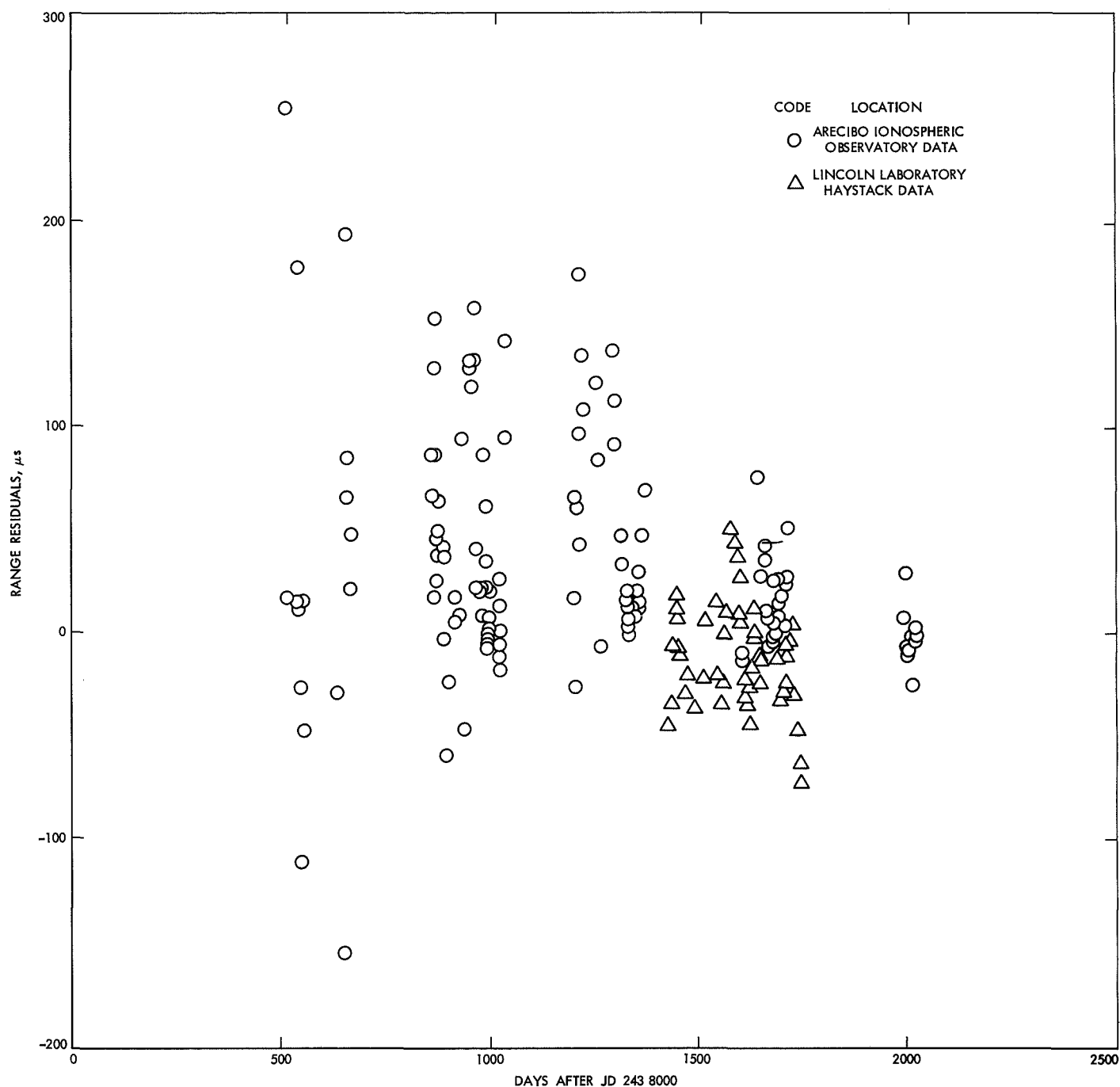


**Fig. 5. Mercury radar range residuals, DE 40**

form of the metric. This yields an isotropic form to the relativity expressions.

A simultaneous solution of 63 parameters of the solar system was obtained. This reflected the comparison of DE 61 with all the data discussed here. The unknowns, which are considered, are the elements of the eight planets except Pluto, the right ascension and declination

limb corrections for Mercury and Venus, the radii of Mercury, Venus, and Mars, the six elements of Mariner, the mass of Venus, and the astronomical unit. After some consideration a rank-55 solution from the eigenvalue-eigenvector analysis was selected for re-integration. This decision was made after looking at the relative magnitudes of the eigenvalues, their contributions to the sum of squares of residuals and their  $\rho$  coefficients.

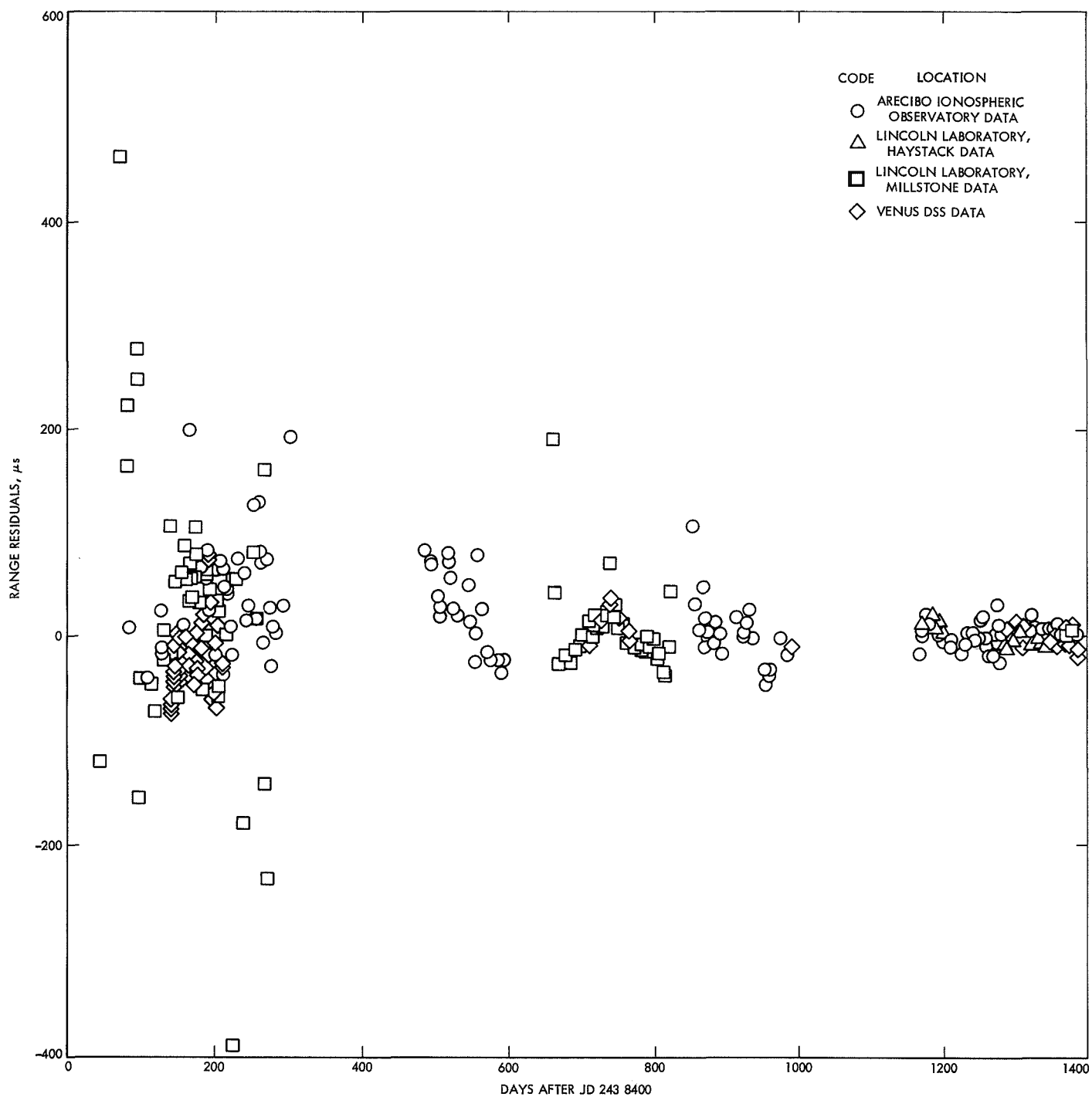


**Fig. 6. Venus radar residuals, DE 40**

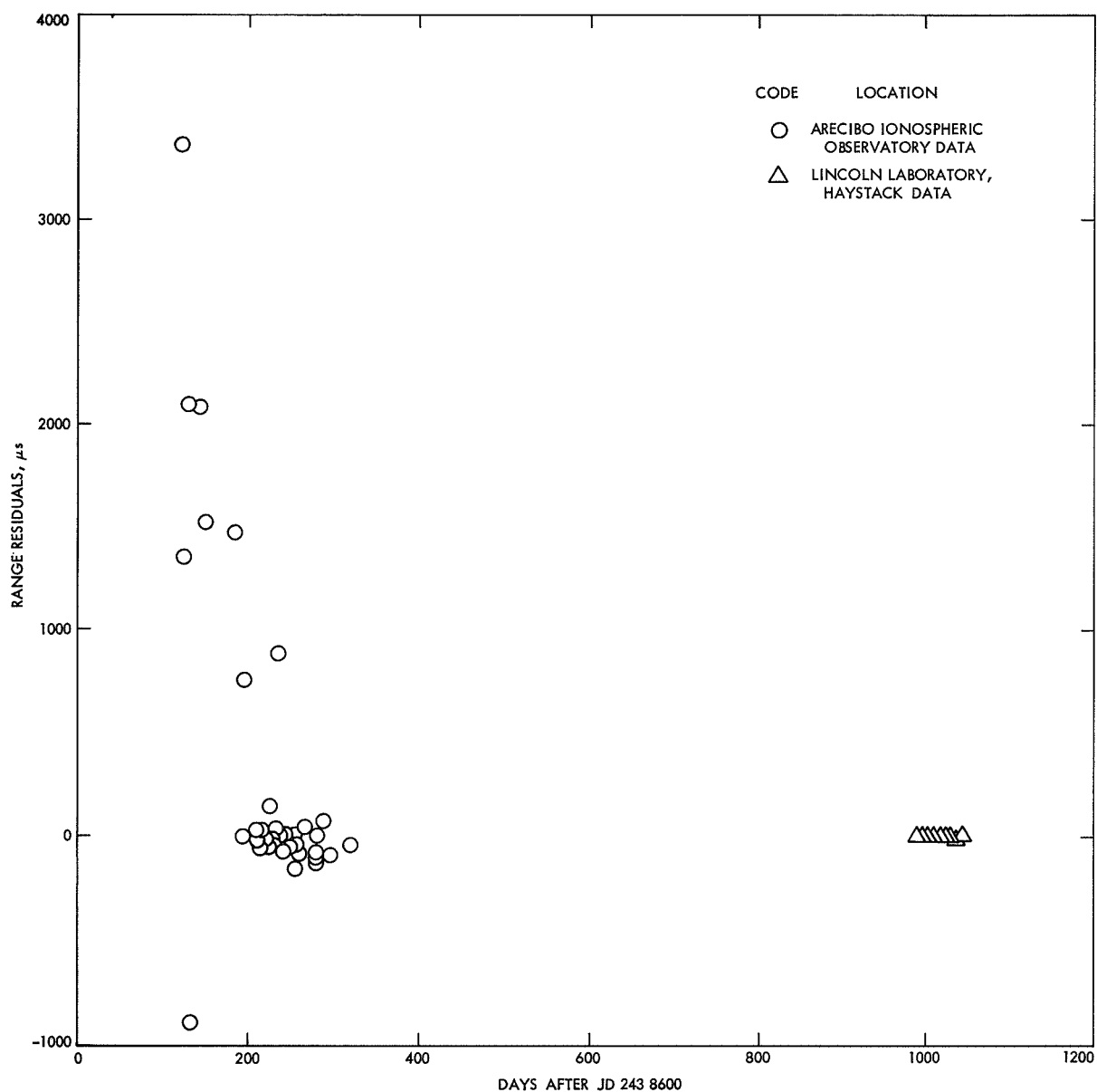


**Fig. 7. Mars radar residuals, DE 40**

**Table 1. Transit circle observations**

Planet	U.S. Naval Observatory Transit Circle, in.	Period	Number of Observations	
			Right ascension	Declination
Mercury	6	241 9937.2-243 9654.3(1913-1967)	1756	1695
	9	242 1867.2-243 1174.2(1918-1944)	550	532
		Total	2306	2227
Venus	6	242 0391.3-243 9679.3(1914-1967)	2761	2582
	9	242 2113.3-243 1129.1(1919-1944)	451	436
		Total	3212	3018
Mars	6	242 4793.8-243 9658.5(1926-1967)	549	528
	9	242 0105.8-243 1164.5(1913-1944)	122	120
		Total	671	648
Jupiter	6	242 4311.8-243 9548.6(1965-1967)	656	624
	9	242 0330.8-243 1165.6(1914-1944)	260	257
		Total	916	881
Saturn	6	242 4607.8-243 9433.6(1926-1966)	660	622
	9	242 0085.8-243 1122.6(1914-1944)	280	280
		Total	940	900
Uranus	6	243 4380.8-243 9595.6(1925-1967)	639	628
	9	242 0321.8-243 1061.7(1914-1943)	247	245
		Total	886	873
Neptune	6	242 4531.8-243 9662.6(1925-1967)	618	606
	9	242 0129.8-243 1214.6(1913-1944)	285	283
		Total	903	889
Sun	6	241 9174.2-243 9682.2(1911-1967)	5973	5695
	9	242 1867.2-243 1444.2(1918-1944)	1696	1668
		Total	7669	7363

**Table 2. Radar range observations**

Planet	Data source	Period	Number of Observations
Mercury	AIO	243 8493.2-243 9363.2(1964-1966)	119
Mercury	Haystack (MIT)	243 9425.3-244 0064.2(1966-1968)	88
		Summary 1964-1968	Total 207
Venus	Haystack (MIT)	243 9161.3-244 0063.2(1967-1968)	63
Venus	JPL (Venus DSS)	243 8541.2-243 9707.6(1964-1967)	284
Venus	Millstone Hill (MIT)	243 8447.0-243 9725.2(1964-1967)	101
		Summary 1964-1968	Total 448
Mars	AIO	243 8719.0-243 8915.0(1964-1965)	39
Mars	Haystack (MIT)	243 9587.7-243 9643.5(1967)	10
		Summary 1964-1967	Total 49

The radar residuals for Mercury have a 1 sigma of 56.6  $\mu$ s for DE 69 (Fig. 8), whereas the 1 sigma for DE 40 was 111  $\mu$ s. The significance of such a reduction is that the AIO data did bias the previous Mercury solution.

The Venus radar residuals do not show any significant change from DE 40. The 1 sigma for DE 40 was 48  $\mu$ s whereas in DE 69 the 1 sigma is 49.7  $\mu$ s. The explanation of this insignificant increase lies in the strength of the

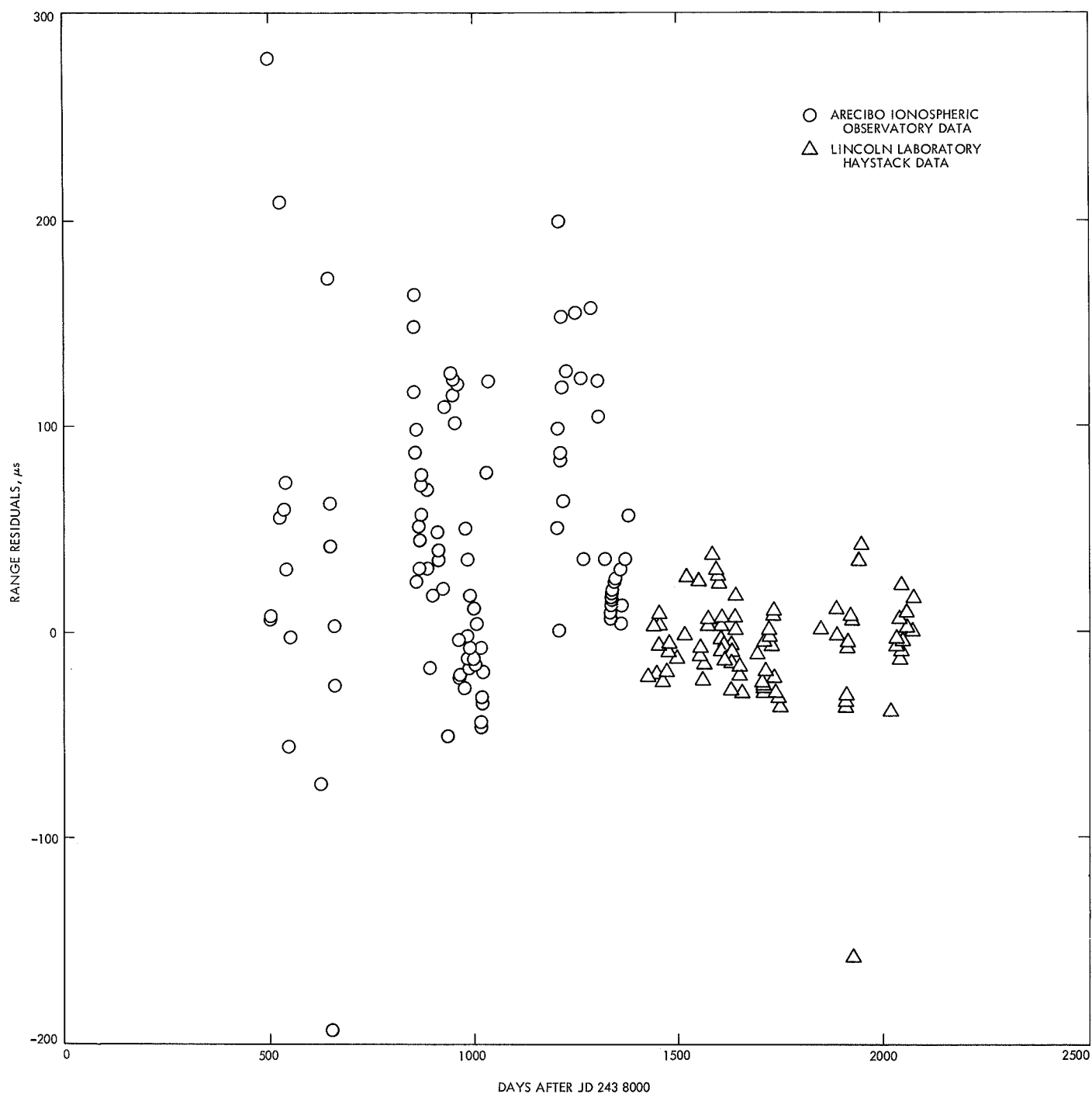


**Fig. 8. Mercury range residuals, DE 69**

*Mariner V* data which was incorporated in the solution and the omission of all AIO data. The structure in the 1967–1968 residuals is not due to a mass error but seems to be in incompatibility between the Haystack and JPL data. It may be a coincidence that if either data set is assumed to be in error by the atomic offset between

universal time and atomic time in the time interval of the ranging and a new fit is made the residuals lie flat-centered about zero as shown in Fig. 9.

In Fig. 10 the *Mariner V* range residuals are shown. They were fit to  $\pm 0.2 \mu\text{s}$ .

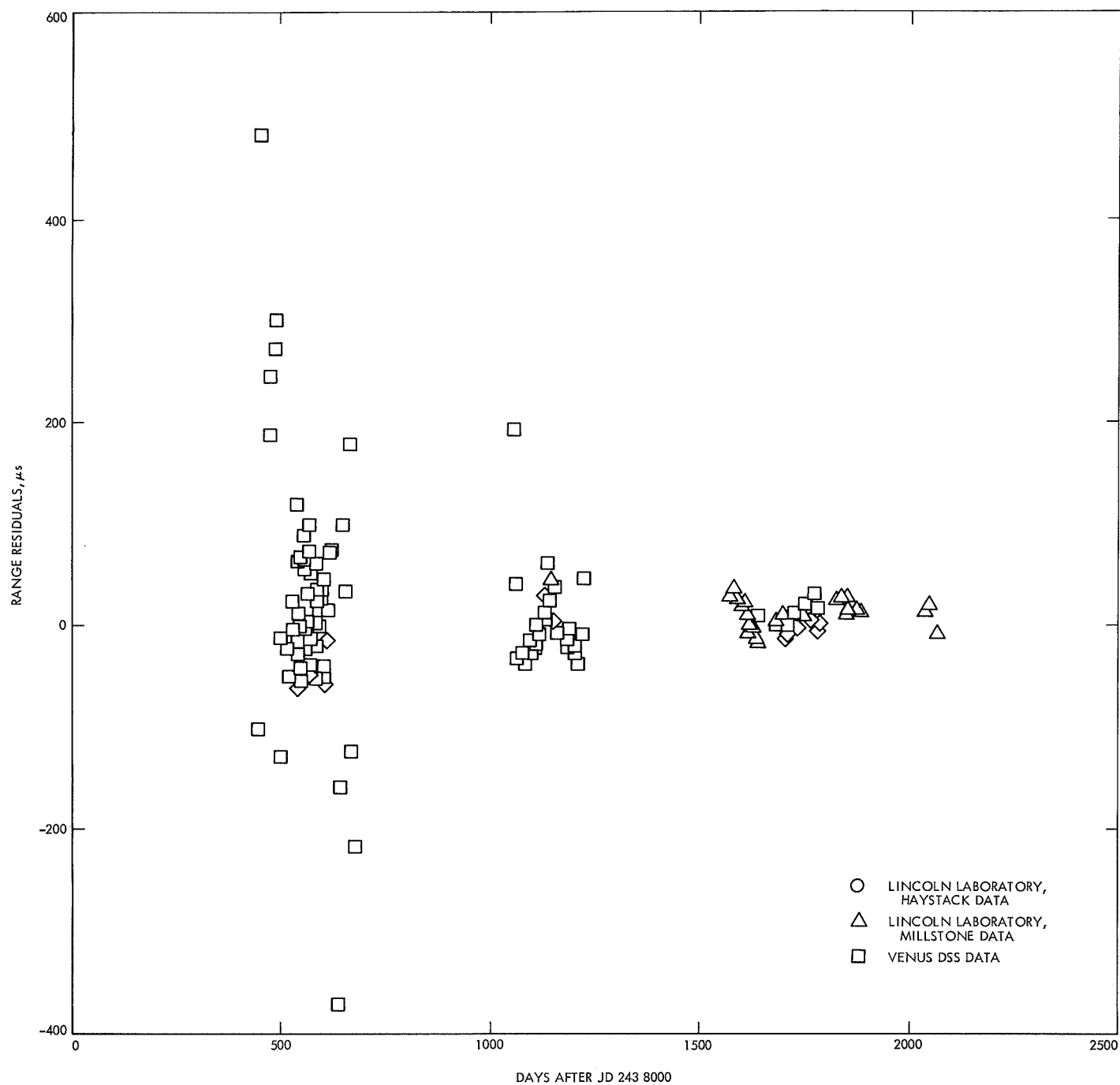


**Fig. 9. Venus radar range residuals, DE 69**



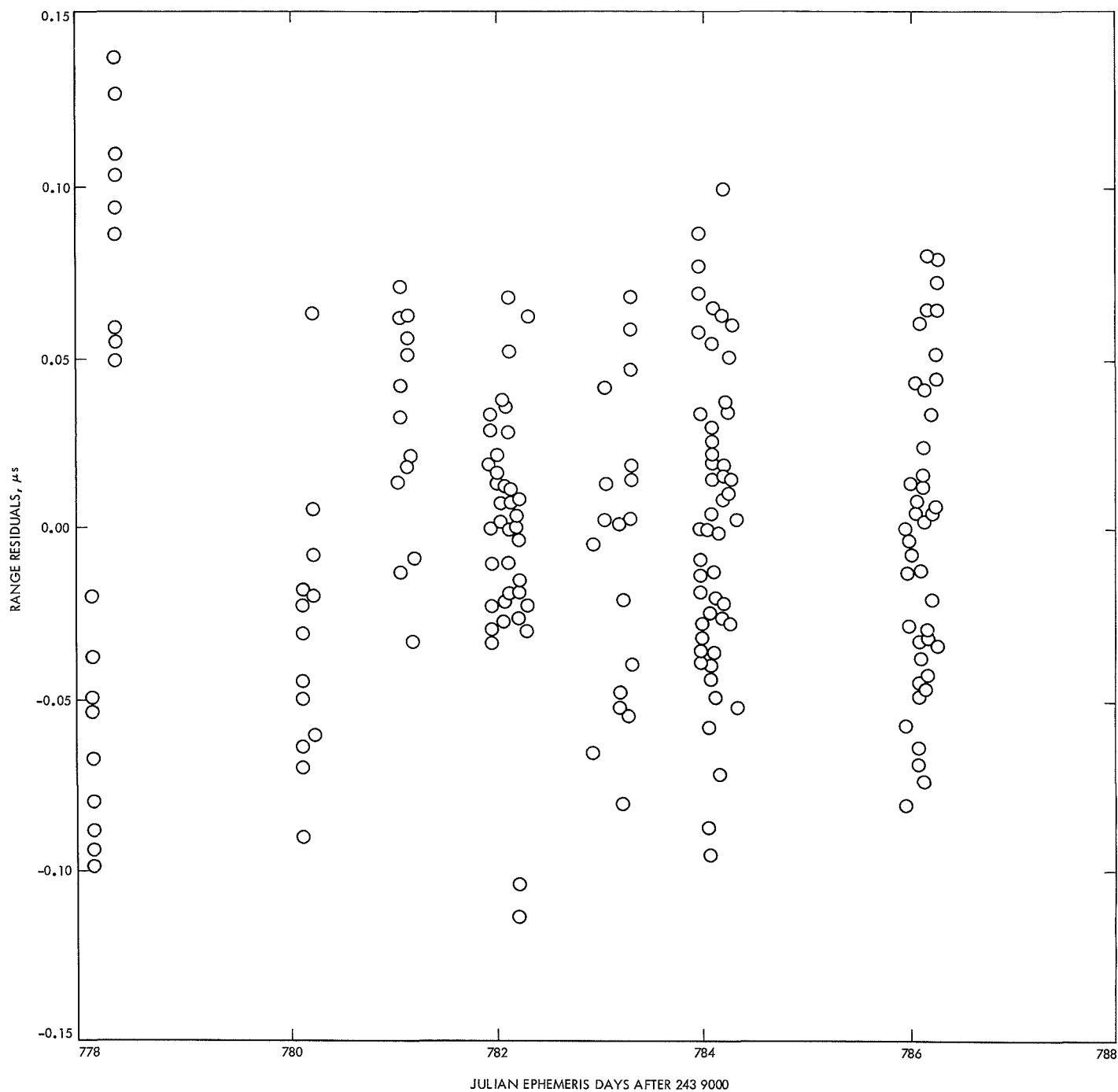


**Fig. 10. Mariner V residuals**

The Mars residuals are shown on Fig. 11. The 1 sigma for DE 69 is 748  $\mu$ s as compared with the 1 sigma of DE 40 which was 734  $\mu$ s. This is primarily a result of the orbit of Venus, since no radar data have been removed from the Mars data set. The large value is dependent upon the rather large residuals early in 1964 and does not represent the accuracy with which we are fitting the modern data.

The ten time-delay measurements shown (Fig. 11) for 1967 are the result of work done by Dr. Pettengill and his colleagues. The 148 range determinations were taken over the period from April 7, 1967 to June 2, 1967 on ten different days. The data shown here represent compressed data corrected for topography. The uncompressed data, which are in publication, without the corrections for topography are plotted against time in Fig. 12. The range of the residuals is +20  $\mu$ s to -60  $\mu$ s. Upon application of the corrections supplied by Pettengill, et al., and comparing the residuals of the uncompressed range to our

ephemeris the accuracy and fine structure of the ten points is apparent (see Fig. 13).

The final values for the astronomical constants for DE 69 are given in Table 3. This ephemeris, which is the 69th evaluation of either planetary or lunar motion, was chosen as the planetary ephemeris for the initial phase of the *Mariner* Twins flyby of Mars.

**Table 3. Astronomical constants for JPL ephemeris DE 69<sup>a</sup>**

Planet	Reciprocal mass	$\sigma$	Radius, km <sup>b</sup>
Mercury	5983000	$\pm 25000$	2440.9 $\pm 2$
Venus	408522	$\pm 0.5$	6053.0 $\pm 2$
Earth + moon	328900.1	$\pm 0.3$	
Mars	3098700	$\pm 100$	
<sup>a</sup> Ephemeris of Venus and earth uncertainties: relative coordinates are; in-plane = $\pm 5$ km and out-of-plane = $\pm 10$ km; 1950.0 equatorial coordinate system = $\pm 100$ km. <sup>b</sup> Astronomical unit = 149597893 $\pm 3$ km.			

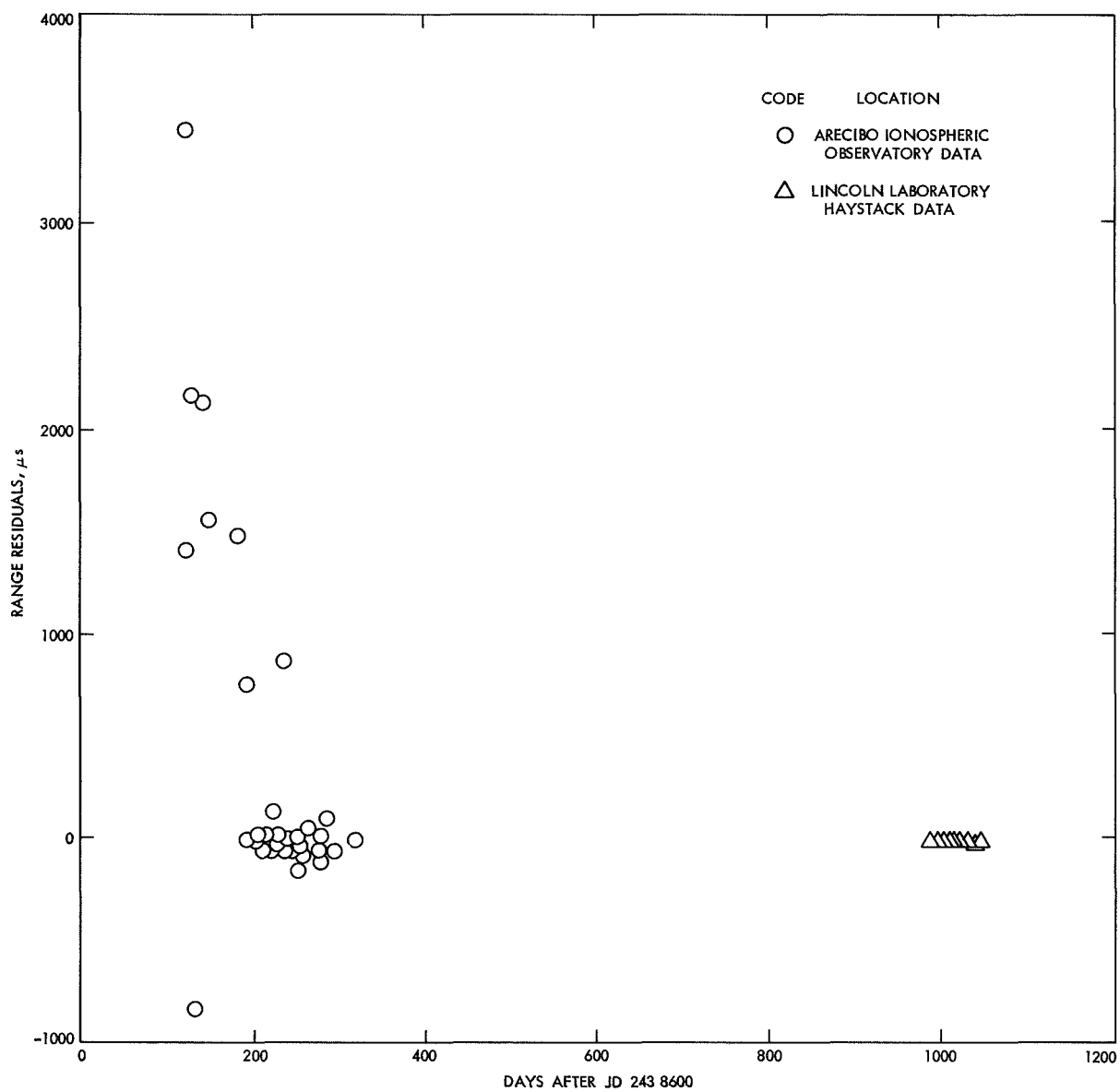


**Fig. 11. Mars range residuals, DE 69**

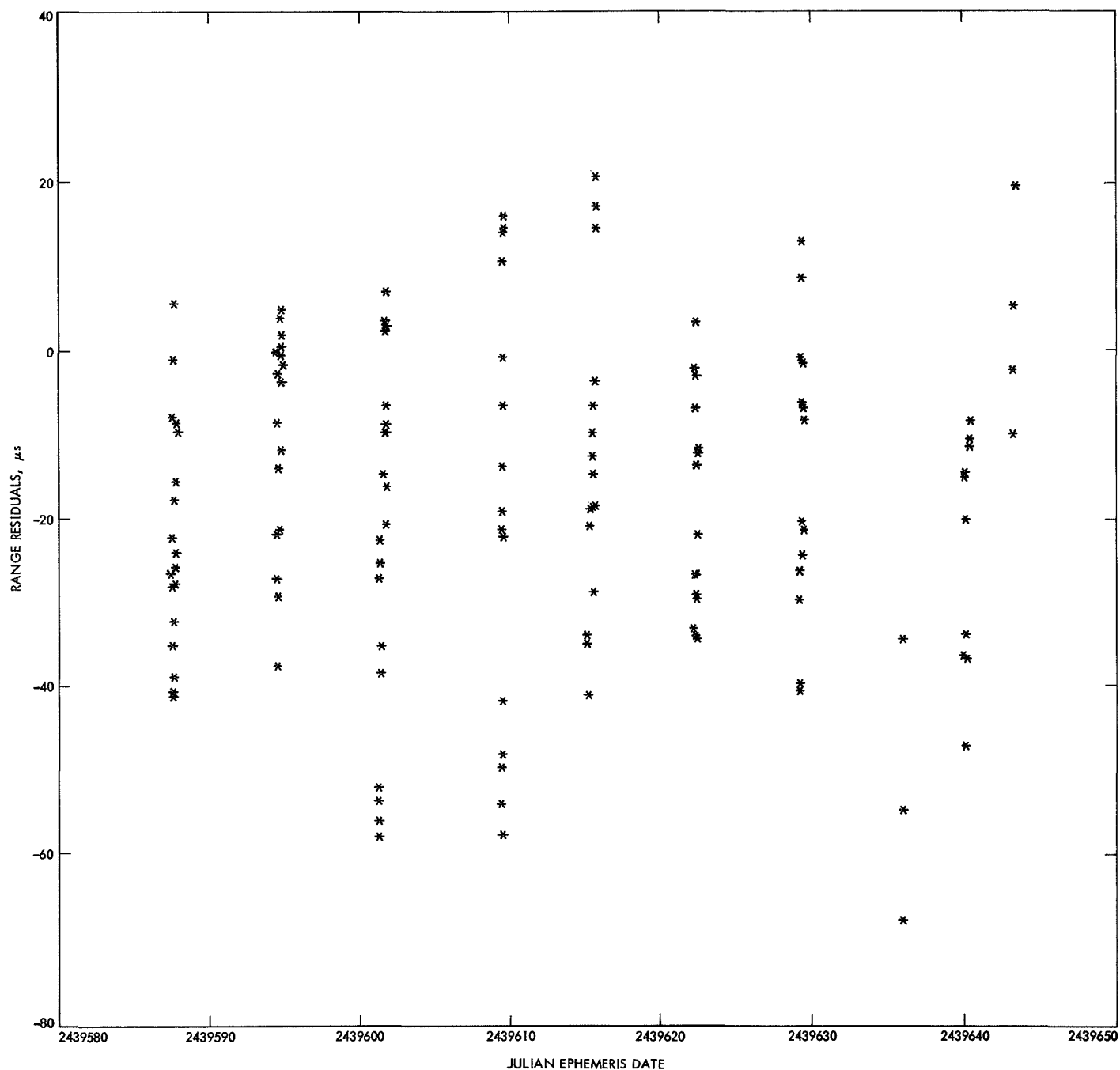


Fig. 12. Time-delay measurements for 1967, uncompressed data

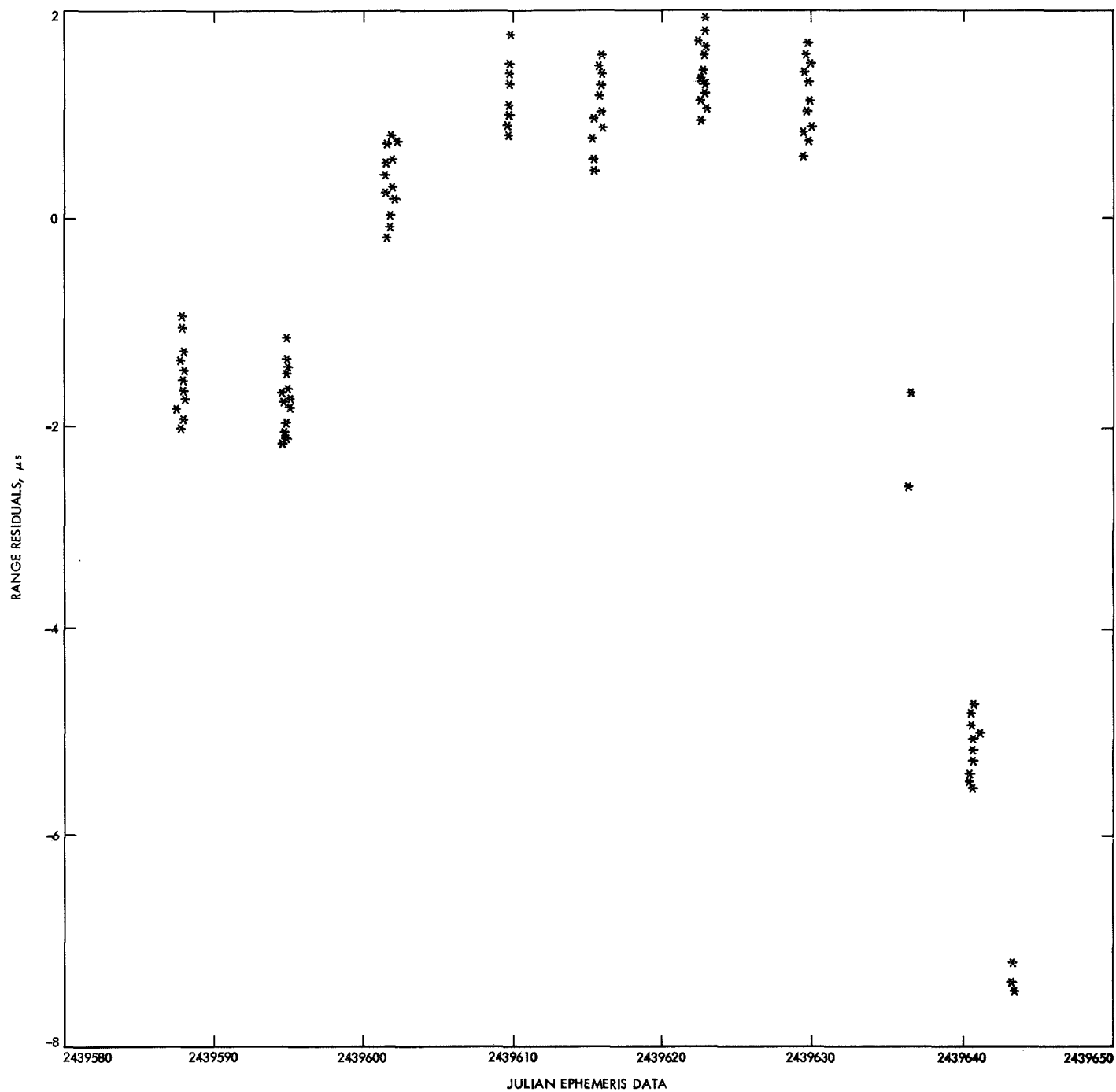


Fig. 13. Time-delay measurements for 1967, corrections applied



# Limitations to Navigation Accuracy in Support of the Planetary Encounter Phase of a Deep Space Mission

D. W. Trask  
Navigation Accuracy Group  
Jet Propulsion Laboratory  
Pasadena, California

*The navigational accuracy, obtainable with earth-based radio tracking data in support of planetary encounter operations, is considered as a function of the limiting error sources. This case is of interest not only because it is amenable to a simplified analysis in a relatively mission independent form and has significant practical applications, but because it represents a situation where phenomena, in addition to the capabilities of the ground tracking station, place inherent limitations on the obtainable accuracy. The uncertainty of the tracking station location on the earth's crust represents the severest limitation, but the state of the art has progressed to the point where uncertainties in the location of the earth's spin axis with respect to the crust of the earth and the angular orientation of earth in space are also significant factors as well as refraction effects of the transmission media.*

## Deductions of Observations of the Solar System

M. E. Ash, I. I. Shapiro, and W. B. Smith  
Lincoln Laboratory  
Massachusetts Institute of Technology  
Lexington, Massachusetts

*Recent results from the simultaneous processing of optical and radar observations of the sun, moon, planets and selected asteroids are presented. Emphasis is given to the determination of planetary ephemerides, astronomical constants and to tests of gravitational theories.*





*Session III*  
*Scientific Exploitation of the Data*

*Session Chairman*  
*Dr. Duane O. Muhleman*  
*Owens Valley Radio Observatory*



# Selected Results From Analysis of Radar and Optical Observations of Icarus and the Inner Planets\*

W. B. Smith, I. I. Shapiro, M. E. Ash, G. H. Pettengill, and R. P. Ingalls

Lincoln Laboratory  
Massachusetts Institute of Technology  
Cambridge and Lexington, Massachusetts

*New results have been obtained from analysis of optical data of the sun and Icarus, and radar and optical data of Venus and Mercury, by the addition of 1968 planetary radar data and Icarus optical data taken near its close approach in 1968. Assuming the contribution of the solar gravitational quadrupole moment to be negligible, we find that the general relativistic perihelion advance of Mercury is confirmed within a (formal) standard error of 1.5%, and the relativistic retardation of radar waves near the sun within a (formal) standard error of 6%. In addition to these parameters, which test the underlying physical laws, new estimates have been obtained for the radii of Mercury and Venus, the AU, the mass of Mercury, and the earth-moon mass ratio. Also, the radar data weakly indicate that the Venus equator may not quite be circular, being out-of-round by about  $1.2 (\pm 0.4)$  km, and that its equatorial center-of-figure may be offset from its center-of-mass by about  $0.8 (\pm 0.2)$  km. Mercury exhibits neither effect within the formal uncertainty of about 0.5 km.*

*The estimated general relativistic perihelion advance of Icarus was 80% of its theoretical value with a formal standard error of 8%; when possible distortions of the observers' reference coordinate systems were parameterized, these values became 96% and 8%, respectively. Icarus data contribute very little to the estimate of Mercury's mass, its uncertainty therefrom being greater by more than an order of magnitude than from other data.*

---

\*This work was sponsored by the U.S. Air Force.

## I. Introduction

Unlike the familiar case for optical data, which often must be patiently accumulated over decades or even centuries to obtain significant improvements in the estimation of astronomical constants, even one additional year of the increasingly accurate radar data allows notably better estimates to be made. The addition to our data set of precise radar observations taken during 1968 has yielded results substantially more accurate than those we reported previously (Refs. 1-4). The greater accuracy is not just an end in itself, but will allow us to distinguish between competing models of the underlying physical laws.

In addition, our Planetary Ephemeris Program (PEP) has been improved and extended in a number of ways. For example, the departure of a target planet from spherical shape has been parameterized; this permits us to report herein some preliminary results regarding the shape of Venus and Mercury.

## II. Description of Data

The meridian circle observations of the sun, Mercury, and Venus were taken from publications of the U.S. Naval Observatory, and comprise two series of observations: 1949-1956 and 1956-1967. The radar data used in the present study were from the Millstone and Haystack observations of Venus and Mercury, 1964-1968.

Prior to the close approach of Icarus to the Earth in June, 1968, there existed just 71 published observations of the asteroid. Of the 235 new observations reported through August, 1968, we have included 160 in our final analysis.

## III. Theoretical Model and Processing Method

The approach used to obtain information about the solar system, both as to the values of certain astronomical parameters and to the underlying physical laws, was described in Ref. 1, except as noted in this section. The approach, and a description of its realization on an electronic computer, was also presented by Ash in Session II of this report.

For consistency with USNO bulletins we have changed the value of coordinate time minus atomic time from

32:20 to 32:15. (For the present paper the small fluctuations between coordinate and atomic times are inconsequential and have been disregarded.) Our numerical integration method retains the variable-step-size approach for strongly perturbed or eccentric orbits, such as those of Icarus and the *Mariner* vehicles, but now uses for the planets an efficient fixed-step-size technique with higher-order differences. In the integration of the equations-of-motion of a body, and partial derivatives with respect to parameters, the coordinates of the perturbing planets used are now obtained from the result of nine-body integrations which can be updated after each significant new fit. Though this slight procedural change is philosophically attractive, its absence was known to have been inconsequential for previous results; still, the *N*-body capability adds efficiency and convenience to our data handling procedures. Finally, the number of parameters for which we can solve simultaneously has been made much larger, approximately 100.

To study anticipated physical effects, and to account for known systematic residuals, a number of new parameters have been added to PEP. For example, it was noticed that residuals for Venus in right ascension possessed a clear systematic component with a synodic period, which we assumed was related to the difficulty of specifying the disk center when the figure of illumination is a crescent (Ref. 1). This phase effect has been modeled by a Fourier series representation, with the coefficients as parameters to be estimated. To allow for the possibility that the star catalog and/or site location used for a given series of observations at a given site may not be quite consistent with that used at another site or for a different series, three new parameters for each series have been added which represent equator and equinox corrections to the coordinate system, and a bias in declination. In order to estimate separately the anomalous perihelion precession of individual bodies, such as Mercury and Icarus, PEP allows the choice of separate relativity-motion factors for each body. This factor is the coefficient of the term in the differential equations of motion (Ref. 5) which causes the relativistic advance of the perihelion; to wit, the factor  $R_f$  in the harmonic-coordinate formulation (Ref. 5)

$$X'' = (\text{Newtonian terms}) + \frac{\gamma M_s}{r^3} - \frac{R_f}{c^2}$$

$$\times \left[ X \left( 4 \frac{\gamma M_s}{r^3} - r^2 \right) + 4X' (r \cdot r') \right]$$

where  $X$  represents a Cartesian coordinate of the planet-sun vector  $\mathbf{r}$  and a prime denotes differentiation with respect to coordinate time. In the equation,  $\gamma$  is the gravitational constant,  $r$  the planet-sun distance, and  $M_s$  the solar mass ( $\equiv 1$ , by assumption). The value unity for  $R_f$  corresponds (to the order of accuracy represented in the equation) to general relativity being correct. When plotted against the longitude on Venus of the subradar point, the time-delay residuals have a systematic behavior, hence, a parametric model was included which allows for asymmetry in the shape of the target planet.

## IV. Discussion of Results

### A. Tests of General Relativity

We first describe the results of a computer experiment designed to test two facets of the theory of general relativity; namely, the non-Newtonian precession of the perihelion of Mercury (characterized by  $R_f$ ), and the retardation (Ref. 2) of a radar wave passing close to the sun. The latter effect is characterized by a parameter ( $R_d$ ) which is a factor in the theoretical expression for excess delay; again,  $R_d = 1$  implies that general relativity is correct.

For the experiment we used the data set as described above, except deleting Icarus data. In addition to  $R_f$  and  $R_d$ , the parameters solved for were: the mass of Mercury, the earth-moon mass ratio, the AU, the six initial conditions each for the earth-moon barycenter, Mercury, and Venus; and the radii, and phase corrections through second order for Mercury and Venus for each of the USNO optical series, a total of 33 parameters. The results were:  $R_f = 1.00 \pm 0.015$  and  $R_d = 1.01 \pm 0.06$  with the quoted uncertainty being the formal standard error in each case.

Our result for  $R_f$  should be compared with Clemence's value (Ref. 6) of  $1.00 \pm 0.01$ , obtained from data that spanned nearly two centuries. The uncertainty quoted comes from Duncombe (Ref. 7) who redetermined the mass of Venus, which had previously been thought to be the largest contributor to the uncertainty in the theoretical value of the Newtonian contribution to Mercury's perihelion advance. To clarify the relative roles of radar and optical data in estimating  $R_f$  and  $R_d$  another analysis was made, this time using radar data alone. The parameter set was a subset of the previous one:  $i$  and  $\Omega$ , which determine the orientation of the orbital plane, were fixed for each planet, since these are poorly determined from radar data; and the phase corrections were deleted, since

their partials are all zero for radar data. The results were  $R_f = 1.02 \pm 0.04$  and  $R_d = 1.00 \pm 0.05$ .

The result for  $R_d$  compares with the previous value (Ref. 2) of  $0.9 \pm 0.1$ . The improvement in the formal standard error is due to the additional year of radar data.

For these analyses the solar gravitational quadrupole moment was assumed to be zero. Prior computer experiments had shown that these data did not allow a useful, simultaneous estimate to be made of  $R_f$  and the solar quadrupole moment.

### B. Planetary Radii, AU, and Masses

In general the values for solar system parameters are theory dependent; for example, the semi-major axis  $a$  is rather strongly dependent upon the parameter  $R_f$ . Hence, to estimate parameters other than  $R_d$  and  $R_f$ , it was necessary first to choose our physical model; we chose general relativity, and set  $R_f = R_d = 1$ . The other parameters and the data were as in Section IV-A above. Some of the results are summarized in Table 1. In comparison with the results in Ref. 1, the formal standard errors are smaller by a factor of about three. Based on experience we consider the formal error for the earth-moon mass ratio to be realistic, but for the other parameters, the actual uncertainty is perhaps three times larger than the formal value.

Table 1. Summary of resultant data

Parameter	Previous value (Ref. 1)	New value	New formal standard error
Radius of Mercury (km)	2434.0	2439.1	0.5
Radius of Venus (km)	6053.5 (Ref. 4)	6049.8	0.4
AU (light, s)	499.004 785	499.004 779	0.000 002
Mercury mass (inverse)	$6.02 \times 10^6$	$6.04 \times 10^6$	$0.015 \times 10^6$
Earth-moon mass ratio	81.302	81.302	0.002

### C. Planetary Shape

Heretofore, there have been no obvious indications in the radar residuals that Mercury or Venus, unlike Mars, has significant variations in the subradar radius; i.e., at subradar latitudes they behaved as spheres. However,

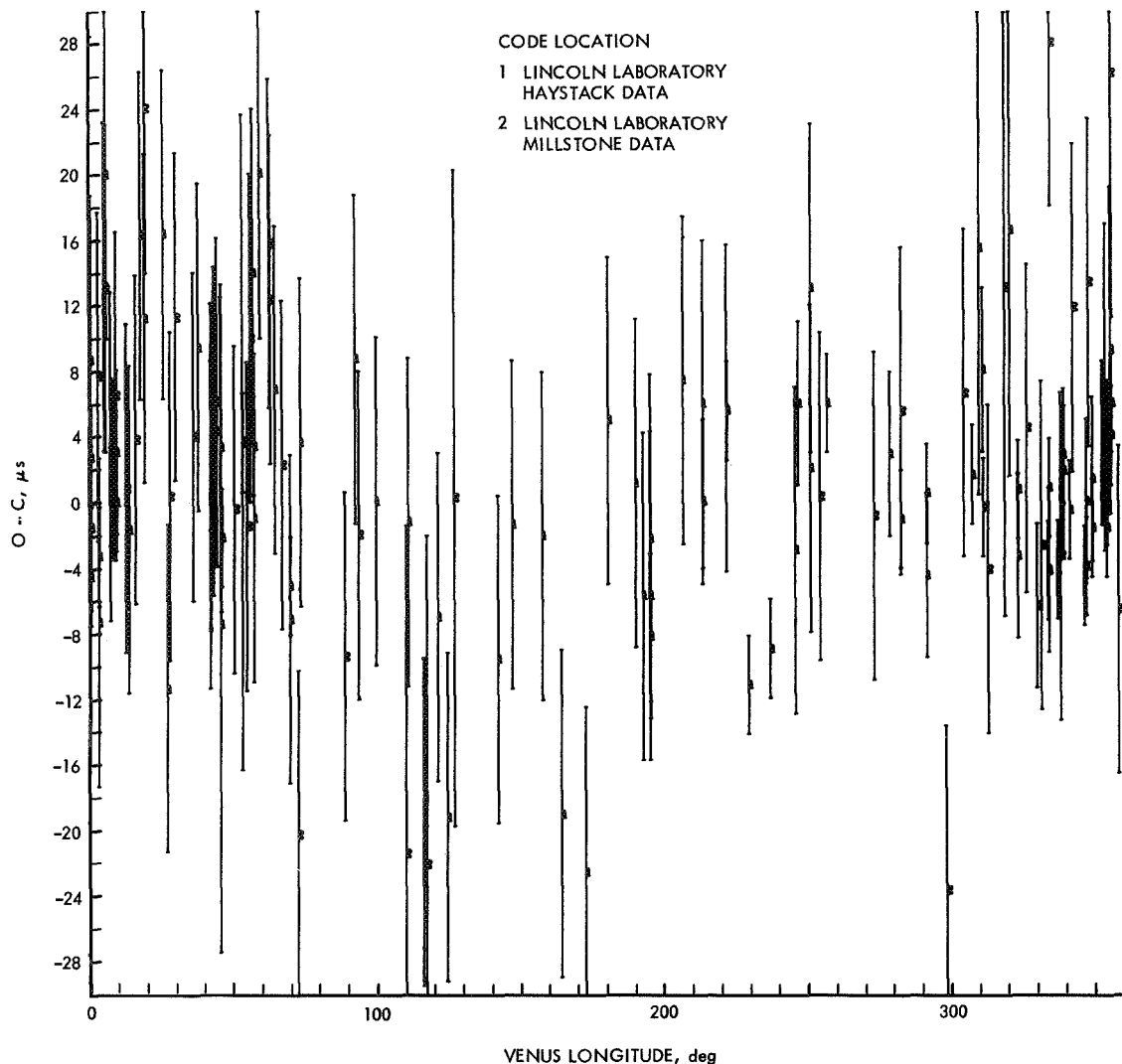


Fig. 1. Earth-Venus radar time-delay residuals as a function of Venus longitude<sup>1</sup> of the subearth point

when 1968 radar data were added, and time delay residuals plotted against Venus longitude (Fig. 1), a slight systematic effect became evident. The implied peak-to-peak height variation of about 2.5 km is much less than the approximately 12-km variations found for Mars (Ref. 8).

The model for planetary shape assumes an ellipsoidal shape around the center of the figure; i.e., that the surface satisfies

$$\left(\frac{u}{a}\right)^2 + \left(\frac{v}{b}\right)^2 + \left(\frac{w}{c}\right)^2 = 1$$

where  $u$ ,  $v$ ,  $w$  is a body-fixed coordinate system. The

model also assumes that the center of the figure is offset by  $\Delta\rho$  from the center of mass. To the order of accuracy supportable by the data it is adequate to assume that  $c = a$ , that  $\Delta\rho$  lies in the  $u$ - $v$  plane, that  $w$  coincides with the axis of rotation, and that the latter is perpendicular to the ecliptic. We have performed an analysis in which the parameters estimated were  $\vec{a}$ ,  $\Delta\rho$ , and  $(1 - b/a)$ , starting with the solution from Section IV-B above. The results for Venus give  $\Delta\rho = 0.8$  km (standard error 0.2 km), and  $a - b = 1.2$  km (standard error 0.4 km). Within the standard error of about 0.5 km, Mercury (in its equatorial region) apparently does not deviate significantly from a spherical shape.

<sup>1</sup>The origin of longitude is near the subearth point at the inferior conjunction.

These "shape" parameters were estimated from the residuals obtained in the first analysis described in Section IV-B above; they were not estimated simultaneously with the other parameters. Assuming that the non-sphericity is real, we would expect the estimates of the non-shape parameters to have been altered somewhat from their "true" values so as to have minimized the residuals for this theoretical model in which the shape parameters had not been included. Consequently, the estimates we obtained for  $a$ ,  $\Delta\rho$ , and  $a - b$  are probably somewhat distorted. In addition the neglected correlations of the shape and non-shape parameter estimates cause our results for the standard errors in the parameter estimates to be somewhat too small. For these and other reasons connected with possible small systematic errors in the data, our numerical results for the shape parameters are only preliminary.

#### D. Icarus and General Relativity

In spite of the small number of observations of the asteroid Icarus, its orbit is such that it provides a significant test of the predicted relativistic perihelion precession. We had previously reported (Ref. 3) the results of such a test for the Icarus data from 1949 through 1967. Here we discuss the modifications introduced by inclusion of the large number of observations obtained from the 1968 close approach of Icarus and the earth (Ref. 9). Some elementary calculations had indicated that, even with the addition of the expected 1968 data, the Icarus observations would be useful only for the estimation of parameters associated specifically with its orbit. In preparation for the present conference, we confirmed this conclusion with a computer experiment in which the Icarus data were added to the data described in Section IV-A above and the parameter set was augmented by the orbital elements of Icarus and its own  $R_f$ . The estimates of all the non-Icarus parameters were virtually unaffected (differences were of the order of one standard deviation or less); in particular, the formal error in the estimate of Mercury's mass was affected only in the fourth place. Further, experiments also showed that (1) the formal errors in the estimates of the non-Icarus parameters are each at least an order of magnitude smaller when determined from the non-Icarus data alone than when determined from the Icarus data alone<sup>2</sup>; and

(2) the estimates for the orbital elements of Icarus and  $R_f$  were each the same, within less than 2 and 0.2 standard deviations, respectively, whether the non-Icarus data and parameters were included or not.

Hence, for the results to be given here, we may consider the orbits and masses of the moon and planets to be fixed in accordance with the prior analyses of the optical and radar observations of these bodies. These latter analyses were carried out, where appropriate, under the assumption that general relativity is correct; i.e., that  $R_f = R_g = 1$ . Since our principal goal was to estimate the parameter  $R_f$  for Icarus (along with its six orbital elements), this assumption seems at first glance to be inconsistent with our purpose. However, the inconsistency is more apparent than real: If we obtain  $R_f \approx 1$ , then self-consistency will prevail; if  $R_f \neq 1$ , then we will have established that either general relativity is incorrect or some other aspect of either our theoretical model or the observations differed from our presumptions. Our result (Ref. 10), obtained in the summer of 1968, was  $R_f = 0.80 \pm 0.08$  compared with the estimate  $R_f = 0.97 \pm 0.20$  that had been obtained prior to the June 1968 close approach from the 71 photographic observations then extant (Ref. 3). The formal standard errors were obtained on the assumption that each observation had an uncertainty of 1.0 arc second. In fact, most observers considered the errors associated with the measurements of the positions of Icarus on the photographic plates to be no more than a few tenths of an arc second. Nonetheless we felt that it would be a bit premature to discard general relativity on this evidence. We finally decided that the explanation for this unexpected result might reside in the star catalogs used in the determination of the Icarus photographic positions. The reference system(s) defined by these catalogs might be severely distorted with respect to the FK4 system to which the planetary optical observations were presumably related. To test this assumption, we estimated equator, equinox, and declination bias corrections along with the original seven. (The photographic data were treated for this purpose as all belonging to one observation series, hence only three additional parameters were added.) The result then obtained was  $R_f = 0.96 \pm 0.08$ . The estimates of the three added parameters were found to be of the order of 0".5 with formal standard errors of about 0".2. Further, radar Doppler observations of Icarus (Ref. 11), though not allowed to affect the parameter estimates, were in substantially better agreement with the results from the 10-parameter solution than with those from the 7-parameter analysis.

<sup>2</sup>Although Lieske, J. H. and Null, G., Ref. 9, obtained Mercury's (inverse) mass from the Icarus data alone with an estimated uncertainty of about 50,000, we find the uncertainty to be about 500,000; see Ref. 13 for further discussion.

## V. Conclusions

If the records from the reduction of the photographic plates are preserved, it will be possible when improved estimates for the relevant star positions become available to repeat this evaluation of  $R_I$ . In the meantime, we conclude that inaccurate positions in the star catalogs

used in the reductions are probably responsible for the anomalously low value obtained for  $R_I$ <sup>3</sup>. Thus, the influence of the star catalog problem on this test of physical laws as embodied by  $R_I$  appears to be marked.

---

<sup>3</sup>A detailed discussion of the Icarus data by I. I. Shapiro, W. B. Smith, M. E. Ash, and S. Herrick is still in preparation.

## References

1. Ash, M. E., Shapiro, I. I., and Smith, W. B., "Astronomical Constants and Planetary Ephemerides Deduced from Radar and Optical Observations," *Astron. J.*, Vol. 72, pp. 338-350, 1967.
2. Shapiro, I. I., et al., "Fourth Test of General Relativity: Preliminary Results," *Phys. Rev. Lett.*, Vol. 20, pp. 1265-1269, 1968.
3. Shapiro, I. I., Ash, M. E., and Smith, W. B., "Icarus: Confirmation of the Relativistic Perihelion Precession," *Phys. Rev. Lett.*, Vol. 20, p. 1517, 1968.
4. Ash, M. E., et al., "The Case for the Radar Radius of Venus," *Science*, Vol. 160, pp. 985-987, 1968.
5. Ash, M. E., *Generation of Planetary Ephemerides on an Electronic Computer*, Technical Report 391. Lincoln Laboratory, Massachusetts Institute of Technology, Lexington, Mass., 1965.
6. Clemence, G. M., "The Motion of Mercury, 1765-1937," *Astron. Papers of The American Ephemeris*, Vol. XI, Part 1, Nautical Almanac Office, U. S. Naval Observatory, U. S. Government Printing Office, Washington, D. C., 1943.
7. Duncombe, R. L., "Motion of Venus, 1750-1949," *Astron. Papers of the American Ephemeris*, Vol. XVI, Part 1, 1958.
8. Pettengill, G. H., Counselman, C. C., Rainville, L. P., and Shapiro, I. I., "Radar Measurements of Martian Topography," *Astron. J.*, Vol. 74, No. 3, p. 315, Apr. 1969.
9. Lieske, J. H., and Null, G. W., "Icarus and the Determination of Astronomical Constants," *Astron. J.*, Vol. 74, No. 2, pp. 297-307, Mar. 1969.
10. Shapiro, I. I., Cited work was presented in preliminary form, *Thirty First Annual Meeting of the Meteoritical Society*, Cambridge, Mass., Oct. 9, 1968.
11. Goldstein, R. M., "Radar Observations of Icarus," *Science*, Vol. 162, p. 903, 1968.



# The Obliquity of Mercury

S. J. Peale

Department of Physics  
University of California  
Santa Barbara, California

*Mercury is likely to be in one of two stable configurations representing extremes in the energy associated with its orientation, where the spin vector and the normal to the orbit plane precess around and remain coplanar with the normal to the invariable plane. The obliquity remains constant and its value determines the moment ratio  $(C-A)/C$  (modified slightly by  $(B-A)/C$ ) for Mercury. The spin axis in one configuration is separated from that in the other by at least 7 degrees. Determination of the configuration which Mercury has assumed but not the precise obliquity will determine respectively a lower bound or an upper bound on  $(C-A)/C$ .*

# Lunar Gravimetrics

P. M. Muller and W. L. Sjogren

Navigation Accuracy Group  
Jet Propulsion Laboratory  
Pasadena, California

*Reduction of Lunar Orbiter radio tracking data has made possible the construction of a high resolution gravimetric map of the lunar earthside hemisphere between  $\pm 100^\circ$  lon and  $\pm 60^\circ$  lat. The gravitational variations have been determined to a precision of 10 mgal, and a resolution of 100 km (equivalent to a 50th order spherical harmonic expansion). This new analysis has utilized all of the suitable Lunar Orbiter data (250 orbits, 25,000 doppler observations), has resulted in extraction of nearly all the gravimetric information possible with the method (the doppler has been fit down to the 0.3 mm/s noise level), and has demonstrated consistency through agreement between the polar and equatorial orbiters. The study has revealed large (50–250 mgal) mass concentrations (mascons) centered in each of the ringed seas (Imbrium, Serenitatis, Crisium, Nectaris, Humorum, Aestuum and Orientale). This 1:1 correspondence between mascons and ringed seas suggests a definite relationship between the two phenomena. Therefore, an analysis is presented of the current implications of the new observations.*



# Mascons: Local Lunar Gravity Features

P. Gottlieb

Future Studies Group  
Jet Propulsion Laboratory  
Pasadena, California

*The recent work of Muller and Sjögren correlating "line of sight" Lunar Orbiter accelerations with locations on the lunar surface, indicates that the largest Lunar Orbiter doppler anomalies are due to concentrations of mass near the surface of the moon. The gravitational effects of these mass concentrations can be reproduced by various sizes of spherical density anomalies located between 40 and 150 km below the lunar surface. The effects can also be reproduced by a grid of mass points located at the lunar surface, and closely spaced to approximate a continuous density distribution. We have constructed both types of model. Both types of model have been constructed and refined to a point where they reduce the peak residuals by more than a factor of 10. The positive features in the Muller-Sjögren map have been corroborated, and the negative features have been washed into a background. The positive feature in the Sinus Aestuum-Medii area shows up quite strongly in the latest models.*

## Interpretation of Lunar Mass Concentrations\*

W. M. Kaula

Department of Planetary and Space Science  
University of California  
Los Angeles, California

*The lunar mass concentrations differ significantly from maxima in the earth's gravity field in that they coincide with topographic minima, which in turn implies a different petrology. Their size makes it difficult to attribute the entire mass to an impacting body. Probably the most important problem of lunar structure would be a resolution between the two alternatives for the low mean density of the moon: (1) deficiency of iron, suggesting fission origin; or (2) excess of volatiles, suggesting low temperature of formation. Hypothesis would in turn suggest the mass concentrations being formed by degassing of lunar material upon impact of an asteroid or comet. To decide which is the more likely type of body we need better mass-frequency statistics and better scaling theory for energy-crater size relationships.*

---

\*Kaula, W. M., Interpretation of Lunar Mass Concentrations, Pub. No. 740, Institute of Geophysics and Planetary Physics, University of California, Los Angeles, Calif.



# Radar Photograph of the Moon at 3.8-cm Wavelength

S. H. Zisk

Lincoln Laboratory

Massachusetts Institute of Technology

Lexington, Massachusetts

*We are now making the measurements for a high-resolution map of the radar scattering across the lunar surface using the 3.8-cm radar at the Haystack research facility operated by the Lincoln Laboratory. The radar return in the expected and orthogonal polarizations are recorded simultaneously with right hand circularly polarized transmissions. A uniform resolution of 2.5 km over the surface of the moon is expected and coverage over the complete subearth hemisphere will be obtained. About half the measurements have been completed and about 20% converted into intensity modulated photographs. Relative accuracy is 1 dB. Photographs and preliminary interpretation will be presented.*

## Recent Results on the Gravitational Field of the Moon and Some Geophysical Applications

W. H. Michael, Jr.

National Aeronautics and Space Administration

Langley Research Center

Hampton, Virginia

*The most recent analysis in a general investigation of the lunar gravitational field at Langley Research Center has resulted in a solution for the potential as represented by spherical harmonic coefficients through degree and order thirteen. The solution is based on 15 data arcs, each of 3 to 5 days duration, from Lunar Orbiters III, IV, and V, with a total of about 13,000 observations. The results are applied to obtain contour plots representing mass anomalies over the whole lunar sphere. The near-side contours have considerable correlation between the positive mass anomalies and the mascon results obtained by a different procedure, but also indicate other positive and negative anomalies over the visible disc. Rather large amplitude, positive and negative, contours are obtained on the far side, but these are probably not very reliable because of data limitations, and they may be modified with analysis of additional data. Applications of the gravitational field results in conjunction with information from physical libration analyses, indicate that the moments of inertia of the moon correspond very closely to overall homogeneous density distribution in the moon.\**

---

\*Additional discussions of these and related results can be found in the papers by W. Thomas Blackshear (Trans. A.G.U., Vol. 50, No. 4, April 1969) and by William H. Michael, Jr.; W. Thomas Blackshear and John P. Gapcynski (XII Plenary Meeting of COSPAR, Prague, Czechoslovakia, May 1969).



*Session IV*  
*Planetary Structure and Atmosphere*

*Session Chairman*  
*Dr. Von R. Eshleman*  
*Stanford University*





# Remarks on the Inference of Neutral Atmospheric Parameters From Microwave Occultation Data

Frederick F. Fischbach  
Department of Aerospace Engineering  
University of Michigan  
Ann Arbor, Michigan

*The phase shift theory as presented by analysis of Mariner IV data is reviewed. The approximations made in deducing the neutral atmosphere of Mars by four methods are considered in the context of their potential application to a system for measuring the earth atmosphere. A preferred inversion technique is suggested. The assumption of spherical stratification on earth is also discussed.*

## I. Introduction

The radio occultation method of inferring neutral atmospheric parameters is certainly well known to many present this afternoon because of the outstanding success in utilizing this method on Mars and Venus by our hosting organization. My remarks will be directed almost entirely toward the consequences of extrapolating that technique to one proposed for use in making measurements of the earth atmosphere remotely from a satellite. I understand that two presentations to follow will be on the same topic, and what I hope to do in my allotted time is to review the current theory as it relates to the earth measurements and set the stage for more detailed comments.

## II. A Review of Pertinent Publications

The radio occultation method of measuring planetary atmospheres was first suggested by Fjeldbo (Ref. 1) in

a dissertation at Stanford in 1964. The theory was published by Fjeldbo and Eshleman (Refs. 2 and 3) in the *Journal of Geophysical Research* in 1965. Subsequent to the *Mariner IV* flight the results were published by Kliore and others (Ref. 4). A paper by Phinney and Anderson (Ref. 5) presented a general theory in 1968, and a paper by Harrington, Grossi, and Langworthy (Ref. 6) commented on the results, also in 1968. In the latter part of 1968, the final data was presented by Fjeldbo and Eshleman (Ref. 7) in *Planetary and Space Science*. A more general theory for several parameters was given by Hays and Roble (Ref. 8) in 1968, also in *Planetary and Space Science*.

The exposition of the radio occultation method for meteorological measurements on earth was made by Tatarskiy (Refs. 9 and 10) in two recent papers in the *Soviet Bulletin of Atmospheric and Oceanic Physics*. His papers are based at least in part on papers by Khvostikov (Ref. 11) and Rozenberg (Ref. 12) in Soviet journals in

1946 and 1949. Werbowetski (Ref. 13) of the Environmental Science and Services Administration suggested a technique in 1965, and Lusignan of Stanford suggested a technique at the Tokyo COSPAR meeting last year. At the same meeting, the theory was discussed by both Kliore and Fischbach. These papers will appear in the next volume of *Space Research*.

As far as unpublished work in this area is concerned, Stanford University (Refs. 14 and 15) and Lusignan in particular have submitted several technical reports and proposals. Sargeant (Ref. 16), of the University of Wisconsin, has analyzed a portion of the theory. Graves and Fischbach (Ref. 17) have analyzed certain aspects of the theory. Harrington and Grossi (Refs. 18 and 19) have considered a Mars orbiter-pair and a similar method dealing with the earth's ionosphere. Their conference report on the latter subject will be published. In addition, a group of interested principals has been commissioned by Goddard Space Flight Center as a microwave occultation study group and has met for the primary purpose of studying the technique proposed for flight test by Lusignan and colleagues at Stanford.

This summary is intended to be comprehensive except for material relative to planetary probes subsequent to *Mariner IV*; any other omissions are my error. I shall appreciate your drawing my attention to any published references omitted.

### III. *Mariner IV* Techniques

The theory as expounded by Fjeldbo in 1964 was that the horizontal transmission of microwaves through a planetary atmosphere would cause a detectable phase shift. If the transmitter was located on a spacecraft traveling in such a direction that the optical path between it and an earth-based receiver traversed all levels of the atmosphere—that is, if there was an occultation of the spacecraft—and if the doppler shift due to relative motion was measured precisely, the doppler residual due to the atmosphere could be detected. Fjeldbo further showed that, if spherical stratification of the refractive index was assumed, an unambiguous retrieval of the refractive index profile was possible.

Several major difficulties had to be overcome. The trajectory of the spacecraft was required with great precision. The motion of the earth stations, the effect of the earth atmosphere, transmitter frequency stability,

and the different path geometry of the transmitted and received signals were complicating factors. That these problems were solved and that a total residual phase excursion of but 40 cycles in 1 min was measured are tributes to the experiment team.

Once the atmospheric phase shift as a function of the spacecraft position is obtained, the method of deducing atmospheric parameters is of considerable interest. The following three methods have been investigated:

- (1) Inversion by the Abel transform along a straight-line approximation to the ray path. This method was adopted by Fjeldbo in his first paper and forms the basis of his final data treatment.
- (2) Model-matching. This method implies computation of a large number of possible atmospheric effects. After measurement is made, the atmosphere is chosen which would have most nearly produced the effect. Because of the practical limit in computation with several variables, there is a loss in precision. In addition, the result is not unique. Nevertheless, this is a valuable technique and was utilized to considerable advantage by the *Mariner IV* experimenters.
- (3) Inversion by the Abel transform applied to the exact ray path. Although this method is mathematically exact and unique, the doppler data is not of a form suitable for input to the equation. In order to provide suitable inputs, Phinney and Anderson demonstrated a technique which was equivalent to inferring the refraction angle from the doppler measurements. I have reservations about the accuracy of that inference. They also suggested approximations in the computations which would reduce complexity. The approximations were shown to be reasonable, but numerical error analyses were not made and a comparison with the straight-ray approximation is not available. This method was not used.

To summarize, the *Mariner IV* data has been analyzed by different methods which are in substantial agreement. Uncertainties still existing are due to unknown composition, both neutral and ionic. The experimenters state that errors in the raw data considerably overshadow any errors introduced by the approximations in the data reduction method. This view has been unchallenged.

#### IV. Earth Techniques

When we attempt to evaluate the radio occultation technique as it might apply on earth, one fact stands out sharply: with the exception of the two recent Tatarskiy papers cited, not a word on the subject appears in the standard literature. This situation seems indefensible, and those of us who have addressed the technique in our researches all share in the blame. I strongly recommend that we correct this at the earliest opportunity.

Because of this lack of published material, this review is necessarily based on technical reports, private communications, proposals, conference reports, study group meetings, and other mystical sources.

In considering the occultation method for earth atmosphere measurement application, the following conditions must be taken into account:

- (1) Transmission must be between spacecraft rather than spacecraft to earth.
- (2) Atmosphere composition is relatively well known except for water vapor content.
- (3) Accuracy of about 1% and many profiles per hour are required for meteorological applications.

Transmitting between satellites in different orbits permits only about two occultations per orbit per satellite pair. There are no occultations in transmissions between two satellites in similar orbits. The problem is solved by transmitting between one master and several slave satellites in similar orbits positioned so that the ray paths are at different tangent heights and we have a continuous pseudo-occultation. That is, the phase delays on several levels can be measured simultaneously. This technique was proposed by Lusignan and is currently under consideration.

With this technique, orbits must be known with great precision. An rms error of a meter is perhaps tolerable. With present knowledge of the gravity field and the best ground tracking, 3 to 7 m is perhaps possible. Lusignan proposes to improve the knowledge of the gravity field by doppler comparison of orbits while the ray path lies above the atmosphere, thus reducing the rms error to less than a meter. This would, by serendipity, be a geodetic breakthrough plus provision of the necessary accuracy for the orbit determination. A possible test of this is currently under study.

Water vapor is a polar molecule and exerts about 16 times the refractive effect of any other constituent of the same mass. As a result, the retrieval of a refractive index profile does not imply the retrieval of density, pressure, and temperature. Above 300 mbar the amount of water vapor is so small that it may be neglected; below 800 mbar the effect is so large that water vapor is mainly measured rather than density. The region between 300 and 800 mbar must be corrected for water vapor. Lusignan has proposed to do this by inference from a combination of data sources. These sources are climatology, temperature determined by other means, scintillation and/or absorption of the prime signal, and adjunct microwave radiometry.

Water vapor also may cause serious problems due to ducting of the signal and transmission on several paths instead of one. This is of particular concern because of the typically severe horizontal stratification of water vapor.

In the analytic inversion processes discussed previously, spherical stratification is assumed. At Michigan, this assumption was found to be negligible in the case of neutral density and pressure, although barely so. We also found, by an analytic process based on certain water vapor measurements, that this assumption in the case of water vapor caused serious error, even when the amount of water vapor on the path was known. Lusignan, using a different method based on different data, found the effect negligible. We are presently attempting to resolve this disagreement.

Now, as regards the data reduction techniques: since there will be no occultations, a continuous function of phase shift with height will not be available. If enough satellites are orbited, interpolation between the measurements will provide a continuous function. In that case, the exact Abel inversion along the refracted ray can be used. The ray path constant can be found to associate with each phase delay in the following way. The unrefracted ray path will have a refractive index equal to unity. A prediction of the index of the next lower spherical shell will be made, and the path geometry and phase delay will be calculated. Comparison will be made with the actual measurement and the prediction corrected. Continuing this iterative process will give the index in that layer. The process will be repeated for the next lower layer, and so on. In each case only the lowest spherical shell is being predicted and corrected, all higher layers having been already determined. This method will provide an exact, unique data inversion

without approximation but with considerable computation. The inherent error is in the interpolation of the basic data, which can be minimized to whatever extent required by a sufficient number of satellites.

A similar process when applied to the Abel inversion of a straight-ray approximation gave a 43% error, according to Grossi (Ref. 18). If corrections to the approximation could be applied which reduced the error by an order of magnitude, the error would still be too large.

Lusignan is pessimistic about the practical possibility of orbiting a sufficient number of satellites to employ an analytic inversion and is presently analyzing a model-matching method. Such a method can of course be used with any number of measurement levels, however small. Lusignan is working with four levels of measurement

and has constructed empirical orthogonal functions from data gathered at Oakland, California. His first results were reported as satisfactory, but the technique cannot be considered proved until properly expounded, which will take more time.

None of the foregoing remarks on data handling apply to the water vapor problems, which must be solved by other means. The Tatarskiy paper (Ref. 10) says flatly that the type of system we are considering will not work below 300 mbar because of water vapor. However, his paper omits any discussion of possible corrections. Hence the question of whether he has considered suggestions such as those made by Lusignan and rejected them or has not considered them at all is moot. It is apparent, nevertheless, that we had best follow his example and attach more urgency to the submission of our analyses for scientific review.

## References

1. Fjeldbo, G., *Bistatic-Radar Methods for Studying Planetary Ionospheres and Surfaces*, Ph.D. dissertation. Stanford University, Stanford, Calif., 1964.
2. Fjeldbo, G., and Eshleman, V. R., "The Bistatic Radar-Occultation Method for the Study of Planetary Atmospheres," *J. Geophys. Res.*, Vol. 70, pp. 3217-3226, 1965.
3. Fjeldbo, G., Eshleman, V. R., Garriott, O. K., and Smith, F. L., III, "The Two-Frequency Bistatic Radar-Occultation Method for the Study of Planetary Atmospheres," *J. Geophys. Res.*, Vol. 70, pp. 3701-3710, 1965.
4. Kliore, A., Cain, D. L., Levy, G. S., Eshleman, V. R., Fjeldbo, G., and Drake, F. D., "Occultation Experiment: Results of the First Direct Measurement of Mars' Atmosphere and Ionosphere," *Science*, Vol. 149, pp. 1243-1248, 1965.
5. Phinney, R. A., and Anderson, D. L., "On the Radio Occultation Method for Studying Planetary Atmospheres," *J. Geophys. Res.*, Vol. 73, pp. 1819-1827, 1968.
6. Harrington, J. W., Grossi, M. D., and Langworthy, B. M., "Mars Mariner IV Radio Occultation Experiment: Comments on the Uniqueness of the Results," *J. Geophys. Res.*, Vol. 73, pp. 3039-3041, 1968.
7. Fjeldbo, G., and Eshleman, V. R., "The Atmosphere of Mars Analyzed by Integral Inversion of the Mariner IV Occultation Data," *Planet. Space Sci.*, Vol. 16, pp. 1035-1059, 1968.
8. Hays, P. B., and Roble, R. G., "Atmospheric Properties from the Inversion of Planetary Occultation Data," *Planet. Space Sci.*, Vol. 16, pp. 1197-1198, 1968.

## References (contd)

9. Tatarskiy, V. I., "Determining Atmospheric Density from Satellite Phase and Refraction Angle Measurements," *Bull. Acad. Sci. USSR, Atmospheric and Oceanic Phys.*, Vol. 4, No. 7, 1968.
10. Tatarskiy, V. I., "The Accuracy Achievable in Determining Atmospheric Density from Satellite Phase and Refraction-Angle Measurement," *Bull. Acad. Sci. USSR, Atmospheric and Oceanic Phys.*, Vol. 4, No. 8, 1968.
11. Khvostikov, I. A., "A Method of Determining Refraction from Accurate Geodesic Measurements," *Proc. Acad. Sci. USSR*, Vol. 51, No. 5, 1946.
12. Rozenberg, G. V., "The Measurement of Atmospheric Refraction," *Bull. Acad. Sci. USSR, Geog. and Geophys. Ser.*, Vol. 13, No. 5, 1949.
13. Werbowetzki, A., "Refraction Data with Multiple Satellites," *Bull. Amer. Met. Soc.*, Vol. 47, No. 3, Mar. 1966.
14. SPINMAP, *Stanford Proposal for an International Network for Meteorological Analyses and Prediction*, Final Report. Stanford University, Stanford, Calif., June 1966.
15. *Proposal to NASA for a Microwave Occultation Experiment on the Nimbus E Meteorological Satellite*, RL 5-68. Stanford University, Stanford Electronics Laboratories, Stanford, Calif., Feb. 29, 1968.
16. Sargeant, D. H., "Ray Analysis of the Refraction of Microwaves Propagated Between Satellites in a Spherically Stratified Atmosphere," Chapter 6 in *Studies in Atmospheric Energetics Based on Aerospace Probing*, Annual Report-1967. Department of Meteorology, University of Wisconsin, Madison, Wis., May 1968.
17. Graves, M. E., and Fischbach, F. F., *Analysis of Microwave Occultation Techniques for Atmospheric Soundings*, High Altitude Engineering Laboratory Report 05863-16-T. University of Michigan, Ann Arbor, Mich., Jan. 1969.
18. *Electromagnetic Probing of the Martian Ionosphere and Atmosphere from an Orbiting Pair*, Final Report on Contract NAS 8-21222, R67-4537. Raytheon Co., Sudbury, Mass., Dec. 19, 1967.
19. Harrington, J. W., and Grossi, M. D., "Global Probing of the Earth's Atmosphere and Ionosphere by a Satellite-to-Satellite Radio Occultation Method," AMS 3rd National Conference on Aerospace Meteorology, New Orleans, May 1968.



# Profile Inversion Processing of Radio Occultation Data for the Determination of Planetary Atmospheres\*

I. Shear, R. R. Bravoco, and P. E. Langevin

Raytheon Company  
Sudbury, Massachusetts

M. D. Grossi

Raytheon Company  
Sudbury, Massachusetts

and

Smithsonian Astrophysical Observatory  
Cambridge, Massachusetts

*A comparative study is presented of various data processing methods applicable to the doppler residuals obtained from radio occultation experiments. The aim of the processing is to construct radial refractivity profiles of a planet's atmosphere and ionosphere along several verticals distributed around the planet. Some of the techniques are methods which use the Abel transform, the model matching, the Herglotz-Wiechert and the Gerver-Markushevich approaches. Emphasis is placed on the problem areas of implementing these methods on a high-speed digital computer, on the possible solutions, and on the evaluation of the computer execution time. An initial analysis is also provided of the expected accuracies of these methods. A brief description of the Hamiltonian ray-tracing program used is also presented.*

## I. Introduction and Summary

A comparative study was made of various data processing methods applicable to the doppler residuals obtained from radio occultation experiments. The aim of the processing was to construct radial refractivity profiles of a planet's atmosphere along several verticals distributed around the planet.

Some of the techniques taken into consideration are based on the Abel transform, the model-matching, the Herglotz-Wiechert, and the Gerver-Markushevich methods. The study has concentrated on the first two methods. It has initiated the evaluation of the last two, widely used in seismology, by identifying the problem areas associated with their use in radio occultation measurements.

The comparison criteria were the ease of implementation, the accuracy, and the machine time requirements.

---

\*The research activity here reported was partially sponsored by the National Aeronautics and Space Administration under Contract NASW-1772.

A ray-tracing computer simulation of a radio occultation experiment with models of the Martian and Venusian atmospheres was performed to generate electromagnetic ray paths between two satellites orbiting outside the planet's atmosphere. Corresponding phase delays were calculated and then used to test the two inversion techniques mentioned above. This same ray-tracing program was also used in conjunction with those inversion methods which required iterative procedures. The study concentrated on the profile inversion of the atmosphere of the two planets, since the inversion for the ionosphere is straightforward.

## II. Atmospheric Models

For the atmosphere of Mars, the model adopted was that presented in Fig. 1. For Venus, we constructed the model depicted in Fig. 2. These models were derived from data published in the existing literature (Refs. 1

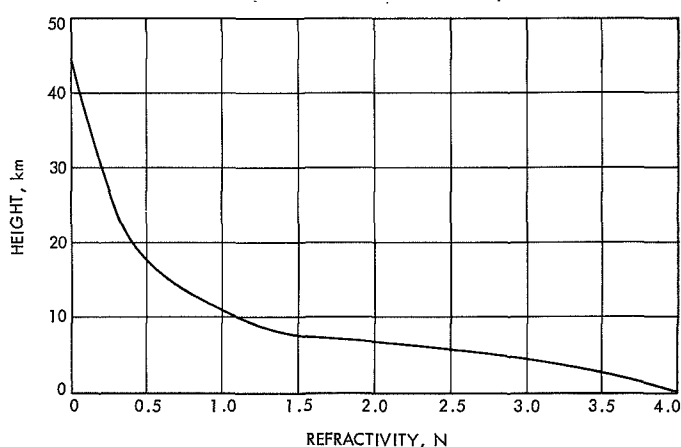


Fig. 1. Refractivity vs altitude for the Martian atmosphere

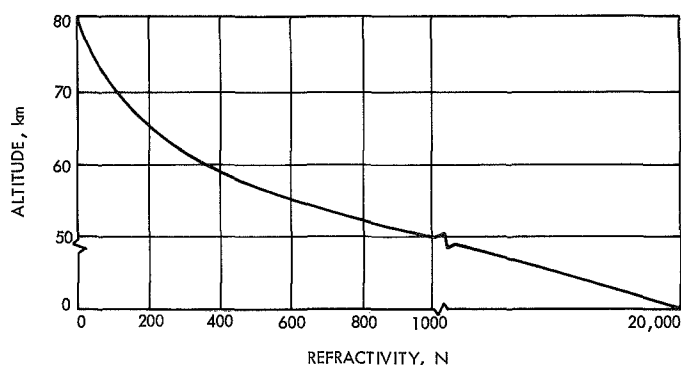


Fig. 2. Refractivity vs altitude for the Venus atmosphere

to 6). The curve shown in Fig. 1 can be approximated by an exponential decay function. For Venus, the data pertaining to the lower atmosphere was too sparse to be fitted meaningfully. Therefore, in Fig. 2 we adopted below 50 km an exponentially decaying model with 20,000  $N$ -units at the base. The refractivity 20,000  $N$ -units is consistent with the assumption that the Venus atmosphere contains solely carbon dioxide. That portion of the Venus model above 50 km is based on data given in Ref. 6.

## III. Simulation of the Occultation Experiment and Construction of Columnar Phase Delay Data

Each of the above models was then inserted into Raytheon's Hamiltonian ray-tracing computer program (Ref. 7). The Raytheon ray-tracing program utilizes Haselgrove's form of the Hamiltonian optic equations. A fourth-order Adams-Moulton integration technique with a Runge-Kutta starter (Ref. 8) was used to integrate the Haselgrove system of partial differential equations. Inputs to the computer program are the initial ray position and direction of the wave normal.

Figure 3 contains a simplified block diagram of the simulation. For the purpose of this simulation it was assumed that the region above the planetary atmosphere limits (i.e., 45 km for Mars and 80 km for Venus) has the refractive index of 1.0 (free space). The transmitter was positioned above the planet's atmosphere, and the directions of the wave normal were selected so that the geometric point of closest approach was within a column

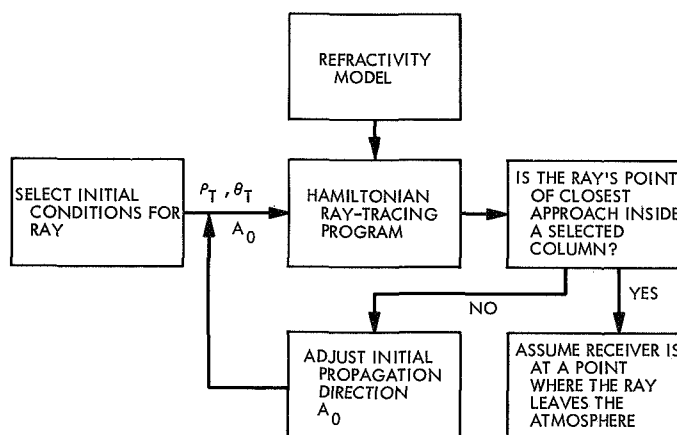


Fig. 3. Diagram for generating phase delays within a column



about the vertical of interest. Transmitter heights of 1000 km and a columnar width of 2 deg were used. The differential phase data generated in this way is used in the same manner as noise-free observational data.

#### IV. Profile Inversion

The differential phase data along a vertical having been generated, the next step was to examine existing profile inversion methods to see how well one can recover the postulated refractivity models of Mars and Venus shown in Figs. 1 and 2. Two profile inversion methods were implemented on a high-speed digital computer—the Abel transform (see Ref. 9) and the Raytheon model-matching techniques. The computer used was the CDC-6600, which is a 60-bit word-length computer.

##### A. Abel Transform

The first profile inversion method considered is the one which makes use of the Abel transform to solve the integral equation that describes the differential phase delay as a function of refractivity and the ray path length. Differential phase delay is defined by the following equation:

$$\Delta\phi(\rho) = \frac{f}{3 \times 10^5} \int_{-\infty}^{\infty} N(r) ds \quad (1)$$

where

$f$  = frequency, MHz

$r$  = distance from the planet's center to a point on the ray path, km

$s$  = ray-path length, km

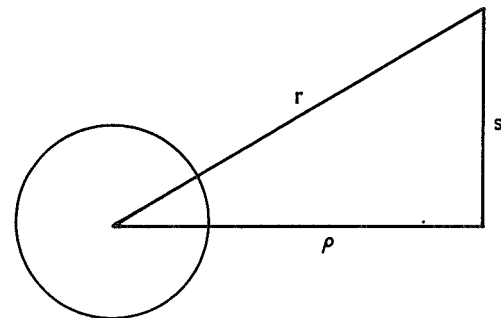
$\rho$  = distance from the planet's center to the point of closest approach, km

$N(r)$  = refractivity in  $N$ -units at a distance  $r$

$\Delta\phi(\rho)$  = differential phase delay in cycles at a distance  $\rho$

Assuming a straight-line ray path, one can apply a transformation which reduces the above to a form that

allows one to apply the Abel transform. The transformation is given as follows:



$$s = (r^2 - \rho^2)^{1/2}$$

$$ds = \frac{r dr}{(r^2 - \rho^2)^{1/2}}$$

The solution to Eq. (1) is

$$N(r) = \frac{-3 \times 10^5}{\pi f r^2} \int_r^{\infty} \frac{\rho \Delta\phi(\rho) + \rho^2 \frac{d}{d\rho} [\Delta\phi(\rho)]}{(\rho^2 - r^2)^{1/2}} d\rho \quad (2)$$

For computational purposes a numerical approximation to Eq. (2) was implemented on the computer. The approximation is based on a linear interpolation between consecutive data points. The equation that was programmed is

$$N(r) =$$

$$C \left\{ A_{m-1,1} \left[ r_m S_m + r^2 \log_e \frac{r_m + S_m}{r} \right] + A_{m-1,2} S_m \right. \\ \left. + \sum_{i=m}^n \left[ A_{i,1} \left( r_{i+1} S_{i+1} - r_i S_i + r^2 \log_e \frac{r_{i+1} + S_{i+1}}{r_i + S_i} \right) \right. \right. \\ \left. \left. + A_{i,2} (S_{i+1} - S_i) \right] \right\} \quad r_{m-1} < r < r_m \quad (3)$$

where

$$A_{i,1} = \frac{\Delta\phi_{i+1} - \Delta\phi_i}{r_{i+1} - r_i}$$

$$A_{i,2} = \Delta\phi_i - r_i A_{i,1}$$

$$\Delta\phi_i = \Delta\phi(\rho_i)$$

$$S_i = (r_i^2 - r^2)^{1/2}$$

$$C = \frac{3 \times 10^5}{\pi f r^2}$$

It can be seen that the above is a closed-form expression which yields refractivity as a function of geocentric distance along a single vertical.

Tables 1 and 2 give a comparison between the postulated and recovered profiles for both Mars and Venus. Note that the first column presents the distance from the center of the planet to the point of "closest" approach as determined by the straight-line approximation mentioned earlier. Since the radius of Venus is about 6055 km, it can be seen from Table 2 that this approximation yields points of "closest" approach below the planet's surface. In reality, all those rays traced that had an actual point of closest approach less than 35 km above Venus hit the planet surface. Therefore, all of the actual points of closest approach were at least 35 km above the planet surface.

Table 1 shows that the Abel transform inversion method reproduces the Mars atmosphere to a high

**Table 1. Mars inversion errors due to Abel transform<sup>a</sup>**

Geocentric radius, km	Differential phase delay, cycles	Refractivity	Refractivity calculated	Refractivity difference	Percent difference
3381.1895177	0.00183463	3.9815000	3.9848104	3.3103864E-03	0.083
3382.0864357	0.00168499	3.7285000	3.7183553	-1.0144707E-02	0.272
3383.8788342	0.00140280	3.2230000	3.2087263	-1.4273740E-02	0.443
3385.6701672	0.00114513	2.7185000	2.6984350	-2.0065039E-02	0.738
3387.4610393	0.00091502	2.2145000	2.1866252	-2.7874785E-02	1.259
3389.2525672	0.00071714	1.7113000	1.6683359	-4.2964082E-02	2.511
3391.0496801	0.00056113	1.2088900	1.1348640	-7.4026029E-02	6.123
3392.8537003	0.00047651	0.9431000	0.9372781	-5.8218820E-03	0.617
3394.6209022	0.00041345	0.8350300	0.8292865	-5.7435106E-03	0.688
3396.3854128	0.00035634	0.7336000	0.7279366	-5.6633779E-03	0.772
3398.1472618	0.00030503	0.6388000	0.6332063	-5.5936541E-03	0.876
3399.9064504	0.00025938	0.5506000	0.5450260	-5.5739584E-03	1.012
3401.6630207	0.00021931	0.4689800	0.4632880	-5.6919788E-03	1.214
3403.4170596	0.00018482	0.3938900	0.3876757	-6.2143216E-03	1.578
3405.1689367	0.00015622	0.3253000	0.3170987	-8.2013143E-03	2.521
3406.9183445	0.00013538	0.2813000	0.2806372	-6.6278034E-04	0.236
3408.6618662	0.00011727	0.2556000	0.2549271	-6.7285230E-04	0.263
3410.4028267	0.00010008	0.2299300	0.2292660	-6.6397611E-04	0.289
3412.1412032	0.00008383	0.2042900	0.2036596	-6.3035870E-04	0.309
3413.8770172	0.00006860	0.1787000	0.1781243	-5.7569006E-04	0.322
3415.6102821	0.00005443	0.1531000	0.1526931	-4.0688224E-04	0.266
3417.3409864	0.00004142	0.1276000	0.1274521	-1.4787799E-04	0.116
3419.0691701	0.00002966	0.1021400	0.1027051	5.6505700E-04	0.553
3420.7948765	0.00001931	0.0767000	0.0828424	6.1424411E-03	8.008

<sup>a</sup>Propagation frequency = 5000.00000 MHz.

**Table 2. Venus inversion errors due to Abel transform<sup>a</sup>**

Geocentric radius, km	Differential phase delay, cycles	Refractivity	Refractivity calculated	Refractivity difference	Percent difference
5984.7417000	4.17665700	839.3700000	2688.8589000	0.1849489+04	220.343
6002.7479000	3.17700570	698.2400000	2176.4756000	0.1478236+04	211.709
6021.7684000	2.27042800	569.1099900	1680.2465000	0.1111137+04	195.241
6039.7306000	1.55666490	457.3000000	1256.4901000	0.7991901+03	174.763
6055.5384000	1.04348840	363.9500000	922.7180900	0.5587681+03	153.529
6069.0452000	0.68986960	287.5000000	669.4908700	0.3819909+03	132.866
6080.3473000	0.45352630	225.7200000	482.7088300	0.2569888+03	113.853
6089.7420000	0.29767040	176.2000000	346.8264300	0.1706264+03	96.837
6097.5917000	0.19490972	136.7500000	248.0363600	0.1112864+03	81.379
6104.1534000	0.12758370	105.4999990	176.7688200	0.7126883+02	67.553
6109.6536000	0.08364145	80.8700000	125.7172550	0.4484726+02	55.456
6114.3079000	0.05484935	61.5600000	89.0710740	0.2751108+02	44.690
6118.2696000	0.03602615	46.5300000	62.9494420	0.1641944+02	35.288
6121.6753000	0.02368468	34.9000000	44.3704290	0.9470430+01	27.136
6124.6408000	0.01554380	25.9700000	31.1196720	0.5149673+01	19.829
6127.2488000	0.01017117	19.1500000	21.7333170	0.2583317+01	13.490
6129.5777000	0.00659668	14.0099999	15.0672804	0.1057280+01	7.547
6131.6857000	0.00420470	10.1500000	10.3351580	0.1851580-00	1.824
6133.6231000	0.00258800	7.2899999	6.9469541	-0.3430459-00	4.706
6135.4297000	0.00148500	5.1900000	4.5035088	-0.6864912-00	13.227
6137.1410000	0.00071300	3.6580000	2.6513239	-0.1006676+01	27.520
6138.7968000	0.00013000	2.5500000	0.0525477	-0.2497452+01	97.939
6339.7387000	0.00000000	0.0000000	0.0000000	0.0000000	0.000

<sup>a</sup>Propagation frequency = 5000.00000 MHz.

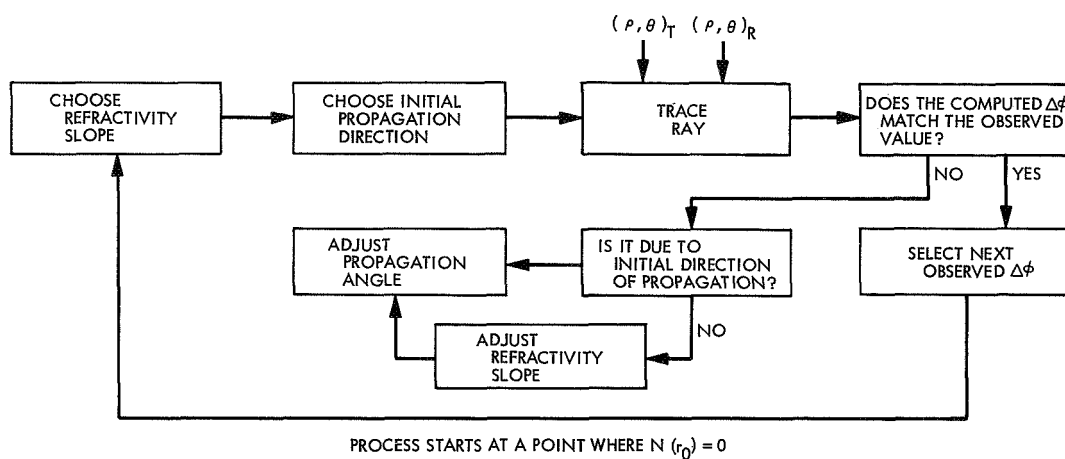
degree of accuracy. Errors in refraction are less than 6.1%, the largest error being 0.074 *N*-units. Applying the Abel transform technique to the atmosphere of Venus gives very poor results (see Table 2). The errors get large very soon after the planet's atmosphere is entered and continue to increase to 1850 *N*-units at an altitude of 35 km above the planet Venus.

## B. Model-Matching

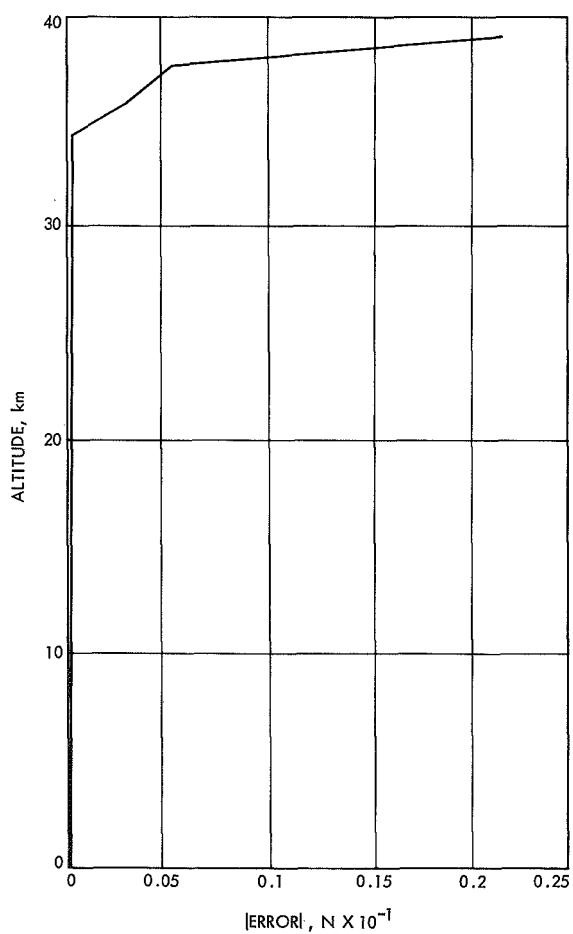
The Raytheon model-matching method is an iterative technique which dynamically adjusts the refractivity model and initial conditions on the ray until the calculated differential phase matches the "observed" value. We start the iteration by selecting a point above the planet's atmosphere (i.e., a point in free space, index of refraction equal to 1), a refractivity slope to the next point, and an initial direction of the wave normal (see

Fig. 4). If the calculated differential phase matches the "observed" value, then it is assumed that the proper slope has been found. Whenever the calculated differential phase differs from the observed, it becomes necessary to adjust the slope of the refractivity curve and/or to alter the initial direction of the wave normal. Unfortunately, this process does not yield unique results. There is more than one combination of refractivity slope and ray direction that will yield the desired differential phase.

In relation to Mars, the ambiguity did not affect the results to a noticeable degree. In the reconstruction of the Venus profile, the ambiguity problem was very severe. Figures 5 and 6 indicate the inversion accuracies achieved by the Raytheon model-matching program. These are graphs of the absolute value of inversion error in *N*-units as a function of altitude for both Mars and Venus. Referring to Fig. 5, one can see that after two



**Fig. 4. Model-matching procedure**



**Fig. 5. Mars data inversion errors obtained by model-matching**

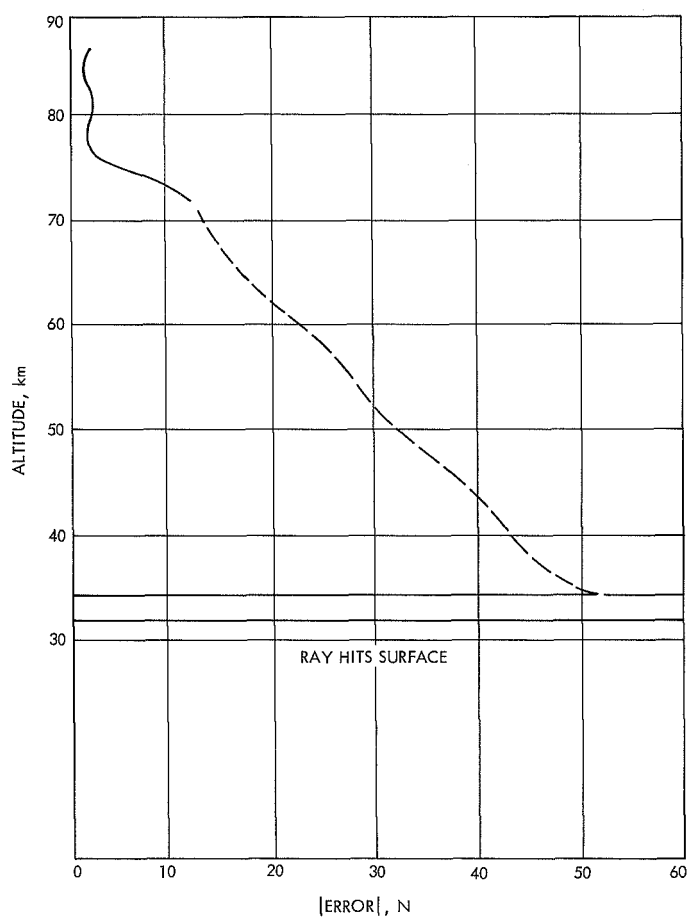


**Fig. 6. Venus data inversion errors obtained by model-matching**

data points the error in the reconstructed Mars profile is essentially zero. Errors less than 0.001  $N$ -units are due to computational noise rather than the inversion technique. Figure 6 shows an entirely different result obtained when the model-matching method is used in conjunction with Venus differential phase data. We were able to get solutions for altitudes of 70 km or more with relative ease. Below 70 km the ambiguity problem became rather severe; computer costs started climbing exponentially, and the computational accuracy requirements on the ray-tracing procedure was so great that it became apparent that we needed a double-precision ray-tracing computer program. At the time of this study we did not have such a program. As it was, a CDC-6600 computer was used. This computer has a word length of 60 bits, which is equivalent to an accuracy of 14 significant digits. Because of the extreme costs, attempts to accurately construct the error curve below 70 km were abandoned. The broken line below 70 km represents a judicious extrapolation based on a limited number of computer runs. All attempts to trace rays which had a point of closest approach less than 35 km failed. We could not find a set of initial conditions that were within the single precision accuracy of the CDC-6600 that would not hit the surface of Venus.

## V. Error Analysis

Most of the errors in the inverted profile were due to one or more of the following:

- (1) Straight-line approximation of the point of closest approach.
- (2) Numerical approximations.
- (3) Lack of a unique solution.

Items (1) and (2) above are the major sources of error inherent in the Abel transform method. In reality, the point of closest approach is now known, and since it is an essential input to the Abel transform it must be estimated. The estimation is done by connecting the transmitting and receiving satellite positions by a straight line and geometrically calculating the distance between the center of the planet and this line (see Fig. 7). In reconstructing the Mars atmosphere, the geometric approximation was very good because of the small amount of bending experienced by the ray as it passes through the planet's atmosphere. A radio ray passing through the

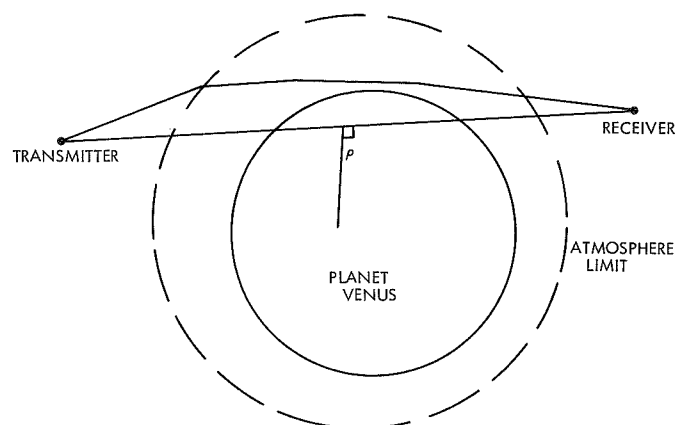


Fig. 7. Geometric approximation to the point of closest approach

Venus atmosphere is severely bent. Because of this bending, the straight-line approximation of the point of closest approach is a poor one. Therefore, it is possible to calculate a point of closest approach which lies below the planet surface (see Fig. 7). The errors due to the numerical approximations inherent in Eq. (3) are insignificant when compared to the errors which result from not knowing the point of closest approach.

As mentioned earlier, the major source of error in the model-matching method is that it does not yield a unique solution. An incorrect refractivity slope affects the next refractivity slope that is computed. This method builds error upon error as one proceeds down the vertical.

## VI. Machine Time Costs

Table 3 contains a summary of computer costs and accuracy in the recovered profile for each of the two profile inversion methods discussed. The rms errors are computed by the following formula:

$$\text{rms} = \left[ \frac{1}{S} \sum_{i=1}^S (N_{c_i} - N_i)^2 \right]^{1/2}$$

where

$N_c$  = recovered refractivity

$N$  = postulated refractivity

$S$  = number of points on the profile

**Table 3. Comparison between Abel transform and model-matching inversion techniques**

Technique	Error, rms		Computer cost, dollars	
	Mars	Venus	Mars	Venus
Abel transform	0.01988	591.72	1.00 (24 pts)	1.00 (23 pts)
Model-matching	0.02215	10.0 <sup>a</sup>	1500.00	7500.00 <sup>a</sup>

<sup>a</sup>Approximation done by extrapolating down to the base.

Overall accuracies achieved in reconstructing the Mars profile are very good for either method. The model-matching method is slightly more inaccurate than the Abel transform method. This is because the Abel transform solution is unique, while the model-matching solution is ambiguous. When one tries to reconstruct the Venus atmosphere, either method gives poor results. Computer costs shown above are based on the CDC-6600 digital computer. The recovered profile consisted of 24 points along a vertical. Computer charges in connection with the Abel transform are insignificant. The cost of \$1.00 shown in the table is mainly due to loading the program into the computer and printing the results. Cost for reconstructing the Mars profile when using the model-matching technique was approximately \$1500. As a result, the model-matching method when used to invert the Mars atmosphere is much more costly and less accurate than the Abel transform method. Comparing the two methods under consideration for reconstructing the Venus atmosphere, one can see that the cost is astronomical; the Abel transform method costs are about the same as those incurred when using Mars data. A computer charge of \$3500 was incurred in recovering that portion of the Venus profile that is above 70 km. The further one proceeded down the vertical, the longer it took for the iteration to converge. To recover the Venus profile down to an altitude of 35 km would cost somewhere between \$7500 and \$10,000.

## VII. Profile Inversion Methods Used in Seismology

Seismologists use profile inversion methods in order to determine velocity-depth profiles in the earth from the observed variation of travel time with arc distance between source and receiver. The analogy with the radio occultation measurements of planetary atmospheres is close. Phinney and Anderson (Ref. 10) have examined the

applicability of the Herglotz-Wiechert method (Refs. 11 and 12) to the planetary atmosphere case and have concluded that the "impact parameter" that is the fundamental quantity used by seismologists in profile inversion can be expressed in terms of doppler data.

Graves and Fischbach (Ref. 13) have cast doubts on this conclusion by Phinney and Anderson. The entire matter requires a close review if an attempt to use seismological methods in radio occultation experiments is to be made.

In case of success, the Keilis-Borok<sup>1</sup> and the Gerver-Markushevich (Refs. 14, 15, and 16) approaches will also become usable, as well as the better-known Herglotz-Wiechert method.

## VIII. Future Plans

In the future we intend to look into techniques other than the Abel transform and the model-matching methods. Also, we will examine the feasibility in combining the Abel transform method with the model-matching method in order to reduce costs and increase the accuracy in recovering the Venus atmosphere. Figure 8 is a flow diagram describing many possible research paths one can take in order to evolve a technique for recovering the Venus atmosphere. One such path is to use the Abel transform method to generate a first approximation of the desired atmosphere and then to use the model-matching method to refine the initial guess. Hopefully, this will reduce the cost and eliminate the ambiguity problem. Up to now no initial guess of the atmosphere is used in the iterative procedure.

We also plan to look into the possibility of using some of the seismological methods indicated in Section VII. In order to use these methods, one must know the "impact parameter." This parameter, like the point of closest approach, can be estimated, and it is quite possible that the errors in estimating it are smaller than the errors in estimating the point of closest approach. Should this turn out to be the case, the seismological methods will be of great help in the inversion of atmospheric profiles where the ray is strongly bent, causing the Abel transform to fail and increasing the cost of model-matching.

<sup>1</sup>"Profile Inversion Algorithms Used in Seismology." MIT Geophysics Department lecture, Jan. 21, 1965.

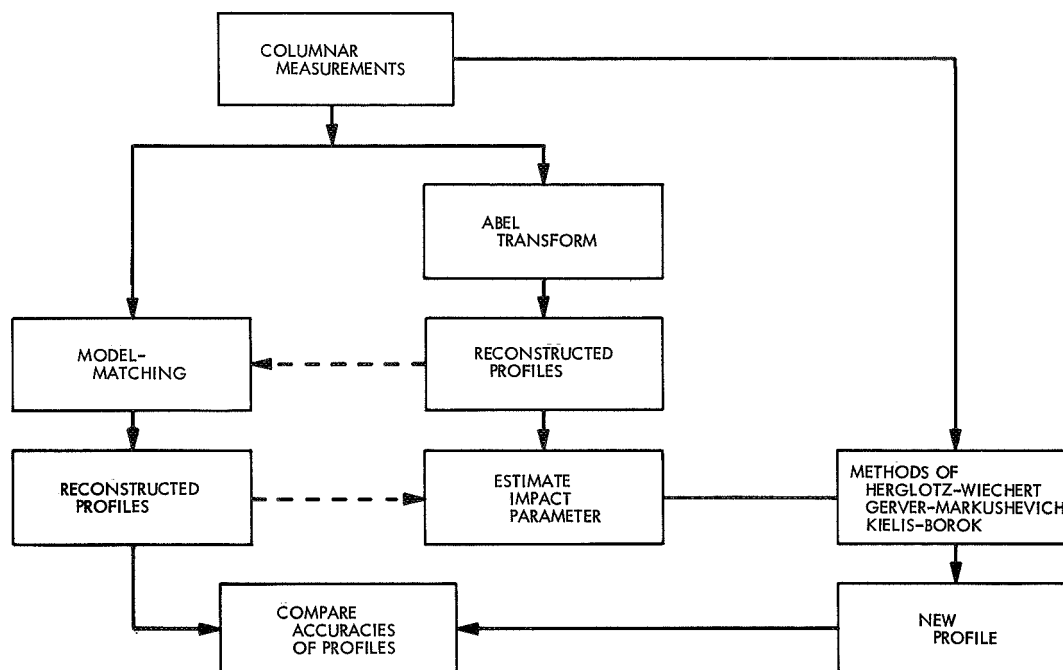


**Fig. 8. Atmosphere recovery methodology**

## References

1. Fjeldbo, G., "Radio Occultation Measurements of Planetary Atmospheres and Planetary Surface Topography," Paper 67-119, presented at the AIAA 5th Aerospace Science Meeting, New York, Jan. 23-26, 1967.
2. Fjeldbo, G., Fjeldbo, W. C., and Eshleman, V. R., "The Atmosphere of Mars: Mariner IV Models Compared," *Science*, Vol. 153, pp. 1518-1523, 1966.
3. Kliore, A., Tito, D. A., Cain, D. L., and Levy, G. S., "A Radio Occultation Experiment to Probe the Atmosphere of Venus," AIAA 5th Aerospace Science Meeting, New York, Jan. 23-26, 1967.
4. Kliore, A., Cain, D. L., and Hamilton, T. W., *Determination of Some Physical Properties of the Atmosphere of Mars from Changes in the Doppler Signal of the Spacecraft on an Earth-Occultation Trajectory*, Technical Report 32-674. Jet Propulsion Laboratory, Pasadena, Calif., Oct. 15, 1964.
5. Mariner Stanford Group, "Venus: Ionosphere and Atmosphere as Measured by Dual-Frequency Radio Occultation of Mariner V," *Science*, Vol. 158, pp. 1678-1683, Dec. 29, 1967.
6. Kliore, A., Levy, G. S., Cain, D. L., Fjeldbo, G., and Rasool, S. I., "Atmosphere and Ionosphere of Venus from the Mariner V S-Band Radio Occultation Measurement," *Science*, Vol. 158, pp. 1683-1688, Dec. 29, 1967.

### References (contd)

7. Shear, I., Bravoco, R. R., and Simon, A., *Report on Applied Research Program in Electromagnetic Energy Ray Paths*, Part III, Report AFCRL-69-0078 (III). Air Force Cambridge Research Laboratories, Cambridge, Mass., Feb. 3, 1969.
8. Scarborough, J. B., *Numerical Mathematical Analysis*. Johns Hopkins University Press, Baltimore, Md., 1955.
9. *Electromagnetic Probing of the Martian Ionosphere and Atmosphere from an Orbiting Pair*, Report R67-4537. Raytheon Company, Sudbury, Mass., Dec. 19, 1967.
10. Phinney, R. A., and Anderson, D. L., "On the Radio Occultation Method for Studying Planetary Atmospheres," *J. Geophys. Res., Space Phys.*, Vol. 73, No. 5, pp. 1819-1827, Mar. 1, 1968.
11. Von Herglotz, G., "Über das Benndorfsche Problem der Fortpflanzungsgeschwindigkeit der Erdbebenstrahlen," *Phys. Z.*, Vol. 8, No. 5, pp. 145-147, 1907.
12. Von Wiechert, E., and Geiger, Ludwig, "Bestimmung des Weges der Erdbebenwellen im Erdinnern," *Phys. Z.*, Vol. 11, pp. 294-311, 1910.
13. Graves, M. E., and Fischbach, F. F., *Analysis of Microwave Occultation Techniques for Atmospheric Soundings*, Technical Report 05863-16-T, Contract NASr-54(03). University of Michigan, Ann Arbor, Mich., Jan. 1969.
14. Gerver, M. L., and Markushevich, V. M., *Determination of the Velocity of Propagation of Seismic Waves from the Travel-Time Curve* (in Russian), pp. 3-51, Order 2726, Doklady AN, USSR, 1965 (in Russian).
15. Gerver, M. L., and Markushevich, V. M., "Determination of a Seismic Wave Velocity from the Travel-Time Curve," *Geophys. J. R. Astro. Soc.*, Vol. 11, pp. 165-173, Sep. 1966.
16. Gerver, M. L., and Markushevich, V. M., "On the Characteristic Properties of Travel-Time Curves," *Geophys. J. R. Astr. Soc.*, Vol. 13, pp. 241-246, Jul. 1967.



# Inverting Radio Occultation Data Using Empirical Orthogonal Functions

Bruce Lusignan  
Center for Radio Astronomy  
Stanford University  
Stanford, California

*A study is presented of a method of describing the atmosphere by means of  
radio occultation data inversion.*

The use of empirical orthogonal functions has been found to be one of the most useful ways of parameterizing the atmosphere. Since these functions are derived from actual data of an atmospheric phenomenon, they have in their own nature the main characteristics of it. If we describe the temperature by a certain number of empirical orthogonal functions, then we need only one more parameter to describe completely the pressure profile, since they are related by the hydrostatic equation. That is, we could express the pressure and temperature profiles as follows:

$$T = \bar{T} + \sum_{n=1}^N c_n \Phi_n \quad (1)$$

where  $T$  is the average temperature taken over an adequate number of observations, the  $\Phi_n$  are the empirical

orthogonal functions, and the  $c_n$  are the coefficients to be determined from the occultation observations.

$$P = P_s e^{-K \int_0^h \frac{dr}{T^*}} \quad (2)$$

where  $P_s$  is the surface pressure,  $K$  is a constant, and  $T^*$  is the virtual temperature given by

$$T^* = \frac{T}{1 - \frac{3}{4} \times \text{specific humidity}}$$

Above 3 km,  $T^* \approx T$ , with an error rarely exceeding 0.6°K in temperate climates.

In order to study the performance of the occultation data in defining the pressure and temperature profiles, we have developed a set of empirical orthogonal functions for a particular situation. The data used consisted of 90 radiosonde profiles taken at Oakland, California, from July to August, 1966. For this particular set it was found that only two orthogonal functions for temperature were needed to match the temperature profiles with an rms error of less than  $2^{\circ}\text{K}$ .

To determine the pressure and temperature profiles from the occultation data, we have to correct for the water vapor effects. This can be done by measuring the atmospheric absorption in addition to the phase. At the occultation frequency, 5 GHz, the water vapor absorption is a small fraction of the total absorption. For this reason we use the fourth harmonic of this frequency, which is near to the 1.35-cm water vapor absorption line, to obtain the adequate sensitivity of water vapor.

Empirical orthogonal functions were also used to describe the water vapor profile. Two empirical orthogonal functions were found convenient to obtain the required accuracy in the water vapor determination.

Our inversion program uses an iterative procedure to estimate the atmospheric parameter. It starts with a guess of what the parameters may be and then converges to the values which minimize the mean square error obtained by subtracting the measured phase and absorption minus the calculated phase and absorption.

The example illustrated by Figs. 1 to 4 is the case of August 16, 1966, at 12:00 GMT. At this date the water vapor content was the maximum in our set of data.

Five satellites were used at nominal heights of 4, 6, 9, 12, and 15 km. Figures 1 and 2 show the initial guess. Dotted curves represent the true profiles; continuous curves represent the estimated profiles for the climatological average for the season. For the pressure, the difference between the estimated and the true profile is used. Figures 3 and 4 show the situation after three iterations. (In Fig. 4, the lowest satellite ray path is above 4 km, which leads to the poor match below that altitude.) The maximum deviation of temperature was  $2.3^{\circ}\text{K}$  at 12 km, and the deviation of pressure at 4 km was 1.7 mbar, which is within the expected performance of the system and clearly shows the capacity of the occultation data to describe the atmosphere.

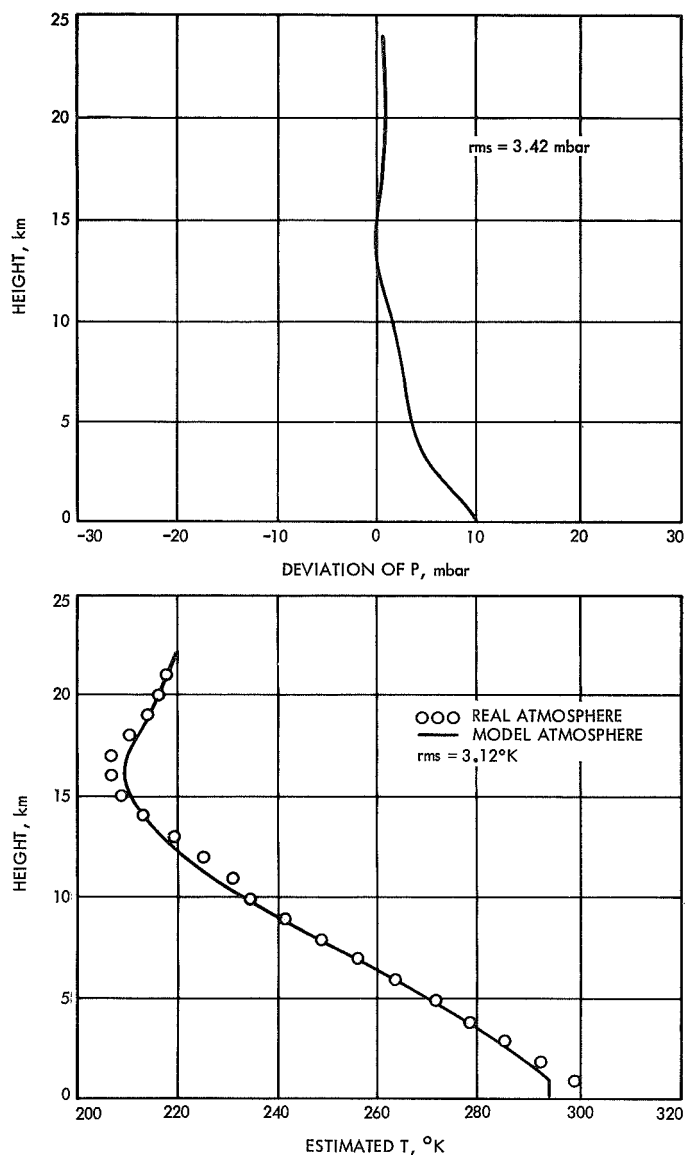


Fig. 1. Initial match between real and model atmospheres

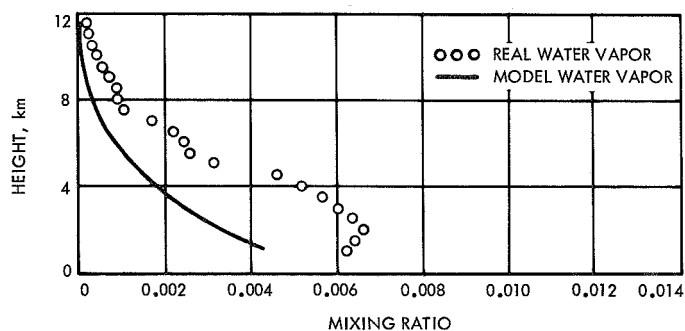
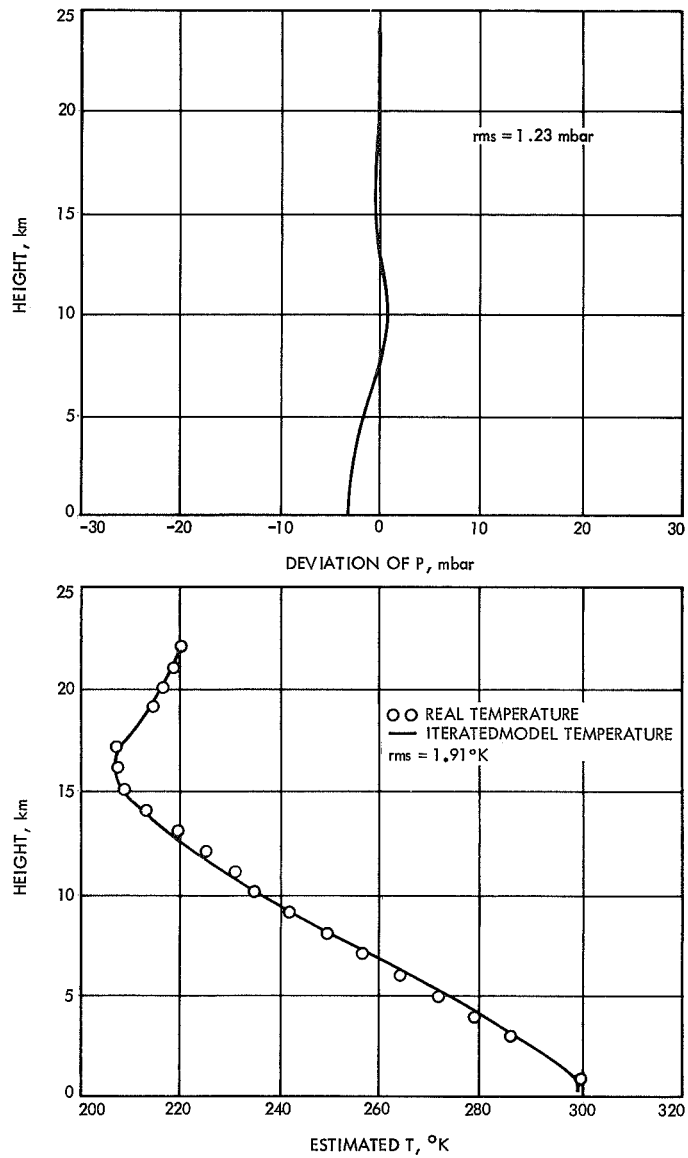
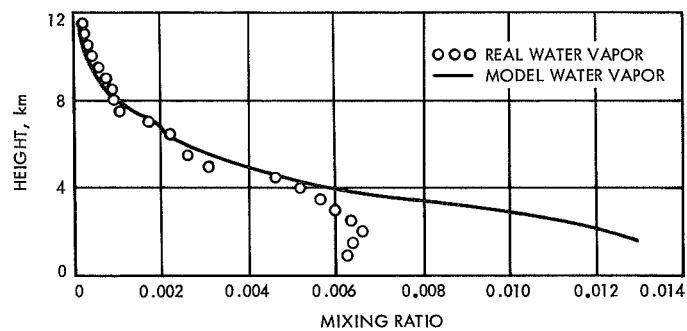


Fig. 2. Initial match between real and model water vapor mixing ratios



**Fig. 3. Third iteration match between real and model atmospheres**



**Fig. 4. Third iteration match between real and model water vapor**



# Some Characteristics of the Solar Atmosphere That May Be Investigated by a VHF Antenna System

Jesse C. James  
Massachusetts Institute of Technology  
Center for Space Research  
Solar Radar Station  
El Campo, Texas

*A series of experiments to furnish information about the sun's corona by means of an earth-based facility is outlined. These experiments are an economical way to obtain a better understanding of the properties of the solar corona to 1 AU. The particular facility considered is the proposed Sunblazer antenna array, which will operate in the frequency range of 70 to 80 MHz and will transmit 1 MW of power.*

*The proposed experiments include a radar study of the sun at 75 MHz and a study of interplanetary plasma by using planets as reflectors of radio energy transmitted from the earth. Also, with the proposed system, radar studies of the sun and all planets out to Saturn should be possible.*

*Some recent results with the 38-MHz El Campo solar radar system are presented to emphasize the need for radar studies at 75 MHz. In particular, radar studies at 75 MHz should lead to a knowledge of the velocity and intensity of compressional waves that heat the corona. Radar waves at this frequency should penetrate the corona to the level of 1.15 solar radii.*

## I. Introduction

The Center for Space Research of the Massachusetts Institute of Technology has designed and plans to construct a large astronomical antenna array. This antenna will have a gain of 50 dB and will cover the frequency range from 70 to 80 MHz. The primary purpose of this array is to receive signals transmitted from Sunblazer spacecraft. This paper is not concerned with the prime

mission of Sunblazer, which is to measure coronal densities from 5 to 100 solar radii, but rather with other valuable experiments that may be performed with the antenna system.

The antenna consists of an array of half-wave dipoles, one-quarter wavelength above ground. Very near each dipole or small group of dipoles are amplifiers and phase

shifters, as indicated schematically in Fig. 1. The switches for phasing and for the transmit-receive operation are controlled remotely. The phase shifters consist of sections of coaxial cables which introduce the same time delay for all frequencies. These cables may be many wavelengths long to preserve the wide-band characteristics of the array. During the transmit period, an exciter signal is fed through the time-delay cables to a solid-state power amplifier of fixed gain and phase shift and then to the radiating element. In the receive mode, the signal from the antenna element is amplified by a low-noise amplifier and then fed through the same time-delay cables. As the signal flows to a central point, it encounters several sets of time-delay cables of various lengths as signal components from various segments of the array are combined. The effective noise figure of the receiver portion of this array is the mean noise figure of all the low-noise preamplifiers. The beam is oriented by adjustment of the switches associated with the time-delay cables. The soundness of most of the concepts and design details has been verified by pilot arrays at the El Campo station.

As indicated in Fig. 2, the array aperture is approximately circular. Figure 2 shows, in particular, the distribution of primary power for the power amplifiers. For minimum cost there is an optimum number of rectifying stations, and for 1,000,000 W of radiated power this optimum number is near 72.

## II. Experiments Involving Planets

A radar study of planets is one endeavor for which the system should be quite useful. The received echo signal-

to-noise ratios for various bodies are shown in Table 1 along with the assumptions required for the computations. Note that all planets out to and possibly including Saturn could be detected. Such a radar study could lead to information about the planets themselves, but perhaps of more importance is a study of the medium between the earth and the planet. In this case the planet would be used as a convenient reflector.

For the Sunblazer experiment, two radio pulses at frequencies of 70 and 80 MHz will be transmitted from the spacecraft, and the difference in propagation time will be measured in the received signal at earth. The plot in Fig. 3 shows the approximate delays expected. For the radar case, when a planet is used as a reflector, these delays will be doubled when the reflecting planet is on the far side of the sun. In order to allow detection of the time delays, the transmitted signals must be modulated in some way with a modulation period of the order of the delay, or less. This means that the receiver bandwidth must be made larger than the CW bandwidths of Table 1 in order to accommodate the modulation. Figure 4 shows the signal-to-noise ratios for the enlarged bandwidths when Mercury and Venus are used as reflectors. In Fig. 4, numbers in parentheses are the pulse lengths (in  $\mu$ s) required to measure the differences in group delays at 70 and 80 MHz; other numbers are the signal-to-noise ratios (in dB) after integration.

Because the planets Mercury and Venus continuously move around the sun, with synodic periods of 116 and 584 days respectively, the solar plasma density may be monitored continuously from the ground under various conditions of solar activity throughout the sunspot cycle.

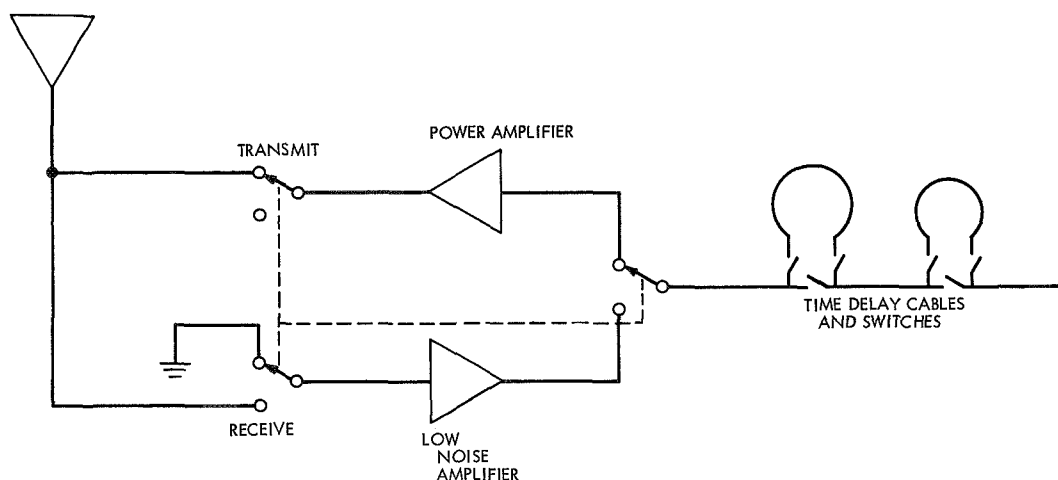
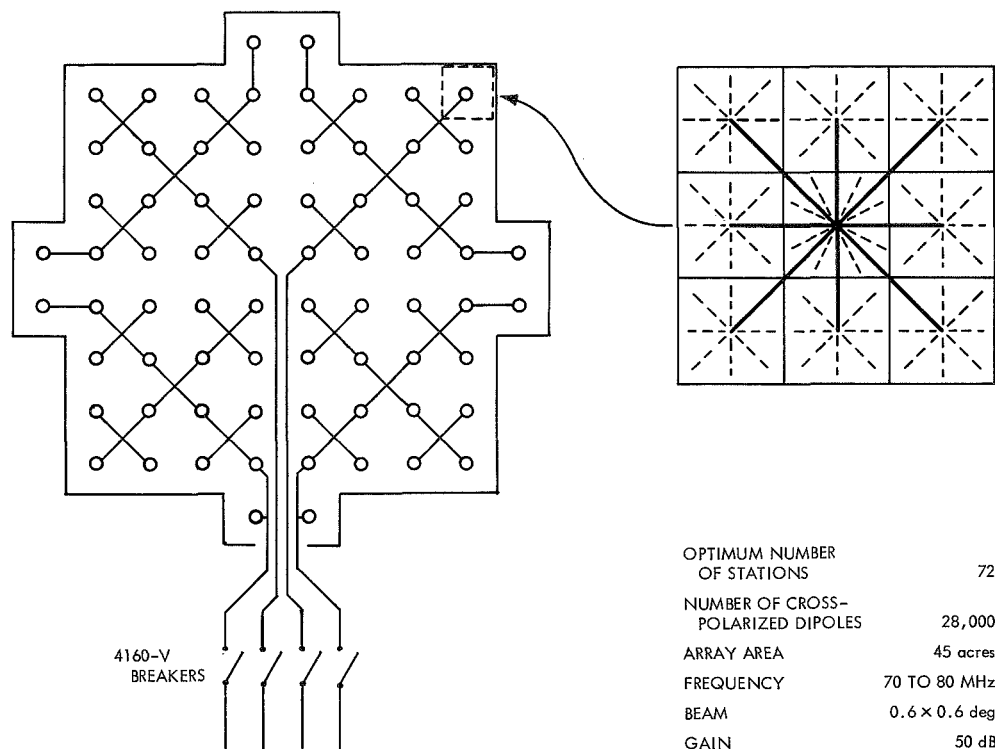


Fig. 1. Field electronics at each array element



**Fig. 2. Power distribution system for transmitting dipole array**

**Table 1. Predicted parameters for radar studies at 75 MHz with a 50-dB antenna and 1-MW transmitted power  
(Background noise temperature is assumed to be 6 dB/290°K)**

Body	Round-trip time, min		Reflectivity, %	Radar cross section, $10^{12} \text{ m}^2$	Received echo power, $10^{-20} \text{ W}$		Bandwidth, Hz	Signal-to-noise ratio, dB					
								No signal integration		5-min integration		Signal integra- tion for round- trip time	
	Min	Max			Min	Max		Min	Max	Min	Max	Min	Max
Mercury	10.0	23.3	6	1.10	68	2.3	2	13	-1.5	27	12	29	15
Venus	4.8	28.3	15	18.1	20600	17.4	2	38	7	52	21	52	23
Mars	6.1	43.2	7	2.54	1090	0.45	100	8	-25	31	-3	31	2
Jupiter	69.9	108.1	8	1290	33	5.7	100	-7	-14	15	8	21	15
Ganymede	69.9	108.1	10	1.92	0.05	0.009	2	-18	-26	-4	-12	2	-5
Saturn	142.1	175.4	10	1146	1.7	0.7	100	-20	-23	4	-1	10	7

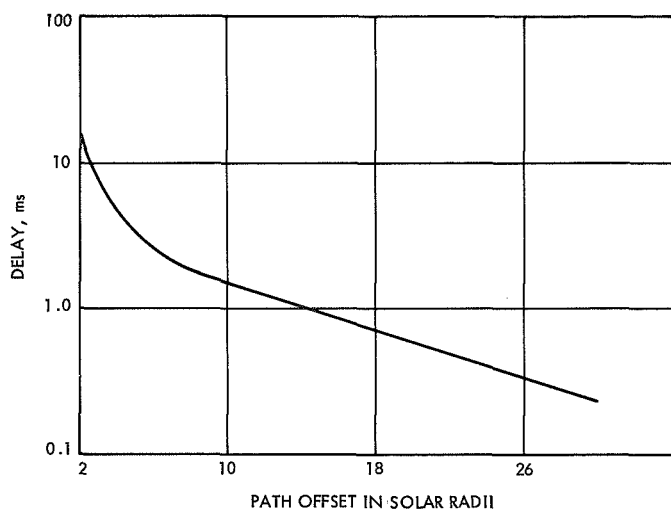


**Fig. 3. Computed differences in group delays of 70- and 80-MHz signals due to one-way propagation to earth from the far side of the sun**

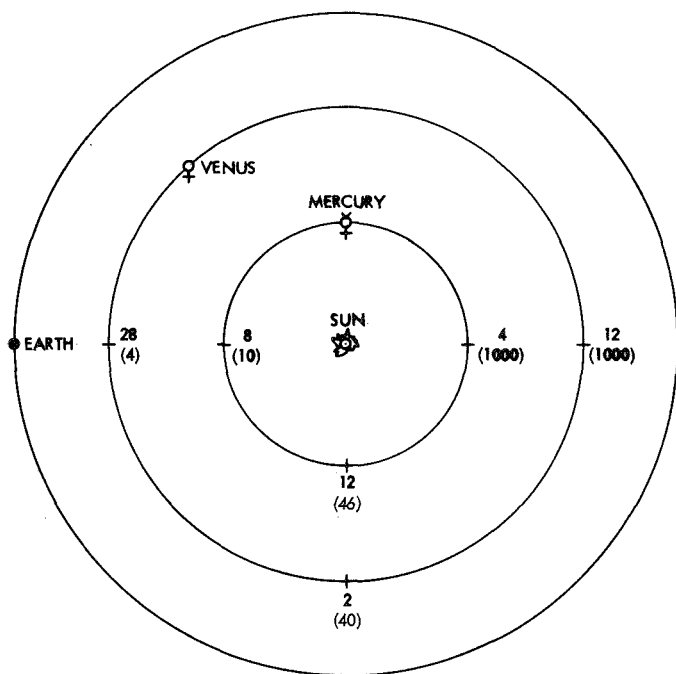


**Fig. 4. Radar signal strengths and pulse lengths for measurements of coronal plasma densities using planets as backscatterers**

The effect of the planets themselves on the echo may be determined after an initial period of study. A similar technique was used by Ingalls, James, and Stone (Ref. 1) to study transmission properties of auroral disturbances by using the moon as a reflector.

### III. Occultation Studies

Another set of experiments involves the occultation properties of the corona. Sources for such experiments may be pulsars, radio stars, backscattered energy from planets, or spacecraft transmissions. A measurement of the size of the occulting disk should lead to a knowledge of the coronal density. See James (Ref. 2) for computations of the occulting diameter for various conditions. The properties of the refracted signal near the point of occultation should indicate the degree of roughness and perhaps shock velocities in the corona. Figure 5 shows the computed amplifications of the refracted signal due to focusing effects near the point of occultation. The function is double-valued because there are a refracted and a reflected ray. At large angles the upper curve is unity and the lower curve approaches zero. Absorption is neglected. A smooth, symmetrical corona was assumed

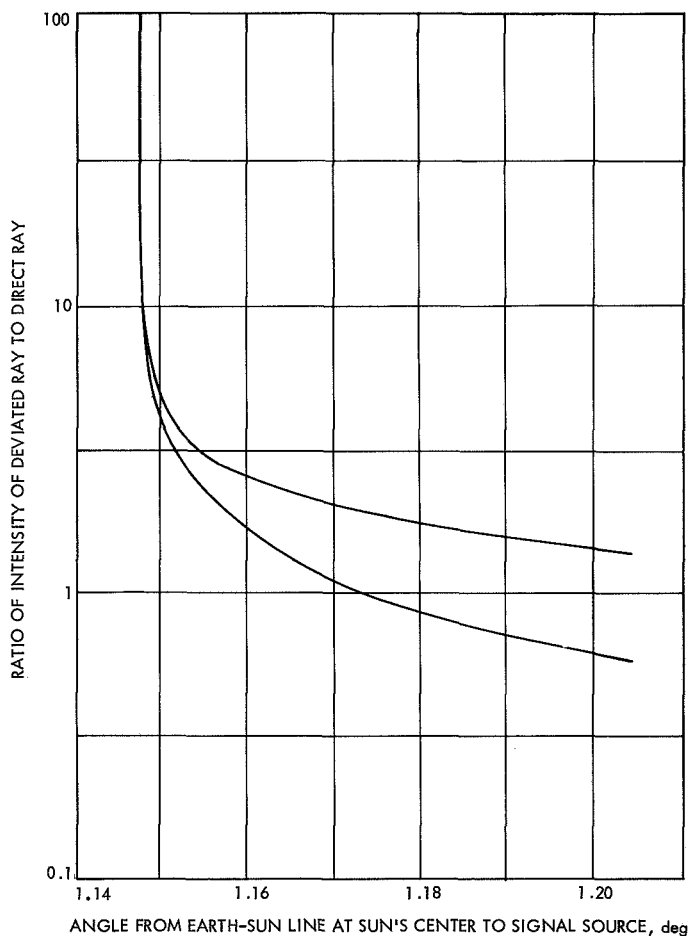


**Fig. 5. The effect of the corona in amplifying the intensity of a point source when it is near occultation for a Baumback-Allen model and for 75 MHz**



for these computations. Note that the source intensity is enhanced near the rim of the occulting zone.

The amount of the enhancement is one measure of roughness. Such enhancements have been observed at times during Crab nebula occultations. See, for example, Blum and Boischot (Ref. 3), Erickson (Ref. 4), and James (Ref. 2).

#### IV. Solar Radar Studies

The solar radar technique is one valuable method for studying the solar corona which has not yet been fully exploited. Figure 6 shows some echo spectra obtained with the 38-MHz system at El Campo, Texas. Note the large doppler spreading of the echo. A doppler shift of 1 KHz is equivalent to about 4 km/s of motion. The velocities reach sonic speeds for a 1,000,000-deg corona. This doppler spreading is attributed to some sort of compressional wave in the corona. Other known methods of

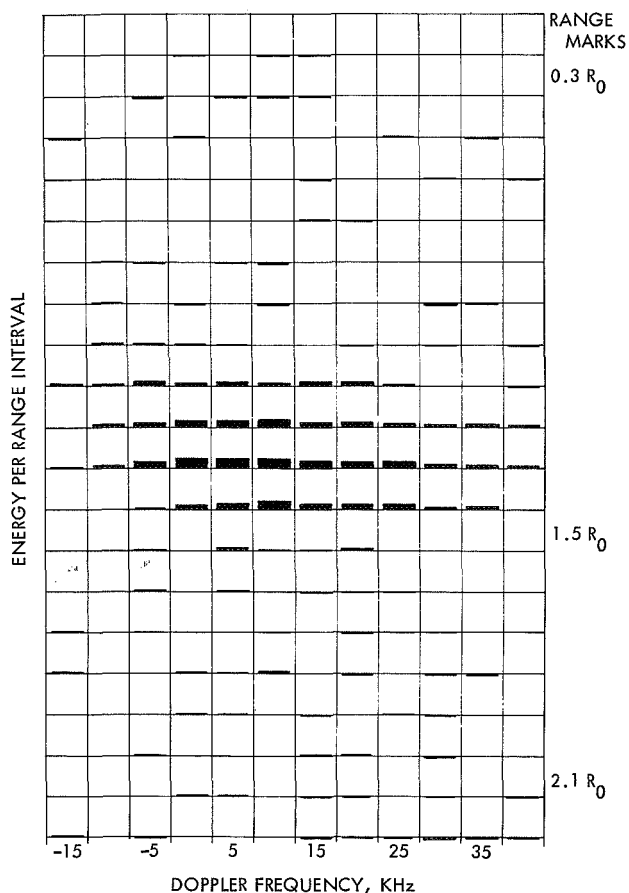


Fig. 6. A distribution of solar echo energy in range and doppler frequency as measured at 38 MHz

reflection either do not explain the experimental results or can be shown not to exist in the corona. Figure 7 shows schematically the reflection of the radar waves by shocks. A shock carries along a dense plasma region, which is a good reflector. When the shock is very intense, the radar wave is reflected from a higher level in the corona, and this results in less signal attenuation. Consequently, there should be a correlation between mean radar range and echo intensity. This sort of correlation is observed.

The variation of signal absorption with depth of penetration into the corona is shown in Fig. 8. Note that the absorption is greatest near the reflecting level for an assumed undisturbed corona. Consequently, when shocks are present, the echo signal is more intense because the wave is reflected above the normal level. The absorption is also a strong function of coronal temperature. See James (Ref. 5) for plots of attenuation vs temperature.

At 75 MHz the echo signal intensity will be a stronger function of shock intensity than at 38 MHz because the absorption near the undisturbed plasma level is greater. This effect is so great that a measurement of radar cross section at 75 MHz will essentially be a measure of shock front intensity. If the shocks are 0.1 to 0.2 solar radii apart, as the 38-MHz data suggests, it may be possible to track individual shocks at 75 MHz.

At 38 MHz the cross section was somewhat larger during times of flare activity. On the average, flares that occurred a few hours prior to the time of the radar

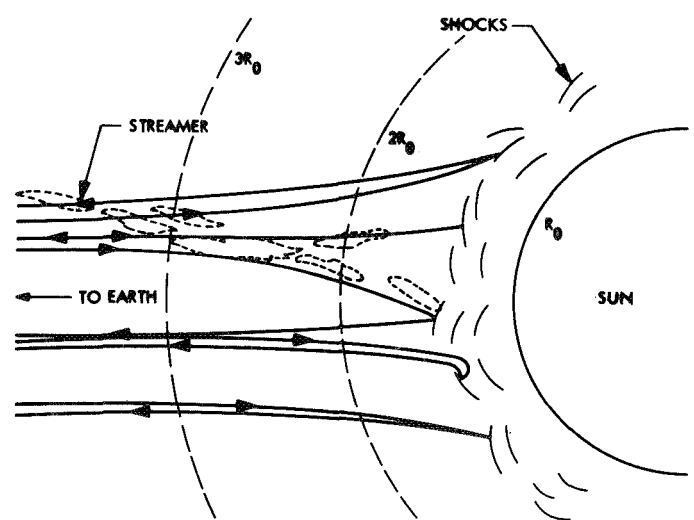
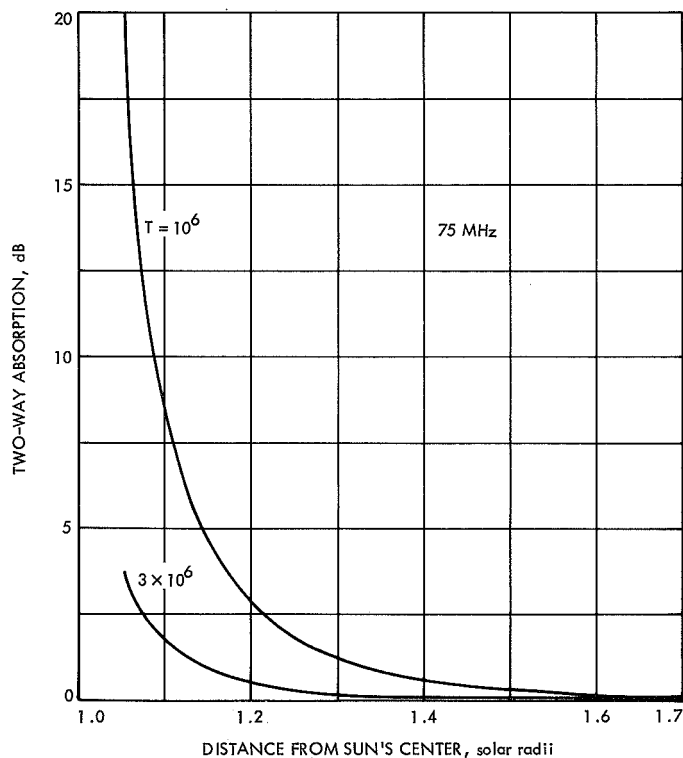


Fig. 7. An illustration of the hypothesized reflection of radar waves by shocks



**Fig. 8. The computed two-way attenuation of a radar signal for the central ray as a function of depth of penetration into the corona**

experiment were more highly correlated with cross section than flares that occurred within a few hours after the time of the experiment. When more flares occurred within 6 h prior to the experiment than for the 6-h period after the experiment, the average cross section was 10 to 20% larger than for times when more flare activity occurred in the 6-h period after the experiment. This effect could be due to a heating of the corona by some mechanism associated with the flares. If so, the effect on cross section should be more pronounced at 75 MHz than at 38 MHz. The effect could also be due to the presence of strong shocks at the reflecting point that were initiated near the point of the flare and that required a few hours to propagate out to the point of reflection. This effect also should be more pronounced at 75 MHz.

Sometimes a double echo is seen at 38 MHz. Figure 9 shows such an echo. The second echo is delayed about 2 s from the main echo. The main echo reflects in the normal manner, but the path of the delayed echo is refracted by a streamer or a dense plasma cloud at 2 or 3 solar radii from the sun's center, as illustrated in Fig. 10. The required density of the plasma cloud is

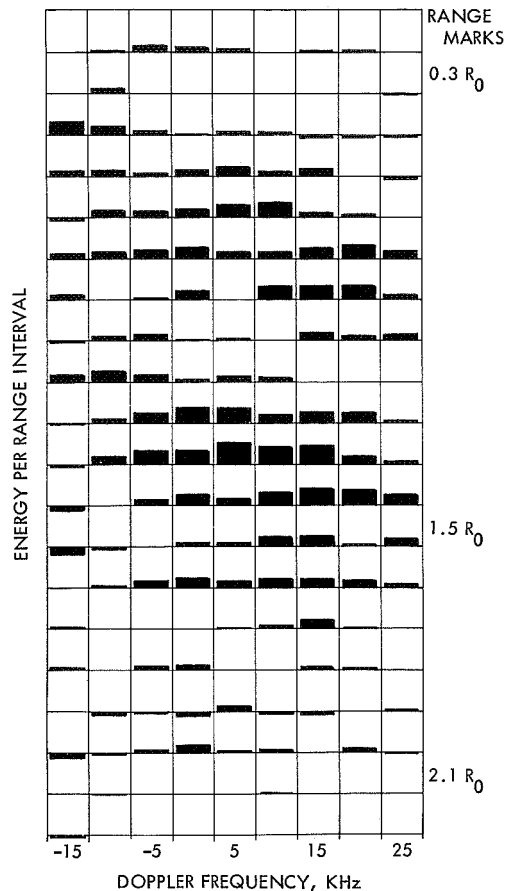


**Fig. 9. A range-doppler plot of a solar radar echo at 38 MHz received at El Campo, Texas**

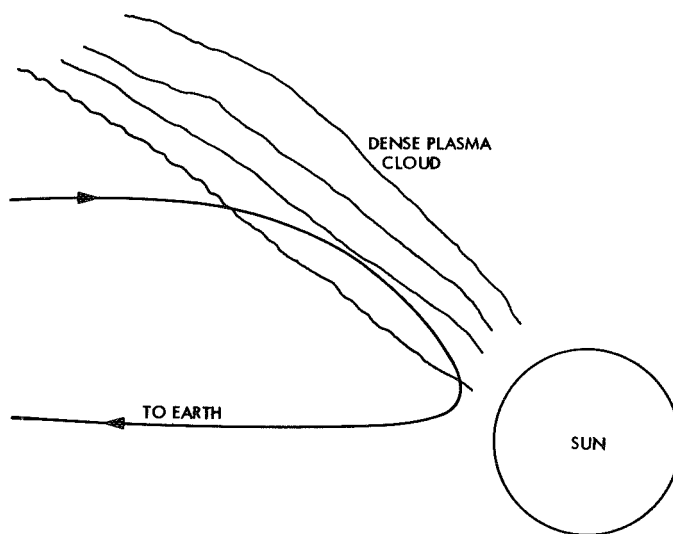


**Fig. 10. A suggested mechanism for delayed echoes**

6 or 7 times that of the normal corona. At 75 MHz this effect may also be present, but the additional delay would be less.

Occasionally, the early part of the main echo is doppler-shifted an unusual amount. This effect is illustrated in Fig. 11, and may be due to solar wind velocities that are nearly sonic at 1.5 solar radii. Dessler (Ref. 6) has shown that the velocity of outward moving plasma must become sonic in the vicinity of 2 solar radii. If this is true, then all regions of the corona must not contribute to the solar wind, because the observed velocity and density of the wind at 1 AU are much smaller than if the wind velocity was sonic at 2 solar radii over the entire sun. Because the high velocity in the early part of the main echo is only seen occasionally, the radar results would seem to agree with Dessler's conclusions; however, there are other possible explanations for the occasional large doppler shift. Radar experiments at 32 and 75 MHz should resolve the problem.

Occasional narrow-band echoes are seen in the high corona as far as 2 or 3 solar radii from the sun's center. An example of these high corona echoes is shown in Fig. 12, a compilation of selected runs in 1963. These echoes are attributed to dense irregularities and not to shock waves. They suggest that in certain regions of the corona the outward expansion velocity is about 20 km/s. This is further evidence that some of the coronal plasma does not reach sonic velocities within 3 solar radii. Figure 13 illustrates one conception of the cause of the high corona echoes. This illustration is not necessarily correct in all details, but is one plausible explanation for the high corona echoes. The main echo would be reflected from the shock fronts.

## V. Conclusions

Solar radar experiments are badly needed over the frequency range from 10 to 100 MHz. More system

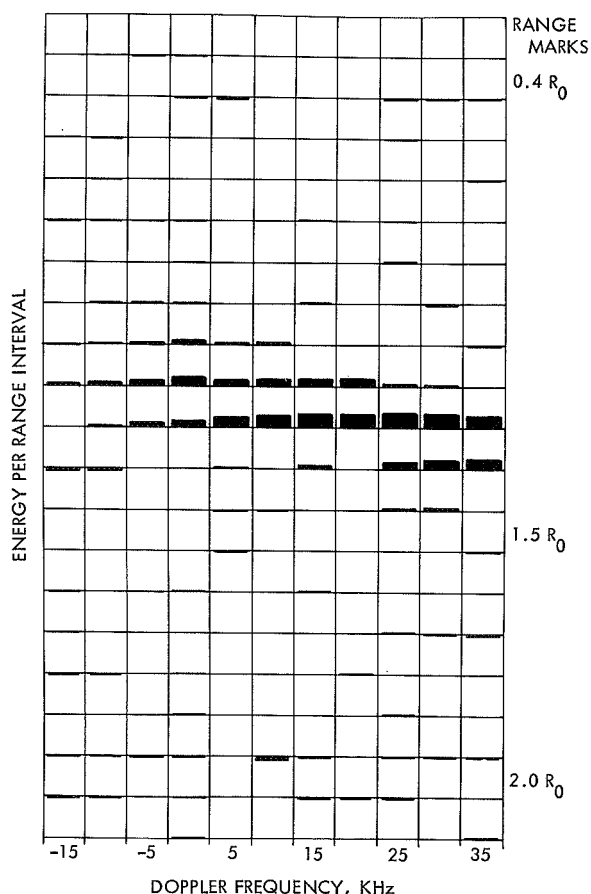


Fig. 11. A distribution of 38-MHz solar echo energy in range and doppler frequency

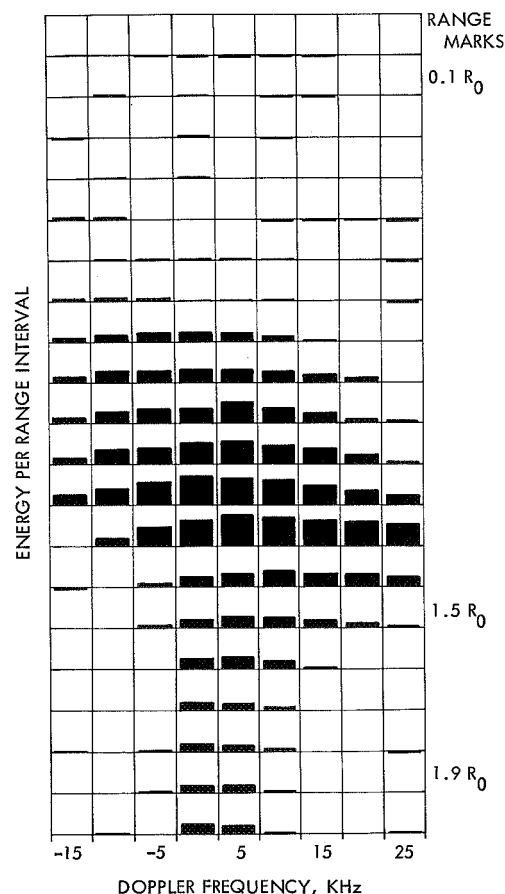
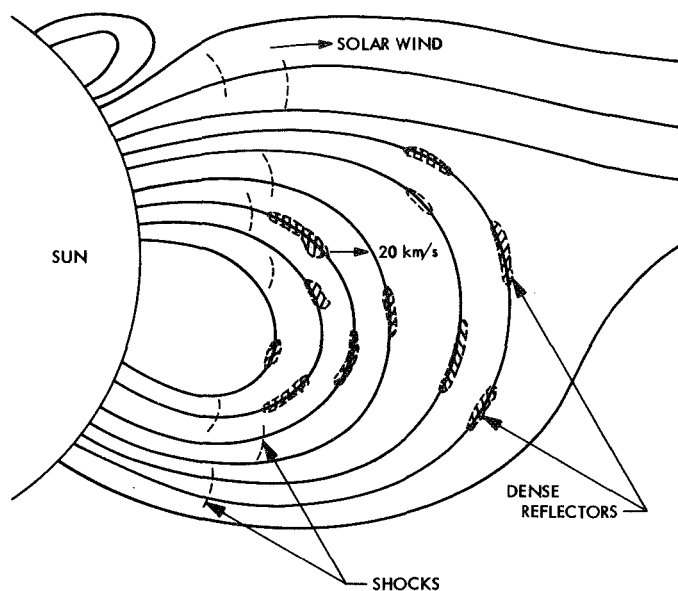


Fig. 12. A distribution of 38-MHz solar echo energy in range and doppler frequency



**Fig. 13. A possible explanation for the high-corona echoes**

sensitivity and more angular resolution than the present El Campo system has would help considerably in the interpretation of the data. Experiments at 75 MHz would permit study of coronal levels as near to the sun's center as 1.15 solar radii. The deepest penetration of the 38-MHz signal is about 1.35 solar radii, which is 2.3 times as far from the photosphere as the 1.15 level.

Radar studies at 75 MHz could lead to a determination of coronal absorption and temperature to the level of 1.15 solar radii. Of more importance would be the variation in temperature, energy deposition, and shock velocities as a function of events in the chromosphere. The velocities of plasma waves at the 1.15-level should help considerably in deciding what types of waves heat the corona. Radar undoubtedly has a future in explaining the solar corona, but significant radar studies at only one frequency have thus far been made.

The Sunblazer radar system has a computed increase in sensitivity of 12 dB over the present 38-MHz solar radar system. This is based on a 1,000,000-deg corona, which is assumed to have 7 dB more coronal absorption at 75 MHz than at 38 MHz. Because of the uncertainties involved, an increased sensitivity of about this much should be designed into the next solar radar system at 75 MHz.

With a 50-dB, 1-MW radar system at 70 to 80 MHz, the density of the very high corona could be monitored continuously from the earth without the assistance of space probes. This could be done by using planets as backscatterers for group-delay experiments and for solar occultation experiments. In addition, the radar properties of all planets out to Saturn could be studied.

## References

1. Ingalls, R. P., James, J. C., and Stone, M. L., "A Study of UHF Space Communications Through an Aurora Using the Moon as a Reflector," in *Ballistic Missiles and Space Technology: Vol. 3*, pp. 272-285. Pergamon Press, New York, 1961.
2. James, J. C., "The Reflecting and Occulting of Galactic Radio Energy by the Sun at 38 Megacycles," *Ap. J.*, Vol. 146, pp. 670-685, 1966.
3. Blum, E. J., and Boischot, A., "Eclipse de la Nebuleuse du Crabe par la Couronne Solaire," in *Paris Symposium on Radio Astronomy*. Edited by R. N. Bracewell, Stanford University Press, Stanford, Calif., 1959.
4. Erickson, W. C., *Observations of an Increase in the Flux From Taurus A During Occultation by the Solar Corona*. Report Department of Physics and Astronomy, University of Maryland, College Park, Md., 1965.
5. James, J. C., "Radar Studies of the Sun," Chapter 7 of *Radar Astronomy*. Edited by J. V. Evans and T. Hagfors. McGraw-Hill Book Co., New York, 1968.
6. Dessler, A. J., "Solar Wind and Interplanetary Magnetic Field," *Rev. Geophys.*, Vol. 5, pp. 1-41, 1967.

# Radar Studies of Venus at 3.8-cm Wavelength

J. V. Evans, T. Hagfors, R. P. Ingalls, D. Karp, W. E. Morrow, G. H. Pettengill,  
A. E. E. Rogers, I. I. Shapiro, W. B. Smith, and F. S. Weinstein

Lincoln Laboratory,\* Massachusetts Institute of Technology  
Cambridge, Massachusetts

*This paper summarizes studies of the reflection properties of Venus at 3.8-cm wavelength performed at the Lincoln Laboratory, Massachusetts Institute of Technology, together with a brief history of the development of these studies.*

## I. Introduction

Since 1961, efforts have been made at the Lincoln Laboratory to study radar reflections from Venus at wavelengths near 4 cm. Attempts to detect the echoes in 1961 and 1962 met with no success but served to show that the cross section could not be as large as observed at longer wavelengths. A successful detection was accomplished in 1964 which established that the cross section was indeed only  $\sim 1\%$  of the projected area of the disk. Later observations in 1966 and 1967 served to show that the cross section of Venus at 3.8 cm is 1.7%; i.e., a factor of 10 less than observed at wavelengths longer than 23 cm.

The scattering properties of the planet have been examined extensively in these recent observations. From a theoretical analysis of these measurements it has been determined that the surface of Venus is significantly

smoother than that of the moon. This should be taken to mean that the surface is less densely covered in structure, having horizontal and vertical dimensions comparable with the wavelength. Also, the rms slope of the surface measured on a scale large compared with the wavelength is lower than that found for the moon. There is, however, a distinct tendency for the surface to appear rougher as the wavelength is shortened in the same manner observed for the moon.

By comparing the radar brightness distribution over the planetary disk with observations at longer wavelengths, it has been established that the limbs are darker at 3.8 cm than would be expected. This effect is attributed to greater atmospheric absorption of those rays that traverse the atmosphere obliquely. From an analysis of this type, it has been estimated that the two-way attenuation of waves propagating vertically through the atmosphere of Venus is at least a factor of 3. This cannot be reconciled with the surface pressure of  $\text{CO}_2$  and

---

\*Operated with support from the U.S. Air Force.

abundance of  $H_2O$  reported by Russian workers from *Venera 4* if these are the only microwave absorbers. It seems, therefore, that other (molecular) constituents may exist in the atmosphere that are more effective absorbers, or that the surface pressure is considerably higher (e.g., 100 atmospheres). Radar ranging measurements to Venus at 3.8 cm (reported elsewhere) have been employed to deduce the radius of Venus, and a comparison of this with the value derived by combining the results of the *Mariner V* and *Venera 4* probes supports the latter conclusion.

Attempts have been made to isolate areas of unusual reflecting properties on the planetary disk by (1) examining the spectra of the reflected signals, (2) employing two aerials for reception in an interferometer, and (3) combined delay-doppler resolution. This work complements that performed at Arecibo (70-cm wavelength) and by the Jet Propulsion Laboratory (12.5-cm wavelength). For the most part, the same features have been identified at all wavelengths. (This provides convincing proof that the 3.8-cm waves do reach the surface of the planet.) The location and nature of these anomalously reflecting surface features are discussed. It is thought that they are chiefly regions of unusual roughness and thus may be the result of relatively recent events on the surface, in view of the general smoothness found elsewhere. At 3.8-cm wavelength the passage of some of these features through the subradar point is accompanied by significant ( $>100\%$ ) increases in cross section, suggesting that some of these regions may also be elevated by a few kilometers above the mean surface.

Radar observations have been made of the moon, Venus, Mercury, and Mars over a wide range of wavelengths (Pettengill and Shapiro, 1965, Ref. 1; Evans, 1966, Ref. 2; Eshleman, 1967, Ref. 3; Pettengill, 1968, Ref. 4). Observations of Venus at either very long or very short wavelengths hold special interest in that they allow examination of effects introduced by the planetary ionosphere or neutral atmosphere, respectively. Studies of the reflection properties of Venus at 3.8-cm wavelength have been performed at the Lincoln Laboratory by Karp et al., 1964, Ref. 5; Evans et al., 1966, Ref. 6; and Evans and Ingalls, 1968, Ref. 7. The section that follows provides a brief history of the development of these studies.

The most remarkable thing about reflections from Venus at 3.8 cm is the poor reflectivity encountered in comparison with that observed at longer wavelengths, although the spectra and other characteristics of the sig-

nals are not markedly changed. Results of measurements of the total reflectivity are presented in Section III. In Section IV the variation of the average brightness over the planetary disk is discussed, and the conclusions concerning the surface roughness that can be derived from this function are given. These same measurements are also employed in Section IV in a comparison with the behavior observed at longer wavelengths to determine the amount of apparent limb darkening caused by atmospheric absorption. This analysis and the cross-section results (Section III) lead to estimates of the one-way zenithal absorption  $A$  in the range  $3 \text{ dB} < A < 5 \text{ dB}$ . The consequences of this conclusion on existing model atmospheres for Venus are briefly mentioned in Section VI. Section V presents results for the existence, location, and nature of anomalously reflecting regions on the surface.

## II. History

Attempts to observe radar reflections from Venus at 3.6-cm wavelength were first made during the 1961 inferior conjunction of Venus, using the Camp Parks terminal of the Project West Ford communications system (Nichols and Karp, 1964, Ref. 8). At that time the transmitter power available was only 12 kW, and proper functioning of the entire radar system was not established until well past the point of close approach. No detection of the reflected signal was achieved. A second attempt was made in 1962, again using the Project West Ford radar system both as a monostatic radar system and bistatically. Prior to these observations the transmitter power was raised to 40 kW, and numerous improvements in the operating procedures were made, which led to greater confidence that the radar was performing satisfactorily. Failure to detect an echo this second time placed an upper limit on the radar cross section of 10% of the projected area of the disk (Table 1).

A third attempt to detect Venus echoes was made in 1964, using the Project West Ford radar system in the bistatic mode. This time the reflected signals were detected after considerable postrectifier integration. From the intensity of the signals, the cross section was estimated to be 1% (Karp et al., 1964, Ref. 5). The spectrum of the echoes was found to be wider than could readily be accounted for in terms of doppler broadening introduced by planetary rotation. However, later work indicates that this broadening seems to have been instrumental in origin. In 1966 and 1967, the Haystack radar system (Weiss, 1965, Ref. 11) was employed to study Venus at 3.8-cm wavelength (Table 1). The parameters of the radar systems employed for these three successful series of mea-

surements are compared in Table 2. The overall improvement in radar performance relative to the first attempt in 1961 is given in Table 1. The later measurements profited considerably from the successive increases in the sensitivity of the apparatus, and thus the reliability of the conclusions reached has improved with time also.

**Table 1. History of Lincoln Laboratory X-band observations of Venus**

Date of inferior conjunction	Sensitivity of apparatus relative to 1961	Radar cross section, %	Observers
1961	1		Unpublished
1962	5	<10	Unpublished
1964	10	~1	Karp et al., 1964, Ref. 5
1966	50	1.2	Evans et al., 1966, Ref. 6 (later revised, 1.7%, Evans, 1968, Ref. 9)
1967	300	1.74	Ingalls et al., 1968, Ref. 10

**Table 2. Parameters of Lincoln Laboratory radar systems employed to study Venus at X-band**

Parameter	June 1964	January 1966	August 1967
Station	Camp Parks/Millstone	Haystack	Haystack
Frequency, MHz	8350	7750	7840
Wavelength, cm	~3.6	~3.9	~3.8
Antenna diameter, ft	60	120	120
Antenna gain, dB	59.8	66.1	66.1
Beamwidth, deg	0.14	0.07	0.07
Maximum average transmitter power, kw	40	105	250-400
System temperature on Venus, °K	74	~120	65
Total waveguide and other losses, dB		0.5	0.5

### III. Radar Cross Section of Venus

The echo power  $P_s$  (in watts) available at the input terminals of the radio receiver in a radar system following reflection from a planet is

$$P_s = \frac{P_t G A \sigma}{(4\pi R^2)^2} \quad (1)$$

where  $P_t$  = peak transmitter power,  $G$  = transmitting antenna gain in the direction of the target,  $A$  = collecting area of the receiving antenna for signals arriving from the direction of the target,  $\sigma$  is the radar cross section of the target, and  $R$  is the range to the target. The radar cross section  $\sigma$  defined by Eq. (1) may be stated as the projected area of a metal sphere which, if placed at the same position as the target, would yield the same reflected power at the receiver. For a planet where the radius  $r_0$  is much larger than the radar wavelength  $\lambda$ ,

$$\sigma = g \rho \pi r_0^2 \quad (2)$$

where  $g$  is a directivity factor which takes into account the ability of the surface to backscatter favorably, and  $\rho$  is the Fresnel reflection coefficient for normal incidence. The reflection coefficient is given by

$$\rho = \left| \frac{(\epsilon)^{1/2} - 1}{(\epsilon)^{1/2} + 1} \right|^2 \quad (3)$$

where  $\epsilon$  is the (complex) relative dielectric constant. In the case of the planets studied thus far, the largest part of the echo power is reflected from the smoother undulating portions of the surface occupying the central region of the disk where the rays are nearly normal to the mean surface (Evans, 1966, Ref. 2). Under these circumstances, the term  $g$  becomes

$$g = (1 + \alpha^2) \quad (4)$$

where  $\alpha$  is the rms surface slope (Hagfors, 1964, Ref. 12). Since typically  $\alpha \sim 0.1$ ,  $g$  is indistinguishable from unity, and thus measurements of  $\sigma$  may be interpreted in terms of the dielectric constant  $\epsilon$  for the planetary surface.

Table 3 summarizes all the measurements of the cross section of Venus at 3.8-cm wavelength accomplished since January 1966, when the Haystack radar system (Table 2) came into use (Ingalls et al., 1968, Ref. 10). The instrumental uncertainty associated with each measurement is estimated as  $\pm 50\%$  ( $\pm 2$  dB) and the relative accuracy from run to run or day to day about  $\pm 20\%$  (i.e.,  $\pm 1$  dB). These values of the cross section are plotted in Fig. 1 as a function of the longitude of the subradar point. It is thought that the marked variations between 50 and 250 deg are real, but additional measurements are needed to

**Table 3. Summary of radar cross-section measurements, 3.8-cm CW observations**

Year	Date	Subradar position at noon <sup>a</sup>		Cross section, % $\pi r_0^2$
		Longitude, deg	Latitude, deg	
1966	Jan 18	316.69	-5.61	1.74
	Feb 1	329.28	-8.07	1.32
	Feb 9	337.72	-8.27	1.61
	Mar 21	52.48	-3.45	1.77
	Mar 30	73.72	-2.26	2.51
	Apr 15	113.11	-0.41	3.50
	May 5	164.09	+1.28	1.60
	May 17	195.24	+1.94	2.75
	Jun 15	271.51	+2.43	2.10
	Jun 27	303.36	+2.26	1.75
1967	Apr 10	2.36	-0.59	1.33
	Apr 12	7.69	-0.68	1.45
	Apr 13	10.36	-0.73	1.34
	Apr 14	13.02	-0.77	1.76
	Apr 21	31.66	-1.08	1.76
	Apr 26	44.88	-1.29	1.50
	Jul 26	266.69	+2.53	1.54
	Jul 27	268.60	+2.70	1.86
	Aug 2	279.47	+3.85	1.81
	Aug 3	281.17	+4.06	1.92
	Aug 10	292.08	+5.53	1.79
	Aug 16	299.93	+6.79	1.66
	Aug 17	301.10	+6.99	1.65
	Aug 23	307.39	+8.03	1.73
	Aug 25	309.26	+8.30	1.79
	Aug 29	312.78	+8.67	1.70
	Aug 30	313.64	+8.74	1.66
	Aug 31	314.50	+8.78	1.74
	Sep 6	319.87	+8.72	1.77
	Sep 7	320.84	+8.66	1.74
	Sep 13	327.29	+8.04	1.67

<sup>a</sup>Coordinate system defined in text.

confirm this. In the coordinate system employed here, the prime meridian is defined as that lying 40 deg to the west of the central meridian on 0.0 h on June 20, 1964 (following Carpenter, 1966, Ref. 13). A pole position  $\delta = 66$  deg,  $\alpha = 270$  deg, and period  $-243.2$  days have been assumed.

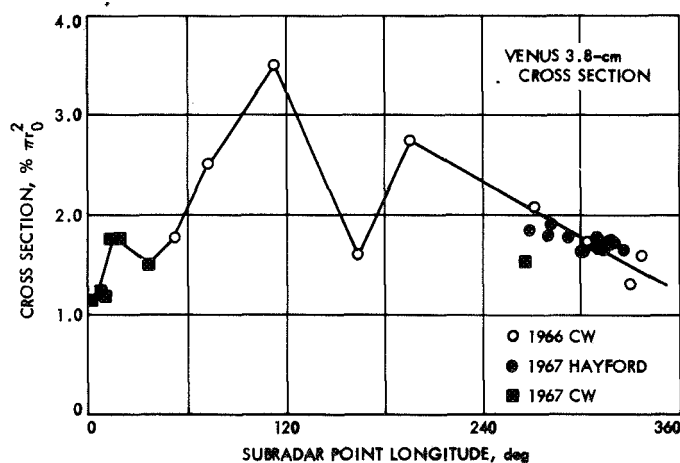
The largest values of the cross section have been observed at longitudes in the range 72-120 deg and near 200 deg. These seem to be associated with the presence of large rough regions on the surface at these longitudes (Evans, 1968, Ref. 9; Goldstein, 1967, Ref. 14). Unfortunately, it has not been possible to schedule the observations to permit extensive measurements of the cross section when these regions lie near the subearth point (occurring several months before or after inferior conjunction).

Figure 1 shows that the 1966 and 1967 measurements agree for the value of the cross section observed near inferior conjunction. Figure 2 shows the variation of cross section observed during the 1967 inferior conjunction. The average of these measurements is  $\sigma = 1.74\% \pi r_0^2$  (Ingalls et al., 1968, Ref. 10) in agreement with the results of 1966 (Evans, 1968, Ref. 9).

Table 4 gives values for the radar cross section of Venus as a function of wavelength according to various observers, and these are plotted in Fig. 3. (The curve is a theoretical one based upon the assumption that the intrinsic cross section is  $16\% \pi r^2$  and that atmospheric

**Table 4. Venus cross section vs wavelength**

Observer	Wavelength, cm	Total cross section, $\pi r_0^2$	Error estimate, dB
Evans, 1968 Ref. 9	3.8	0.017	$\pm 2$
Carpenter, 1966 Ref. 13	12.5	0.114	$\pm 0.5$
Evans et al., 1965 Ref. 15	23	0.15	$\pm 1$
Kotel'nikov et al., 1965 Ref. 16	40	0.19	( $\pm 2$ )
Pettengill et al., 1962 Ref. 17 (revised by Evans et al., 1965, Ref. 15)	68	0.13	$\pm 2$
Pettengill et al., 1967 Ref. 18	70	0.14	+2 -3
Klemperer et al., 1964 Ref. 19	600	0.20	( $\pm 2$ )
James and Ingalls, 1964 Ref. 20	784	0.15	( $\pm 2$ )



**Fig. 1. Cross section of Venus vs subradar longitude based on all the 3.8-cm observations of Venus made at Haystack to date (Table 3)**



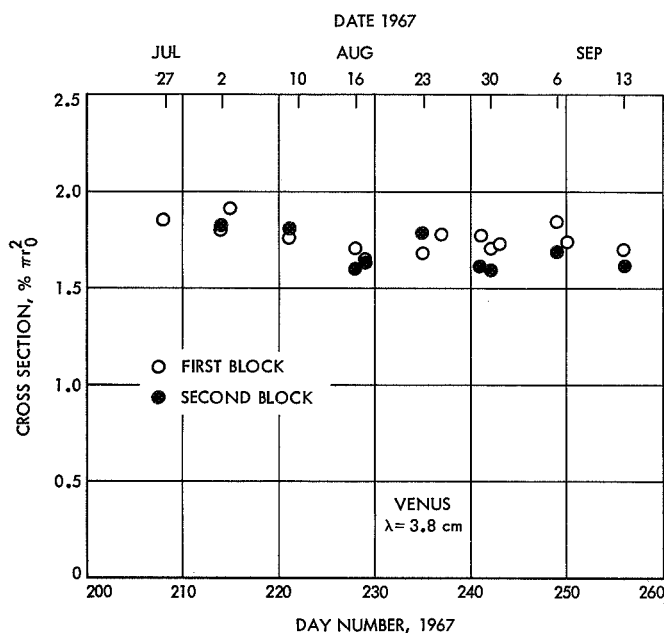


**Fig. 2. Variation of the radar cross section around inferior conjunction (August 30) as obtained from the Haystack CW results**

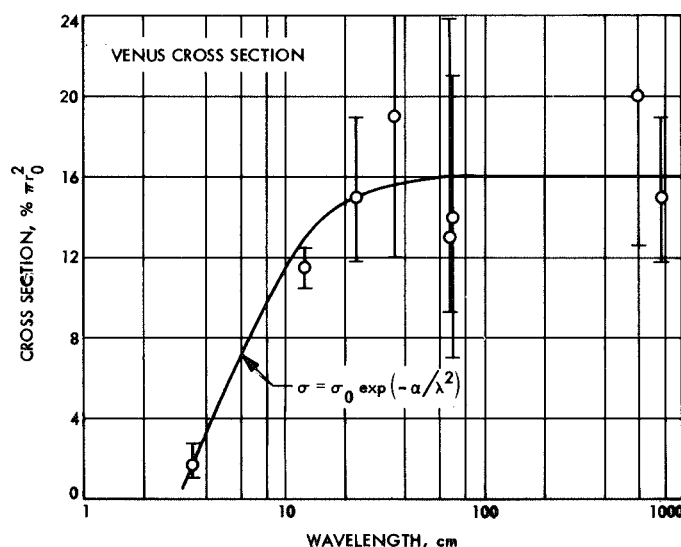


**Fig. 3. Variation of the radar cross section of Venus with wavelength according to various observers (Table 4)**

absorption is responsible for lowering the cross section, the optical depth depending on the square of the frequency.) The marked variation of cross section with wavelength is in sharp contrast with that observed for the moon, which is known to have no atmosphere. This leads to the suggestion that the atmosphere of Venus is responsible for absorbing the short-wave signals.

Since the largest part of the echo is returned from a region around the subradar point where the rays penetrate the atmosphere nearly vertically (Section IV), we may neglect the curvature of the surface and to a first approximation write

$$\sigma = \sigma_0 \exp(-2\tau) \quad (5)$$

where  $\sigma_0$  is the intrinsic cross section (observable if Venus had no atmosphere), and  $\tau$  is the "optical depth" defined in

$$\tau = \int_0^\infty \kappa dh \quad (6)$$

where  $\kappa$  is the absorption coefficient per vertical height element  $dh$ . For an atmosphere of  $\text{CO}_2$  we would expect

$$\kappa \propto \frac{1}{\lambda^2} \quad (7)$$

in which case

$$\begin{aligned} \sigma &= \sigma_0 \exp \left[ -2\tau \left( \frac{\lambda_0}{\lambda} \right)^2 \right] \\ &= \sigma_0 \exp \left( -\frac{a}{\lambda^2} \right) \end{aligned} \quad (8)$$

Included in Fig. 3 is a law of this form, in which it has been assumed that  $\sigma_0 = 16\%$  (i.e., the mean of all values in Table 4 for  $\lambda \geq 23$  cm), and the curve has been made to pass through  $\lambda = 3.8$  cm by setting  $\lambda_0 = 3.8$  and  $\tau = 1.13$ . This value for the optical depth implies a value for the one-way vertical attenuation  $A$  at 3.8 cm of  $A = 4.9$  dB. It should be noted, however, that it is possible to fit to the results shown in Fig. 3 a law of the form  $\sigma = \sigma_0 (-b/\lambda)$ , which implies an ever larger value for  $A$ , and based upon the experimental data alone it is not possible at present to exclude this alternative model.

The cross section of Venus observed at long wavelengths ( $\sim 16\%$ ) implies a surface dielectric constant  $\epsilon = 4.5$  (Pettengill, 1968, Ref. 4). This suggests that, unlike the moon (and probably Mars), the surface material on Venus is not porous to any considerable depth, or alternatively is not completely eroded into fine particles.

It seems, therefore, that Venus has a more compact surface than the moon, and consequently the penetration depth of the signals at all wavelengths will be less. This being so, it becomes quite difficult to account for the reflectivity variation with wavelength (Fig. 3) by means of varying the electrical properties of the surface material as a function of depth unless very stringent and artificial conditions are adopted.

## IV. Angular Scattering Law

### A. Results

The radar reflectivity over the planetary disk may be explored in a number of different ways (see, for example, Green, 1968, Ref. 21). In the case of Venus, this distribution has been explored at 3.8-cm wavelength by determining the power frequency spectra of the signals following reflection. Owing to the apparent spin of the planet with respect to a terrestrial observer, a monochromatic signal transmitted from earth is doppler-broadened on reflection. Figure 4 shows the mean spectrum obtained during the 1967 inferior conjunction after averaging some 159 runs. The amplitudes of these spectra were normalized according to Eq. (1) to allow for variations in the radar parameters and range, and their widths were adjusted to be the same by plotting them on a normalized frequency scale  $f/f_{\max}$ , where  $f_{\max}$  is the difference between the doppler shift encountered by signals reflected from the limb and for signals reflected from the disk center.

The curves in Fig. 4 are dissimilar. The systematic difference is attributed to the presence of anomalously bright reflecting regions, the majority of which lay on the receding hemisphere during the course of these measurements. The apparent rotation of the planet has smeared the contributions from these regions so that they no longer give rise to discrete features in the spectrum. Accordingly, the curve for the approaching side has been adopted as representing the average scattering properties.

We may define a function  $P(\phi)$ , called the angular power spectrum, which is the power reflected per unit surface area into unit solid angle for unit incident flux when viewed at an angle  $\phi$  with respect to the mean surface normal. When defined in this fashion, a surface covered with isotropic scatterers would obey the law

$$\bar{P}(\phi) \propto \cos \phi \quad (9)$$

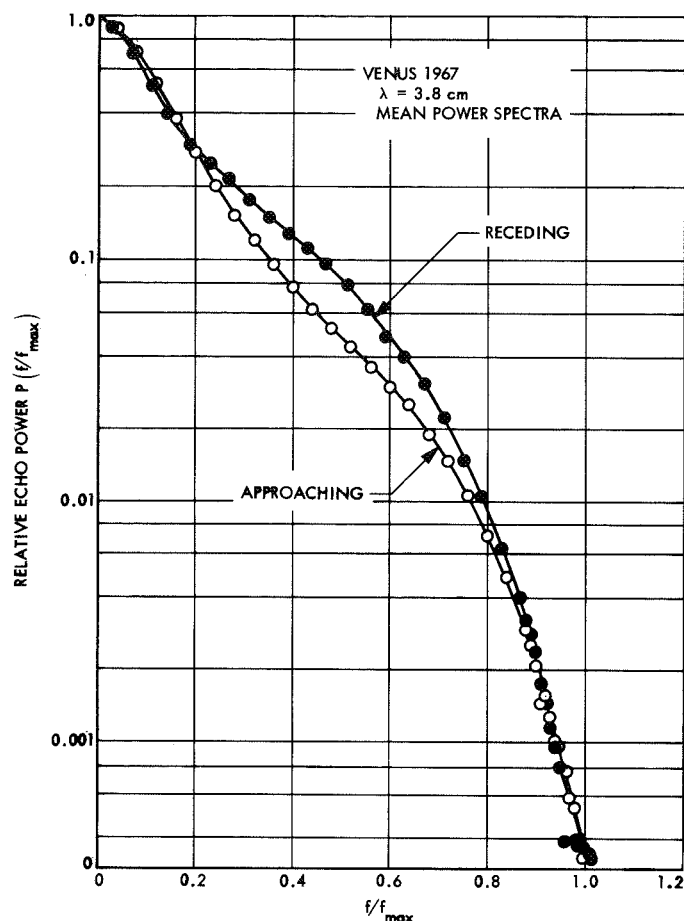


Fig. 4. Comparison of the mean frequency power spectra  $\bar{P}(f/f_{\max})$  observed for Venus echoes in the Haystack CW experiment for the approaching and receding halves of the disk

The function  $\bar{P}(\phi)$  can be recovered from spectra such as those shown in Fig. 4 by a suitable transformation (e.g., Evans et al., 1966, Ref. 6). In Fig. 5 triangles represent the mean angular power spectrum  $\bar{P}(\phi)$  obtained for Venus echoes from the frequency power spectrum  $P(f/f_{\max})$  shown in Fig. 4 for the approaching hemisphere by means of a Bessel transformation (Evans, et al., 1966, Ref. 2). Also included as points are estimates obtained from measurements with short pulses. It can be seen that the two methods agree well, and the full line is the curve finally adopted. It should be noted that in obtaining  $\bar{P}(\phi)$  from measurements of echo power vs delay or frequency it was assumed that rectilinear propagation holds. Consideration of the effects of refraction suggests that these will be significant. For  $\phi = 60$  deg, the total bending of the ray will be  $\sim 4$  deg if the surface pressure is 100 atmospheres. Thus for  $\phi > 60$  deg, the shape of the curve in Fig. 5 may be in error.

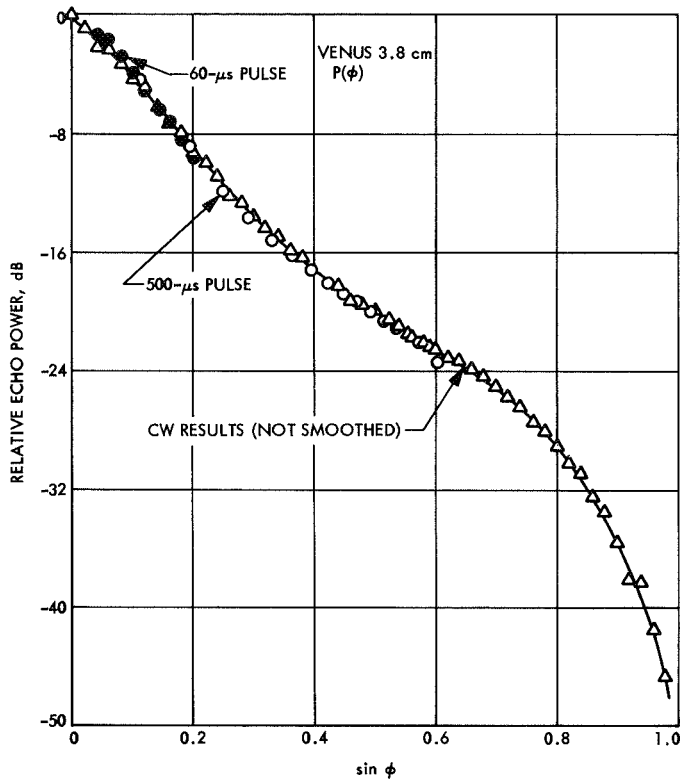


Fig. 5. Relative echo power obtained for Venus echoes

### B. Limb Darkening

In the absence of refraction, the effect of atmospheric absorption will be to modify the intrinsic scattering law  $\bar{P}_0(\phi)$  so that one observes

$$\bar{P}(\phi) = \bar{P}_0(\phi) \exp(-2\tau \sec \phi) \quad (10)$$

If  $\bar{P}_0(\phi)$  were known from theory or some other way, the optical depth  $\tau$  could be determined from the secant dependence in Eq. (10). Previously, we attempted to circumvent the difficulty that  $\bar{P}_0(\phi)$  is unknown by comparing curves of  $\bar{P}(\phi)$  obtained at two frequencies (Evans et al., 1966, Ref. 6). Thus the mean power spectrum results for 12.5 cm published by Muhleman (1965, Ref. 22) were transformed to obtain  $\bar{P}(\phi)$  by the same method as the 3.8-cm results. Figure 6 compares the two curves. The difference in behavior for  $0 < \phi < 10$  deg is believed to be due to variations in the behavior of the surface at the subradar point. For  $\phi > 20$  deg, the difference is thought to stem from the larger amount of atmospheric absorption encountered at Venus by the 3.8-cm waves.

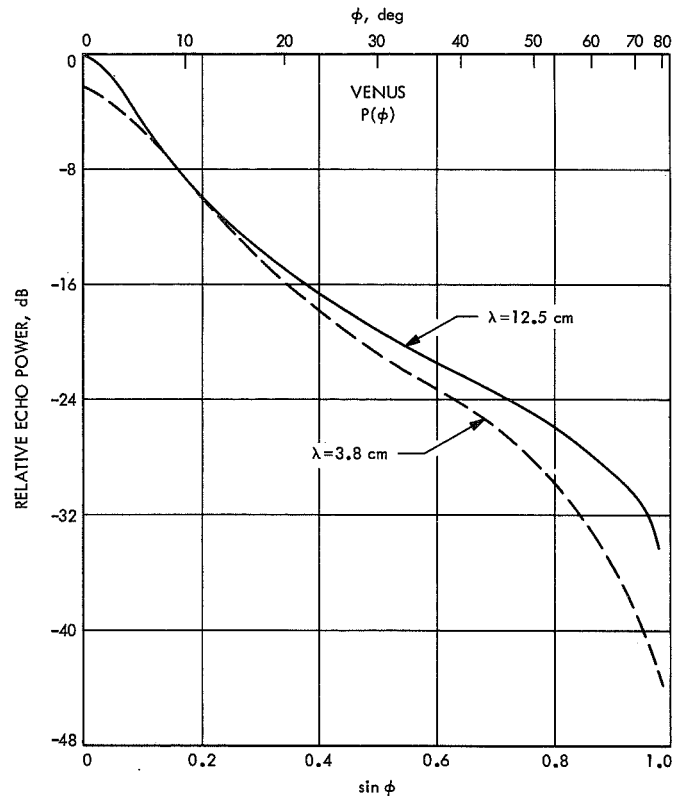


Fig. 6. Comparison of the angular scattering laws  $\bar{P}(\phi)$  derived from the mean frequency power spectra  $\bar{P}(f/f_{\max})$  observed at 3.8 cm (Fig. 4 approaching side) and 12.5 cm

If the scattering properties of the surface of Venus at 3.8 and 12.5 cm were identical, and the atmosphere introduced only absorption, we would expect the scattering laws  $\bar{P}(\phi)$  observed at the two wavelengths to be related in

$$10[\log_{10} \bar{P}(\phi)_{12.5} - \log_{10} \bar{P}(\phi)_{3.8}] = 2A \sec \phi \quad (11)$$

where  $A$  is the difference in the one-way zenithal absorption (dB) in the Venus atmosphere at the two frequencies. When the effects of refraction are considered, this equation may be expected to break down. However, since the ray paths are the same at both frequencies, the difference in the two curves (Fig. 6) should be relatively insensitive to refraction effects, at least up to  $\phi \leq 60$  deg. When refraction becomes important, the angle  $\phi$  associated with a given doppler shift will be too large, and thus the observed power difference will be smaller than predicted by Eq. (11).

Figure 7 shows the difference in the relative echo powers plotted in Fig. 6 as a function of  $\sec \phi$ . Over the

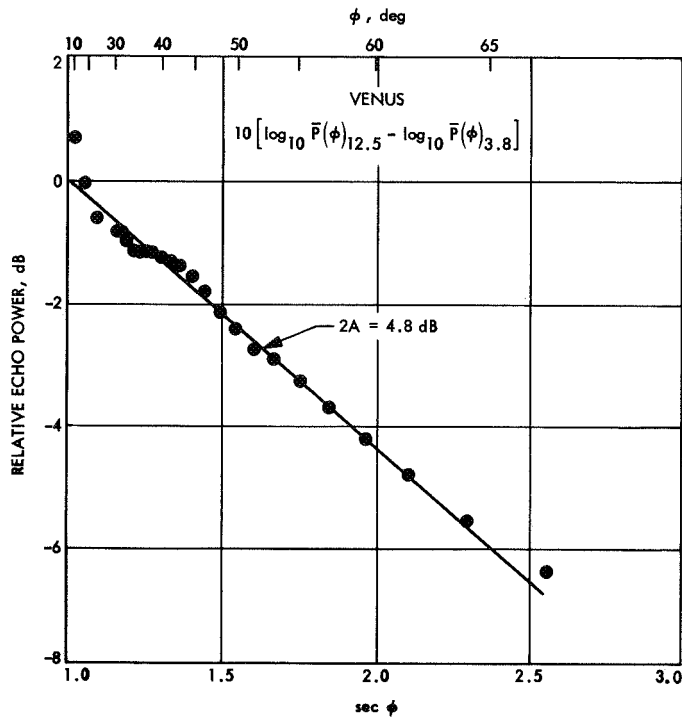


**Fig. 7. Difference in relative echo power for Venus echoes**

range  $20 \text{ deg} < \phi < 60 \text{ deg}$ , the results fit a straight line quite well with the dependence  $2A = 4.8 \text{ dB}$ . For  $\phi > 60 \text{ deg}$ , the curve departs in the manner expected owing to the neglect of atmospheric refraction in the interpretation. The linear dependence on the secant of the local zenith angle  $\phi$  supports the view that atmospheric absorption is responsible. The estimate of the two-way zenithal absorption obtained here must be a lower limit, because (1) there may already be some absorption at 12.5-cm wavelength, and we are only examining the difference, and (2) the intrinsic scattering law of the surface may change with wavelength (as in the case of the moon) to cause the reflectivity of the limbs relative to the disk center to be higher (in the absence of atmospheric absorption) at the shorter wavelength. The next section provides evidence that this is in fact the case.

### C. Theoretical Behavior

Hagfors (1964, Ref. 12; 1966, Ref. 23), among many others, has discussed the scattering behavior of planetary surfaces at radio wavelengths. For many surfaces in which the autocorrelation function describing the horizontal variation of surface height is exponential, the power scattered per unit mean surface area per unit solid angle as a function of the angle of incidence  $\phi$  on

the mean surface is of the form

$$P(\phi) \propto (\cos^4 \phi + C \sin^2 \phi)^{-3/2} \quad (12)$$

where  $C = (d'\lambda/4\pi h_0^2)^2$  is a constant in which  $d'$  defines the horizontal correlation scale, and  $h_0^2$  is the mean square height deviation of the surface.

The scattering of the moon and Venus can be characterized by two components, one of which obeys a law of the type Eq. (12) and a second shows less angular dependence (Evans, 1965, Ref. 24; Evans et al., 1965, Ref. 15)

$$P(\phi) \propto \cos^{3/2} \phi \quad (13)$$

These components have usually been termed "quasi-specular" and "diffuse," respectively. The diffuse component has been attributed to structure on the surface comparable in dimension to the wavelength (e.g., boulders) and hence capable of scattering into all angles. Since the diffuse component appears to be responsible for all the echo power for  $\phi > 50 \text{ deg}$  in the case of the moon (Evans, 1965, Ref. 24) and  $\phi > 60 \text{ deg}$  for Venus (Evans et al., 1965, Ref. 15), it would be unreasonable to expect Eq. (12) to describe  $\bar{P}(\phi)$  for all  $\phi$ , even neglecting absorption and refraction effects discussed above.

We have computed theoretical curves of  $\bar{P}(\phi)$  according to Eq. (12) modified for the effects of atmospheric absorption as in Eq. (10) and compared these with the mean curve of Fig. 5. Figure 8 shows illustrative examples of such curves computed for various values of  $C$  and the one-way absorption. It can be seen that the absorption controls the behavior in the region  $\phi > 30 \text{ deg}$ , i.e., in a region where the theory is beginning to break down. It follows that this is not a reliable method by which to estimate the optical depth  $\tau$  (Eq. 10). However, it is also evident that the value of  $C$  derived should not be too sensitive to the assumed value of the absorption. Based upon this comparison we estimate that at 3.8 cm the appropriate value of  $C$  is  $\sim 75$ , and the fit between the theory and experimental points is shown in Fig. 9.

Figure 10 summarizes the values of the parameter  $C$  that have appeared in the literature (Beckman and Klemperer, 1965, Ref. 25) and includes the point obtained here. The values shown for the moon differ slightly from those published by Evans and Hagfors (1966, Ref. 26) because the "diffuse" component has not

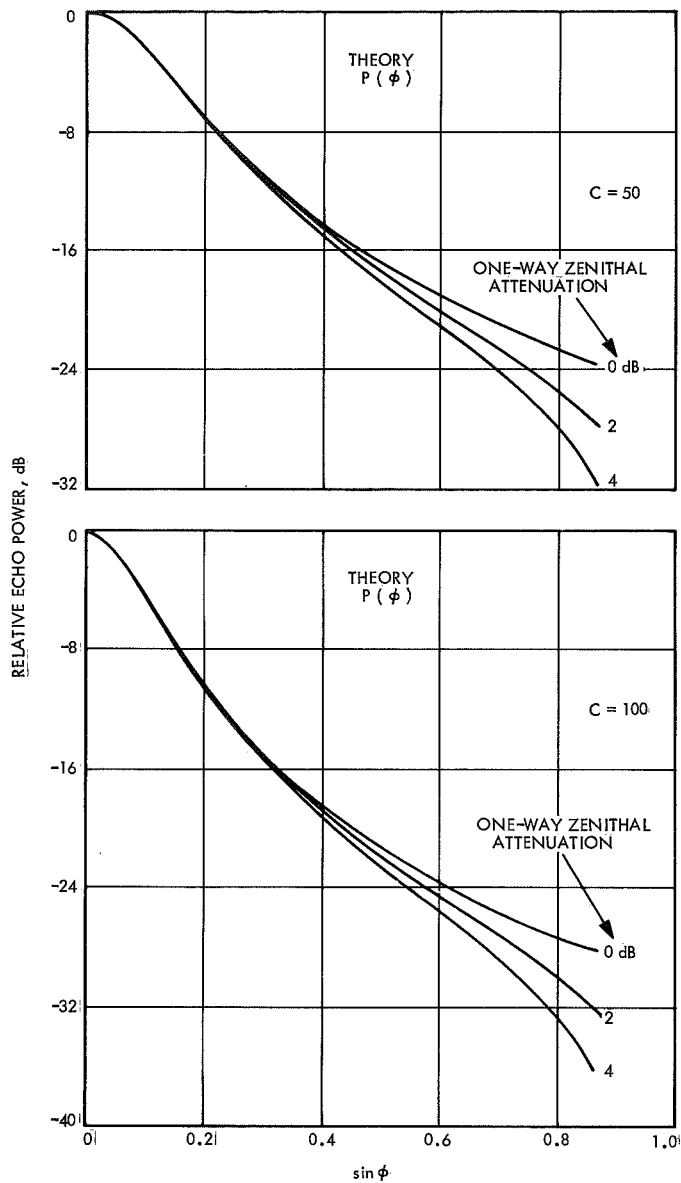


Fig. 8. Theoretical curves for the angular scattering law according to Eq. (12) when effects of atmospheric absorption (Eq. 10) are included

been subtracted out. In the case of the moon there is a clear wavelength dependence, indicating that the surface appears smoother at longer wavelengths. In the case of Venus the value of  $C$  for  $\lambda = 23$  cm is known to be too high owing to the way in which the curve for  $\bar{P}(\phi)$  was constructed. At  $\lambda = 41$  and  $\lambda = 68$  cm, the values are probably lower estimates because of the lower resolution of the measurements. Thus it appears as if there is also a wavelength dependence in the apparent roughness for Venus, and a crude relation between the moon and Venus is to suppose that  $C(\lambda)_{\text{moon}} = 1/2 C(\lambda)_{\text{Venus}}$ .

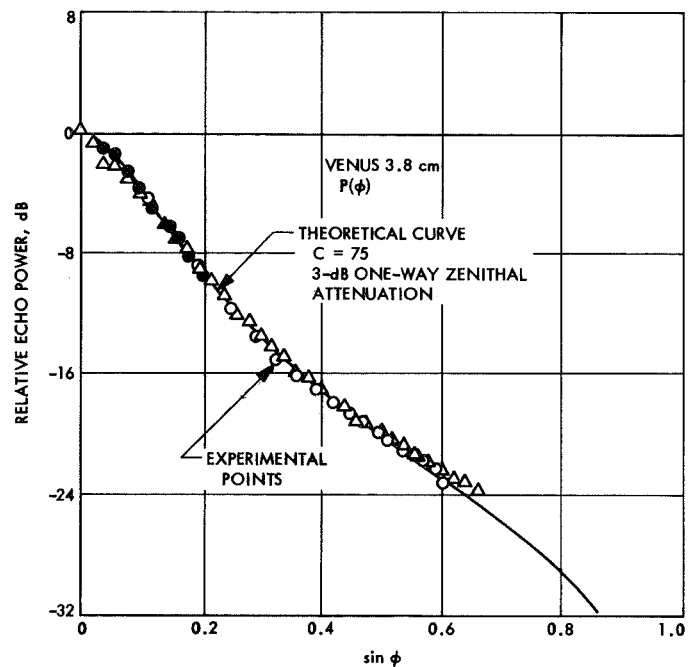


Fig. 9. Comparison of the experimental data points shown in Fig. 5 with a theoretical curve (cf. Fig. 8) for  $C = 75$  and 3-dB, one-way vertical attenuation

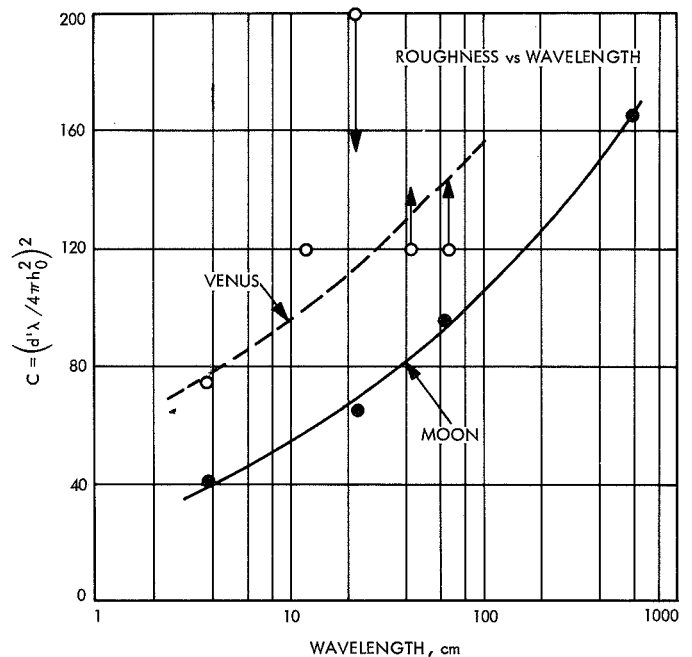


Fig. 10. Values for the parameter  $C$  vs wavelength for the moon and Venus

The relationship between  $C$  and the rms slope of the surface is far from straightforward (Hagfors, 1966, Ref. 23). There are difficulties associated with defining

what is really meant by a slope when the surface is described by an exponential autocorrelation function and the horizontal scale over which the sampling is carried out is unknown. Recent studies (Lincoln Laboratory, unpublished) have shown, for the case of the moon, that the horizontal scales of importance in determining the effective slope sampled by the wave extend down to the size of the wavelength. Further, the effective scale length changes with the angle of incidence  $\phi$ . That is, the effect of the wavelength is to filter out certain components of the spectrum of surface roughness in a way which depends upon  $\phi$ . Thus the ratio between the effective vertical and horizontal scales  $h_e$  and  $d'_e$  is approximately (Hagfors, 1966, Ref. 23)

$$\frac{h_e}{d'_e} \approx \frac{\cos \phi}{(2C)^{1/2}} \quad (14)$$

The rms surface slope  $\theta_{\text{rms}}$  averaged over all possible directions over the surface is

$$\begin{aligned} \theta_{\text{rms}} &= (2)^{1/2} \frac{h_e}{d'_e} \\ &\approx \frac{\cos \phi}{(C)^{1/2}} \end{aligned} \quad (15)$$

Substitution into this expression leads to values  $\theta_{\text{rms}} \sim 6$  deg at  $\lambda = 3.8$  cm and  $\sim 5$  deg for  $\lambda \geq 23$  cm.

The increased roughness found at the shorter wavelength implies that the limb darkening (Section IV-B) is less than would be expected as a consequence of atmospheric absorption alone. Thus we conclude that, as a lower limit, we may take  $A = 3$  dB on the basis of the results presented here, and from Section III we place an upper limit on the one-way absorption of  $A = 5$  dB.

## V. Anomalous Scattering Regions

### A. Location of the Features

Spectra of the signals reflected from Venus frequently show irregular structure, which persists from run to run and moves from high to low frequency in the manner expected if caused by anomalous scattering from discrete regions on the surface. Figure 11 provides an example of this behavior. The presence of these features is more readily apparent when the ratio is taken of the spectrum observed on a given day to the long-term average of spectra obtained over several weeks. Figure 12 shows

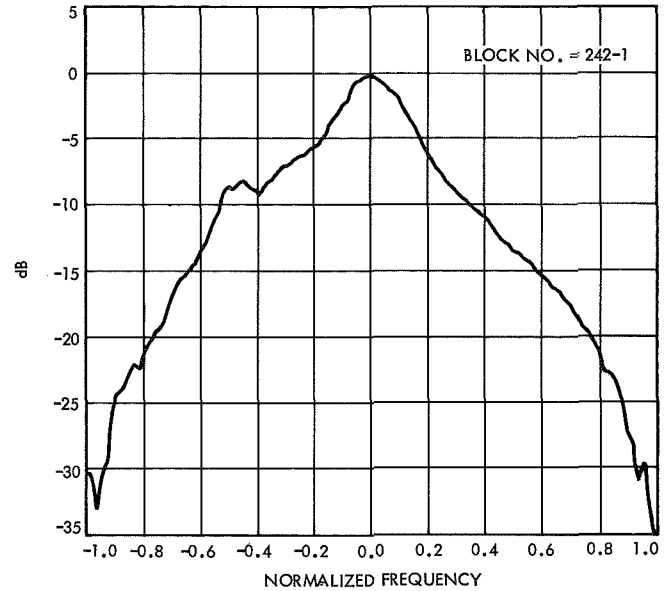


Fig. 11. The original echo power spectrum  $P(f/f_{\text{max}})$  from which Fig. 12 was derived

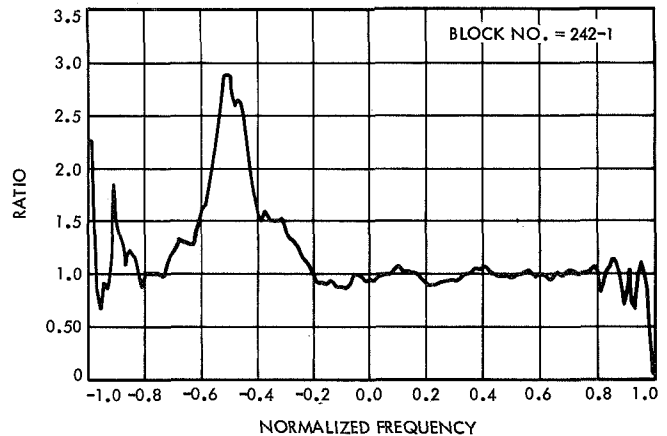


Fig. 12. The ratio of the echo power  $P(f/f_{\text{max}})$  observed on a given day to the long-term average over several weeks

such a ratio plot, with a group of features clearly evident on the receding half of the disk. In both Figs. 11 and 12 the existence of anomalous scattering regions is evident, but the presentation in Fig. 12 is somewhat more useful.

The speed with which these features move through the spectra is related to the latitude, and the longitude can be established by noting the time when the feature lies at zero normalized frequency. However, it is not easily possible to determine in which hemisphere the region lies unless the orientation of the projected axis of rotation changes significantly during the observing

period. Carpenter (1966, Ref. 13) and Goldstein (1965, Ref. 14; 1967, Ref. 27) have located a number of anomalously bright reflecting regions from studies of spectra such as Fig. 11 obtained at 12.5-cm wavelength. Spectra obtained at 3.8 cm appear to exhibit the same features found by these authors, but in view of possible ambiguity in locating the responsible regions by this method we have sought other means of establishing the positions.

One technique employed at Lincoln Laboratory has been to resolve the echo power both with respect to time delay and frequency by transmitting a chain of phase-coherent pulses. This so-called delay-doppler technique permits the echo power to be mapped as a function position with respect to the apparent equator. However, the power from the northern and southern hemispheres is folded together. Figure 13 shows maps of this type obtained with 60- $\mu$ s pulses. The effective resolution obtained is about  $50 \times 70$  km. In these plots the variation in the reflectivity is presented as it would appear from the south planetary pole. Only the region surrounding the subradar point was examined, and the longitude of this changed with time. Features lying in the southern hemisphere will then be seen as bright areas lying at a fixed longitude, while contributions from regions in the northern

hemisphere will appear to move in longitude. Real features seen in these plots should appear to line up vertically. The locations of the features Haystack V (considered reliable) and Haystack E, F, G, and H (considered probable) are indicated.

The most ambitious attempt thus far to map these variations in reflectivity was undertaken by Rogers et al. (1968, Ref. 28), who employed the 120-ft-diam Haystack antenna in conjunction with one of the 60-ft Westford antennas (Table 2) for reception as an interferometer. The spacing of these two antennas was such as to place about 10 interferometer fringes in a N-S direction across the planetary disk. The E-W resolution was then achieved by spectrum analysis of the echoes. In order to determine the particular fringe in which strong echoes lie, it is necessary to allow earth rotation to change the effective baseline length and hence the fringe spacing on the disk. Figure 14 shows the effective beam pattern achieved in these observations. Owing to the unfavorable orientation of the interferometer baseline together with restrictions on the allowed observing time, the synthesized beam (Fig. 13) has high side lobes. This results in a number of "ghost" or spurious bright regions in the map obtained (Fig. 15). Table 5 summarizes the features identified in

**Table 5. Location of radar features on Venus**

Feature	Location from Haystack		Probable JPL identification	Location from JPL	
	Longitude, deg	Latitude, deg		Longitude, deg	Latitude, deg
Haystack I	$-1 \pm 2$	$-26 \pm 3$	{ Goldstein $\alpha$ Carpenter F	$0 \pm ?$	$-29 \pm 2$
Haystack II	$-81 \pm 2$	$+24 \pm 2$		$0 \pm 0.7$	$-26.7 \pm 1.8$
Haystack III	$-78 \pm 2$	$+31 \pm 2$	Goldstein $\beta$ center =	$-78 \pm 6$	$+23 \pm 4$
Haystack IV	$-65 \pm 3$	$-7 \pm 3$	Carpenter C	$-68.9 \pm 1.3$	$-6.8 \pm 5.8$
Haystack V	$-73 \pm 1$	$-1.5 \pm 0.5$	Carpenter C2	$-70.0 \pm 0.7$	$-2.5 \pm 3.7$
			Other possible features		
Haystack A	$-68 \pm 2$	$+23 \pm 2$	{ Carpenter D2	$-70.0 \pm 0.7$	$+22.7 \pm 1.7$
Haystack B	$-81 \pm 3$	$-12 \pm 3$	{ Goldstein $\delta$	$-69 \pm ?$	$+26 \pm ?$
Haystack C	$-36 \pm 3$	$-13 \pm 2$	Carpenter B1	$-75.8 \pm 0.6$	$-11.9 \pm 4.4$
Haystack D	$-39 \pm 4$	$+10 \pm 4$	None		
Haystack E	$-49 \pm 1$	$+3 \pm 0.5$	None		
			Carpenter E	$-49.3 \pm 0.9$	$+6.4 \pm 8.5$
Haystack F	$-61 \pm 1$	$+2 \pm 0.5$	{ Carpenter D	$-61.0 \pm 1.8$	$-1.7 \pm 7.1$
Haystack G	$-70 \pm 1$	$+5 \pm 2$	{ Carpenter D3	$-60.5 \pm 0.7$	$-2.5 \pm 4.1$
Haystack H	$-77 \pm 1$	$+4 \pm 2$	None		
			Carpenter B	$-78.1 \pm 2.6$	$-3.3 \pm 8.7$

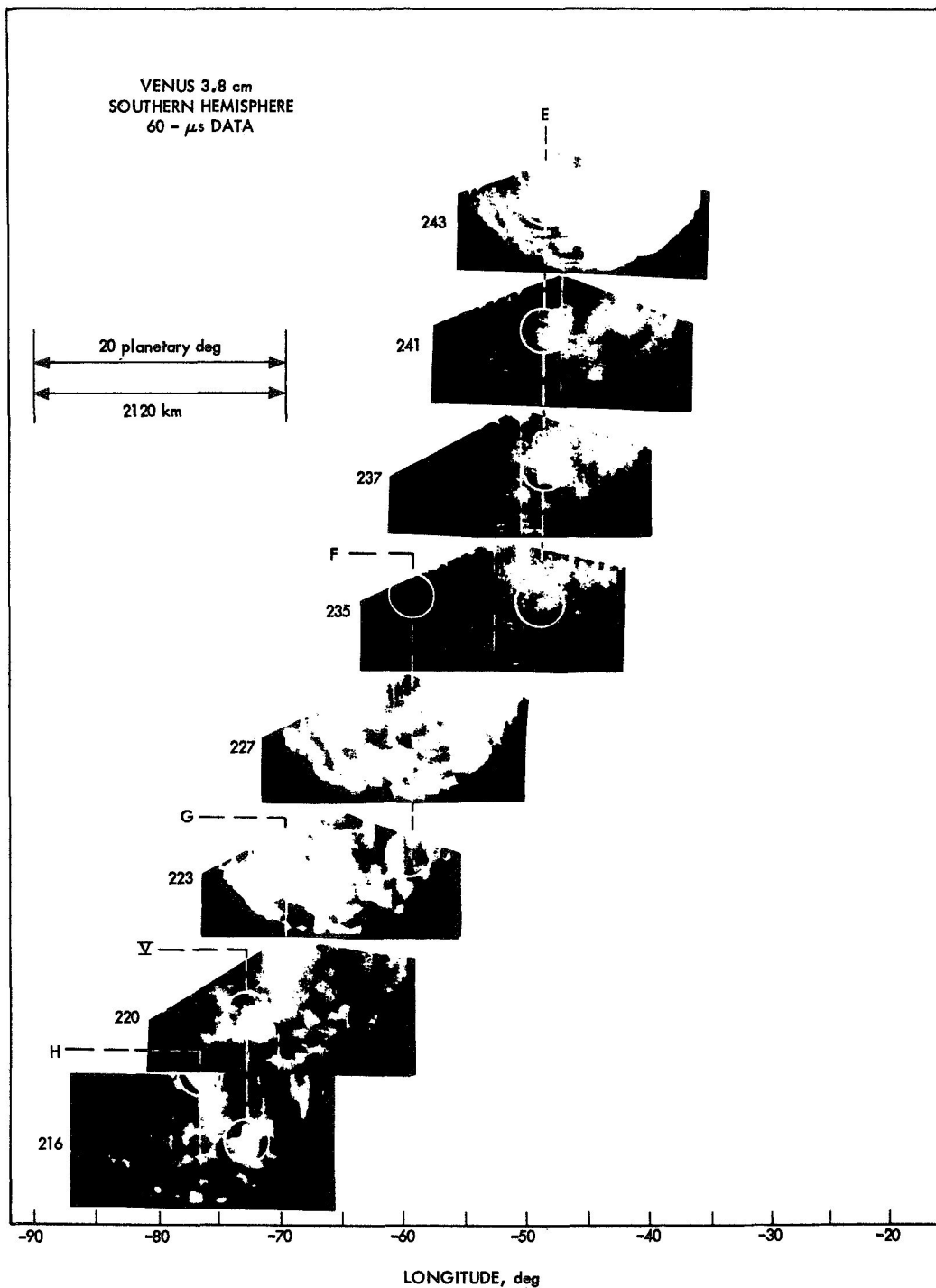
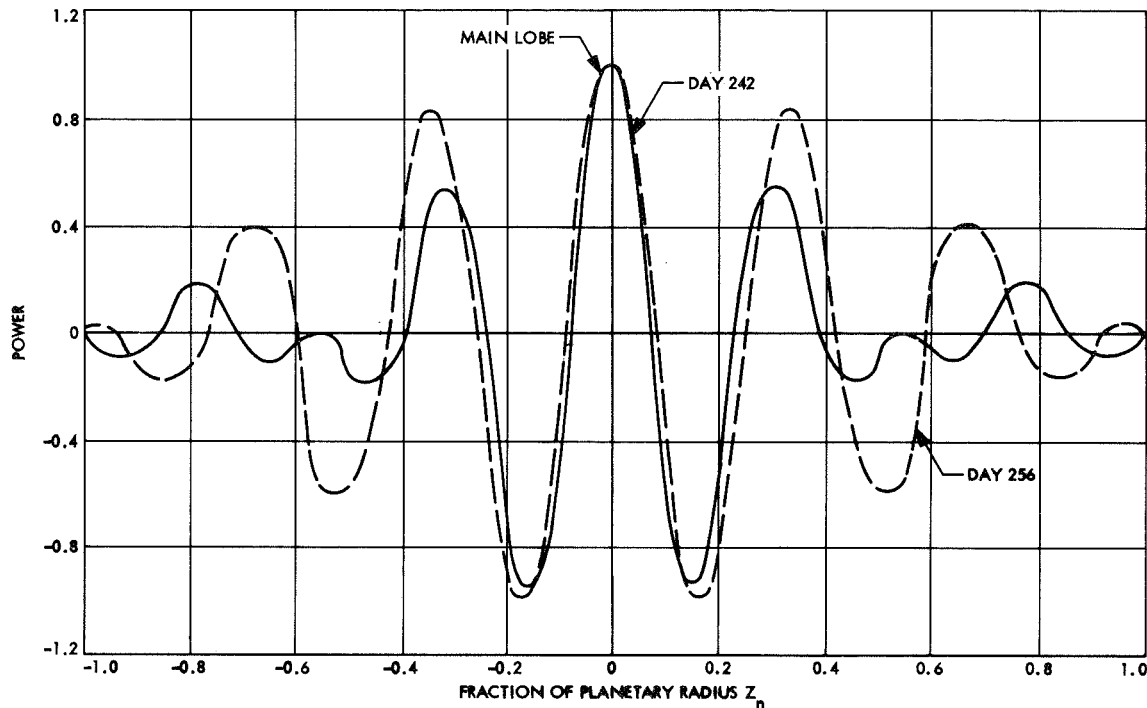


Fig. 13. Maps of reflectivity vs latitude and longitude for Venus obtained with 60- $\mu$ s pulses





**Fig. 14. Examples of the antenna patterns synthesized in the interferometer experiments of Rogers et al. (1968, Ref. 28)**

this work and in observations carried out near the time of the 1967 inferior conjunction. Also given in Table 5 is the corresponding position of what is probably the same feature as given by Carpenter (1966, Ref. 13) or Goldstein (1967, Ref. 14). The Haystack observations are separated into two classes. Those given a roman numeral are regarded as definite identifications; those given a letter are somewhat less reliable, either because there remains some uncertainty as to the hemisphere or because the feature is not very pronounced. Figure 16 shows the locations of all these features on a diagram having a Venus-centered coordinate system.

#### **B. Nature of the Anomalous Scattering Features**

There are three possible ways of accounting for the local excess radar brightness of certain regions on the disk of Venus, viz: (1) the dielectric constant and hence reflection coefficient is higher in these regions; (2) these are regions in which the surface is locally rough on the scale of the wavelength and thus backscatter preferentially; and (3) these are regions which are high (e.g., mountains), and the atmospheric absorption to the tops is less than that to the mean surface. Possibly more than one mechanism is involved, and different mechanisms may predominate in various cases. Evans (1968, Ref. 9)

reported that the increased cross section observed at longitudes near 100 deg (Fig. 1) appeared to coincide with the passage of a large anomalous region (identifiable as  $\gamma$  in Goldstein's list (1967, Ref. 14) across the disk, and suggested that this was an elevated region. On the other hand, radar ranging measurements appear to indicate a very uniform value for the equatorial radius (I. I. Shapiro, private communication). If a region was elevated, one would expect it to appear increasingly bright relative to its environs as it approached the limb, owing to the secant dependence of the absorption along the path. We have tested this prediction for the isolated feature A in Carpenter's list (1966, Ref. 13). Figure 17 shows the relative intensity of A obtained from ratio plots such as Fig. 12 as a function of the longitude. There seems no definite tendency for A to brighten as it approaches the limb, and thus we conclude that this feature at least is not particularly elevated. Figure 18 shows a similar plot for Haystack II (i.e., the peak of the complex region identified by Goldstein as  $\beta$ ). It is interesting to note that this region brightens relative to its environs as it moves away from the subradar point, as would be expected if it was rough. Yet it does not yield a lower reflectivity than an equivalent smooth area when it lies at the subradar point. This must mean that, in addition to being rough, the average reflectivity is higher

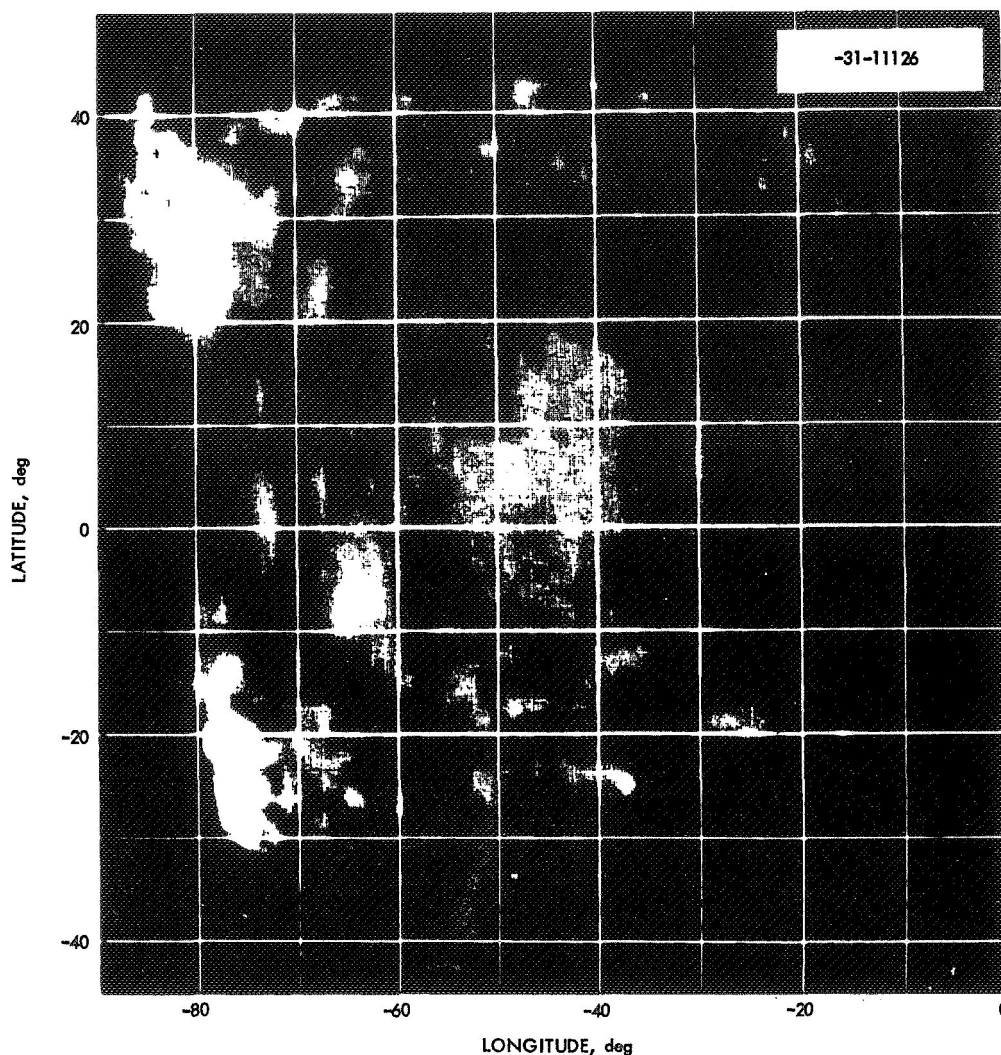


Fig. 15. Map of the radar brightness of Venus after normalizing for the mean dependence on  $\phi$  (Fig. 6) obtained by summing maps made with an interferometer system over a number of days (Rogers et al., 1968 Ref. 28)

also. An increase in reflectivity, on the other hand, cannot be made to account for the increased relative brightness as the feature moves from the subradar point. Thus it seems that increases in both the roughness and reflection coefficient are involved in the case of Haystack II. In view of the smooth appearance of the largest part of the surface of Venus, we are tempted to conclude that (as on the moon) an efficient erosion process is at work. If this is so, then these rough regions are presumably young features on the surface and may even be of impact origin.

## VI. Discussion

The atmospheric attenuation of radio waves at 3-cm wavelength in a  $\text{CO}_2$  atmosphere has been discussed by,

among others, Barrett (1961, Ref. 29) and Barrett and Staelin (1964, Ref. 30). Since  $\text{CO}_2$  is a symmetrical molecule possessing no dipole moment, it is not a resonant absorber and can be made to absorb only in a transient manner, i.e., during the course of a collision. The absorption coefficient thus varies with the square of the pressure. Calculations performed by Barrett (1961, Ref. 29), Kuzmin (1968, Ref. 31), and others suggest that the microwave emission spectrum of Venus is consistent with a surface pressure of the order of 20–30 atmospheres of  $\text{CO}_2$ , provided that the surface temperature is raised to 650–700°K. This model cannot, however, account for the absorption of 3.8-cm radar signals inferred from the measurements reported above ( $3 \text{ dB} < A < 5 \text{ dB}$ ). If the Soviet pressure and temperature curves are extrapolated to higher values, then it would appear that the total

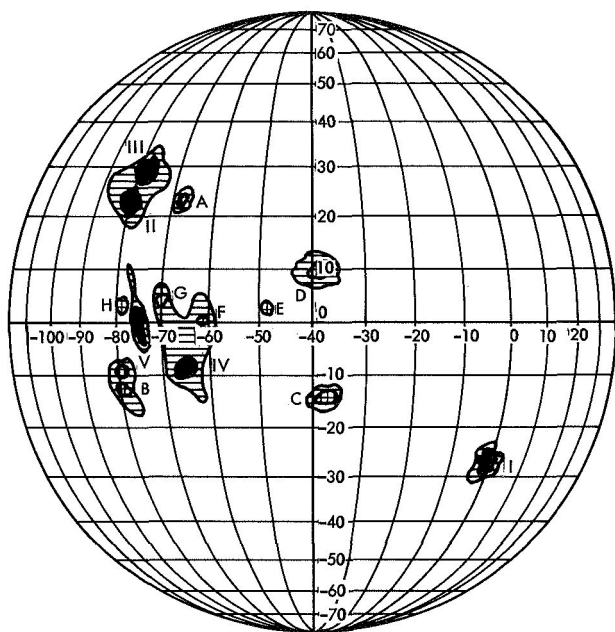


**Fig. 16.** Locations of features identified in Haystack observations as anomalously reflecting regions (Table 5)

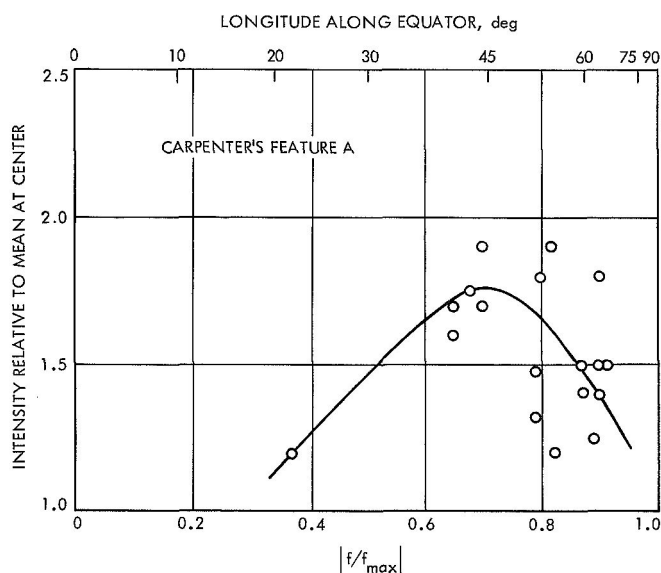


**Fig. 17.** Plot of the relative intensity of the isolated feature "Carpenter A" as a function of position in ratio plots such as Fig. 11

absorption implied by the radar results can be attained when the surface pressure is raised to  $\sim 100$  atmospheres (Kuzmin, 1968, Ref. 31; Thaddeus, private communication). This value depends somewhat upon the assumptions

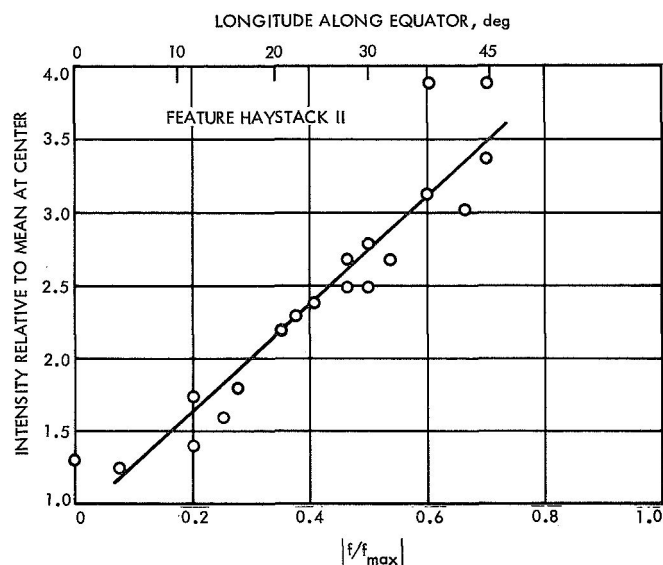


**Fig. 18.** Plot of the relative intensity of the complex region Haystack II as a function of position in the plots such as Figs. 11 and 12

made concerning the presence of water vapor and the precise way in which the temperature and pressure curves are extrapolated. Alternatively, the observed absorption can be achieved by introducing into the atmospheric model a resonant microwave absorber. Water vapor is one such molecule, but limits on the amount that may be invoked exist from (1) the presence of a detectable absorption line in the microwave emission spectrum at 1.34-cm wavelength, and (2) the Soviet probe results which seem to preclude  $H_2O$  as the responsible absorber. The radar range determination of the radius of Venus as  $\sim 6050$  km (Ash et al., 1967, Ref. 32, and 1968, Ref. 33; Melbourne et al., 1968, Ref. 34), together with the results of the *Mariner V* probe (Kliore et al., 1968, Ref. 35) suggest that the former explanation (high surface pressure) is the correct one.

Measurements of the average scattering behavior show that Venus is significantly smoother than the moon, although as regards the moon there is a tendency for the apparent roughness to increase as the wavelength of the exploring signal is shortened. Regions of anomalously high reflectivity have been located by means of experiments carried out using, among others, a radar interferometer. Table 5 summarizes the location of those features visible near inferior conjunction.

In summary, the new work reported here confirms and extends somewhat earlier observations at JPL of the

location of anomalously reflecting regions on the disk of Venus. Using the coordinate system defined in Section III, we find that the largest regions of anomalous reflectivity are centered approximately at  $-80$  deg longitude,  $26$  deg latitude, and  $-70$  deg longitude,  $-5$  deg latitude. Each of these extends over a region of the order of  $10 \times 10$  deg and appears to contain a number of centers. Since these two features tend to lie at the same doppler shift, it is difficult to separate them using doppler and/or delay-doppler resolution alone, and the interferometer measurements of Rogers et al. (1968, Ref. 28) represent a considerable advance. Despite this, some misidentification may have been made, and in any event it seems doubtful that these regions have been fully resolved. When this is done, it is likely that they will be seen to be so complex that the idea of locating individual features will have to be abandoned. Elsewhere on the disk there are isolated regions of high reflectivity that have not been fully resolved in the measurements made thus far.

It is suggested that the principal difference between the anomalously bright regions and their environs is that the bright regions are rougher on a scale comparable with the wavelength and probably also denser. The reason for such differences is not known. Possibly these features are of external origin (e.g., impact craters) though internal effects (e.g., convection cells) may be capable of giving rise to differences in surface roughness.

### Acknowledgment

We are indebted to numerous colleagues for their help in operating the Haystack and Westford radar systems with which these results were obtained. We are also grateful for the continued interest and support of J. S. Arthur, H. H. Hoover, P. B. Sebring, M. L. Stone, and others responsible for the management of these facilities. The work reported here was supported by the U.S. Air Force.

### References

1. Pettengill, G. H., and Shapiro, I. I., "Radar Astronomy," *Ann. Rev. Astron. and Astrophys.*, Vol. 3, pp. 377-410, 1965.
2. Evans, J. V., "Radar Signatures of the Planets," *Ann. N.Y. Acad. Sci.*, Vol. 140, pp. 196-257, 1966.
3. Eshleman, V. R., "Radar Astronomy," *Science*, Vol. 158, pp. 585-597, 1967.
4. Pettengill, G. H., "Radar Studies of the Planets," in *Radar Astronomy*, Chapter 6. Edited by J. V. Evans and T. Hagfors. McGraw-Hill, New York, 1968.
5. Karp, D., Morrow, W. E., Jr., and Smith, W. B., "Radar Observations of Venus at 3.6 cm," *Icarus*, Vol. 3, pp. 473-475, 1964.
6. Evans, J. V., Ingalls, R. P., Rainville, L. P., and Silva, R. R., "Radar Observations of Venus at 3.8 cm Wavelength," *Astron. J.*, Vol. 71, pp. 902-915, 1966.
7. Evans, J. V., and Ingalls, R. P., "Absorption of Radar Signals by the Atmosphere of Venus," *J. Atmos. Sci.*, Vol. 25, pp. 555-559, 1968.
8. Nichols, B. E., and Karp, D., "West Ford Radar and Microwave Equipment," *Proc. IEEE*, Vol. 52, pp. 576-588, 1964.
9. Evans, J. V., "Variations in the Radar Cross Section of Venus," *Astron. J.*, Vol. 73, pp. 125-134, 1968.
10. Ingalls, R. P., et al., *Reflection Properties of Venus at 3.8 cm*. Lincoln Laboratory, Massachusetts Institute of Technology, Cambridge, Mass. (report in preparation, 1968).

## References (contd)

11. Weiss, H. G., "The Haystack Microwave Research Facility," *IEEE Spectrum*, Vol. 2, pp. 50-69, 1965.
12. Hagfors, T., "Backscattering from an Undulating Surface with Applications to Radar Returns from the Moon," *J. Geophys. Res.*, Vol. 69, pp. 3779-3784, 1964.
13. Carpenter, R. L., "Study of Venus by CW Radar," *Astron. J.*, Vol. 71, pp. 142-152, 1966.
14. Goldstein, R. M., "Radar Studies of Venus," in *Moon and Planets*, p. 126. Edited by A. Dollfus. North Holland, Amsterdam, 1967.
15. Evans, J. V., et al., "Radio Echo Observations of Venus and Mercury at 23 cm Wavelength," *Astron. J.*, Vol. 70, pp. 486-501, 1965.
16. Kotel'nikov, V. A., et al., "Radar Observations of Venus in the Soviet Union in 1964," *Dokl. Akad. Nauk.*, No. 3, pp. 50-53, 1965.
17. Pettengill, G. H., et al., "A Radar Investigation of Venus," *Astron. J.*, Vol. 67, pp. 181-190, 1962.
18. Pettengill, G. H., Dyce, R. B., and Campbell, D. B., "Radar Measurements at 70 cm of Venus and Mercury," *Astron. J.*, Vol. 72, pp. 330-337, 1967.
19. Klemperer, W. K., Ochs, G. R., and Bowles, K. L., "Radar Echoes from Venus at 50 Mc/s," *Astron. J.*, Vol. 69, pp. 22-28, 1964.
20. James, J. C., and Ingalls, R. P., "Radar Observations of Venus at 38 Mc/s," *Astron. J.*, Vol. 69, pp. 19-22, 1964.
21. Green, P. E., "Radar Measurements of Target Scattering Properties," in *Radar Astronomy*, Chapter 1. Edited by J. V. Evans and T. Hagfors. McGraw-Hill, New York, 1968.
22. Muhleman, D. O., "Radar Scattering from Venus and Mercury at 12.5 cm," *J. Res. NBS*, Vol. 69D, pp. 1630-1631, 1965.
23. Hagfors, T., "Relationship of Geometric Optics and Autocorrelation Approaches to the Analysis of Lunar and Planetary Radar Echoes," *J. Geophys. Res.*, Vol. 71, pp. 379-383, 1966.
24. Evans, J. V., "Radar Studies of the Moon," *Radio Sci.*, Vol. 69D, pp. 1637-1659, 1965.
25. Beckmann, P., and Klemperer, W. K., "Interpretations of the Angular Dependence of Backscattering from the Moon and Venus," *Radio Sci.*, Vol. 69D, pp. 1669-1677, 1965.
26. Evans, J. V., and Hagfors, T., "Study of Radio Echoes from the Moon at 23 Centimeter Wavelength," *J. Geophys. Res.*, Vol. 71, pp. 4871-4899, 1966.
27. Goldstein, R. M., "Preliminary Venus Radar Results," *J. Res. N.B.S.*, Vol. 69D, pp. 1623-1625, 1965.
28. Rogers, A. E. E., et al., *A Radar Interferometer Study of Venus at 3.8 cm*, Technical Report 444. Lincoln Laboratory, Massachusetts Institute of Technology, Cambridge, Mass., Feb. 14, 1968.

### References (contd)

29. Barrett, A. H., "Microwave Absorption and Emission in the Atmosphere of Venus," *Astrophys. J.*, Vol. 133, pp. 281-293, 1961.
30. Barrett, A. H., and Staelin, D. H., "Radio Observations of Venus and the Interpretations," *Space Sci. Rev.*, Vol. 3, pp. 109-135, 1964.
31. Kuzmin, A. D., Paper Presented to the 2nd Arizona Conference on Planetary Atmospheres, Tucson, Arizona, Mar. 1968.
32. Ash, M. E., Shapiro, I. I., and Smith, W. B., "Astronomical Constants and Planetary Ephemerides Deduced from Radar and Optical Observations," *Astron. J.*, Vol. 72, pp. 338-350, 1967.
33. Ash, M. E., et al., "The Case for the Radar Radius of Venus," *Science*, Vol. 160, pp. 985-987, 1968.
34. Melbourne, W. G., Muhleman, D. O., and O'Handley, D. A., "Radar Determination of the Radius of Venus," *Science*, Vol. 160, pp. 987-989, 1968.
35. Kliore, A., Levy, G. S., Cain, D. L., Fjeldbo, G., and Rasool, S. I., "Atmosphere and Ionosphere of Venus from the Mariner V S-Band Radio Occultation Measurement," *Science*, Vol. 158, pp. 1683-1688, 1967.

# Radar Measurements of Lunar Surface Roughness

Allan Shapiro, E. A. Uliana, and B. S. Yaplee

E. O. Hulburt Center for Space Research

Naval Research Laboratory

Washington, D. C.

*Direct topographic information about planetary surfaces is obtained from radar measurements if the transmitted pulse is sufficiently narrow to resolve the surface structure. The height distribution of the reflecting areas in the observed region can be derived from the shape of the radar echo rise time. The Naval Research Laboratory high-range resolution lunar echoes are presented to illustrate the effect of surface topography on the shape and structure of the early part of the radar echo. Earth-based radar observations of planetary surfaces are limited by restricted coverage and sensitivity requirements. These limitations can be overcome by utilizing radar observations from planetary orbiters with high inclination. In particular, observations from an orbiting radar around Venus would probably provide the only direct information about the planet surface topography.*

## I. Introduction

Planetary radar measurements in the past have been primarily concerned with the determination of radar reflectivity of the observed surface. For the moon, the reflectivity of the surface was obtained with relatively high spatial resolution (Ref. 1). The variations of the radar reflectivity over the lunar surface provide estimates of surface roughness and structure.

When the radar range resolution is sufficiently increased so that the surface structure is resolved, and the observations are restricted to the initial portion of the reflecting surface, then the height variations of the sub-

radar region can be directly measured. The height discrimination of the radar probing pulse reveals the distribution of reflecting areas at different heights as the pulse traverses sequential layers of the surface structure. Thus an analysis of the early part of the radar echo will provide a description of the associated topography by relating the amplitude of each range interval with reflecting surfaces at the given height. In this paper the basic relations between the shape of the radar echo rise time and the physical structure of the reflecting surface are discussed, and experimental results are presented by comparing the rise time of lunar echoes with photographs of the observed surface structure, which confirms the expected relationship.

## II. Geometry of the NRL Lunar Radar Observations

The basic geometry and measurement procedure of the Naval Research Laboratory (NRL) lunar radar observations have been described by Shapiro et al. (Ref. 2). As shown there, the incident pulse resolves the curved surface of the moon into a series of concentric annular rings, whose projected areas are equal. The radius of the first circular area for a  $1\text{-}\mu\text{s}$  range resolution is about 20 km on the moon and corresponds to an angular resolution of 20 arc seconds.

## III. Effect of Surface Structure on Pulse Echo Rise Time

The effect of a few basic types of possible surface structures on the shape of the radar return rise time will be considered. To simplify the analysis, it is assumed that the reflected energy is proportional to the projected area in the layer for a given range interval and variations of the reflection coefficient will be neglected. In Fig. 1, the expected radar returns from a smooth surface (that is, a surface whose structure is less than 1 range resolution) and a uniformly rough surface extending to 5 range resolution intervals are compared. For the smooth surface, the energy in the first range interval is reflected from the whole initial circular area, and thus the radar echo in-

creases to its full amplitude within 1 range interval. For the rough surface, on the other hand, the energy in the first range interval is reflected from the projected areas of the highest layer on the initial circular region, which for the assumed uniform height distribution corresponds to only 1/5 of the full amplitude. In the second range interval, the energy is reflected from the second layer of the circular area and thus increases the radar echo to 2/5 of the full amplitude. The returned energy increases linearly until the lowest layer of the circular area is reached, which for the assumed conditions occurs after 5 range resolution intervals. When the full amplitude is attained, the energy is reflected from five different layers, ranging from the top layer of the fifth annular ring to the bottom layer of the initial circle. The amplitude in the following range intervals will remain invariant, as the corresponding energy is reflected from five contiguous annular rings, whose radii progressively increase with the number of range intervals. Thus the rise time for this rough surface is increased by a factor of 5, and in general the rise time is proportional to the size of the surface roughness.

## IV. Nonuniform Height Distribution

The actual surface of a planet or the moon will consist of both rough and smooth structure in a given resolved area, and the particular combination will determine the shape of the radar echo rise time. In the general case, the early part of the radar echo can be divided into five distinct groups of range resolution intervals, as shown in Fig. 1, whose associated amplitudes will define the type of surface that is being observed. The amplitudes in the first and fifth group can be used as reference amplitudes for the given echo, establishing the noise level and the average return of the given region. The radar return in the fifth group is not greatly affected by any variations in elevation or depression, since the width of the annular rings decreases rapidly as the range increases, and thus any features on the surface that are located in those annular rings and beyond contribute very little to the amplitudes in the fifth group. The amplitudes of the third group of range intervals correspond to the main part of the rise time and will be associated with the large smooth areas of the observed surface. The amplitudes of the second and fourth groups are associated with reflections from mountains that are located either in the flat areas of the initial concentric annular rings or in the general vicinity. For example, consider a single mountain in a flat area with a plateau of sufficient reflecting area at the top so that the radar return can be detected. If the height

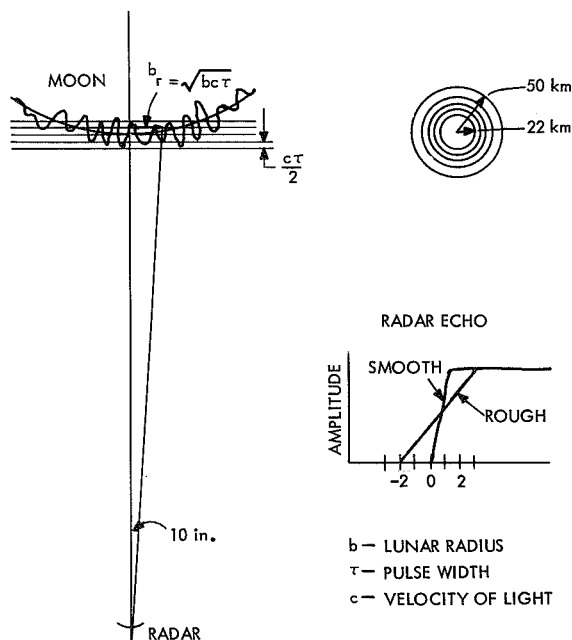


Fig. 1. Simplified geometry of lunar radar reflection with narrow pulse



of the plateau exceeds the range resolution, and the slope of the mountain is sufficiently steep, the radar echo will appear as a precursor, which precedes the main part of the echo. The separation between the precursor and the main part of the echo indicates the minimum height of the mountain structure. The actual height equals the measured height only if the feature is located in the initial circular area. Since a higher mountain located in one of the later annular rings would produce the same precursor, it is not possible from one observation to associate the location of the mountain with a particular annular ring. If, however, the radar beam scans the observed surface, as is usually the case, and the position and motion of the radar beam relative to the surface are known, the location and height of the feature can be derived from an analysis of the time motion of the precursor relative to the main echo. The equations for such an analysis are derived in an appendix. They show that at least three independent observations are required to determine the coordinates of one feature and that the accuracy of the position determination improves as the distance between the mountain and the subradar point increases. However, the position determination has, in general, a two-fold ambiguity, except when the feature is located directly on the subradar track. This ambiguity can be resolved if the region is scanned from two different directions.

Alternately, if a large mountain or depression is present in one of the later annular rings, it will add or subtract energy in one or more of the later range intervals and thus introduce fine structure into the echo after the main part of the rise time. The location and height of such a feature can be similarly obtained, using the analysis described in the appendix, if its time history relative to the main part of the rise time is traced as the radar scans across the region.

When two or more features are present that are resolved either in height or location by the radar system, the location and height of such features can be obtained from the same analysis if more independent observation equations are available. In general, quantitative description of the observed region is possible, indicating both the extent of roughness and relative abundance of mountain structure and smooth areas. In complex regions, the flat areas may appear as plateaus or depressions at different heights which will introduce fine structure into the main part of the radar echo rise time. Thus it can be expected that lunar radar echoes with a range resolution that resolves the surface structure should show variations of rise time structure, which after proper analysis can provide information about the lunar surface topography.

## V. Experimental Results

The NRL lunar radar measurements obtained radar echoes from different surface structures ranging from relatively smooth areas near Hyginus and Mösting to considerably more complex areas near the Ukert and Herschel craters. In Fig. 2, six typical radar echoes are shown. The echoes have been arranged in order of increasing surface roughness starting from the top. The first three echoes are associated with large smooth surfaces, as can be deduced from the steep slope of the rise time. The top echo comes from the Hyginus region, and as seen in the photograph of the region in Fig. 3, the subradar surface for the first several range intervals is relatively smooth except for a few small craters and the Rima Hyginus. In Fig. 3, circles represent nominal spatial resolution due to  $1\text{-}\mu\text{s}$  incident pulse (1-10, 16). The radar moves left toward Triesnecker E located between Ukert on top and Triesnecker at the bottom. In the later range intervals, the rapid increase in elevation near Triesnecker and the high mountain ridges near Ukert causes the fine structure in the latter part of

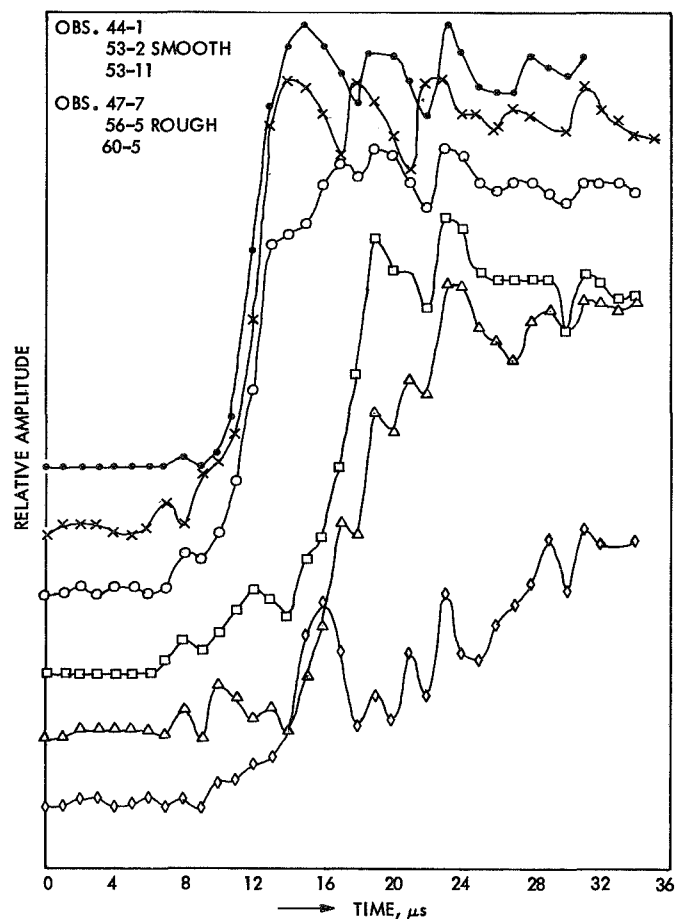


Fig. 2. Typical lunar radar echoes from different areas

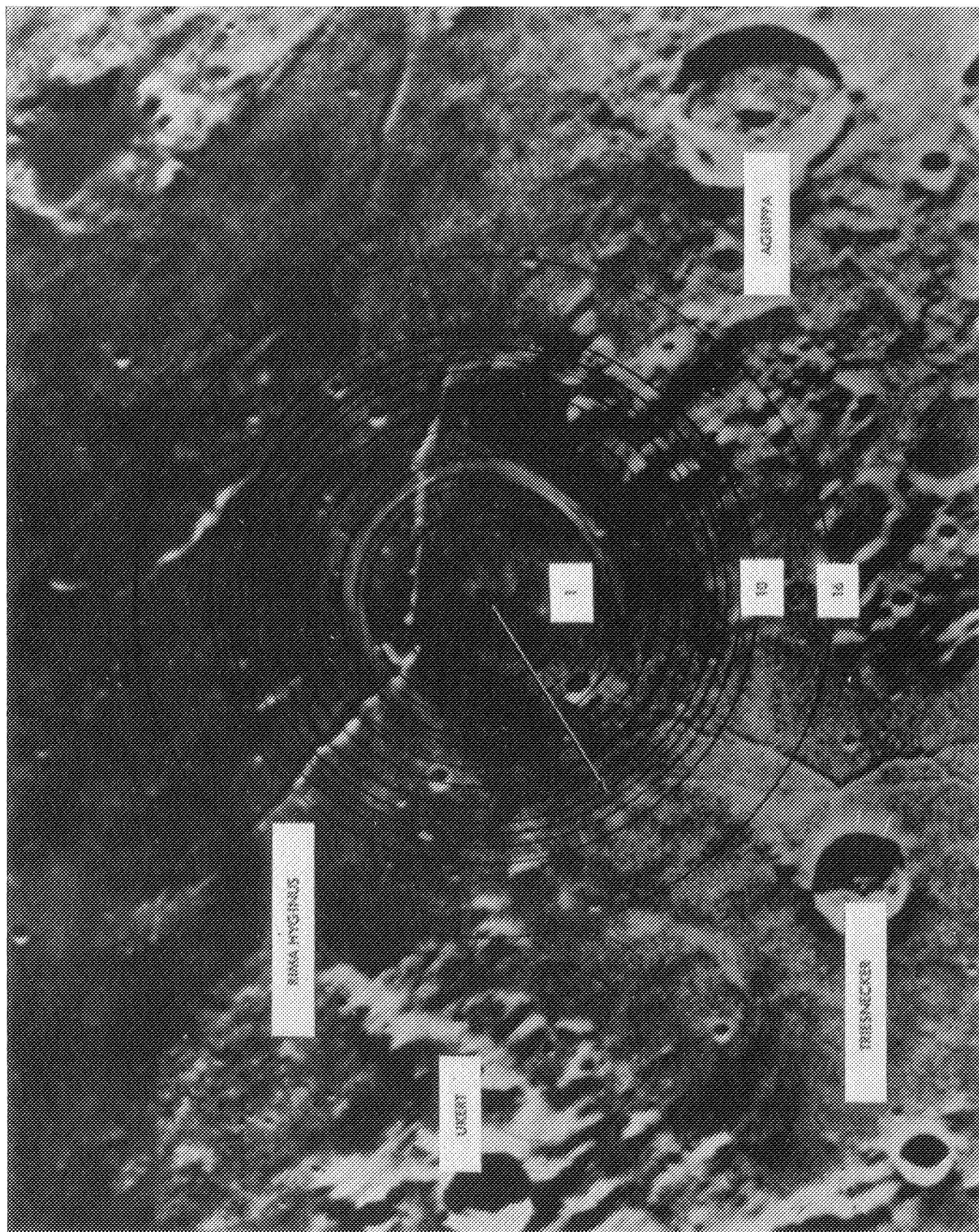
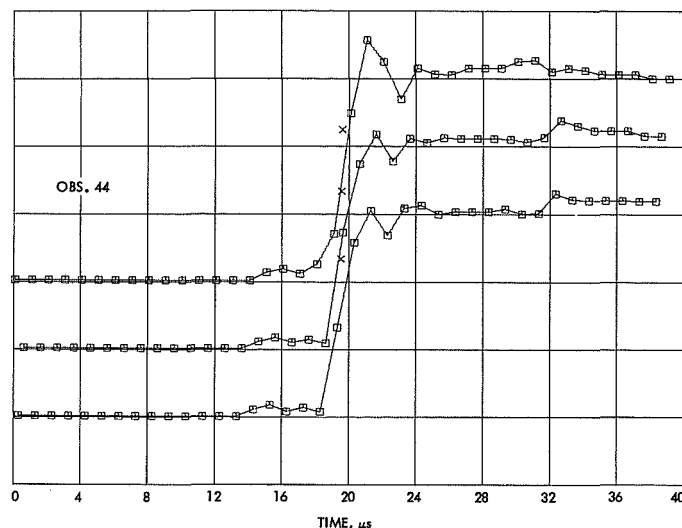


Fig. 3. Hyginus region

the echo. This is more evident in Fig. 4, where the time shift of the fine structure is seen as the radar subearth point approaches the Triesnecker and Ukert ridges. The echoes in Fig. 4 as well as in the subsequent radar echo time displays are obtained at about 1-h intervals, corresponding to a displacement of the subradar point by a few kilometers.

The second and third echo come from the Mösting region shown in Fig. 5. Mösting is located in the southwest. The radar moves toward Mösting, and the last observation is located just above Mösting wall. This area, although mainly flat, has a few mountains (Sömmering) in the subradar region. These can be deduced from the precursor of the radar echo to be about 600 m high. The fine structure in the latter part of the echo can be again associated with the increase in elevation near the Mösting crater, and the motion of this feature is shown in the radar echo time history of Fig. 6, as the crater is approached by the radar. At the same time, the displacement of the Sömmering mountains relative to the subearth point is observed from the joining of the precursor with the main part of the rise time in the later echoes. The second peak is probably associated with the Schroeter and Sömmering ridges and with the height variations near Flammarion.

The bottom three echoes of Fig. 2 are associated with areas of considerable roughness, and this is indicated both by the large precursor and long rise time of the radar echo. These echoes are more difficult to interpret, for the radar return is made up of the reflected energy from many areas, which may be located in different spatial resolution intervals, but which all happen to be in the same range interval as viewed from the radar system. However, the width of the precursor and the width of the main part of the radar echo will provide quantitative description of the minimum height distribution and roughness of the observed area. For example, the surface for the fourth echo is located directly in the Ukert region, as seen in Fig. 7. The radar moves parallel to the Ukert ridge. The presence of the large smooth area in the Hyginus region preserves the monotonic rise of the main part of the echo, but the slope is decreased by the presence of considerable height variations in the northern part near Ukert. The extended precursor indicates a minimum height of 1.5 km for the mountain structure. The height of the mountain ring around Ukert is about 2.5 km from optical measurement, and owing to the displacement relative to the subradar point should appear as about 1.8 km in the radar echo. As the radar scans the plains parallel to the mountain ridges of Ukert, the fine



**Fig. 4. Radar echoes associated with Hyginus region**

structure does not move appreciably relative to the main part of the rise time (see Fig. 8).

The next echo comes from a similar region except that a large plateau is present. The region is shown in Fig. 9 and is located near Lalande on the left. The radar moves toward Lalande, passing Lalande E on the south. The presence of the large southern plateau introduces fine structure into the main part of the rise time, but this structure is interrupted during the middle of the scan by the depression of Lalande R as seen in Fig. 10.

Finally, the last echo of Fig. 2 is associated with a complex area, where rather extensive mountain structure is interspersed with flat areas at different heights. The region is shown in Fig. 11 and is located near the crater Herschel. The radar moves away from Herschel (on the right) toward Flammarion; the large smooth southern area is Ptolemaeus. The considerable complexity of the area produces a fine structure in the main part of the rise time of the echo where the peaks are associated with large plateaus at the given range intervals. The time history of the radar echoes shown in Fig. 12 indicates that one of the plateaus is located in the path of the subradar point and that its depression relative to the mountain peaks is at least 900 m.

To show the consistency of the effect of the surface structure on the pulse rise time, two radar echoes which were measured on two different days from the same area are shown for both a rough and smooth area in Figs. 13 and 14. Little variation is seen in the radar rise time structure.



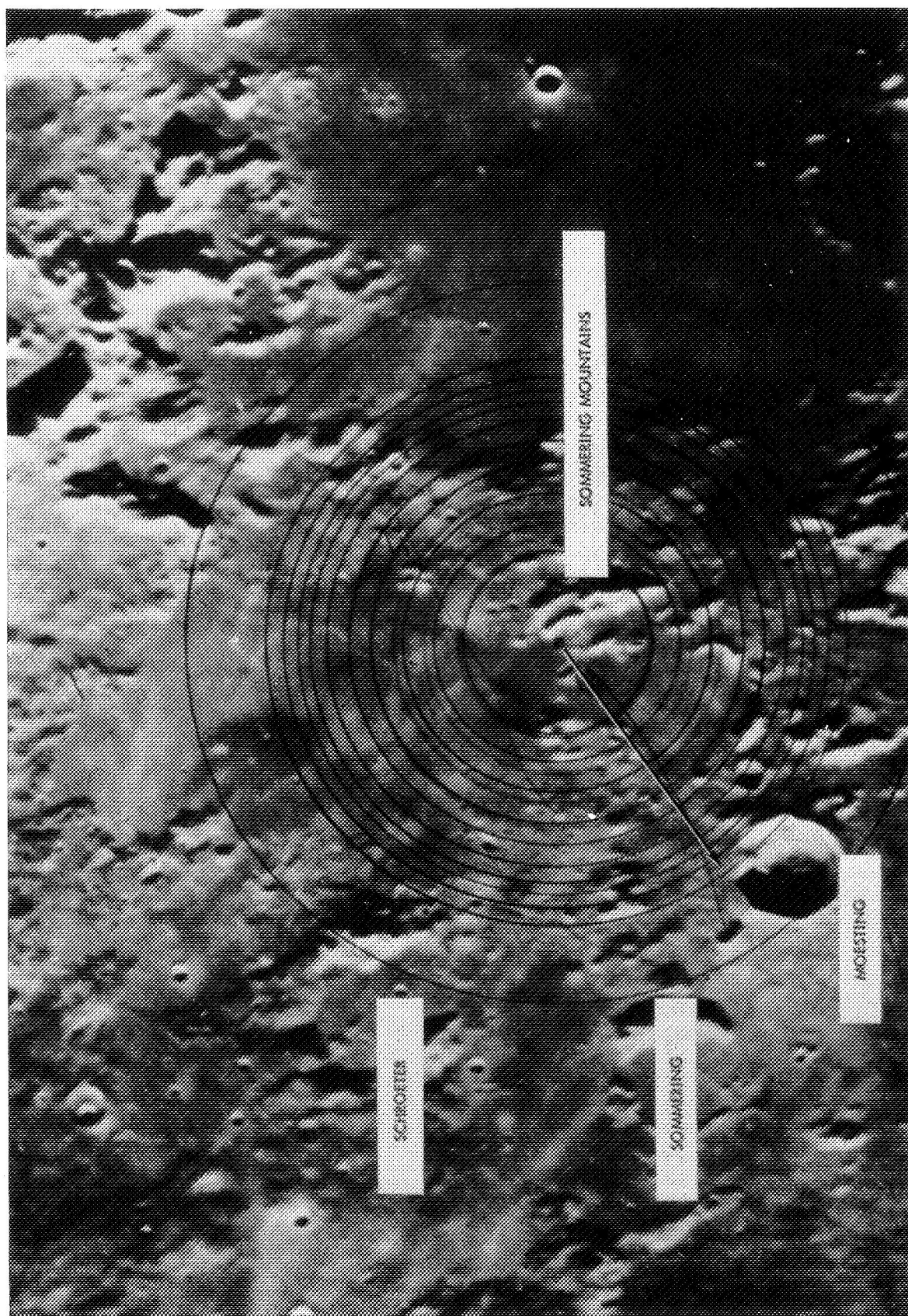
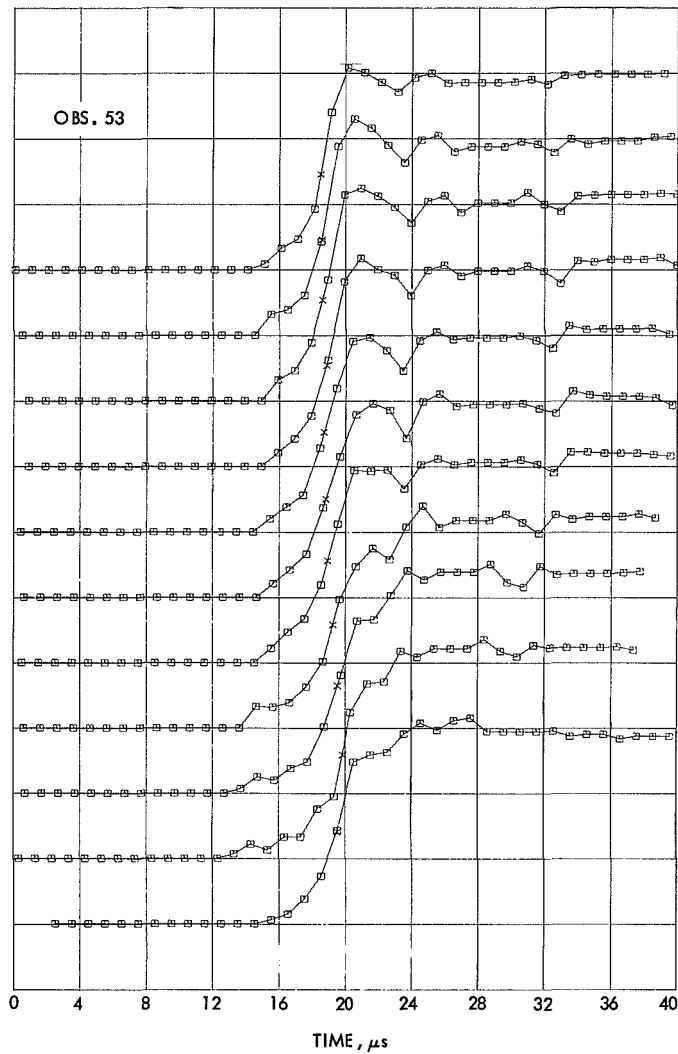


Fig. 5. Mösting region



**Fig. 6. Radar echoes associated with Mösting region**

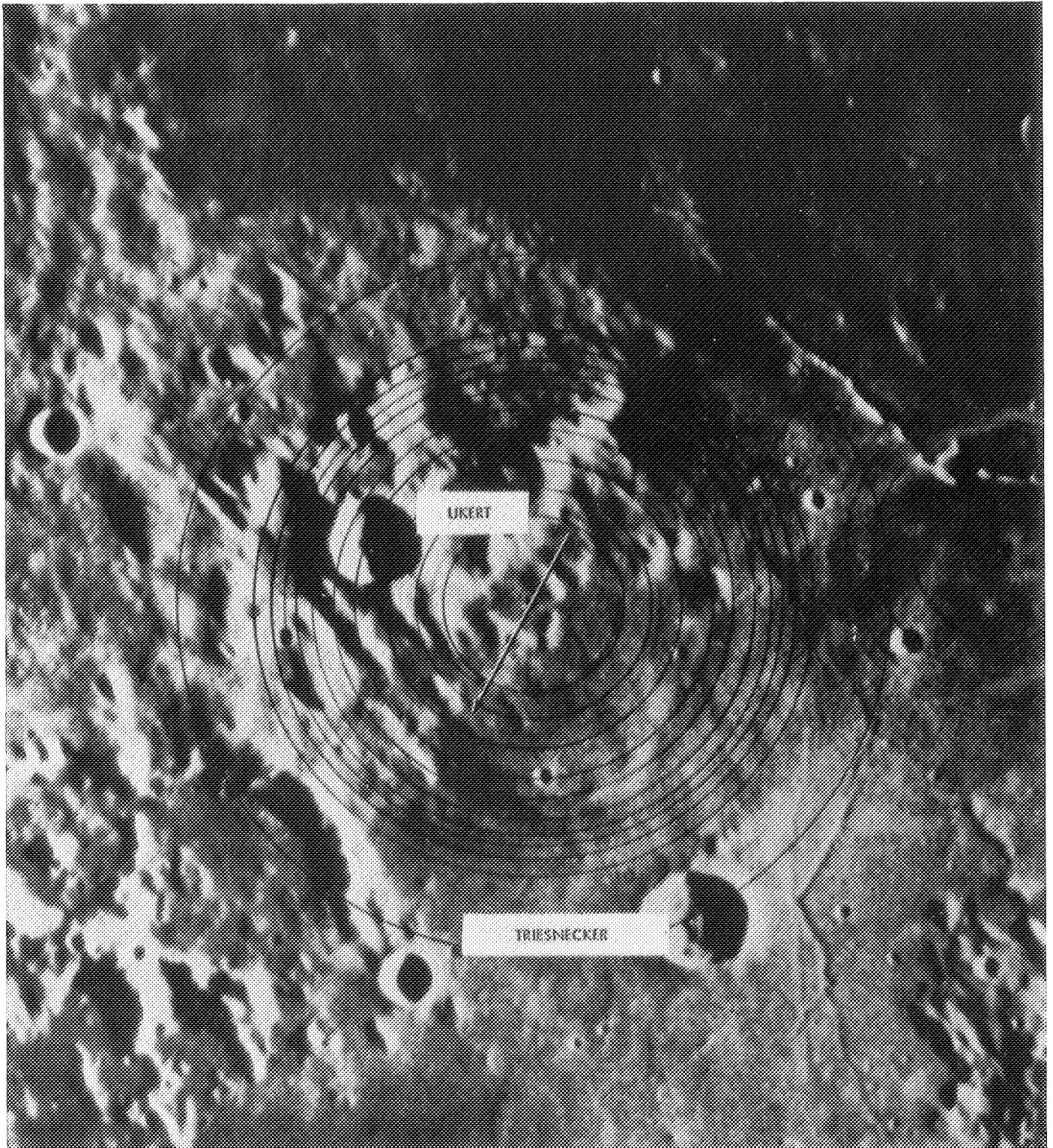
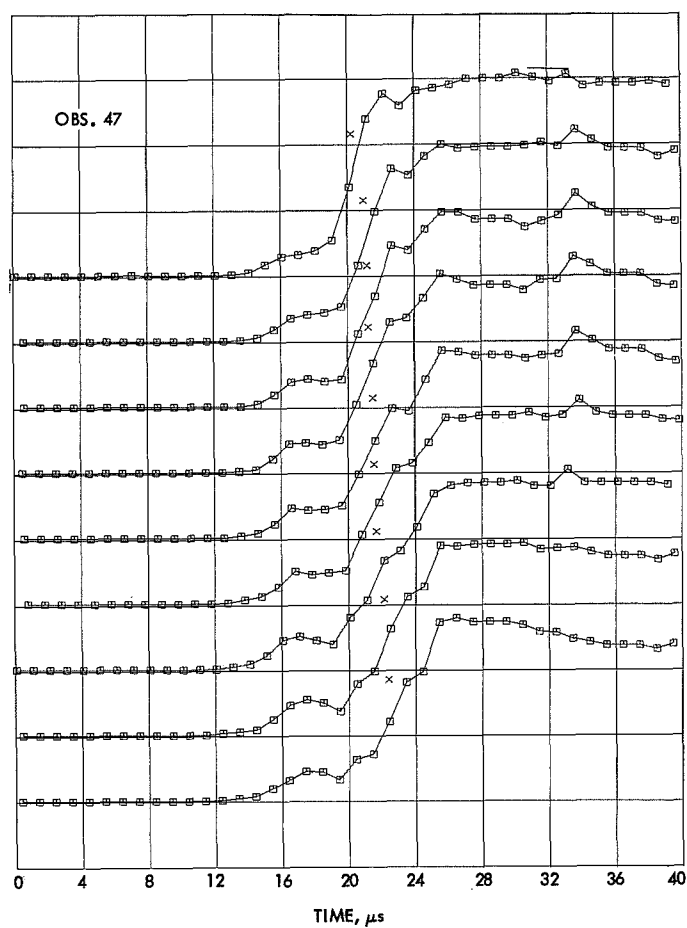


Fig. 7. Ukert-Hyginus region



**Fig. 8. Radar echoes associated with Ukert-Hyginus region**



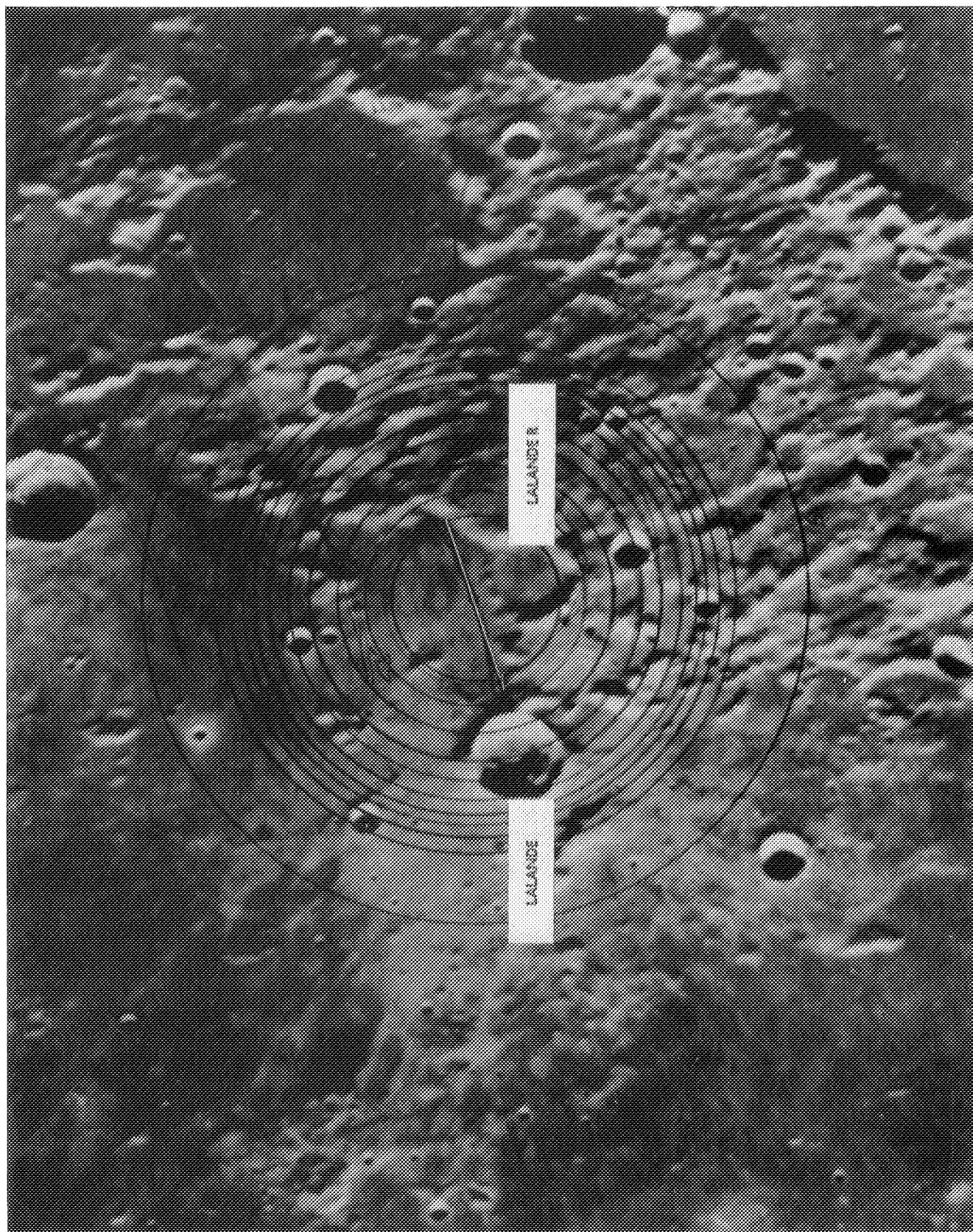
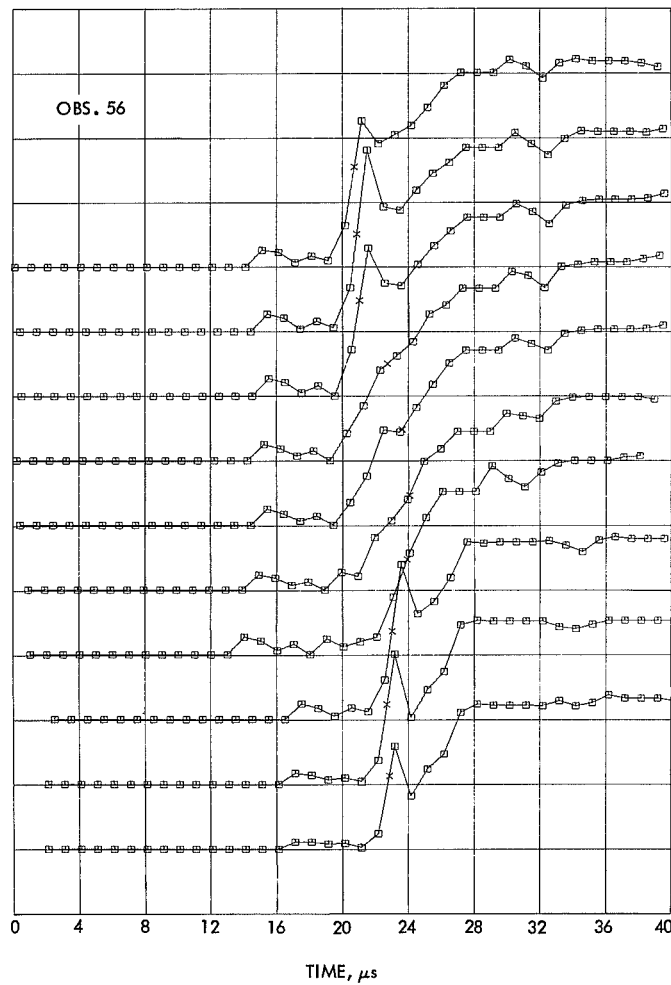


Fig. 9. Lalande region





**Fig. 10. Radar echoes associated with Lalande region**

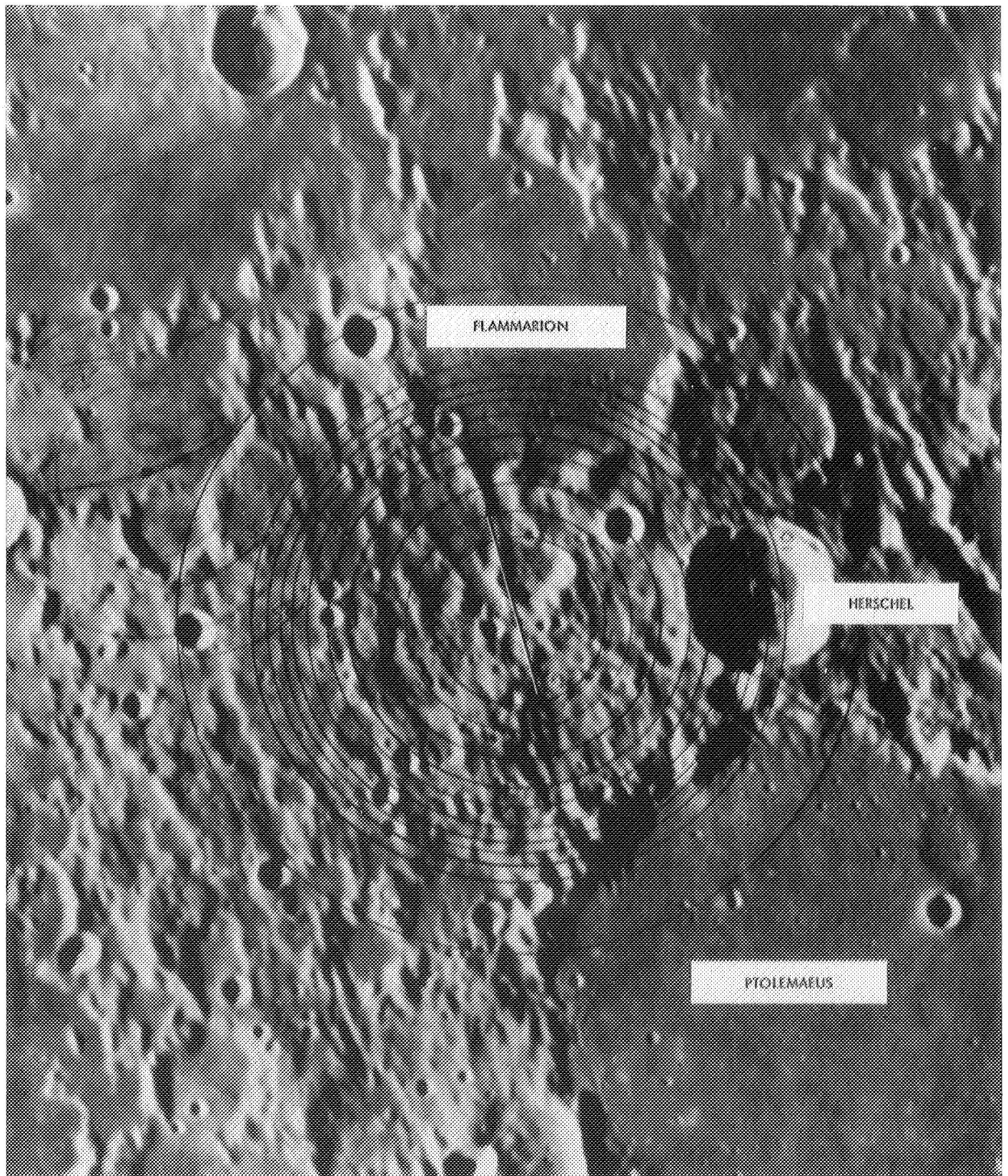
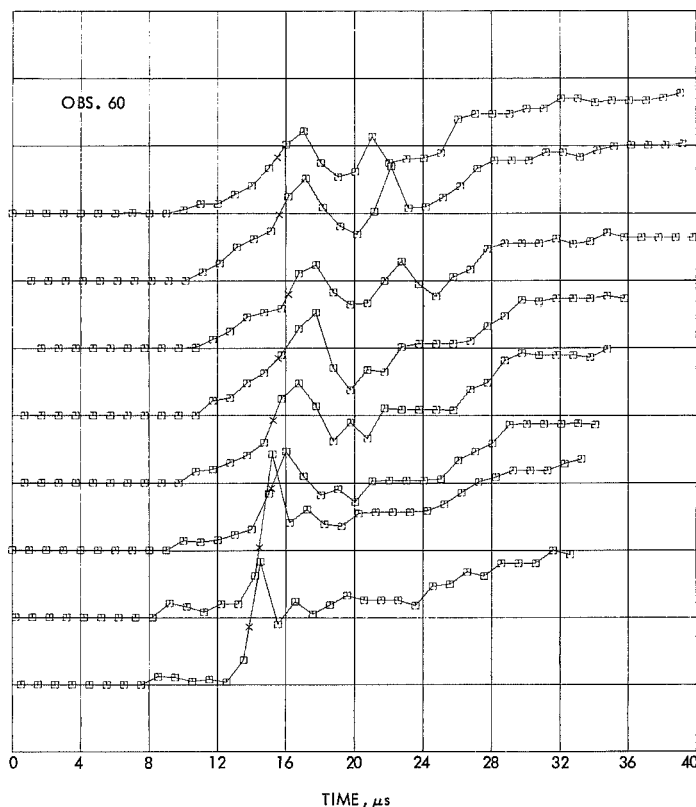
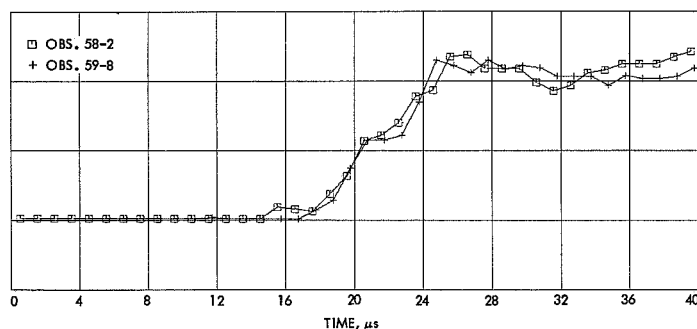


Fig. 11. Herschel region



**Fig. 12. Radar echoes associated with Herschel region**



**Fig. 13. Comparison of radar echoes from same rough area**

## VI. Discussion and Conclusions

The combination of accurate height determination with moderate spatial resolution can provide useful information about surface topography in many applications. The ability to determine the height variations and extent of roughness of a given area and the location and height of prominent features on planetary surfaces can complement the photographic observations where available. In addition, estimates of the peak, mean, and minimum height can be associated with each observed area.

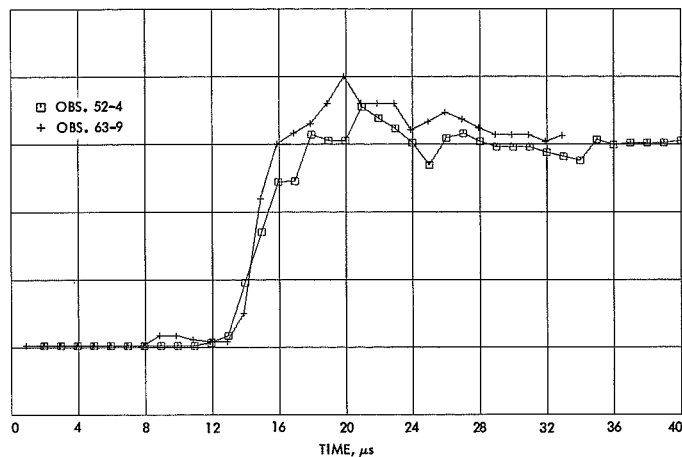


**Fig. 14. Comparison of radar echoes from same smooth area**

Radar observations from the earth are restricted in coverage to the subearth region on the moon and limited by sensitivity requirements when applied to the planets. However, if radar observations were made from two planetary orbiters, utilizing a polar and high-inclination orbit, unambiguous topographic information could be obtained over most of the planetary surface. Such measurements would also provide an accurate determination of the geometric size and shape of the given planet.

In applying this method to planetary exploration three different cases could be considered.

1. Where photographic and optical height observations are available, such as for the front side of the moon, the optical height variations could be used to calibrate the radar measurements, and the radar measurements could then be applied to obtain additional height information about the backside of the moon. Furthermore radar reference points could be established for future earth-based radar observations. Such reference points would permit high-accuracy lunar distance measurements for such applications as celestial mechanics, navigation, time synchronization, and geodesy.

2. Where photographic evidence is available or can be obtained, such as for Mars and Mercury, the radar measurements could be combined with the optical information to obtain more accurate height information.

3. However, the most interesting application of this technique is in the case of Venus, where no optical information is available. In this case, the radar observations

will probably provide the only direct information about the geometric surface structure, size, and shape of the planet. It is in this application where high range resolution radar observations may make the greatest contribution.

Finally, the radar observations could be utilized to provide estimates of the reflection coefficients of different areas, if the extent of the reflecting areas at different heights can be derived from optical observations.

### References

1. *Radar Studies of the Moon, Vol. 2*. Lincoln Laboratory, Massachusetts Institute of Technology, Cambridge, Mass., Apr. 18, 1969.
2. Shapiro, A., Uliana, E. A., Yaplee, B. S., and Knowles, S. H., "Lunar Radius from Radar Measurements," in *Space Research VIII, Moon and Planets II*, pp. 34-46, Proceedings of the VIIIth International Space Science Symposium, London. North Holland Publishing Co., Amsterdam, 1968.

## Appendix

### Plateau in a Flat Region Determination of Height and Location of an Elevated

Assume a coordinate system with the  $xy$  plane on the surface of the planet, and neglect the small curvature, for location determination of less than 200 km from the subradar point. Let  $x, y, z$  be the true location and height of a given feature, and let  $x_{0i}, y_{0i}$  be the coordinates of the subradar point, whose position and motion are known. In Fig. A-1 the radar echo at a given time and the corresponding surface structure are shown.

Let the measured height of the feature relative to the smooth flat area be  $\rho_i$ . Then the true height  $z = \rho_i + (n_i + 1/2) c\tau/2$ , where  $n_i$  corresponds to the  $n$ th annular ring in which the feature is located, and the factor  $1/2$  places it somewhere in the middle of this ring.

The number of the annular ring is then given by

$$n_i = \frac{z - \rho_i}{\frac{c\tau}{2}} + \frac{1}{2}$$

The distance of the feature relative to the subradar point can be expressed as

$$(x - x_{0i})^2 + (y - y_{0i})^2 = \left(n_i - \frac{1}{2}\right) b c \tau$$

where  $b$  is the lunar radius. Substituting for  $n_i$ , we can express the equation in terms of the coordinates of the feature, the known quantities  $x_{0i}, y_{0i}, b, c, \tau$ , and the measured quantity  $\rho_i$ , as

$$(x - x_{0i})^2 + (y - y_{0i})^2 = 2b(z - \rho_i)$$

or

$$\rho_i = z - \frac{(x - x_{0i})^2}{2b} - \frac{(y - y_{0i})^2}{2b}$$

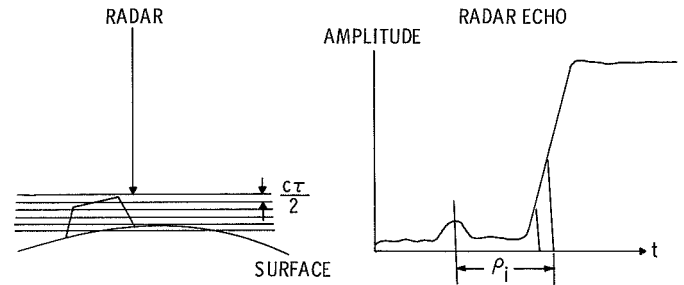


Fig. A-1. Plateau in flat region

From a series of observations made as the radar scans the region, the values of  $x, y, z$  can be derived, if three independent observations are available. However,  $x$  and  $y$  will have a two-fold ambiguity due to the squared relationship.

If an initial estimate of the position of the feature can be made from optical information, a least square fit can be applied. In this case,

$$\Delta\rho = \Delta z - \frac{x - x_{0i}}{b} \Delta x - \frac{y - y_{0i}}{b} \Delta y$$

It is seen that the accuracy of  $\Delta x$  and  $\Delta y$  is degraded since

$$\frac{x - x_{0i}}{b} \text{ and } \frac{y - y_{0i}}{b} \sim 0.01 - 0.1$$

and the accuracy of the position correction will depend on the distance of the feature relative to the subradar point being of the order of 1.5 to 15 km for a  $1\text{-}\mu\text{s}$  pulse, while the accuracy of the height measurement is equal to the range resolution of 150 m. If more than three observations are used, the accuracy for both the height and position should improve as  $(N)^{1/2}$  where  $N$  is the number of observations.



# Topography and the Surface of Mars

Alan B. Binder  
IIT Research Institute  
Chicago, Illinois

*Topographic data obtained by radar ranging along the +21-degree parallel of Mars have been correlated with surface detail. The data show that the high areas are deserts, the canals occur in broad and frequently deep valleys, and the maria occur in low areas or on slopes. The data confirm the concept that frost is deposited predominately in the high areas and add support to the concept that the dark areas are biological in nature.*

# Probing Planetary Surface and Subsurface Structures With Bistatic Radar

G. Leonard Tyler  
Center for Radar Astronomy  
Stanford University  
Stanford, California

*Bistatic-radar experiments conducted on the Moon are sensitive both to the surface and subsurface structure of the lunar crust. The available data suggest that conditions on Mars are probably equally conducive to electromagnetic soundings of surface properties. In the case of Venus, radar may provide the only method for surveying the surface for some time. At lunar ranges useful experiments have been performed using only "leftover" radiation from spacecraft telemetry systems. Proportionally greater gains are expected from systems designed specifically for radar sounding of surfaces.*